RICE UNIVERSITY

The Effect of Material Organization on the

Structural Properties of Porous Architectures

by

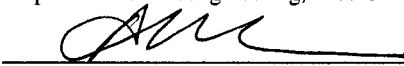**Matthew Wettergreen**

A THESIS SUBMITTED

IN PARTIAL FULFILLMENT OF THE

REQUIREMENTS FOR THE DEGREE
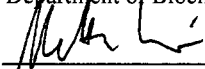
Doctor of Philosophy
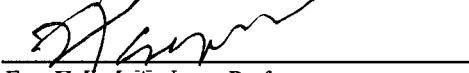
APPROVED, THESIS COMMITTEE:

Michael A. K. Liebschner, Assistant Professor
Department of Bioengineering, Rice University

Antonios G. Mikos, Professor
Department of Bioengineering, Rice University

Matteo Pasquali, Associate Professor
Department of Chemical and Biomolecular Engineering, Rice
University

Eser Yuksel, Assistant Professor
Department of Surgery, Baylor College of Medicine

HOUSTON, TEXAS

APRIL 16th, 2008

ABSTRACT

The Effect Of Material Organization On The Structural

Properties Of Porous Architectures

by

Matthew Wettergreen

Tissue engineered scaffolds are often considered "black boxes." Post implantation, they are solely expected to provide temporary mechanical support and foster tissue ingrowth while *de novo* tissue forms around its matrix. This is rarely the case however, as the post implantation interaction between this foreign body and the host biological system is largely uncontrolled. A growing body of concrete results is overwriting previous holistic knowledge to provide firm and hierarchical guidelines for successful scaffold design. Two areas have recently demonstrated fertile ground for progress: 1) the mechanical strength of architecture and 2) the fluid flow properties of that architecture, both of which act on different void phases. Mechanical properties are controlled by the solid phase of the matrix, while the void space determines fluid flow characteristics.

The objective of this dissertation was to demonstrate the benefits of an analysis of the structural properties of tissue engineered scaffolds combined with the specific design potentials of computer-aided tissue engineering (CATE) for orthopaedic applications. Two overarching goals directed this research. The first was focused on antipodal properties and addressed solutions which included an interplay between opposing poles while matching biological properties and secondly, to apply that knowledge towards the design of patient specific implants. Two antipodal properties were studied; 1)

modification of the solid phase was addressed with respect to structural mechanical properties and 2) modification of the void phase was studied to determine fluid flow characteristics of porous architectures. These concepts were then applied in real applications using CATE towards the goal of tissue engineered scaffolds for bone repair and drug regimen.

Acknowledgements

The first thanks go to my mentor Dr. Guy Adami of the University of Illinois-Chicago who taught me to think critically and fostered my burgeoning love of research: he is responsible for my choice to attend graduate school. The guidance of Drs. Gerald Graff, Jeff Lewis and Paul Malchow was instrumental in the creation of the Undergraduate Research Symposium and cementing pedagogy as a career interest.

The person at Rice that I am most indebted to is my advisor Dr. Michael Liebschner who always stuck up for me, was always available for us to bounce ideas off of and to troubleshoot the best solution to problems. His ideas are disruptive and seek to circumvent current trains of thought in biomechanics and bioengineering and it was an honor to take part in the several of those projects. My committee of Drs. Mikos, Pasquali and Yuksel provided key support and guidance through multiple roadblocks in my thesis. Maria Oden gave me the respect of a colleague and co-instructor, providing me for three years the opportunity to practice my teaching skills through the CAD section of Senior Design and finally as an instructor for Systems Physiology.

My labmates Jeremy Lemoine, Kay Sun, Wafa Tawackoli and Alistair Templeton were instrumental in day-to-day functioning from working through procedures to our less productive activities. I am especially grateful to Brandon Bucklen who was a perfect research partner, friend and rock over our time in Houston and Philadelphia. The CATE Lab of Drexel University provided a home for Brandon and me for the majority of 2006 and collaboration with Dr. Wei Sun, Bobby Chang, Binil Starly and Lauren Schor formed the groundwork for all of Brandon and my CATE work.

Table of Contents

List of Figures

List of Tables

LIST OF ABBREVIATIONS

ALP	Alkaline Phosphatase
BAPO	bis-(2,4,6-trimethylbenzoyl) phenylphosphine oxide
BMU	Basic multicellular unit
CAD	Computer Aided Design
CATE	Computer Aided Tissue Engineering
CT	Computed Tomography
μCT	micro-Computed Tomography
DA	diacrylate
DEF	diethyl fumarate
DEXA	Dual Energy X-Ray Absorptiometry
DMT	N,N-dimethyl-p-toluidine
EAE	Energy Absorption Efficiency
FEA	Finite element analysis
FEM	Finite element modeling
FDM	Fused deposition modeling
MES	Minimum effective strain
PDMS	poly (dimethyl siloxane)
PLGA	poly(lactic-glycolic acid)
PPF	Poly(propylene fumarate)
PPF/PPF-DA	Poly(propylene fumarate)/poly(propylene fumarate)-diacrylate
RP	Rapid prototyping

Rhino   Rhinoceros3d

PDMS   poly (dimethyl siloxane)

SFF   Solid freeform fabrication

Chapter 1: Introduction and Objectives

1.1 Introduction

The overall goal of this dissertation was to determine relationships that govern the apparent properties of architectures evaluated solely from a material arrangement standpoint. This work specifically evaluated the structural and material properties of regular architectures that exhibit symmetry, homogeneity, and order (outside-in). Additionally, this work evaluated the apparent properties of architectures composed of random pore distributions (inside-out). These properties and their relationships were determined through modulation of the solid material and manipulation of the void space. Characterization of these structures was then used in the application of Computer Aided Tissue Engineering (CATE) for the design of novel implants and tailored solutions to clinical problems stemming from tissue defects. Applied focus was specifically for the design of implants for bone regenerative scaffolds or other mechanically modulated systems. Numerous studies have demonstrated effects of specific scaffold architecture on tissue ingrowth [1-15]. As of yet, no rules have been generated to explain the structure's exact effect nor has any quantifiable difference ever been demonstrated for given architectures as a result of their material organization [16] Therefore, the global hypothesis of this research was that material spatial organization significantly influences the material properties of a scaffold at multiple structural levels, specifically its surface mechanical environment, apparent biomechanical properties, and permeability [17]. Furthermore, the use of design principles to create structures and scaffolds with specific architectures may be used to characterize mechanisms that dictate tissue regeneration in therapeutic scaffolds.

The architectural components (examination of the solid phase, examination of the void phase) of these studies were chosen for two reasons. First, the simplicity of a general shape exhibiting symmetry and homogeneity allows for the construction of relationships between material organization and resulting structural properties. Architectures of this type have previously been explored as constructs for tissue regeneration scaffolds [18-21]. Utilizing a randomized system of pore architectures, while a less general case than the ordered one, should follow similar rules. Random architectures such as these are the simplest to generate and have been used repeatedly as constructs to facilitate tissue ingrowth and regeneration [10, 14, 15, 22-28]. The expected benefit of this research is that the determination of which architecture, if any, plays a role in the modulation of tissue regeneration for bone tissue engineering.

1.2 Overall Objective

The engineering goals of this dissertation work included the construction of relationships that relate the arrangement of material to structural and material properties of the global architecture. These architectures may then be used *in vitro* and *in vivo* to evaluate the effect of design on selection by biological systems for tissue regeneration and laboratory investigation tools.

The dissertation work has goals structured around specific aims:

1.3 Specific Aims and Hypotheses

1.3.1 Specific Aim #1(Chapter 3)

To determine the effect of material organization (strut length, strut diameter, connectivity, material volume) on the mechanical properties (structural stiffness, strength, structural modulus, ultimate stress) of solids based on regular, porous architectures.

Hypotheses

- A deliberate arrangement of architecture can be used to usurp density as the dominant controlling factor of strength

- For a constant density, tailored mechanical properties can be obtained through reorganization of architecture.

- Rapid Prototyped models can be used as accurate representations of modeled cellular solids and can replicate finite element modeling results of the structural and material properties of the porous architectures.

1.3.2 Specific Aim #2 (Chapter 4)

To determine the effects of void phase organization (pore size, surface to volume ratio, pore architecture, total void volume) on the mechanical properties (structural stiffness, strength, structural modulus, ultimate stress) and flow properties of solids based on particulate leached systems with defined pore architectures.

Hypotheses

- A derived relationship exists between surface to volume ratio of a void architecture and its resulting permeability.

- A derived relationship exists between surface to volume ratio of void architecture on the structural properties of a random porous architecture.

- A derived relationship exists between porosity and permeability for defined architectural parameters and porosity values.

1.3.3 Specific Aim #3 (Chapter 5)

To apply the derived relationships in Specific Aim 1 and 2 through material rearrangement towards the design of tissue regenerative scaffolds employing the steps of Computer Aided Tissue Engineering

Engineering Objectives

- Utilize architectures characterized in Specific Aim 1 in the design of tissue regenerative scaffolds for a load-bearing system to determine the dominant design principles governing the success of such an implant.

- Utilize derived relationships from Specific Aim 2 in the design of implants which will require fluid transport and determine the dominant design principles governing the success of these implants.

Chapter 2: Background

The inability of bone to regenerate itself in cases of gross trauma poses a problem still unsolved. The complexity of bone tissue itself is compounded by the requirement that it provides structural support for the patient. Successful treatment should stimulate new bone growth resulting, at the end state, in native bone tissue with no trace of the regenerative device. Bone scaffolds have shown promise in regenerating some critical size defects in non-load bearing anatomic sites but results vary with anatomy and species [29]. Additionally, problems arise in load bearing sites where the scaffold must endure a modicum of mechanical loading. Success requires insight into the mechanisms that dictate bone growth as well as thorough characterization of the intended implanted scaffold. Currently, research has begun to characterize input parameters such as morphology, porosity, permeability and their effect on the resulting tissue ingrowth [30, 31]. The use of techniques such as Computer Aided Tissue Engineering (CATE) may in the future promote the regeneration of a functional bone system where a defect once lay [32]. The following sections will illustrate the importance of structure for function in nature and more specifically in bone. The subsequent architectural discussion will be framed in the effects of specific parameters of architecture and the past work that has attempted to incorporate these concepts into scaffold design.

*2.1 Bone Structure and Hierarchy**

Bone is a composite material that exists on at least 5 hierarchical levels: whole bone, architecture, tissue, lamellar, and ultrastructural level (Figure 1). The whole bone

---

* This section adopted from Liebschner MA, Wettergreen MA *"Optimization of Bone Scaffold Engineering for Load Bearing Applications."* In Ferretti P., Ashammakhi N.: Topics in Tissue Engineering, e-book on tissue engineering, T. Waris & N. Ashammakhi, Chapter 22, www.tissue-engineering-oc.com, 2003.

is at the greatest scale and represents the overall shape of the bone. This structure is composed of the architectural level, which contains the microstructure that defines the spatial distribution. Below the architectural level is the tissue level, which is inherent to the actual material properties of bone. The lamellar, or cellular level is below the tissue level and is composed of sheets of collagen and minerals deposited by osteoblasts [33]. The minimal scale level is the ultrastructural level which incorporates chemical and quantum interactions [34]. These five levels comprise structural differences in size magnitude between the subsequent levels, spanning from the whole bone to the chemical and quantum level [35]. In order for the research community to expedite a full characterization of bone, each separate constituent that contributes to the system as a whole must be evaluated. There are certain advantages that can be gained by separating the structure into microstructural organizational levels. By viewing bone at different hierarchical levels it is relatively easy to compare different structures and tissues. Additionally, it is much simpler to define characteristic levels to use for analysis. Each level depends on the levels below it to provide function and structural support for the load transfer it experiences from the level above (Table 1).

Whole Bone Level

The top level of bone is the organ level, or whole bone level, and it represents the summation of the structural and material properties of all the levels of bone. At this level, the bone functions on the order of magnitude of the organism, providing structural support and aiding with locomotion. The mechanical characteristics of whole bone are a result of the complete structure's geometry (Figure 2). Interaction between whole bone
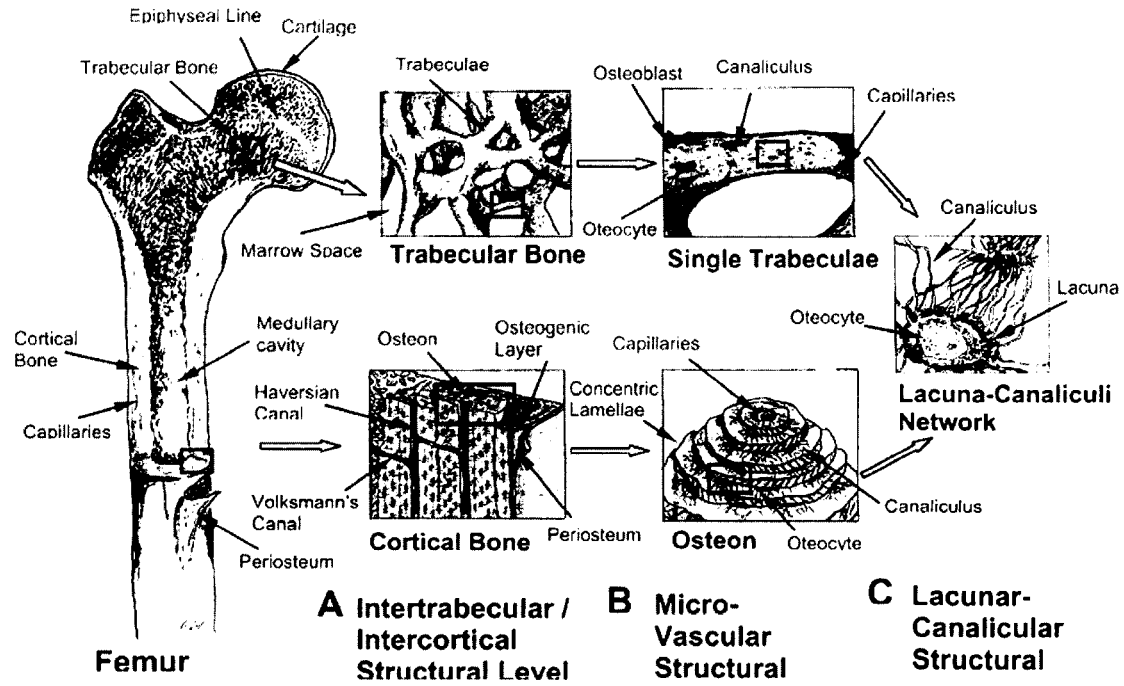
Figure 1. Illustration of structures corresponding to hierarchical levels of bone. [36].

Table 1. Structural Hierarchy and Mechanical Properties of Bone [36].

Level	Dimensions
Whole Bone	3 mm – 750 mm
Architectural Level	75 – 200 µm (T); 75 µm – 8 mm (S) 100 – 300 µm (C); 100 µm – 5 mm (S)
Tissue Level	20 – 75 µm (T) 20 – 100 µm (C)
Lamellar Level	1 – 20 µm (T) 3 – 20 µm (C)
Ultrastructural Level	0.06 – 0.4 µm (T) 0.06 – 0.6 µm (C)

T = Trabecular Bone; C = Cortical Bone; S = Scaffold

and other constituents of the body may include tendons, ligaments, muscles and other

bones.

Optimization at this level is not seen in a shape change, but as a net mass change

resulting from external/internal factors.

Shape changes are minimal and the

mechanical strength of the structure is

derived from the total geometry of the

bone and the distribution of tissue.

Remodeling that may occur at lower levels

is measured as percent increase or

decrease in mass in the overall bone [38].

Architectural Level

The architectural level of bone

relates to the characteristic micro-

architecture of bone tissue, specifically

cortical and trabecular bone (Figure 3).

These structures serve to provide

Figure 2. Example of Whole Bone Level. Human Femur [37]

mechanical stability to the global structure of bone distributed throughout the osteons

and/or trabeculae. This is the first level at which the remodeling of the organism can be

visualized as a change in architecture. Architectural reorganization also affects the

apparent properties of the structure. Two different architectures arise depending on

anatomical site and loading conditions. Trabecular bone, contained in the ends of long

bones and the site of bone marrow synthesis, exhibits anisotropy as a result of its rod and

Figure 3. On left, SEM of trabecular bone illustrating thinning of the trabecular in the center forefront. On right, photomicrograph of cortical bone illustrating the individual osteons and osteocytes [39, 40].

plate organization. Cortical bone is highly compact and orthotropic due to the circular nature of the osteons that make up its structure. One illustration of the micro-architectural differences between the two architectures is that cortical bone contains only microscopic channels through the center of the osteons whereas trabecular bone is highly porous (Figure 3) [41]. Mechanical function at the architectural level is to provide support for the overall bone structure and, specifically in trabecular bone, to act as a shock absorber and resist compressive loads [42]. The mechanical strength can be related to but is not limited to several geometric constraints such as trabecular thickness, trabecular spacing, bone mineral density, and bone surface to bone volume ratio. These constraints can be obtained from imaging techniques used to evaluate trabecular tissue [43]. Strain sensed in the bones at this architectural level causes the cells on lower hierarchical levels to remodel the gross arrangement of the micro-architecture at the surface [44]. Although gross reorganization of the bone micro-architecture is seen at this level as a change in geometry and architecture, the deposition and resorption occurs at the cellular level. Orientation and mechanical qualities change between anatomical sites and between bones as a result of dynamic loading and stress on bone tissue. The mechanical characteristics of the architectural level are largely due to the spatial distribution of the tissue (micro-

architecture) and less so due to the properties of the material composing bone. The remodeling at this stage does not take an ordered path and thus may appear random, but the structure that results from it is anything but unordered. The rods and plates that compose the trabecular bone follow a pattern of resorption and deposition according to the mechanotransduction principles of the bone. Due to the complexity of the bone, previous models have attempted to approximate the bone as simpler solids, such as open-celled foams or tetrakaidecagons [8, 16]. This will be discussed later in the mathematical approximation of trabecular bone.

Tissue Level

Below the architectural level of bone is the tissue level, which directly addresses the mechanical properties of the tissue. The material properties at this level provide support for the geometry of the architectural level above it. Remodeling of bone at this stage of the hierarchy alters the material properties of the bone tissue. Tissue properties are those that relate directly to the mechanical characteristics of the bone independent of the micro-architecture. Properties such as stiffness, Young's Modulus, yield point, and energy to fracture can be dealt with on a fundamental material level. The optimization that occurs at this level is as a result of the modification of the material properties, and is responsible for the apparent properties of the architectural level. There is growing agreement within the biomechanics community that cortical bone and trabecular bone biomechanical properties do not differ at this structural level [45]

Lamellar Level

Below the tissue level of bone is the lamellar level (Figure 4); the layers of bone deposited by single cells. Lone structures, the lamellae are laid on top of each other like

composite board in directions that vary by up to 90 degrees in orientation. These laminations are deposited by the basic multicellular unit (BMU). This process involves the recruitment of osteoclasts that resorb bone; osteoblasts are then recruited to deposit bone; the process ends with the encapsulation of the osteoblasts
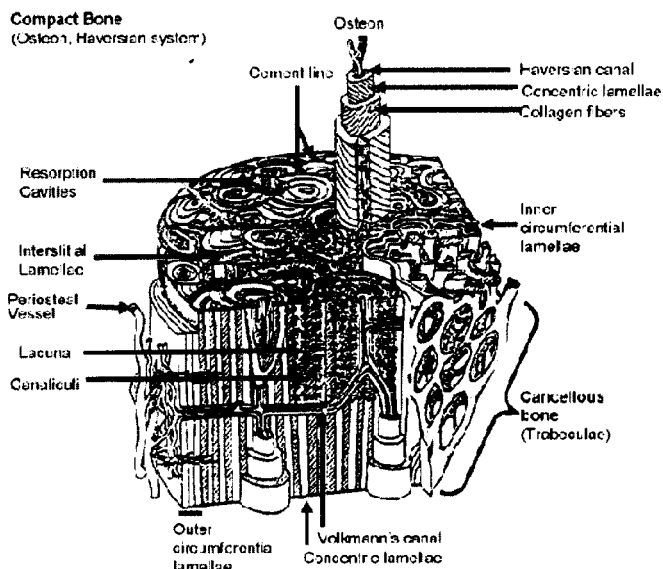
Figure 4. Illustration of Lamellae.

in the bone matrix before they differentiate into mechanosensing osteocytes; finally, the osteoblasts deposit a layer of hydroxyapatite onto a woven bed of collagen [41, 46]. The sheets of lamellae are on the order of 3-20μm in thickness [35]. It is this process that produces all of the lamellar bone (Figure 4) in the body, which is a much stronger and better form of bone than embryonic or woven bone. The deposition and resorption of bone occurs only at the surface, however, the lowest layers of lamellae are not affected unless massive bone loss is experienced, as in osteoporosis.

Ultrastructural Level

The lowest level of the bone hierarchy considered in this review is the ultrastructural level. At this level chemical and quantum effects can be addressed. The order of magnitude for this level allows the analysis of the mechanics and architecture of the collagen fibers with the minerals [34]. The ultrastructural level is on the order of calcium and other minerals that are a part of bone, such as phosphate and magnesium.

The advantage of viewing bone at this level is that it allows the study of an additional function of bone that cannot be addressed until this size. This function is the use of bone as mineral storage for the organism. Mineral storage and the effects of chemistry are the main functional points at the ultrastructural level as is the orientation of collagen in the lamellae [33]. The design of bone at this level illustrates how the micro-architecture of the structure must be evaluated as well as the nano-architecture. Several studies have been completed on the difference in ultrastructural mechanical properties as a result of the collagen orientation and the amount of mineral deposition on the collagen beds. The degree of mineralization will affect the final stiffness of the bone itself as well as the overall ash content [35].

2.2 Mechanical Aspects of Tissue Engineering[*]

It is well known that biological activity is regulated to a varying degree by mechanical signals. Evidence of this exists in the mechanical stimulation of axons through stretch [47], regulation of bone shape and Wolff's Law [48-51], induction of biochemical cellular responses [52], the modulation of vascular diseases such as hyperplasia through pressure modification [53, 54], etc. Nevertheless, very little success has been achieved using basic science information about mechanosensitivity for the goal of designing tissue engineered constructs (TECs). An underestimation of the importance of mechanical cues (with respect to issues such as cellular differentiation, growth factor

delivery, and material development), and an uncertainty of how to apply the known information can be attributed to this lack of published knowledge.

Tissue engineering is a gateway into a future where few will suffer because of organ availability or maladies caused by dysfunctional organs. Its development impacts all branches of medicine and certain areas of plastic surgery. Insofar as it relates to the latter, mechanical knowledge is most critical when the tissue in question has a mechanically functional role. Even still, aesthetic reconstructions with no obvious function still require mechanical support in order to maintain the shape (e.g. soft tissue reconstruction of the ear)[*]. The tissues that stand to benefit the most from the addition of a mechanical component to the tissue engineering paradigm will be orthopedic in nature (i.e. bone and muscle); again, where the structure is intimately related to the function. For example, in partial glossectomy, an ideal tongue reconstruction demands the coordination of soft tissue and muscle function to account for speech, food digestion, and aesthetics [55].

2.2.1 Instances Of Mechanical Considerations In Tissue Engineering

Before delving specifically into orthopedics, it is worth summarizing some advances in tissue engineering that utilize biomechanical principles. Even traditional "mechanical tissues" are often not tissue engineered via direct mechanical stimulation. For example, cell therapy and growth factors are frequently used for tendon, ligament and cartilage [56, 57]. The rationale is that these tissues have a limited capacity for regeneration of non-fibrous tissue and have repair cascades which are sensitive to growth

---

[*] And vice versa, a (mechanically functional) reconstruction with no obvious shape requirement still will need to follow local rules for tissue growth (spinal cage).

factors. Thus, a biochemical catalyst may operate in place of native mechanical loading. Biochemical strategies which replace mechanical strategies are an exception to the rule, but nonetheless portray the status of a field which has had great success in material development and chemistry.

Mechanically induced tissue formation could be considered the fourth factor of the tissue engineering paradigm. This paradigm is a generalized schema whereby some combination of a). cells, b). growth factors, and c). substrate are combined into an implantable replacement. Mechanical aspects like the appropriate mechanical cues, and the frequency and magnitude of these cues, remain elusive; yet, arguments that tissue is accentuated under biomechanical culture [58], and has superior cell distributions [59], can scarcely be refuted.

There has been significant ground work investigating the role of biomechanics for a wide variety of tissues. In cartilage, dynamic loading of chondrocytes as well as other cell types [60] is stimulatory as evidenced by markers of mature cartilage like hydroxyproline and glycosaminoglycan [61]. Subsequently, tissue substitutes using chondrocytes seeded in hydrogels [62] or other scaffolds have been cultured under physiological deformation which is believed to be responsible for tissue maintenance and to bring about the appropriate zonal morphology [63]. Ion channels in vascular endothelial cells can be regulated by static stretch which has implications for cardiac tissue as well as blood vessel formation [64]. Moreover, on the tissue level, it was found that a human saphenous vein responded differently to static culture, constant pressure, and flow perfusion [65]. The latter two raised the levels of a protein-kinase involved in the signal transduction pathway of vascular remodeling. Indeed, this is relevant in tissue

engineering as vascular tissue appears susceptible to mechanically induced pathologies such as high pressure or shear stresses [54]. Skeletal and cardiac muscle is also biomechanically active. With respect to cardiac muscle, it has been shown that human heart cells align in the direction of loading, and demonstrate an increased maximum tensile strength under cyclic strain [66, 67]. Cardiac tissue engineering strategies may be carried out by either injecting cardiomyogenic cells (from various cell sources) directly into the myocardium or through substitute tissue equivalents [68]. A recent study proposed a promising tissue equivalent consisting of parallel-oriented polymer micro-fibers acting as a conduit for skeletal myoblasts [69]. These examples represent just a portion of the large volume of research that is currently being done in mechanobiology.

The majority of research thus far linking biomechanics to tissue engineering suffers because it is limited to the cellular level, and the genesis of tissue. Therefore, no distinction is made as to which mechanical cues are necessary to coordinate growth past its developmental form. Likewise, there is little hope to bring into light information on the reference frame of measurement unless a concerted effort is made to apply a unifying metric of scale, in which the mechanical conditions of similar experiments may be compared. Coincidentally, there is very little known regarding the mechanical aspects of continuum portions of a tissue or a whole organ, with the exception of one tissue, bone.

2.2.2 Mechanical Requirements Of Tissue

Each tissue in the body has a unique function, and therefore a different set of mechanical requirements. Bone has an exceptional list which includes the capability to provide structural rigidity, act as a reservoir for ions and calcium regulation, and provide

a framework for the transfer of muscle forces [70]. The inability of bony defects to be adequately and quickly replaced has led to a conglomeration of research seeking to provide cell seeded scaffolds for both mechanical support and biological functionality. This need arises in a number of clinical situations including tissue degeneration due to osteoporosis [71, 72], voids caused by tumor resection [73], damage due to trauma [74], and a variety of other genetic diseases affecting the formation of mature bone [75].

Mechanical Usage. Because bone is a living tissue, the manner in which local mechanical signals are transduced is salient. If a tissue's mechanical usage may be understood, then tissue engineering solutions may be formulated accordingly. Wolff's Law, theorized in 1892, was the first to credit bone mechanics for bone shape [76]. His trajectorial theory stated that trabecular bone struts intersected at right angles that were aligned with the principle stress axes, which has since been proven incorrect and updated [77, 78]. A mechanical usage window was introduced by Harold Frost in order to explain the metabolic adaptation of bone to mechanical signals (see Figure 5, adapted from [79]). This terminology as well as his "mechanostat" theory helped to explain the apparent level biological machinery of bone. The "usage" of bone is defined as the voluntary mechanical loads on a skeleton during a typical week [80], and is delineated by units of strain. Studies have shown that strain levels and strain rates in all matter of humans and animals are predominately constant [81], which makes strain a robust metric of consideration.

Frost's "mechanostat" was one of the first theories to adequately explain many facets of mechanically induced bone formation through a lumped-parameter model.

Without considering all the cellular detail, his model describes a control process of bone mass/strength changes. The term "mechanostat" comes from the analog to thermostat; where deviations from a set point trigger the mechanism to turn "on", while with no deviation the mechanism remains "off" [82]. Frost's model was able to predict thirty-two verifiably occurring phenomena related to bone, such as the existence of a safety factor in load bearing bones [79].

The usage is described in four quadrants as seen in Figure 5. In the disuse window (DW), strains below $50\mu\varepsilon$ cause an osteopenia-type loss of mass where material near marrow is evenly resorbed such as occurs in age-related osteoporosis. In the adapted window (AW) that spans the remodeling and modeling thresholds, strains between $100 - 1000\mu\varepsilon$, trigger conservation remodeling – where architecture and strength are maintained with "old" tissue replaced by "new" tissue. In the mild overload window (MOW), bone mass increases not because of a higher remodeling metabolism, but because of lamellar modeling drifts which seek to restore the lower strain levels of the AW. At strains larger than $3000\mu\varepsilon$, microdamage is proportionally larger than the reparation by remodeling drifts, resulting in decreased strength in the pathological overload window (POW) [83]. Additionally, the intermediate set points, or thresholds, may be subject dependent or altered by a state of disease to explain bone drifts [41].

There are some limitations to Wolff's Law and the "mechanostat" theory made evident in recent years. Dynamic loading is not elegantly addressed although this is critical in the mechanotransduction of at least bone [84] and cartilage tissue [85]. In bone, a short bout of dynamic loading increased bone formation by recruitment of surface cells [86], while longer loading regimes at similar magnitudes appeared to be detrimental to a
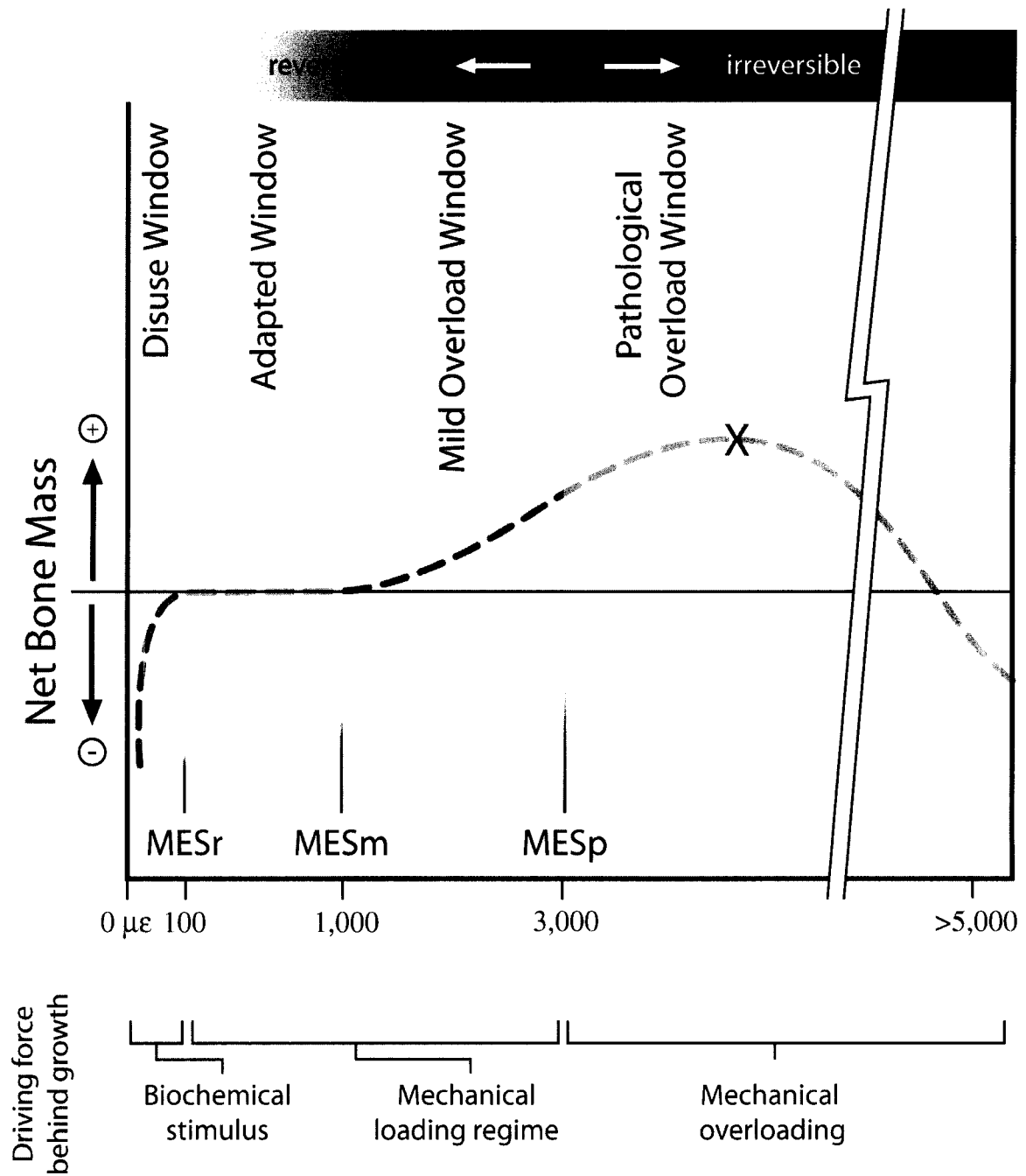
Figure 5. Mechanical Usage Window of bone. MESr, MESm, and MESp are the remodeling, modeling, and pathological mechanical thresholds, respectively. Below the MESr, biochemical stimuli is required to drive adaptation. Within MESr – MESm, mechanical loading is the dominate force. Below the MESp, mechanical loading is reversible, while above the MESp, irreversible damage may occur.

loaded implant within a rat tibia, when compared to static controls [84]. Alternative cell types also have differing sensitivities to magnitude of loading. Cartilage cells prefer smaller dynamic loading [61], while it is unclear if there is a preference in bone. Thus the effect of the magnitude and type of loading is not addressed by Wolff's Law or the "mechanostat"; neither does each qualify completely why the architecture of bone appears the way it does morphologically.

Structural Considerations. Mechanical properties are not constant in each structural reference frame. The structural hierarchy from largest to smallest is the whole bone, architectural, tissue, lamellar, and ultrastructural levels (see Table 1). The whole bone level (3 – 750mm) describes the most macroscopic look at bone, including muscles and tendon attachment sites. The two distinct architectural regions (75 – 300μm) are trabecular bone composed of rods and plates found in the ends of long bones, and cortical bone, comprising the concentric shaft of long bones. The tissue level (20 – 100μm) consists of individual trabeculae or osteons which have properties determined from the constituent material, a combination of organic matrix and mineral, as opposed to apparent properties that include void space [87]. The lamellar level (1 – 20μm) is one step smaller, and is composed of sheets of collagen and minerals deposited by osteoblasts [33]. The ultrastructural level (.06 - .4μm) is the smallest basis which consists of chemical interactions and quantum level relations, and is less often considered due to difficulty in its characterization [87].

The ability to determine mechanical properties at each individual level is somewhat limited due to mechanical testing protocols, yet there is much information on

the tissue and architectural levels. For an in-depth review see Liebschner et al [29]. As per Table 1, the architectural modulus values for trabecular [88] and cortical bone [35] are less than that of the its respective tissue properties [35, 89]. This occurs because the former is estimated from a continuum composite of bone and void, while the latter captures the mineral phase and as result is an order of magnitude larger. Naturally, the whole bone level [29] yields a wider spectrum of modulus values – as the structure of the whole is composed of its individual hierarchies, each of which has an associated range.

The architecture has a terrific impact on the structural properties of bone, and in turn, on its mechanobiology. Native tissue "sees" mechanical stresses coincident with the shape and stress patterns on the local level, which are not adequately capture by a single "modulus" value. The structural hierarchy of bone is one of the most compelling arguments for a biological machinery, and ranges from the radial configuration of growing osteons, to the rods and plates of trabecular architecture, to the symmetric interface which occurs during endochondral ossification [83]. One simple example illustrating the importance of architecture may be seen in Figure 6. Consider a composite bone/cell or scaffold/tissue arrangement where the composite experiences a uniform level of deformation, or isostrain. In the case of the bone/tissue arrangement, tissue will deform consistent with the scaffold but will experience much lower internal stresses (assuming tissue has a lower modulus). Isostress, where each constituent receives an equal stress, results in proportionately larger deformation of the softer material, in this case the tissue. All bone architectures may be viewed as receiving some combination of isostress and isostrain. Therefore, a given architecture contains a complex milieu of stress and strain profiles which are a function of the geometry.

Isostrain

$$\varepsilon = \varepsilon_{scaffold} = \varepsilon_{de\ novo\ bone}$$

$$\sigma = \sigma_{scaffold} + \sigma_{de\ novo\ bone}$$

Displacement continuity
across all layers

Isostress

$$\varepsilon = \varepsilon_{scaffold} + \varepsilon_{de\ novo\ bone}$$

$$\sigma = \sigma_{scaffold} = \sigma_{de\ novo\ bone}$$

Stress continuity
across all layers
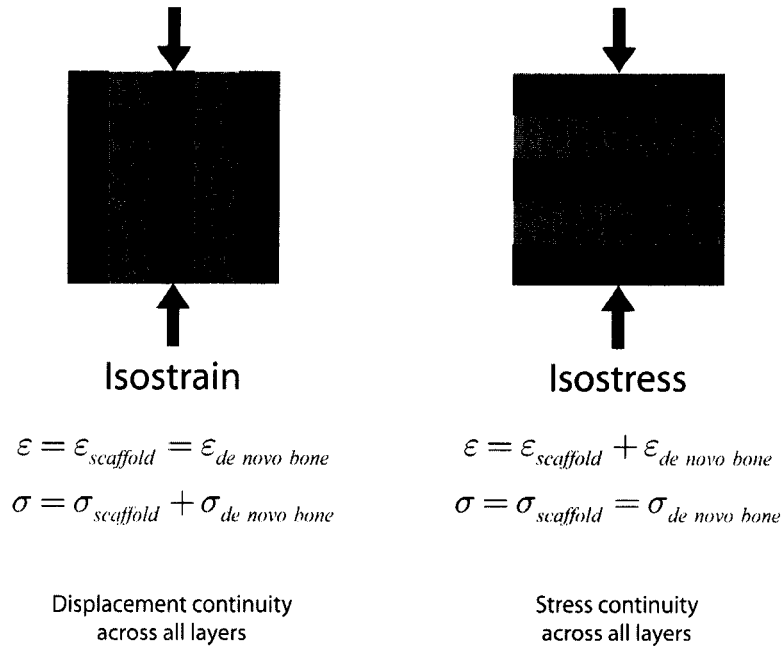
Figure 6. Isostrain and Isostress of a composite material. In isostrain each component has a uniform deformation, while in isostress each material has a uniform stress. The stress and strain, for isostrain and isostress, respectively, are in general "additive" but depend on the moduli and volume fraction of each component.

Bone architecture is not only patient-specific, but site-specific. The ratio of trabecular bone to cortical bone, bone mineral density, and boundary geometry of a femur will be different than that of a vertebral body. Figure 7 illustrates some of these key architectural differences for a trabecular portion of a human vertebral body and iliac crest. The former, has a combination of rods and plates, while the latter is composed of thicker plate sections, devoid of a truss-like structure. Aside from morphological differences, there are clear structural anisotropy distinctions. The vertebral sample is more aligned in the superior-inferior direction in accordance with the direction of load due to weight in the spine. The iliac crest is less organized in its fabric directions. Additionally, the two samples (though unmeasured) probably have similar yield and ultimate strains on the apparent level, but the stresses they experience are drastically dissimilar [43]]. Disuse osteoporosis, which is sensitive to mechanics, will affect the vertebral body, causing perforations and reductions in trabeculae, though the iliac crest will not be vulnerable. The implication for tissue
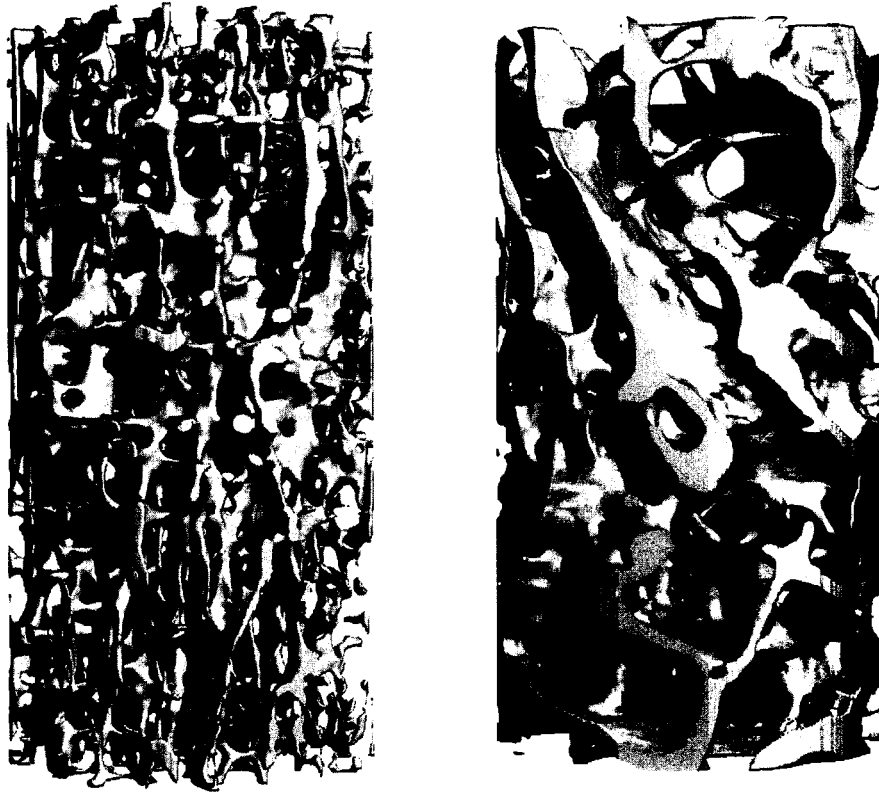
Figure 7. Site-specific architectures of the trabecular portion of a human, lumbar vertebral body (left) and iliac crest (right).

engineering is that constructs must be designed with *a priori* information on the site, its boundary geometry, and the loading it experiences.

Mechanotransductive Considerations. The previous arguments give rise to further questions regarding the mechanotransductive nature of bone. If in fact, a certain variety of bone cell is responsive to a stress-derived parameter as opposed to a strain-derived parameter; shouldn't the tissue engineering design strategy be tailored accordingly? Similarly, won't the significance of isostress and isostrain vary with this dependence? On the other hand, if the scaffold material or bone tissue can be considered linearly elastic, shouldn't the independent variable, strain, be considered as the mechanotransductive

element? The reality is that it is unclear which signaling events are prominent for the evolution of structure under mechanical loading.

Nevertheless, experiments have addressed this issue and arrived at varied conclusions. One problem involves the difficulty in isolating an experimental loading type. For example, how does one apply strain to a substrate in culture media without inadvertently creating fluid flow conditions (causing stresses)? Additionally, since cell seeding always requires adhesion to a substrate, much of the literature inherently provides information about substrate-cell relationships [90] which, while helpful for the whole of tissue engineering, only adds complexity to the investigation of mechanostransduction.
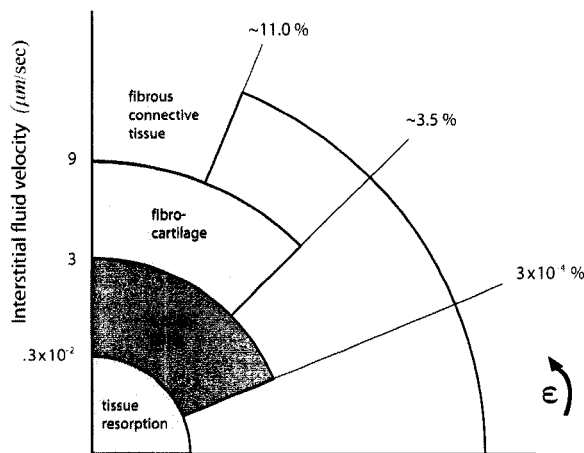
Figure 8. Tissue differentiation based on combinations of strain and interstitial fluid velocities.

Three types of mechanical indicators have been considered: 1). fluid shear stress, 2). direct deformation, and 3). changes in stored energy. Fluid shear stress is believed to be a major mode of cell transduction. Small diameter canals surrounding osteocytic cell processes cause large pressure gradients even when small mechanical loads are applied to the exterior. These loads are thought to induce a fluid gradient which then acts as a shear stress on the osteocytes [91]. One way mechanical signals influence tissue formation is through differentiation of cells. Figure 8 portrays the relationship between interstitial fluid velocity, strain, and the differentiation pathway [50, 92] It is clear that bone tissue

prefers a balance of small strain and small fluid velocities, while an overexposure (to either) will promote fibrous tissue. You et al. found that human and rat osteoblastic cells are less sensitive to substrate deformation than oscillatory fluid flow, at least in regards to expression of mRNA levels of osteopontin and intercellular calcium concentrations, two factors thought to be responsible for bone cell recruitment and proliferation [93]. Despite these findings, there is certainly evidence of strain mediated remodeling at the cellular level. Cowin et al. described how strain may be amplified in the lacuna-canalicular network. His argument is that flow generated through the canaliculi pass over the fiber glycocalyx and causes a hydraulic resistance. This resistance will then distend the cell producing a hoop stress [94] and a straining of the cell in the direction of flow. You et al. further deduced that the effect of the drag force on the pericellular matrix to be an order of magnitude higher then the shear stress, which can lead to hoop strains 10-100 times larger than the applied strain [95]. Direct experimental measures of stored energy have been much sparser because there is no good experimental protocol for its measurement. Kunnel et al. suggested that hysteresis energy may be a valid indicator of anabolic growth in bones upon mechanically applying cyclical load to neo-natal mouse tibias [96]. Inferences to stored energy, however, are most often accomplished through model techniques where the mechanical properties of the tested material are known so that the stresses may be ascertained [48]. Ruimerman's model on three dimensional representations of trabecular micro-architecture concludes that strain energy density leads to the closest approximation in trabecular bone morphology [97]. This conclusion was based on comparing the results of his simulations with reasonable values of volume

fraction, trabecular spacing, and net full turnover, with those values observed experimentally.

2.2.3 Designing Mechanical Tissue Engineered Constructs

Designing TECs for bone is a daunting task, in part, because of the wealth of mechanical factors discussed. Realistically, only a few of these criteria may be optimized at once. Ideally, the TEC would have an architecture that 1). conforms to the boundary, 2). has mechanical properties that are site-specific to the defect region and is inhomogeneouos to capture native tissue anisotropy 3). exists within the mechanical usage window (at least on the architectural level), 4). degrades in a time frame that is synchronous with the sum of the infiltrating and developed tissues, and 5). promotes tissue growth by supplying the appropriate mechanical cues on the tissue and cellular level.

Computed tomography and magnetic resonance imaging have had success in isolating the boundaries of bone [98]. Computed tomography produces three-dimensional reconstructions of X-ray attenuation coefficients, which can be correlated to density and apparent level properties. This, in turn, is useful in creating finite element models which can predict the internal stresses and strains within an architecture or be correlated to whole-bone strength [99].

Many of the design criteria are particularly amenable to computer aided design which has spawned the field of computer-aided tissue engineering (CATE). For example, *in vivo* applications like computer assisted surgery prohibit obtaining mechanical data through experiment testing of bone samples. However, if an *in vivo* scanner can delineate

the necessary bone tissue, it may be possible to model the internal stresses and architecture of the undisturbed environment.

Site-specific and patient-specific mechanical design may be addressed by CATE (see Figure 9). CATE describes a complete process of using imaging techniques to determine the boundaries of an implant region, modeling and/or optimization techniques for the scaffold, and computer-aided design methods of manufacture (with or without cellular components) most often utilizing rapid prototyping and negative molding techniques [100]. Results of finite elements models involved in the second step may provide approximations to continuum elastic moduli.
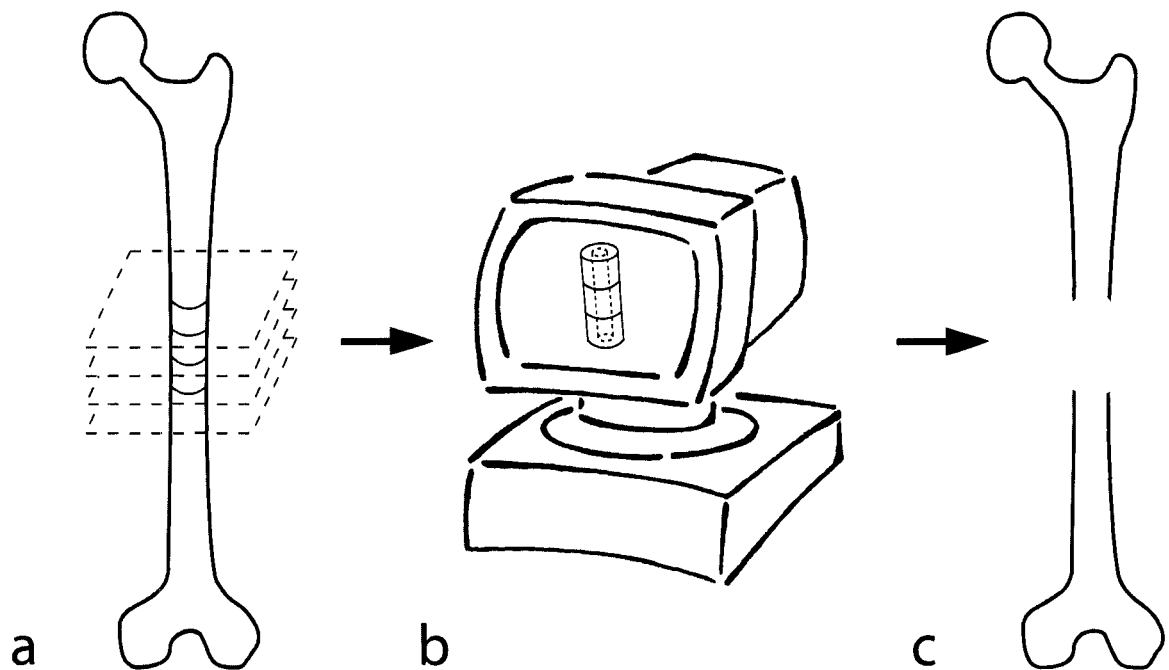
Figure 9. Process of CATE. The three components are a). imaging, b). modeling, and c). manufacturing.

Implant   ● Isostress

■ De Novo Bone   ○ Isostrain

t_0 $t_{\frac{1}{2}}$ t_∞
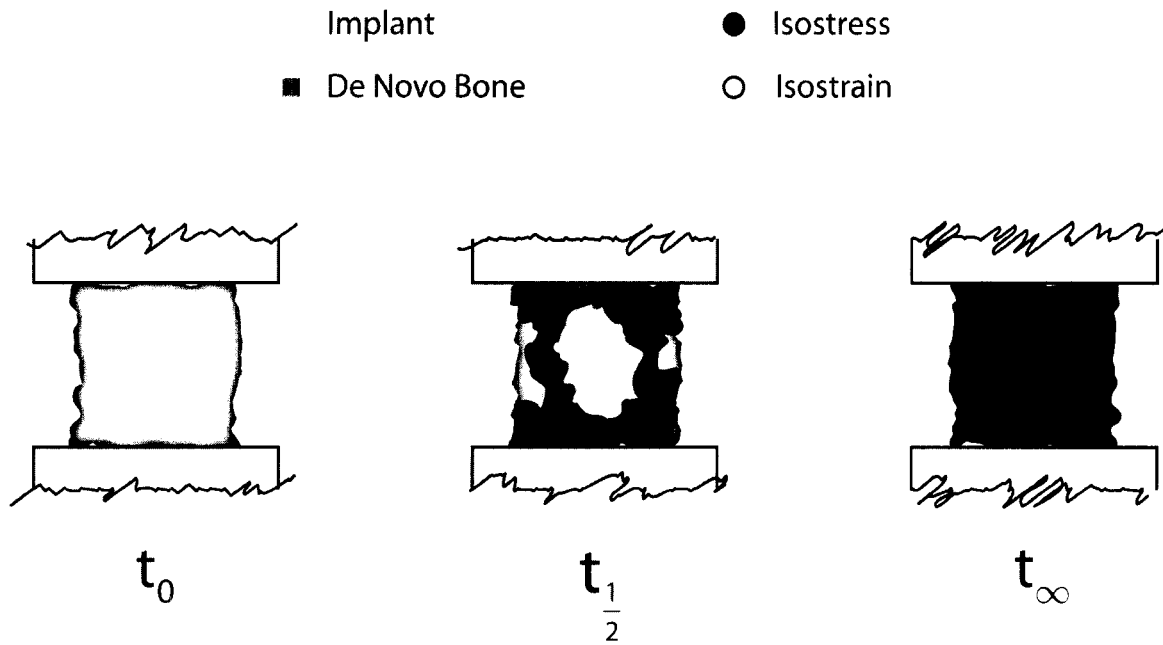
Figure 10. Degradation of scaffold and infiltration of new tissue into a TEC over time.

The rate at which a TEC degrades is critical and should be proportional to the rate of tissue infiltration and production. In practice, this matter has met with little success. The degradation depends on the type of biomaterial, its surface chemistry, and the local environment. Since design constraints of scaffold micro-architectures have not been identified, material scientists have been unable to develop biomaterials that have the sufficient strength of bone tissue and the rapid degradation rates required for metabolic turnover. Additionally, the degradation profile severely affects the tissue, if not the apparent, mechanical properties. As the tissue accumulates in the scaffold domain, the locations of *de novo* tissue determine the isostress and isostrain relationships (see **Error! Reference source not found.**). Hutmacher proposed a degradation profile where initially, at time t_0, the implant accounts for the entire mass and volume of the design space while at t_∞, after scaffold

degradation, the bone will be self-supporting [101]. An augmented version is presented in Figure 11, with emphasis on the mechanical properties as opposed to mass. As the volume of tissue within the TEC slowly increases, the apparent mechanical properties of the new tissue will increase only after sufficient extra-cellular matrix has deposited to support loading. It remains unclear what strength characteristics of the scaffold need to be present initially in order to achieve a final desired strength. Should the construct be stiffer initially or maintain a constant strength? Figure 11 (bottom) presents three proposed schema which, with the combination of degradation profiles, could define tissue viability during the regeneration process.

Based on current beliefs, the TEC will only support loads within the DW to AW (see Figure 5). In the DW, a tissue engineered solution should support

Figure 11. Time rate of change of design space volume, normalized modulus (with respect to the scaffold), and possible scaffold strength schema.

biofactors which stimulate growth despite insufficient loading. In the AW, a combination of loading and biofactors should be issued, or incorporated within the scaffold. At strains larger than the modeling threshold, mechanical regulation must be minimized, though it is unknown whether or not biofactors will be useful (by speeding up metabolism) or detrimental (by adding mass) within this loading range. The mechanical environment of the defect site is not likely to change, therefore the manner in which the tissue infiltrates and scaffold degrades will be responsible for determining the position along the abscissa in Figure 5. If the mechanical usage reaches the POW, and the right combination of isostress/isostrain exist, irreversible cell and tissue apoptosis will occur via mechanical overload. A scaffold's usage may be dictated quite well with CATE [32, 100] or topology optimization [18, 102, 103] techniques on the apparent level, but limitations with computing technology prevent similar methodologies on the tissue level hierarchy. One study used 7.6 million partitions to discretize the femur geometry at a resolution suitable to obtaining tissue level stresses [104]. Even so, it is not clear what mechanical objectives should be met at this level, once the stresses are determined.

There is some empirical evidence witnessed in nature for a uniform surface hypothesis. In one example, it was shown that bone responds through minimizing the stresses at the surface which is believed to reduce the probability of fatigue fracture or crack propagation [105]. Mattheck implemented a simple optimization routine that dramatically improves the fatigue life of structures by the reduction of peak stresses [106], which could be characterized as a tissue level optimization goal. Apart from this generalized surface criteria, little is known of the impetus behind bone shape evolution and thus an appropriate scaffold configuration at the tissue level. The best research to

date has been focused on the design of directional, anisotropic moduli of bone on the apparent level [107], which adds specificity to the scaffold design problem, but does not increase additional hierarchical information.

Material Considerations. Scaffold material determines both mechanical robustness and biological coupling of the scaffold with its environment. While previous studies have used materials that may have been biocompatible, they may have not been mechanically stable for use in a bone implant. The loading conditions that exist for bone defect sites are often much higher than the strength a biodegradable material can provide. Using a material that makes the construct stronger than the bone can also be a problem due to stress shielding or detrimental effects caused by unexpected surface oxide reactions *in vivo* that differ depending on base material [108]. A large problem noted early on in the development of hip replacements was stress shielding: a phenomenon whereby the brunt of the load carried by the stiffer material, titanium or cobalt chrome steel, resulted in reduced loading of the surrounding bone to below equilibrium states, stimulating osteoclastic bone resorption and eventual implant loosening [109]. Materials such as polyglycolic acid, polylactic acid or blends of the two have been well characterized and have been demonstrated as useful for implantation into the body with few detrimental effects. Unfortunately these and other biocompatible materials, materials which minimize an immune response, do not in most cases have the mechanical strength or stiffness to mimic bone (less than 1/10 the properties of bone). These materials should not be discarded, however, as they may be favored biologically through hydrolytic breakdown, or through their ability to cause minimal pH changes in the environment. The use of

ceramics which have the desired mechanical properties of bone and also are a closer chemical match than to the other polymers have also showed success in tissue regeneration.

Composites have been explored as a natural compromise, since no one material possesses all of the ideal properties for a given problem or anatomical site. Composites can be as simple as the application of peptide sequences onto a carbon-carbon backbone, or as complex as developing negative stiffness or "smart" materials. Many biocomposites seek to offer surface modifications or specify binding for a particular application. Other types of composites make use of a biocompatible base material enforced with stronger nodules such as carbon nanotubes. These materials offer a good compromise in gross properties, but increase the complexity of chemical interactions occurring within the architecture. This makes them more difficult to study and safely apply. The use of ceramic composites with polymers has also been successful. These blends combine to result in a scaffold with the elastic properties of the polymer and the compressive properties of the ceramic.

Archictectural Considerations. It has long been decided that a regenerative scaffold should be in a porous form. A porous architecture will dictate the amount of initial tissue ingrowth and thus the primary functionality of the tissue. For bone tissue, it may be that the type of ingrowth will determine the mechanical properties of the resulting mineralization. Success in the stimulation of bone has been shown for scaffolds with random architecture and porosity similar to bone. Utilizing basic chemistry and/or the simple properties of the polymers, generation of scaffolds with specific methods results

in scaffolds that are non-uniform with respect to several different parameters such as porosity, pore architecture, and anisotropy. Although these scaffolds are of a far inferior quality compared to the engineered scaffolds, simple protocols combined with positive results have fueled their use. The most often used random methods to produce architecture are with solvent casting, gas elution, or melt molding [22, 110]. The advantage of these methods is that they can be combined with processes that generate global structure, and even with rapid prototyping to result in a scaffold optimized on the whole bone level with a random architecture at the tissue level. All of the methods center around the incorporation of a solid into a polymer which can then be removed following the solidification of the polymer.

Solvent casting involves the incorporation of solid particles, such as NaCl into a liquid polymer. Following gellation or casting of the polymer, the particles are leached using a solvent, usually water or Ethanol [111]. This process is always completed in a weight percentage basis because volumetric analysis is more complex when working with polymers of varying densities. The resulting global structure contains architecture that is a result of the random spatial organization of the particles in the polymer, with limited fine control over anisotropy and porosity range however porosity of the final solid can be adjusted based upon weight percent. In order to achieve an open cell architecture required for vascularization and nutrition flow, the porosity of these randomly organized scaffolds needs to be very high, greater than 60 vol% [112, 113]. Sieving can also be used to obtain specific particle size resulting in a range of pore sizes in the final solid [22, 113]. Previous studies have demonstrated the effect of varying the pore size of the scaffold on the resulting tissue ingrowth. Ishaug-Riley has shown that for a pore size between the

boundaries of 110-710 µm, no discernable difference in bone tissue ingrowth was recorded [114, 115].

Melt molding is similar to the process of porogen leaching but uses gelatin micro-spheres which are subsequently melted out with a temperature above their glass transition temperature. Following cooling, the gelatin particles are leached out of the material by immersion in a water bath [22]. This method assumes that the polymer used in the scaffold is not destroyed at high temperatures and that the microspheres are not fully encapsulated.

Gas leaching involves the incorporation of a CO_2 precursor into the initiator of a polymer. The polymer is then fabricated and during initiation of the crosslinking, the CO_2 is leached from the solid creating a porosity regulated by the amount of precursor ingredients added [116]. The final composition of the pore size and the total porosity can be measured by mercury porosimetry or µCT [116, 117].

While there have been several successes in the creation of architecture based on these random scaffold generation methods, there are several more steps to accomplish for the generation of completely characterized scaffolds. There are several problems associated with these scaffold manufacturing techniques that go beyond the inability to create an engineered micro-architecture. The first problem is that pore size is often not tightly regulated resulting in non-homogeneous mechanical properties. If this scaffold is subjected to mechanical loading, the most porous region, which generally coincides with the mechanically weakest region, will fail prematurely and cause a catastrophic failure of the implant. The apparent material properties of the scaffold therefore do not depend on the average mechanical properties of the scaffold but rather on the properties of the

weakest region within the scaffold. This problem will arise not just with the CO_2 porogen but even after sieving has been done with NaCl and gelating micro-spheres.

Scaffolds that have been optimized for architecture deal mostly with the second structural level of bone, which is the architectural level. Hollister *et al.* have published much work detailing the development of scaffolds with engineered micro-architecture as a function of the desired or predicted stress concentrations existing in bone scaffolds [118]. These scaffolds exhibit internal architecture that is regular throughout the structures with porosity values comparable to trabecular bone. The desired stress concentrations are similar to what is experienced *in vivo* regardless of the material used in the scaffold construct because the architectural and tissue level properties control the stress distribution not the material properties. However, many materials lack the mechanical strength to support stress levels or architectures similar to the *in vivo* environment [119-121]. Still, many other scaffolds have been designed for intended use in bone scaffold engineering that have a regulated, engineered internal architecture [122]. These scaffolds are designed to be loaded and may be globally shaped into the desired shape. While these scaffolds are designed for load bearing applications, they fail to be designed for biological considerations such as cellular ingrowth. These scaffolds will only produce bone as a result of mechanotransduction by the osteoblasts, which may not even adhere to the scaffolds.

To that end, emergent fabrication methods are being employed which attempt to take into consideration the tiered levels of bone hierarchy for the designed creation of scaffolds. These methods utilize designed fabrication paths resulting in scaffolds which are fully repeatable with defined architecture and architectural properties, unlike the

randomly generated solids which have fewer variables controlled in the global scaffold. These new scaffold fabrication studies take the desire for a porous structure and the need for a repeatable architecture for modeling purposes and employ tools like rapid prototyping and computer design to arrive at a tailored structure. Several different systems exits that are able to achieve levels of magnitude based upon diverse design principles and methods. Utilization of these novel procedures results in scaffolds that contain internal architecture that is regulated with the proper porosity, density, pore size, crystallinity and diagonal length of struts. New methods are being employed to create designed scaffolds such as digital light processing [123] but state of the art processes still include fused deposition modeling (FDM), stereolithography, and particle binding.

Fused deposition modeling utilizes an inkjet printer-like delivery with a variable z-stage. The print heads deposit a material onto the stage in a two-dimensional pattern representative of a slice through the geometry (Figure 12). A secondary support material is often used to allow oblique angles to be built on slices higher than the current print layer. The final object is retrieved from the build surface through melting or dissolution of the support material. This process can be geared to be used with several different materials, the limiting factor being the melting temperature and the cooling time upon deposition to the platform. The PatternMaster (SolidScape, Manchester, NH, USA) utilizes two thermoplastic waxes for build and support and several different solvents to remove the materials [110, 124]. Multiple studies have been completed by Hollister's UMich group utilizing this machine to create burnout molds which have been filled with PLGA and ceramic materials [4, 124]. Thermo-reversible hydrogels have been delivered using an FDM process [119]. The FDM process has also shown promise with agarose
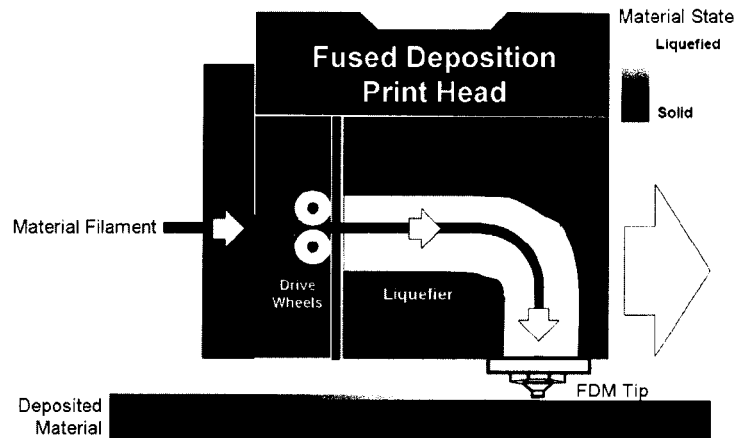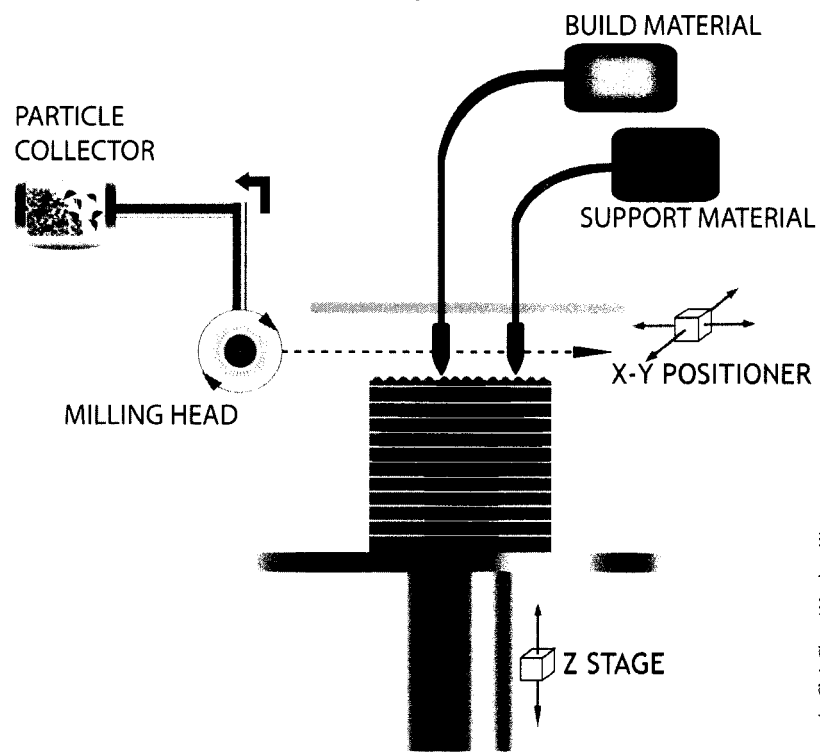
Figure 12. Diagram of Fused Deposition Modeling. Top, filament based Fused Deposition Modeling. Bottom, wax based Fused Deposition Modeling.

which has an extremely low melting temperature [125]. The Computer Aided Tissue Engineering Laboratory at Drexel University has developed a direct cell writing, syringe driven, alginate based fused deposition modeling system [126]. These systems are devoid of support material and rely upon the structure to be rigid enough to support subsequent layers. One disadvantage with hydraulic driven syringe based systems is anisotropy in the XY plane with respect to the Z stage [110]. With respect to direct printed scaffolds for mechanically active systems, the most frequently used material is polycaprolactone which has favorable material properties and a well characterized degradation profile [28, 127].

Stereolithography creates three-dimensional structures by photo-polymerizing a liquid polymer. A movable stage is contained in the bath of a liquid polymer and is moved down a slice following the crosslinking of one layer of material (Figure 13). The photopolymerization may occur with the use of a masked lamp or a laser, with the laser allowing a higher resolution [110]. 3D Systems offer a stereolithography machine that utilizes a UV laser to build models with a resolution down to ~40 μm feature size. Because the material is contained in a bath, vertical support structures are built of the same material complicating mechanical removal of the struts in delicate areas.

Another disadvantage of this technique is the large amount of material that is exposed to open air that may become damaged or contaminated following repeat use of the process. Although the initial disadvantage of Stereolithography was the limitation of photopolymerizable materials, several groups have worked to improve the techniques of the past several years. Advances have been seen in novel photopolymerizable materials [128] as well as multi-staged Stereolithography systems [129]. The advantage of using

STEREOLITHOGRAPHY
3D Systems, Inc.
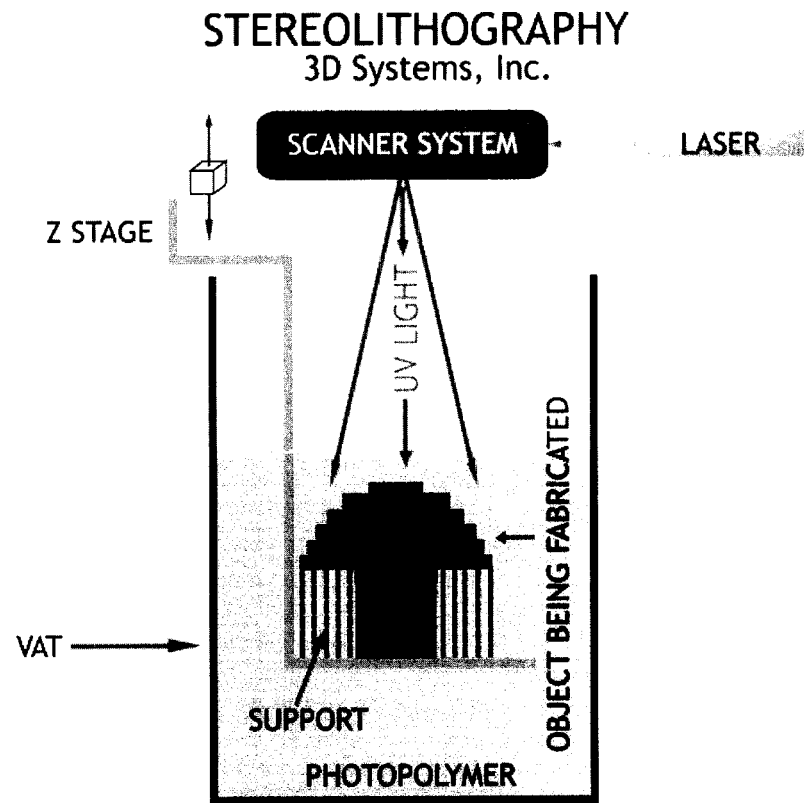
Figure 13. Stereolithography.

stereolithography is that the scaffold can be generated immediately without the required

use of secondary processes to obtain the required geometry, architecture, and material

composition [130].

3D PRINTING
ZCorp (systems)
Therics Corp. (biomaterials)

LIQUID ADHESIVE SUPPLY

ROLLER

INKJET HEAD

SELF SUPPORT

POWDER BED

POWDER
DELIVERY
SYSTEM

Z STAGE
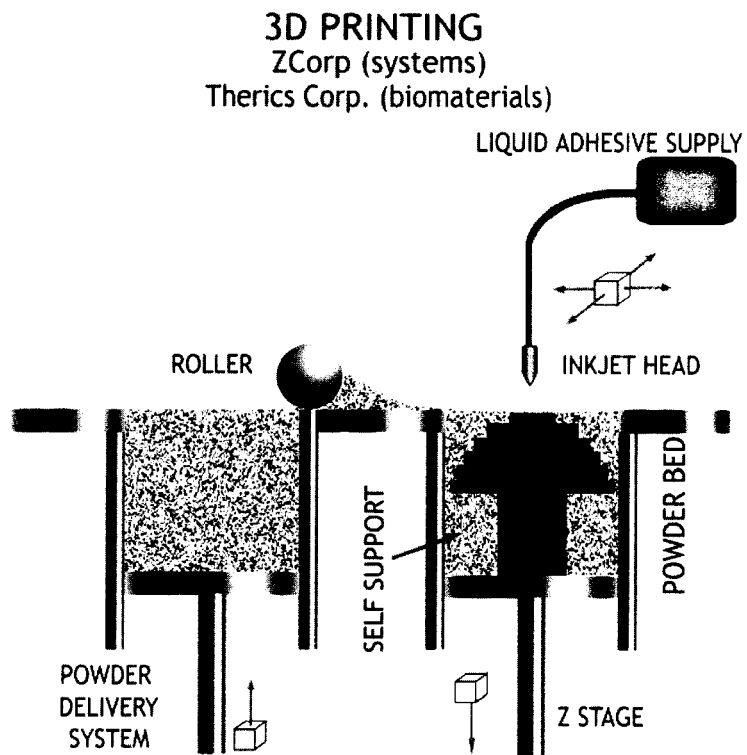
SELECTIVE LASER SINTERING
3D Systems, Inc.

LASER

SCANNER SYSTEM

HEAT

ROLLER

SELF SUPPORT

POWDER BED

POWDER
DELIVERY
SYSTEM

Z STAGE
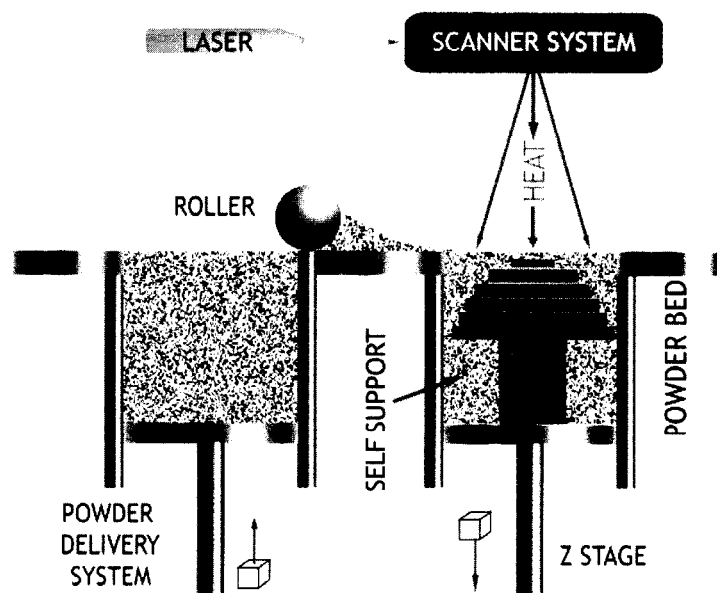
Figure 14. Particle Binding. Top, Particle binding system provided by Zcorporation. Bottom, Selective Laser Sintering.

Particle binding creates a global structure by gluing particles together in a three-dimensional arrangement either via a binder or by fusing them via raising the local temperature above the glass transition temperature via a laser. In either case following a print layer the stage moves down and a fresh layer of particles is rolled on top of the previous level (Figure 14). This type of process is self-supporting with unbound particles providing a solid matrix upon which oblique angles may be built. This process has demonstrated success in the creation of scaffolds from ceramic particles, such as hydroxyapatite. Therics, Inc. (Princeton, NJ, USA) has developed a system that allows the incorporation of growth factors, peptides, and even drugs into the binder and subsequently the scaffold [131]. While the disadvantage of this technique is high surface roughness, the eventual reduction in laser wavelength presents the possibility of high resolution on the near horizon.

Several secondary methods exist that may be combined with the previously detailed techniques to create regular architectures from materials not possible to prototype directly. These methods are not limited to injection molding, lost wax, and +/- molding processes. The use of prototyped scaffolds with these methods in combination with other imaging techniques providing geometric boundaries will produce scaffolds that can be site and patient specific and also built with the desired material properties and resolution. When using a process such as stereolithography or FDM, the fabricated model can be used as either a positive or a negative for mold creation. This mold can then be injection molded with a functional material or can be used to generate a completely new

structure [124, 132]. Molding material choice is dependent upon the design demands of the implant.

Few examples of scaffolds built with either direct or random methods exist that can detail the incorporation of all of the hierarchical levels of bone. The previous examples for each level have served to indicate that it is necessary to evaluate and address all components of the desired effect of the healing agent in order to accomplish the clinical goal of healing of bone defects in sites experiencing load bearing. Added to the fact that few [133-137], if any studies have created an implant that is both mechanically stable and addresses all design components, there exists little literature detailing the tests of scaffolds in a load bearing setting. The majority of bone growth studies have been accomplished in cranium models, however the total number of clinical cases with cranium defects is relatively low compared to other orthopaedic cases. For us to know if a scaffold will truly be successful in a load bearing application, we must test our work in such a setting. It is only after this testing that we can determine that the regrown bone is in fact quality bone and will be able to sustain the desired load. The lack of research that is being conducted in load bearing applications leads us to believe that the current designs for scaffolds are not fully taking into account the final target, which is to regenerate bone in a critical size bone defect that experiences mechanical loading.

When creating an architecture with any of the previously detailed methods, there are secondary effects. These effects, such as porosity and permeability affect both the amount and degree of tissue ingrowth. Additionally, as has been shown by Agrawal [9], they can increase or decrease degradation time. As an extension to this point, a low

porosity actually has been demonstrated to create regions of extreme pH's that would be extremely detrimental to cell viability. The following sections illustrate both the importance and effect of porosity and permeability as secondary effects to the creation of architecture in a scaffold.

Porosity Considerations. A simple definition of a porous media is a "solid with holes". In a realistic sense, some solids have more void space than solid space. Bone tissue is one example of this case. Functionally speaking however, the solid architecture provides strength and the porous nature allows fluid flow. This indicates a need to characterize porous media accounting for such parameters as overall porosity, interconnectedness, and effective pore volume. Experimentally, effective pore volume has been shown to be the most important parameter for the evaluation of the pore network [138, 139]. This quantity does not take into account the contribution of trapped pores and or pores that are too small to factor into the total porosity. In a scaffold, this value would dictate the volume of fluid flow, the surface area which cells can interact with as well as the shear stress. Other parameters vary wildly in a random porous network and it is difficult to determine with accuracy the actual values for those parameters [140]. In tissue engineering, porosity is usually determined by the dry weight percentage due to the difficulty in accurately calculating volume of high molecular weight polymers [141]. While studies have demonstrated the relations between the dry weight porosity and the volumetric porosity, notably Fisher *et al.*, the weight does not correlate well with the volume. Also, the end goal for the implant should be to obtain a volumetric porosity which could be helpful in comparing scaffolds to values of bone porosity [113]. One of

the important requirements for an adequate porosity is to have enough void volume to promote cell ingrowth, the other is to have an adequate fluid perfusion through the scaffold. An important conclusion of the study completed by Fisher *et al.* was that pores are interconnected at porosities greater than 80 wt%.

Measurement of the effective porosity of a solid is important for several reasons relating specifically to fields such as tissue engineering and hydrology. First, the determination of the void volume dictates the amount of fluid that the scaffold will be able to hold. This can be used in flow perfusion calculations and in the determination of the possible shear forces that may affect the scaffold. Additionally, the determination of the porosity is important for characterization of the scaffolds and for comparison between groups in experimentation purposes. While the overall porosity may mimic the levels seen in bone, the structure is random, not designed, and therefore may not be completely interconnected. Two evaluation techniques, mercury porosimetry and micro-computed tomography may be used to determine the porosity and pore size but both with their own caveats. Porosimetry can underestimate the porosity if the scaffold is not fully connected and μCT can overestimate the porosity by including trapped or restricted pores [5, 116, 142]. The problems with these techniques further demonstrate the need for specific scaffold generation methods.

Micro Computed Tomography (μCT) is an imaging modality which obtains a three-dimensional approximation of the tissue with the use of X-rays that are shot at the target. This technique is able to generate CAD data of the solid for use in computational modeling as well as rapid prototyping. Resolution of the machines are on the order of 10μm, below the level that cells could invade and grow on but not a pore size that is

restricting to fluid flow. The greatest advantage of this technique is the ability to image non-destructively [116]. One important purpose would be for the spatial determination of the degradation of a scaffold which has been completed only infrequently as of yet. One problem with this technique however, is the integration and scanning time required to obtain the three-dimensional file of the object which is prohibitively long [26]. Stochastic methods have been employed to calculate the effective pore volume and other porosity parameters by combining serial images taken with μCT [139, 143-146].

Mercury porosimetry is another method to obtain values for the porosity of the architecture. This technique forces liquid mercury through a porous solid at an increasing pressure for the determination of not only the effective porosity, but also the pore distribution throughout the scaffold [30]. This technique, unlike μCT is destructive thus requiring serial scaffolds to obtain data. This technique has several limitations/advantages depending upon what the researcher is looking for. The correct use of this technique presupposes that the pore architecture is that of a sphere or closely approximating it [142]. Therefore, with a porous network of pores more complex than a sphere, there may be problems with the correct measurement using this technique. Still, the great advantage of this technique is the validated previous research and that the values that are obtained from mercury porosimetry are much more accurate than other currently available methods with relation to the functional volume available inside a porous architecture [5, 139].

Permeability Considerations. While previous studies have been occupied attempting to generate a porous architecture in a scaffold sufficient to sustain fluid flow and tissue

ingrowth, little focus has actually been turned towards the requirements for the proper fluid flow environment of a scaffold. Properties resulting from porosity such as pore volume, permeability and surface area will all affect the type and amount of tissue growth into a scaffold [10, 114]. Future characterization of the scaffolds should include analysis of such parameters. One of the current problems in scaffold generation is the requirement for a scaffold to be permeable for fluid flow to promote tissue ingrowth as well as nutrient delivery and waste removal. However, only porosity can be created because permeability is a parameter that only exists as a definition of a combination of variables.

Permeability is the ability of a fluid to flow through a porous solid and the properties of this number are due solely to the solid matrix itself [139, 147]. The earliest stating of this quantity is by Darcy who calculated this value to describe the flow of water through an amount of sand [148]. The units of the value are in m^2 but can be derived several different ways based on initial assumptions about the system [138]. The importance of permeability is that it is a measure of the ability of fluid to flow through a porous media. Hydraulic permeability is probably one of the oft used derivations of the law and the majority of the methods used to calculate this employ a permeameter [149], which was the apparatus that Darcy used to examine the flow of water through a column of sand [9, 147, 148]. The device measures the amount of a liquid (usually degassed water) to pass through a porous media for a given amount of time, taking into account dynamic viscosity, temperature, and cross-sectional area. Mathematically, specific models exist to determine these relations that once again are based upon the type of scaffold and the initial conditions. Two of the most prevalent for porous scaffolds are hydraulic radius theory or theories for packed solids. Again, stochastic methods have

shown promise in the calculation of such parameters relating to porosity. HYMOSTRUC was the thesis of van Breugel, and is a computational method to determine the fluid flow characterisitics of porous media using image capture and mathematical morphology [145, 150, 151].

It has been previously shown that tissue ingrowth is dependent upon the perfusion of the scaffold with fluid both to remove the degradation products of the scaffold material and to deliver nutrients to the scaffold [10]. If the media is impermeable, then the pressure that is forcing the fluid through the media may be too high. Numerous mathematical models have been constructed to attempt to relate permeability to porosity, but simply put, with a lack of success [138, 139, 148]. The basic value for porosity gives nothing more than a volumetric amount of material or void volume. It has no way of describing the architecture of the pores or even the distribution that could be used to relate the two quantities together. Further work has been completed into the creation of models that include pore structure parameters in an effort to further quantify the structure of the pore area so that the architecture of the pore volume can be included into the equation for permeability. Permeability is affected by a number of variables, temperature, pressure of the liquid, dynamic viscosity of the liquid, pore volume, tortuosity, pore neck, throat, surface charge, are just the simple variables that affect this quantity. Correct parameterization requires construction of a model that incorporates some architectural description of the pore parameters and relates them to permeability. Recently, Hollister's architectural adaptive algorithm has included permeability as a variable in addition to elasticity, resulting in a set of scaffolds with a range of moduli and permeability values. Results for the design of craniofacial scaffolds with varied values has shown no

difference in tissue invasion for a fully connected scaffold containing pore sizes between the values shown by Ishaug to support bone tissue ingrowth [31].

Although the majority of the literature has stated and agrees that a scaffold must be both porous and permeable, there is a terminology mix-up. When papers in tissue engineering state a scaffold must be permeable, they simply mean that fluid must be able to flow through it. These statements are purely qualitative. An important point is that a scaffold can be porous without being permeable because encapsulated voids contribute only to the porosity and not the permeability.

2.5 Summary

Based on the review of bone hierarchical levels it can be seen that there is as schema which allows for the reordering of material into structures that both fulfill the function that is required for the system and exhibit order and symmetry. Trabecular bone organizes itself into a complex structure, providing difficulty to the task of modeling and determination of mechanical properties. Several methods have shown success both in the evaluation of the mechanical properties of the actual structure as well as approximations of that structure. The complexity of bone creates considerable hurdles when searching for a suitable replacement therapy as there are number of mechanical issues to consider when fabricating tissue engineered constructs. The design cannot be as simple as finding a biomaterial which matches the apparent stiffness of tissue. The following issues are mission critical: scale considerations, the influence of the scaffold geometry on the cellular loading levels, defect/scaffold boundary matching as well as the apparent and/or tissue level properties within the mechanical usage window. In the future design criteria for a baseline TEC will need to be established to address all of these concerns as well as

the ones covered in detail in the previous section. A universal protocol for a generic tissue type is doubtful, and thus solutions will be unique to the particular case considered. Quantification of scaffold parameter is required to completely assess the amount and type of bone growth in order to characterize the mechanisms of bone growth. Scaffold architecture needs to be designed in a manner which exhibits control over the architecture allowing a quantifiable comparison to be completed following implantation studies. Complete characterization of bone tissue properties and scaffold design parameters can lead to the discovery of both bone growth mechanisms and requirements.

Chapter 3: Determination of the effect of material organization on the architectural properties of regular architectures.

The focus of this dissertation project was on the study of the effects of material arrangement on the structural properties of architectures that are based on regular polyhedra. Detailed here is the attempt to quantify the effect of material spatial organization in porous architectures encompassing similar material volumes on the structural properties of those architectures. By holding the architectures to the same material volumes (porosity), we directly compared the effect of material organization between architecturally dissimilar architectures. We hypothesized that as a result of material organization, diverse values could be obtained for structural properties such as stiffness and strength and material properties such as modulus and ultimate stress. Specifically, by varying the strut length, strut diameter, and number of struts for a regular architecture we investigated relationships between architectural components (strut length, strut diameter) and structural and material properties as well as the dominant characteristics contributing to these properties. These relationships can be used to generate basic equations derived from a combination of continuum mechanics, homogenization theory, and the theory of cellular solids that may allow for the determination of structural properties for a given architecture based solely on material organization.

To relate computational studies to relevant real world results, finite element models combined were utilized as well as rapid prototyped models. These studies are relevant to the global field of cellular solids for the prediction of the strength of materials based solely on their material organization.

All of these experiments relied solely upon the effect of structural organization of material to influence the properties such as strength and stiffness. All of the evaluation between the structures was conducted using the same values of a) porosity and b) material definitions (i.e. trabecular bone, titanium, etc.). By evaluating these structures all with the same material, the effect of material variations was removed and only the structural organization was evaluated. By evaluating these structures with all the same porosity, comparisons were drawn between completely dissimilar architectures. Data obtained from this section was used to compare to the relationships obtained in Specific Aim 2 for random structures. The control architecture for this chapter was trabecular bone because the application of this research could be directly applied to the use of the architectures as tissue engineering scaffolds.

3.1 Geometric Characterization and Finite Element Structural Comparison of Platonic and Archimedean Solids[*]

3.1.1 Introduction

Minimization schema in nature, across scale, affects the material arrangement of objects. Geometries intending minimal energy expenditure (soap bubbles) or structural integrity (wood microstructure, honeycombs, bone) give rise to highly ordered systems with defined, repeated architecture [8, 152, 153]. Sometimes the focus of the minimization is on the structural arrangement itself; in the case of cancellous bone and honeycombs, a high strength is obtained even with the arrangement of low material volumes [154, 155]. High strength to weight ratios such as these are of high interest in engineering design systems and the acute focus of the field of cellular solids [26, 156-158].

The arc of the field of cellular solids has progressed from the full characterization of two dimensional symmetric, regular (congruent faces and identical vertices) and non-regular architectures to the characterization of non-regular three-dimensional architectures. Early studies modulating volume fraction in molded two-dimensional honeycombs of homogeneous material were instrumental for proof of the power law relationship between architectural modulus and volume fraction [16]. The constant, C, in equation (1) is a poorly understood combination of the constants of proportionality related to the cell geometry and the value of the exponent, 1<n<4, categorizes the

$$E^*/E_s = C\left(\rho^*/\rho_s\right)^n \tag{1}$$

---

[*] This section to be submitted as: Wettergreen MA, Bucklen BS, Mikos AG, Liebschner MAK. "Structural Properties of Regular Architectures, Part 1: Geometric Characterization and Finite Element Structural Comparison of Platonic and Archimedean Solids."

deformation pattern of the architecture; cell wall bending (n=3), edge bending (n=2), or cell wall stretching (n=1). This equation holds for all cellular solids and aids in the contextualization of published values for dissimilar architectures. Later studies using motion-tracked dynamic deformation resulted in material-independent, geometrically derived equations governing mechanical properties for any variation of two-dimensional regular, symmetric honeycombs [159]. Steps taken to geometrically characterize three-dimensional architectures can be bookmarked by Roberts and Garboczi's development of relationships between global cell wall properties (cell wall thickness, side number, connectivity) and mechanical properties through deformation studies of simulated and real, random, three-dimensional architectures [160]. Further computational models applied to additional irregular, non-symmetric architectures have demonstrated high correlation to the apparent properties of trabecular bone and were used to model situations similar to osteoporosis through random beam removal [161, 162]. Recent studies into regular symmetric three-dimensional architectures have matched results demonstrated with previous random porous architecture studies and those of two dimensional honeycombs [134]. A systematic decomposition of the geometric properties of three-dimensional architectures executed similarly to previous two-dimensional analyses combined with deformation mechanisms could lead to material-independent geometrically derived equations governing mechanical properties for complex three dimensional architectures, such as bone .

Headway towards this goal could be made with a systematic exploration of regular architectures with slight geometric variation across a range of material volumes. The Platonic and Archimedean solids are architectures which fulfill this requirement: they are

the simplest geometric shapes which exhibit symmetry and regularity. Additionally, these architectures arise in nature through minimization schema in specific structural systems like the microarchitecture of wood, bone, and other plant life [163] [152]. The symmetry, regularity and similarities across the set of polyhedra lend themselves to simple modeling and geometric characterization [164].

This study characterized the variation in mechanical properties of a subset of the Platonic and Archimedean solids which, while containing similar material volumes, have different material arrangements. These are the first steps toward a set of rules governing the geometric and mechanical relationships of regular, three dimensional architectures and mechanical properties of these architectures. Design parameters, which control structural minimization schema, can be developed through a systematic exploration and characterization of these architectures. These constructed models will then be applied to naturally occurring structural systems such as bone or tissue engineered scaffolds.

3.1.2 Methods

Figure 15 shows four shapes chosen for characterization from the Platonic and Archimedean set displayed here in their ball and stick approximations. A Hexahedron (H), at left, and a Truncated Hexahedron (TH), second from left, were chosen to represent the simplest approximations of beam structures. A Rhombitruncated Cuboctahedron (RC), second from right, and a Truncated Octahedron (TO), right, from the Archimedean
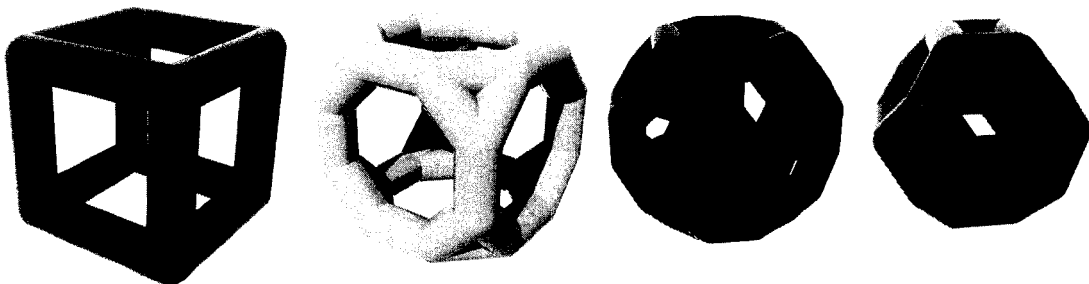
Figure 15. Wireframe renderings of selected polyhedra. Left to right: Hexahedron (H), Truncated Hexahedron (TH), Rhombitrunctated Cuboctahedron (RC), Truncated Octahedron (TO). Polyhedra in this figure are displayed at 80% porosity.

set, were chosen in comparison to the Platonics. All polyhedra are open celled. Parametric models of the polyhedra were generated as ball and stick approximations using computer aided design (CAD). Each polyhedra was created at five volumetric porosities (50, 60, 70, 80 and 90) with a constant material envelope (bounding box), allowing for a direct comparison between the specific arrangement of material in each architecture. Each architecture was quantitatively classified according to porosity, beam length, beam diameter, surface area, space filling and pore size ratio.

Polyhedra were subjected to a linear finite element simulation using unconfined compression. Architectures were meshed with greater than 18,000 tetrahedral elements, as determined via a convergence study (Figure 16). Architectures were compressed with a prescribed displacement to 1% of the total height of the architecture. A material modulus of 2000 GPa was assigned for each shape, allowing direct comparison of material arrangement effects. Stiffness and elastic moduli were calculated for each porosity. Stiffness was calculated as the reaction force summed over the top nodes
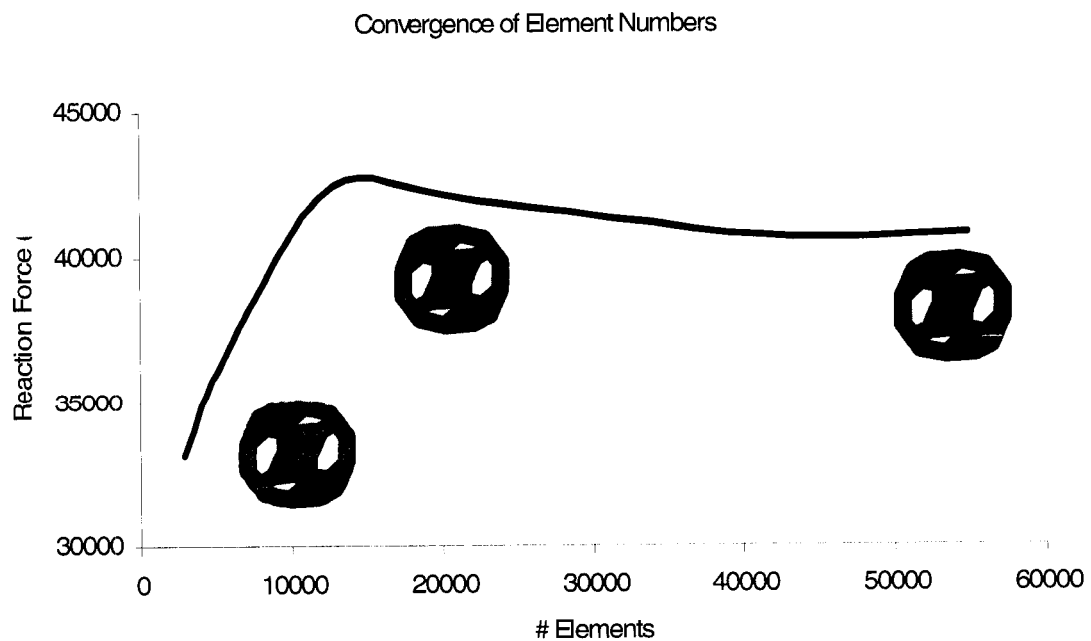
Figure 16. Convergence study to determine adequate mesh density versus computational expenditure.

divided by displacement. Elastic modulus was derived from the reaction force calculated from the top nodes divided by the surface area of the top face of the bounding box divided by the described strain. The power law relationship between modulus and volume fraction (Equation 1) was explored for all architectures. Elemental principle stress distribution was evaluated for each polyhedra to characterize the loading with respect to spatial material arrangement. Von Mises stress was visualized to locate stress concentrations and stress-free elements. Space filling efficiency (outer volume / inner volume) was calculated across the porosity range for each polyhedra. Outer volume was defined as the Boolean subtraction of the space filling form of the polyhedra and the ball and stick form from the bounding box volume [165]. This volume amounts to the space exterior to the polyhedra. The interior volume was defined as Boolean subtraction of the ball and stick form of the polyhedra from the space filling form of the polyhedra. This volume amounts to the space interior to the polyhedra. A pictorial representation of these Boolean processes can be found in Figure 17. Pore volume ratio was explored for each polyhedra. The outer pore diameter is marked by the minimum inscribed sphere diameter fully enclosing the exterior of the polyhedra. The inner pore diameter is the maximum inscribed sphere diameter inclosing the interior of the polyhedra.

3.1.3 Results

The geometric characteristics of the surveyed polyhedra are shown in Table 1. The Truncated Hexahedron (TH) and Truncated Octahedron (TO) have the same number of beams, vertices and connectivity index but the material is arranged in a different fashion. The TO and the TH have twice the number of beams as the H, and the Rhombitruncated

Table 2. Geometric characteristics of Platonic and Archimedean polyhedra.

	Hexahedron	Truncated Hexahedron	Rhombitruncated Cubocatahedron	Truncated Octahedron
# Struts	12	36	72	36
# Vertices	8	24	48	24
Connectivity Index	3	3	3	3

Space Filling (**A**) Ball & Stick (**B**) Bounding Box (**C**)

Inner Volume
A - (A∩B)

Outer Volume
(cut away for illustration)
C - (A∪B)
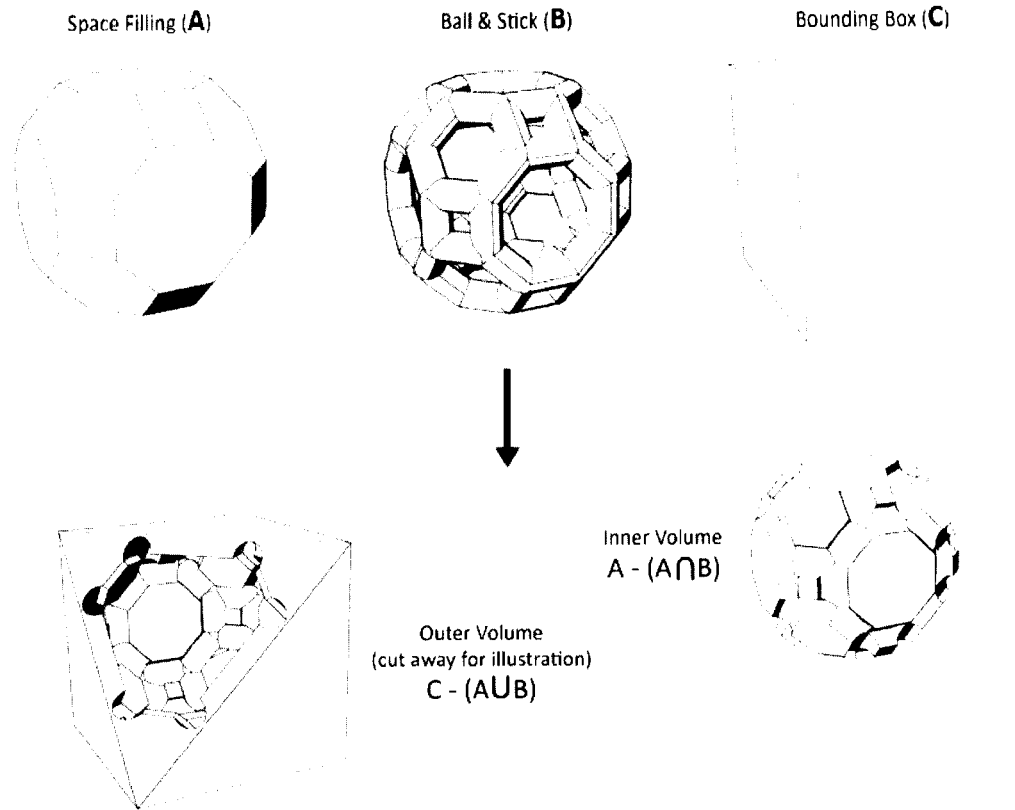
Figure 17. Boolean operations to obtain outer volume and inner volume for each polyhedra. Shown here is the Rhombitruncated Cuboctahedron as example.

Cuboctahedron (RC) has twice the number of beams and vertices as the TH and TO. Note that in Figure 18, beam length and diameter linearly relate to volume fraction. The slope of this line varies across the polyhedra set, however, the beam lengths, diameters and slopes are similar for all polyhedra (ranged between -0.26 and -0.38) except the Hexahedron (exactly -1.0). Additionally, strut lengths for the Hexahedron are ≈2.3 times higher than the strut lengths of the Truncated Hexahedron, the most similar architecture. The most complex shapes (RC and TO) exhibit similar slopes though the range of beam diameters for the TO is 25% greater than the other three polyhedra.
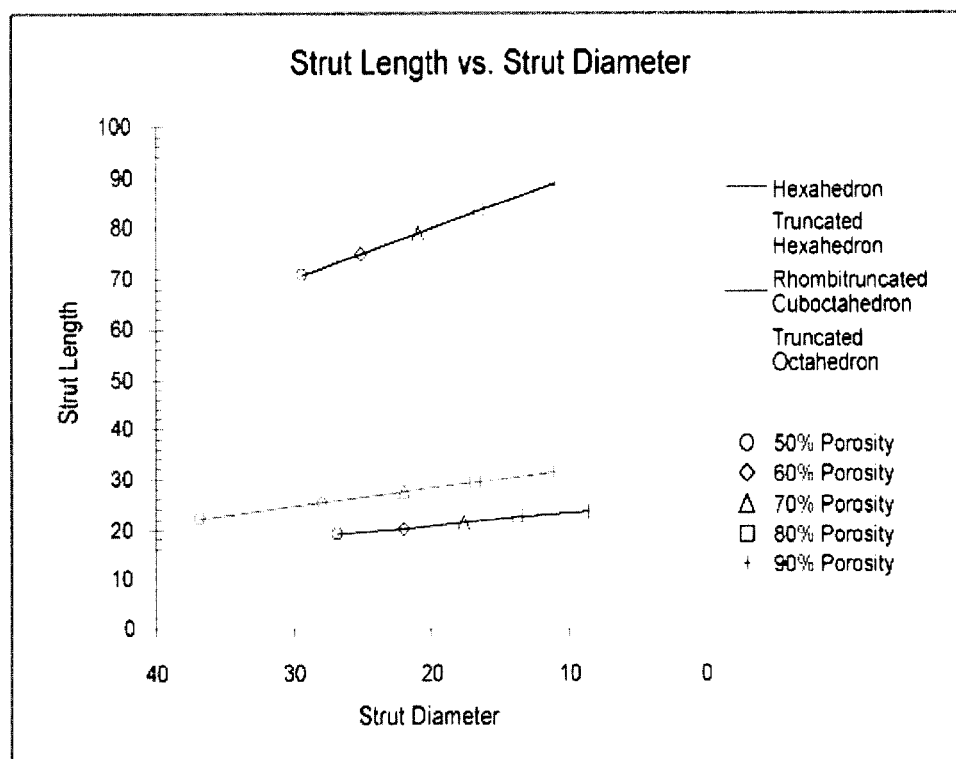
Figure 18. Morphological characterization of regular architectures: Beam Length versus Beam Diameter.
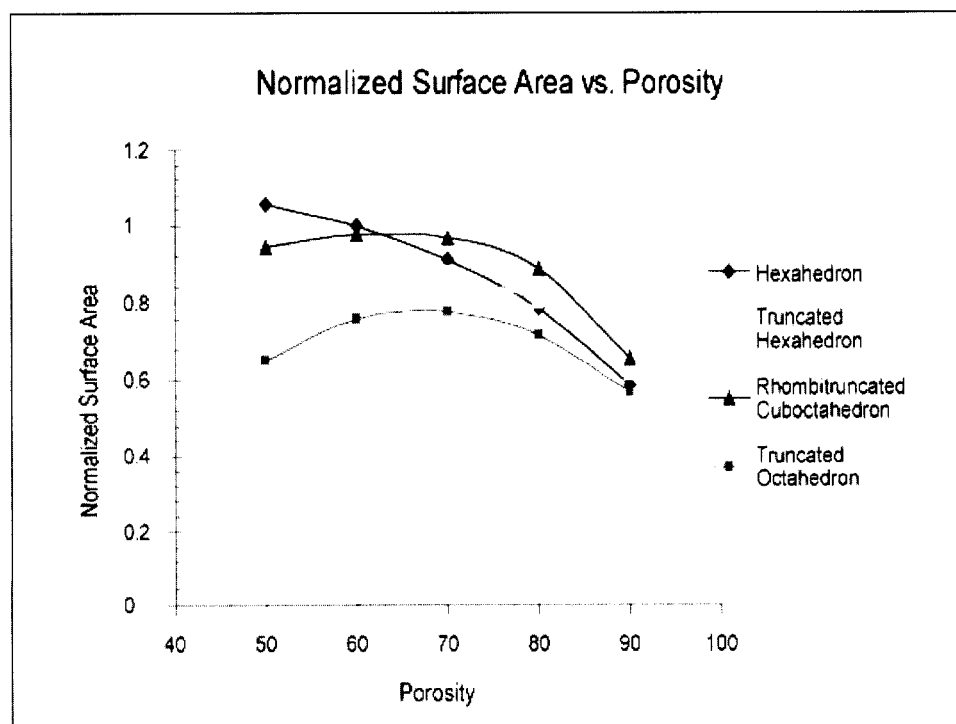
Figure 19. Morphological characterization of regular architectures: Surface Area versus Porosity.

Surface area is a function of beam diameter and length, thus as expected, the surface to volume ratio of all polyhedra increased exponentially with an increase in porosity. The nature of surface area dependency on material density varied for each geometry in an interesting fashion. The surface area of the simplified architectures (H, TH) decreases when material volume decreases. The complex shapes (RC, TO) exhibit a parabolic response with a surface area maxima near 70% porosity (Figure 19). And at lower porosities, the Truncated Octahedron demonstrates considerably lower surface area in comparison to the three other polyhedra.

Each polyhedra has a unique material architecture, meaning that the space filling pattern is also unique. This space filling pattern can be measured as the *space filling efficiency* which is a ratio of the volume external to the polyhedra versus the volume interior to the polyhedra. The space filling efficiency of the polyhedra at each volume fraction is shown at left in Figure 20. A closed-cell hollow sphere at equivalent porosities is included for comparative purposes. Excluding the Truncated Octahedron and speaking only of porosities between 60% and 90%, the ratio of outer volume to inner volume varies linearly for the polyhedra. Below 60% porosity all shapes exhibit a significant drop in the inner volume consistent with a power law change. The architecture with the lowest rate of change in shape conservation (60:90%) is the Hexahedron; that with the highest is the Rhombitruncated Cuboctahedron with a slope near twice the Hexahedron and Truncated Hexahedron. Now, speaking only of the Truncated Octahedron, the space filling efficiency follows a power law between 50% and 90% porosity, close in trend to that of a hollow sphere, shown in the graph for comparison.
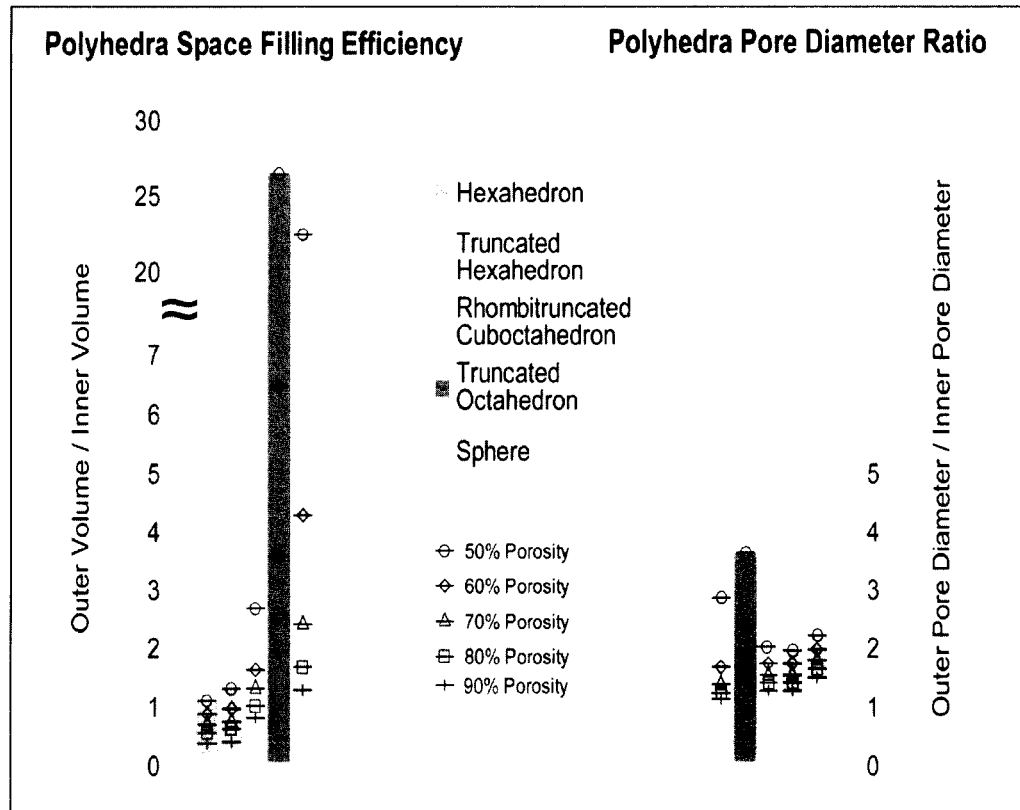
Figure 20. Space filling efficiency of polyhedra.

Architectural complexity affects the spacing in beam arrangement; at low porosities more complex shapes shrink inward towards the centroid. A measure of this compaction is the *pore diameter ratio* which is the ratio of the outer pore diameter versus the inner pore diameter, shown in Figure 20. A hollow sphere at identical porosities is included for comparison purposes. Excluding the Truncated Octahedron, the pore diameter ratio varies linearly for all polyhedra across porosities and the slopes are near equal (ranged 1.67 to 1.78). The pore ratio for the Truncated Octahedron is nearly twice that of the other polyhedra at 50% porosity but is nearly equal to the Rhombitruncated Cuboctahedron at >70% porosity. The slope of the line describing pore ratio vs. porosity for the Truncated Octahedron is characteristic with a power law and again similar in trend to the slope of the pore ratio vs. porosity for the closed cell hollow sphere.
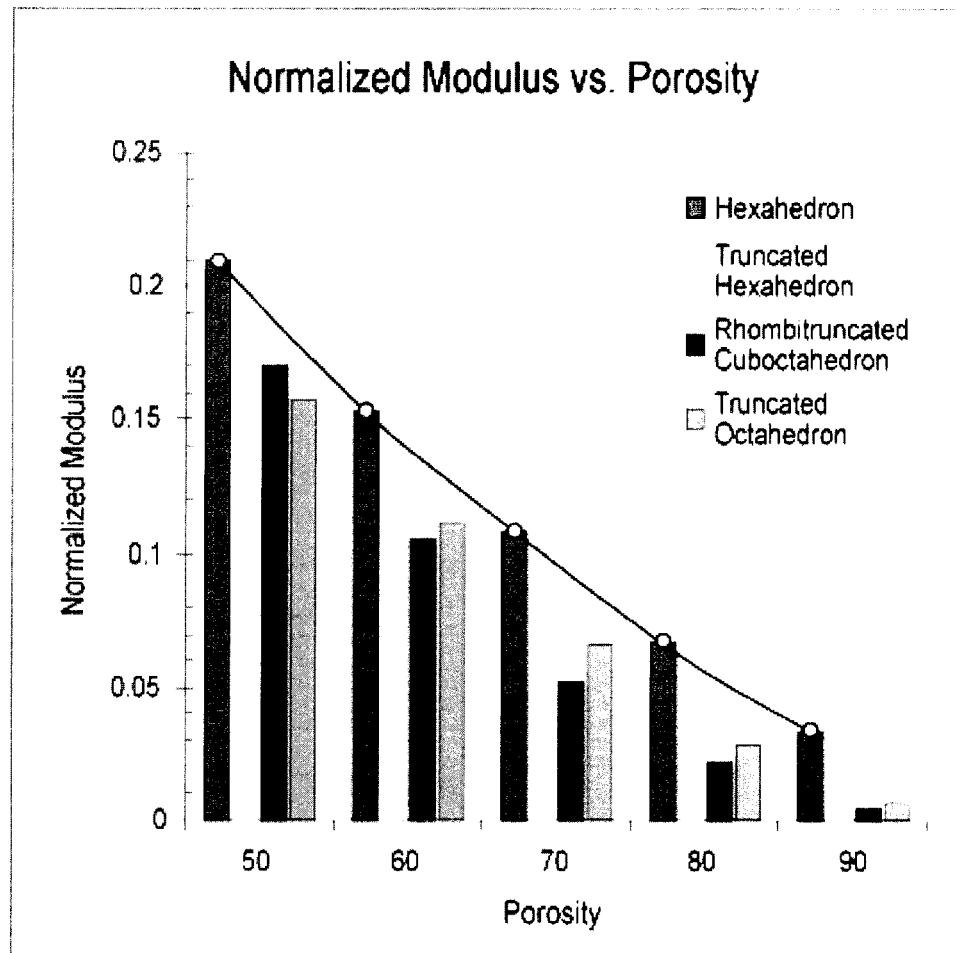
Figure 21. Structural Modulus of single regular polyhedra at 4 porosities. The line overlaying the Hexahedron set exhibits the power law relationship between modulus and volume fraction.

Linear, displacement-controlled finite element analysis illustrated that architectures which contain the same material volume but with a different material arrangement exhibit significantly different mechanical properties (Figure 21). The most explicit difference is witnessed between the Truncated Octahedron and the Truncated Hexahedron, two architectures with the same connectivity index and number of beams. The TH has a superior modulus at 50% porosity, but with any uniform reduction of material in the two architectures, the TO wins out as the strongest of the two. A similar effect is seen in the TH and RC, who possess similar moduli and are the second and third strongest shapes at

50% porosity but fall behind to the weakest spot at greater than 50% porosity. Across all architectures and porosities the modulus of the Hexahedron is between 19 to 88 percent higher in the uniaxial loading curve.

The power law relationship between modulus and material volume was calculated for each architecture. The curve overlaid on Figure 21 illustrates the power law curves which were generated for each of the architectures from which the values for C and n were derived. An n of one corresponds to cell was stretching, an n of 2 means deformation through edge bending and an n of 3 corresponds to cell wall bending. The values of C and n for each of the architectures are displayed in Table 2. The value of n for the Hexahedron (~1) is consistent with cell wall stretching deformation which we have seen is different for the rest of the architectures which are based on n value (~2) and exhibit edge bending deformation.

Table 3. Modeling of deformation patterns of regular architectures.

	C	n	r^2
Hexahedron	0.49	1.23	0.9993
Truncated Hexahedron	0.81	2.24	1.0
Truncated Octahedron	0.54	1.76	0.9991
Rhombitruncated Cuboctahedron	0.81	2.25	0.9998

A relationship between architecture and porosity is shown by the elemental stress distribution of the architectures. Displayed in Figure 22 is the histogram of elemental stress distribution of the Hexahedron architecture for the five different porosities. The ratio of tensile to compressive stress over the entire dynamic range of the porosities is always relatively the same, with about 16.5 percent of the stress values lying in the tensile range. The observational mode is represented as the peak fractional element for either tensile or compressive data sets.
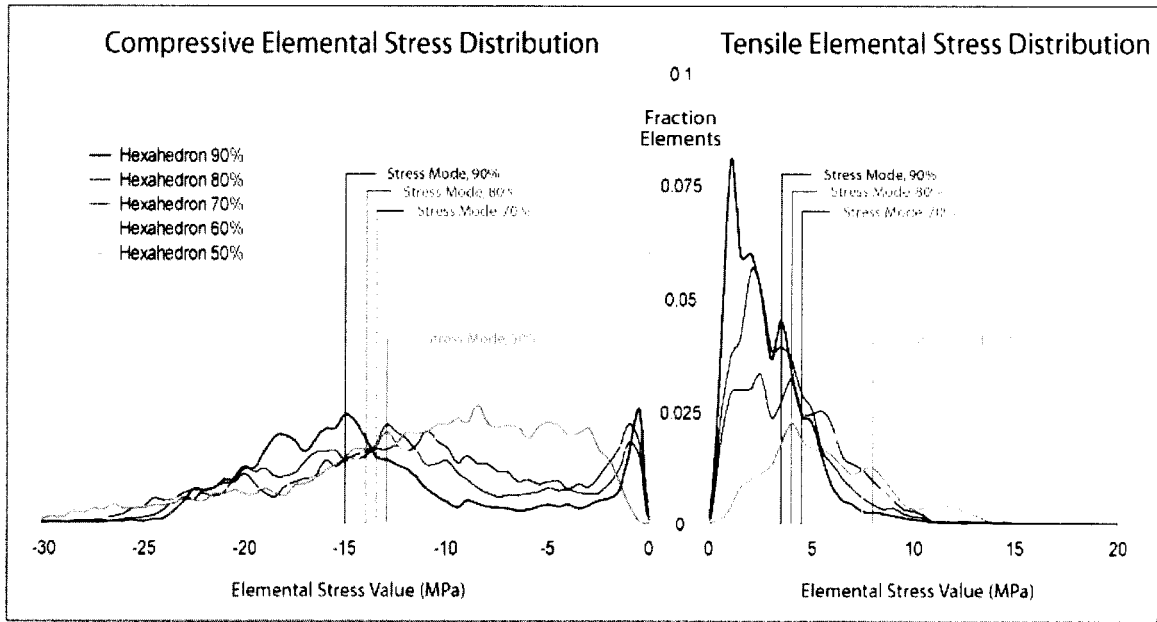
Figure 22. Elemental stress distribution of the same architecture (Hexahedron) at varying material volumes. Observational mode (highest number of occurrences) are displayed as the peaks of each data set. Stress value means are indicated by vertical ticks.
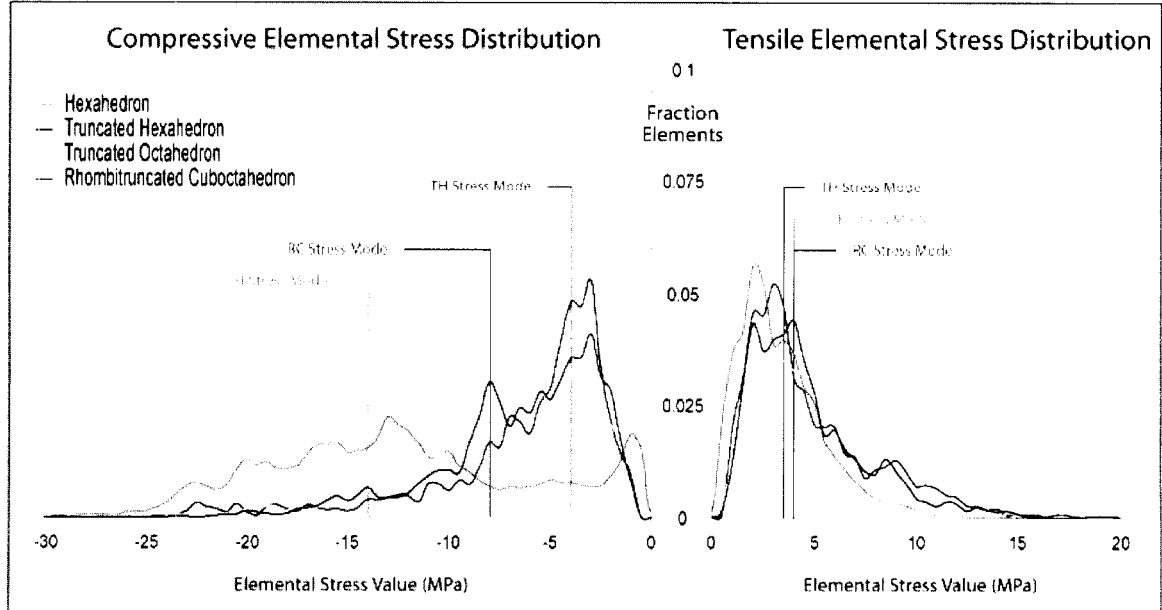
Figure 23. Elemental stress distribution of dfferent architectures at the same material volume (80%). Observational mode (highest number of occurrences) are displayed as the peaks of each data set. Stress value means are indicated by vertical ticks.

The elemental stress distribution can also be used to highlight the stress dependence of specific architectural features. In Figure 23 we see the stress distribution pattern of each architecture at 80% porosity. The loading of the Truncated Hexahedron is nearly equal in tension and compression with 41% of the total elements in tension. And while the range of compressive stresses in the TH are as large as the other architectures, the stress mode is the lowest of the shapes. The architecture with the highest modulus (Hexahedron) also exhibits the highest stress peak in the compressive region. This stress peak ranges from -10 to -30 MPa. The Truncated Octahedron is loaded in compression and tension with the compressive peak near -7.5 and and a lower tensile peak at ~2.5 MPa. The Rhombitruncated Cuboctahedron illustrates a three peak profile, with the tensile peak centered at around 5 MPa and the compressive peaks at -4 and -8 MPa respectively. The RC and the TO have the exactly same mode in the compressive region.

3.1.4 Discussion

The goal of this study was to provide preliminary analysis of three-dimensional structures for the determination of a rule set explaining mechanical properties as a function of geometry. A geometric characterization akin to previous research on two-dimensional counterparts was carried out on four polyhedra from the Platonic and Archimedean solids. Holding the density constant allowed a comparison of completely dissimilar architectures due to their quantifiable simplicity in beam structure, regularity and symmetry. We included metrics demonstrated by previous studies [166] as essential to understanding mechanical behavior through geometry: connectivity, beam number, beam geometries, modulus and deformation pattern. We included additional geometric parameters such as surface area, space filling efficiency and pore diameters.

We selected the four polyhedra based on their geometric variation and their propensity to appear in natural systems and designed material systems [8, 134, 153]. The Hexahedron (H) has most of its material oriented in the loading direction (Figure 15, at left). The Truncated Hexahedron (TH) has slightly less material oriented out of the loading direction due to the truncation of the corners (Figure 15, second from left) but 16 additional beams as a result of this truncation. The Truncated Octahedron (TO) and the TH contain the same number of vertices and beams, differing in material arrangement and beam spacing distance. The Rhombitruncated Cuboctahedron (RC) has twice the number of beams as the TO and TH, and is attractive to study because the successive tessellation of the sides cause it to approach the architecture of a hollow sphere. All polyhedra have the same connectivity index (3) which at high numbers has been demonstrated to be a strong indicator of the strength of polyhedra [167].

Studying these polyhedra at constant porosities provided information about the geometric arrangement of the beams and the space filling characteristics that arise from these beam arrangements. The number of beams and the complexity of their arrangement affected the rate of change of beam length/diameter with respect to porosity. Low beam lengths (y-intercept, Figure 18) indicated high beam numbers contained in an architecture. This is shown elegantly in the case of the H which contained the lowest number of beams (12 beams total) and whose y-intercept has ~2.3 times higher than the other architectures. The range of beam diameters gave us information on how drastically an architectural changes. Of the four architectures, the TO had the widest range, roughly one third greater than the other architectures. The greatest shift was between 60 and 50%

porosity where the diameter increased by a third to achieve the desired porosity, forcing the architecture to resemble a hollow sphere.

The complexity and arrangement of beams in an architecture additionally affected the resulting surface area of that architecture. The simplest shapes (H, TH) had a surface area maxima at 50% porosity and decreased with subsequent material removal because beam spacing largely prevents overlaps. The TH, although containing an increased number of beams as compared to the H, had a similar surface area profile because the complexity of these extra beams occurred at the corners of the architecture and the remainder of the shape was closely similar to the Hexahedron. The more complex shapes (TO, RC) had tightly arranged beams with diameters which encroach upon the beam spacing distance. At high material volumes, the diameters of these beams were larger than the spacing distances, causing them to obscure the clarity of the architectural skeleton. This result predicted the parabolic surface area profile across the volume range for the TO and RC. The markedly low surface area of the TO versus the TH (both with the same beam numbers) at low porosities indicated that the beams had surpassed the beam spacing distance and highlights the transition of the architecture to the resemblance of a hollow sphere. Independent of beam arrangement complexity, all architectures approached the same surface area limit at porosities greater than 90%. Below 90% porosity, there were also regions of intersection where dissimilar architectures shared the same surface area (Figure 19). One example of this is at point A, the cusp for the TH, where adding more material will surpass the beam spacing distance and below which the architecture has a higher surface area than the H because the beams do not overlap.

Another metric of beam arrangement complexity is the measure of how polyhedra fill their bounding box, referred to as space filling. Architectures with a high connectivity index have the ability to equally distribute material whereas architectures of lower connectivity (such as we studied here) do not afford that possibility. Nonetheless, at high porosities all architectures acted in a similar fashion, sharing space equally on the exterior as well as the interior. At low porosities, architectures with high beam numbers or those who are architecturally complex eventually overlap themselves, dependent upon the topology of the vertices. Efficient space filling across all material volumes can be seen in the low beam numbered H, whose space filling followed a linear transition with material evenly arranged at the perimeter and interior with a ratio of outer/inner volume near 1.0 (Figure 20), providing mechanical stability and maintaining architectural specificity. In the complex architectures (RC, TO), shape transition towards low porosities followed a power law which indicated a greater modification to the overall geometry of the object, in converse to the higher porosities where small topological differences result in large changes in mechanical properties and surface area. Therefore, the majority of the architectural change when moving towards a higher porosity had more to do with surface area contraction/expansion than volumetric arrangement which promotes mechanical stability or architectural complexity. This explained why at the lowest porosity the TO performed so poorly; transverse beams dominate the architecture causing it to mimic the deformation pattern of a hollow sphere which is unsupportive in the loading direction. Additionally, the TO is indistinguishable from a hollow sphere because the outer volume is 27 times greater than the interior volume.

Below the critical porosity where an architecture begins to follow a power law path of shape modification the architectural topology or skeleton is difficult to distinguish. Below these porosities the architectures may be modeled as a closed cell structure instead of an open-celled with different mechanical deformation patterns and shape transition characteristics. While outer volume modification occurred, the polyhedra's outer pore diameter versus inner pore diameter changed little or at least continued to vary linearly. So while the outer extents of the shape are maintaining their general size and the inner pore itself was also not varying greatly. Therefore, the mechanism behind changing the polyhedra's outer volume was the shrinking or closing off of smaller pores. In an architecture with high beam numbers, a volume change affected only the smallest pores, or rather the most complicated architectural features, but had little to no bearing on overall mechanical properties, except in the case of the Truncated Octahedron (which performs like a hollow sphere). This was corroborated in the measure of outer/inner pore diameter (Figure 20): the TO has a ratio of outer/inner volume which for every porosity was higher than that of a hollow sphere.

Geometric arrangements of material directly affects the mechanical properties of architecture. To demonstrate this, the polyhedra were compressed using finite element analysis in the orientation as shown in Figure 15. Unsurprisingly, the Hexahedron was the strongest polyhedra due to the highest percentage of material oriented in the loading direction. The most interesting result was that optimal solutions for architectural arrangement vary with actual porosity value, meaning, the strongest architecture at a discrete porosity was not the strongest architecture at a different porosity. This can be seen by comparing all of the architectures (save the Hexahedron) between 50 and 60%:

witness that the TH was the second strongest architecture and the TO was the weakest. At 60% porosity, the TO was the second strongest and the TH was the weakest (see Figure 21). This was because below 60% porosity the TO performing as a closed cell solid which had a lower Hashin-Shtrickman limit than an open-celled solid.

Deformation patterns of architectures can be obtained from the power law relationships relating modulus and volume fraction. Viewing equation 1, the C value is due to a number of undetermined geometric arrangements but the n value illustrates the type of deformation an architecture exhibits during compression. Reading from Table 3 the Hexahedron had an n of 1.23, very close to the value for cell wall stretching. The Truncated Hexahedron and the Rhombitruncated Cuboctahedron both had the same n value of 2.25 meaning that the deformation pattern of the architectures was the same, via edge bending.

Elemental principle stress distribution was evaluated as a method to characterize the loading on each architecture solely as a function of the contribution of the spatial arrangement of material. Unsurprisingly, the results showed that the material volume played a large role in the determination of the stress loading upon the architectures. For the Hexahedron, the peak of the stress profile shifted towards higher values with an increase in porosity. When porosity increased, the compressive modes shifted towards the tensile region and the tensile modes increased in stress in the tensile region. As porosity decreased, the range of stress values increased. Higher porosity architectures had more elements loaded towards the compression region indicating higher bending of the beams. Localization of the stresses along the length of the beams corroborates this (data not shown). For the Hexahedron at 50% porosity, a near equal percentage of elements were

subjected to loads between -3 and -10 MPa. Higher porosity architectures began to show a stress peak below 10MPa.

The stress distribution of dissimilar architecture aids in the demonstration of the difference in deformation patterns of the architectures. Additionally, among similar architectures, analogous deformation patterns can result in dissimilar stress distributions. The visualization of the architectural contribution to peak stresses can help to determine the stress backbone of the architectures and which features are structurally unimportant. All architectures showed a higher stress mode in compression than in tension. The compressive modes of the architectures may not be related to the modulus: the compressive stress mode of the Truncated Octahedron was the same as the Rhombitruncated Cuboctahedron, an architecture which at 80% porosity, had a modulus which was 28% lower. There was a marked reduction in beam bending in the more complex shapes as a result of tight material arrangement. An increase in the number of beams in an architecture resulted in a decrease in the high stress concentrations at the interface between the matching of beams. Through the finite element analysis we can see that some elements were completely unloaded and thus do not contribute to the mechanical integrity of the architecture in the current shape. The results also demonstrated that small differences in the arrangement of material can result in large differences in the overall mechanical properties of a structure, regardless of the material.

An important reason to provide a robust geometric analysis of these three-dimensional architectures is that the field of cellular solids has shown us that that density alone cannot predict the strength of an architecture, therefore results related to density provide no more information than a theoretical range for mechanical properties,

something easily calculated from the Hashin-Shtrickman equation [168]. Beyond that reason though, study of these architectures is directly applicable to the study of growth mechanisms where generally speaking, the arrangement of material plays a significant role in the future success of that construct. The fact that the design of architectures in nature promotes minimum energy expenditure, maximum strength and simplicity in design means that we can draw conclusions on the types of structures which are favored in nature. In organic systems which utilize surface based deposition processes, such as bone or tissue engineered scaffolds, composite structures may be formed of multiple numbers of single celled units, each repeat unit similar to the geometries surveyed. In these systems, high beam numbers may be favored because they promote connection between adjacent units, provide multi-axis mechanical reinforcement and because successive tessellation increases adaptability between structures of varying beam numbers and surface areas. While surface area does not directly relate to mechanical properties, a growth path along lower surface area expenditure towards a point of higher strength would be favored over a greater surface area expenditure for a comparable strength increase. This is because material deposition/reduction allows for the ability to shift between shapes, as we have seen that different architectures are mechanically favored at specific porosities. For example, while the Hexahedron is the strongest shape, it provides no path to reach an architecture of varied properties that isn't along a path of strength reduction, which is a sub-optimal solution. Previous bone related studies have shown that a uniform stress state may be responsible for the growth of bone and other natural mechanisms [134]; as can be seen from the elemental stress distribution graphs, lower porosity architectures have more of their architecture loaded in compression, while

higher porosities or architecturally complex architectures have lower stress peaks which are more evenly spaced between compressive and tensile loading (architectures were uni-axially compressed but due to beam arrangement some regions exhibited tensile stress). For the purpose of tissue engineered scaffolds, architectures with low compressive stresses and higher regions of tensile stress stand to fare better than those with high compressive stress and large compressive stress ranges as most bone fractures are due to compressive stress and bending (Müller et al. in J Biomechanics 31:150 1998).

3.1.5 Conclusion

In this study we detailed a comparison of architectures containing the same material volume but dissimilar architectural arrangements. We demonstrated that for similar material volumes, a range of structural properties exist which are dependent upon the amount of material arranged about the loading axis. We showed that the strongest surveyed configuration is the Hexahedron which outperforms the other architectures across the porosity range but also exhibits high compressive stress. We demonstrated that in architectures with high beam numbers surface area exhibits a parabolic relationship with a maxima near 70% porosity. The contribution of surface area contraction/expansion was shown to have a greater effect than volumetric arrangement when transitioning between porosity values. We illustrated that while density is the strongest factor in controlling modulus, optimal material arrangement can result in equal modulus values even with volumetric discrepancies of up to 10%. We showed that at low porosities, loss of architectural complexity allows these architectures to be modeled as closed celled solids. At these lower porosities, the smaller pores do not greatly contribute to the overall modulus of the architectures and that a stress backbone is responsible for the modulus.

This completed study represents the first step in an analysis of architecture for the goal of creating a logic set of rules which can explain the structural properties of an architecture based solely upon its material arrangement (geometry). We plan to exploit this system for the decomposition of bone and the simplification of its structure.

3.2 Experimental Validation of Finite Element Structural Comparison and Development of a Correlative Geometric Model[*]

3.2.1 Introduction

Cellular solids in nature gravitate towards specific architectures; the strength of these architectures are a function of architectural arrangement, not as a fundamental design demand for density. This is not to refute the fact that density is the strongest determinant of strength for architectures with dissimilar density, but when considering architectures with same density, the morphological parameters are more important. For example, great discrepancies can be seen between two architectures which share the same density. Thus, there are arrangements which promote or detract from the overall strength of architectures and it is these morphological parameters that ultimately control the strength of the objects, especially considering objects of similar density. At same material volumes, it is the morphological parameters that control the deformation properties and ultimately the strength of these architectures. It is the goal of current cellular solids research to isolate which factors correlate to the mechanical properties of objects. If correlations between these parameters and architectural strength was found, objects could be designed with specific strengths and deformation properties for a wide range of applications. With correlations between strength and morphological parameters, the growth cycle of naturally occurring architectures could be posited based on the found architectures strength and morphological parameters. A library of known architectures

---

with corresponding properties could be used to design materials with varied strength and deformation properties for a wide range of mechanical applications.

While exhaustive theoretical work has been completed by Gibson and Ashby studying the effects of material organization for specific three dimensional cases, experimental validation of general cases has been limited to regular, two dimensional extruded structures such as honeycombs [159]. With the advent of rapid prototyping, not only can complicated three-dimensional objects be replicated for repeatable exploration, but modifications to the architecture can be completed simply and in a short turn around time to explore further relationships. Using these novel techniques for architecture replication, correlations between mechanical properties and morphological parameters can be useful for materials design or information pertaining to growth mechanisms in nature. A recent study by Woesz et al. [167] utilized rapid prototyping to generate assembled structures based on variations of cubic polyhedra and the Gibson-Ashby structure (which fails due to bending). The results of the study demonstrated that strength, stiffness and energy absorption efficiency can be modified independently via architectural modification but leave the generation of a rule set for future work.

As previously studied (section 3.1), we have obtained the geometric characteristics of a set of regular, symmetric polyhedra; using that set and those polyhedra we can measure the deformation and mechanical properties. Using the measured deformation and mechanical properties we conducted regression analysis to determine which, if any of the morphological parameters controls the overall strength of the object. Additional regression was used to determine which parameters control the deformation properties of the architecture. It is the deformation properties and failure

mechanisms which are truly of most interest for future mechanical designs. Applying mechanical testing data to the morphological characteristics will allow for others to derive a set of parameters which can be applied to architectures in a biological study to explore the function of variation of these parameters on the mechanical properties of architectures which grow as a result of biological properties. This is important for mechanically mediated systems such as trabecular bone where the final strength of the object is of the highest importance. In addition, the ideal failure mode should b that of a ductile material as it may allow recovery through tissue growth compared to a catastrophic failure of a brittle material. These growth mechanisms are what we are interested in elucidating and through the combination of mechanical testing data and derived morphological parameters we can begin to arrive at a model which predicts strength based on architecture.

The goal of this study was to correlate geometric characteristics of architecture with mechanical properties and deformation attributes. We used rapid prototyping to generate three-dimensional samples of previously explored computational models and tested them in unconfined uniaxial compression. We then explored the results by correlating theoretical calculations to experimental data for the construction of a library or rule set of morphological parameters and how they affect mechanical strength of objects.

3.2.2 Methods

Polyhedra from the Platonic and Archimedean set were generated as discussed in section 3.1.2 as CAD files. The polyhedra were resized to bounding box dimensions of 2cm X 2cm X 2cm and exported as a stereolithography format (.stl) for rapid prototyping.

Polyhedra were fabricated from polyamide on a Sinterstation 2000 commercial SLS machine (3D Systems Inc., Valencia, CA). Polyamide powder was obtained and prepared as described in Lohfeld et al. [169]. A CO_2 laser was used to fuse the sectioned 2D profile of each architecture in a layer by layer fashion to build the three-dimensional polyhedra. Four copies of each architecture and porosity were created for testing. Solid blocks of material were created as well to determine the material properties of the laser sintered polyamide.

Polyhedra were scanned using Microcomputed Tomography (Scanco Medical, μCT 80, Bassersdorf, Switzerland) [116]. Three dimensional morphology of the prototyped polyhedra was accomplished by measuring their porosity and surface area (Figure 25). One specimen of each of the architectures was scanned at an energy of 80 kV and an intensity of 120 μA to adequately visualize the polyhedra. The specimens were scanned at a 27 μm isotropic resolution. Thresholding was conducted to optimize the visualization for quantification of morphological parameters. The threshold level was varied and the change in cross-sectional area of the actual polyhedra was adjusted to the threshold level in an attempt to obtain the actual porosity and surface area of the shapes.

Polyhedra were compressively tested to failure with an Instron using a cross head speed of 1.0 mm/min. Stiffness was calculated as the slope of the initial force deformation curve. Compressive modulus was calculated as the slope of the linear portion of the stress-strain curve and ultimate stress was derived from the peak of the stress-strain curve. Energy absorption efficiency (EAE) was calculated as the ratio of the energy absorption of an ideal plastic material versus the area under the stress-strain curve [167].

Multi-variable regression analysis was conducted on the morphological characteristics of the polyhedra. We used morphological values taken from the finite element exploration of the polyhedra corresponding to the idealized versions of the polyhedra. The parameters measured were strut number, vertice number, slope of beam diameter / beam length, surface to volume ratio, outer volume / inner volume, pore diameter ratio, the value of n, C and the mode of stress values in the tensile and compressive regions. Additionally predicted were the experimental parameters of modulus, stiffness, EAE and ultimate stress and strain.
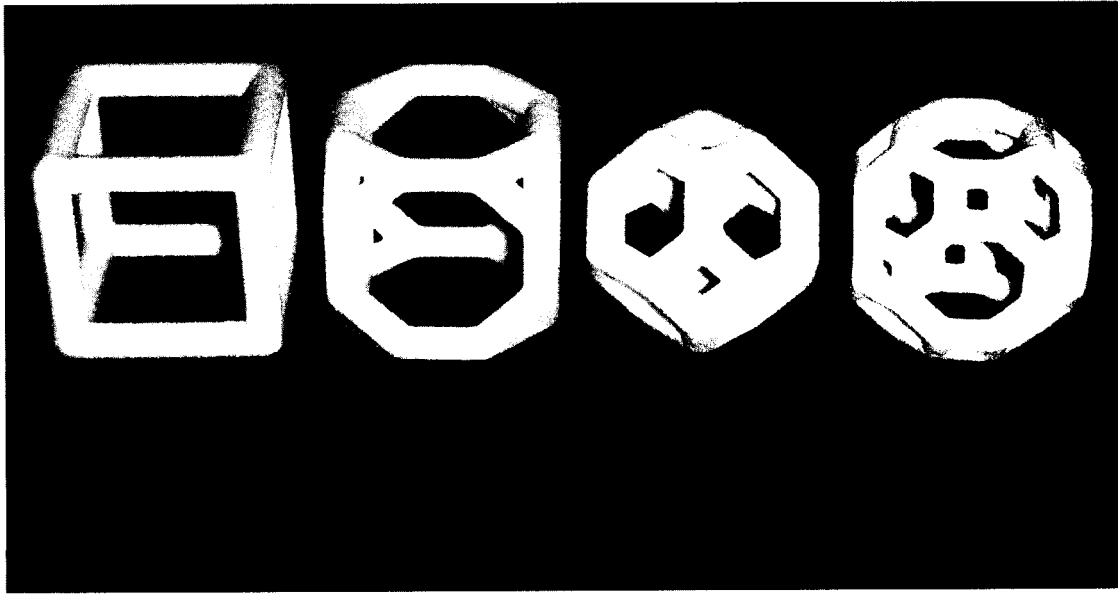
Figure 24. Polyhedra rapid prototyped using a Sinterstation 2500plus solid laser sintering machine. Displayed polyhedra have a bounding box of side length 2cm and are 80% porous.

3.2.3 Results

Rapid prototyped models were built using Selective Laser Sintering (SLS). Figure 24 shows the polyhedra (white) and the build process which has imbued the polyhedra with a rough surface topography. To verify the accuracy of the build process the architectures were scanned with microcomputed tomography. Optimal thresholding was found by matching the slice surface roughness to the actual surface roughness of the architecture, ensuring that the reconstruction was a valid approximation of the polyhedra, with a solid interior containing no gaps. The accompanying microcomputed tomography scans (Figure 25) illustrate the roughness that comes from the sintering of the particles together to make the architecture. This surface roughness precluded an exact match between the actual surface area, yet it was within an acceptable tolerance at approximately 5 %. In Figure 26 we can see that even with proper thresholding and reconstruction of the polyhedra the idealized porosities of the architectures were not met. For example, the TH at 85% and the TO and H around 87% porosity, were larger than

5 0 mm
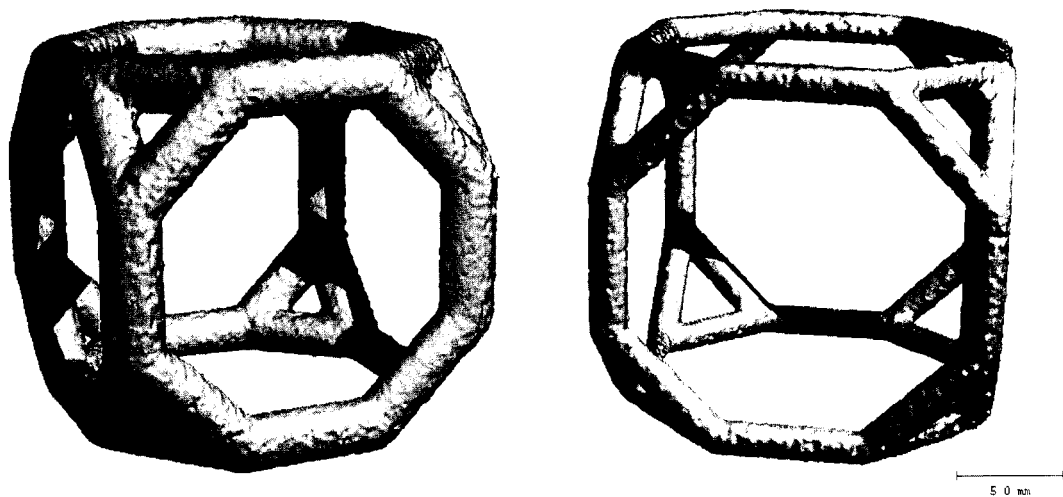
Figure 25. Microcomputed Tomography reconstructions of rapid prototyped architectures highlighting the surface topography and material grain due to sintering process.

their designed porosity of 80%.

Polyhedra designed to be 90% porosity maintained a smaller relative error of less than 5.0%. TH and RC were the closest to the intended porosity, regardless of the 80% or 90% groupings.
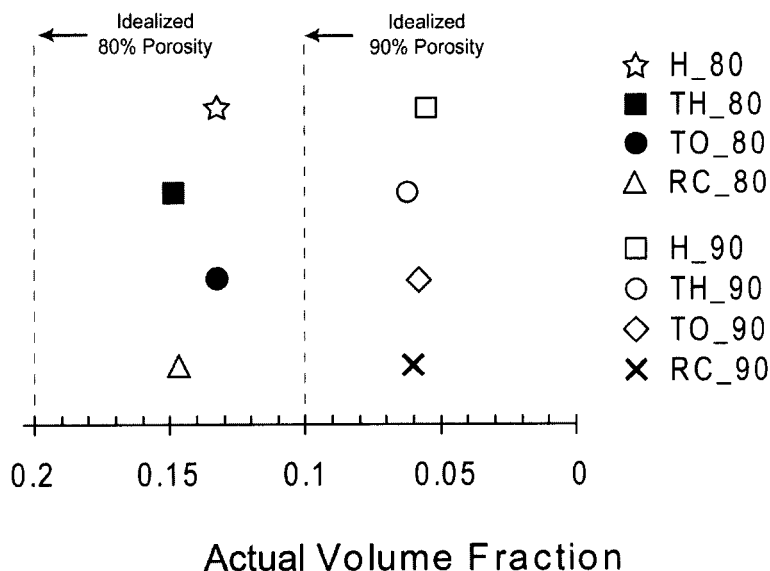
Figure 26. Porosity of the SLS models measured via uCT. There is a correlation between actual volume fraction and the surface area of the architecture. Higher surface areas leads to closer approximation of the intended porosity.

The architectures were mechanically compressed to failure with video capture. Pictures of the deformed 80% porosity architectures can be seen in Figure 27. The Hexahedron showed the highest Yield Point but also the greatest variability. The H and the TO shared similar values for fracture strain although the H had a larger plastic region.
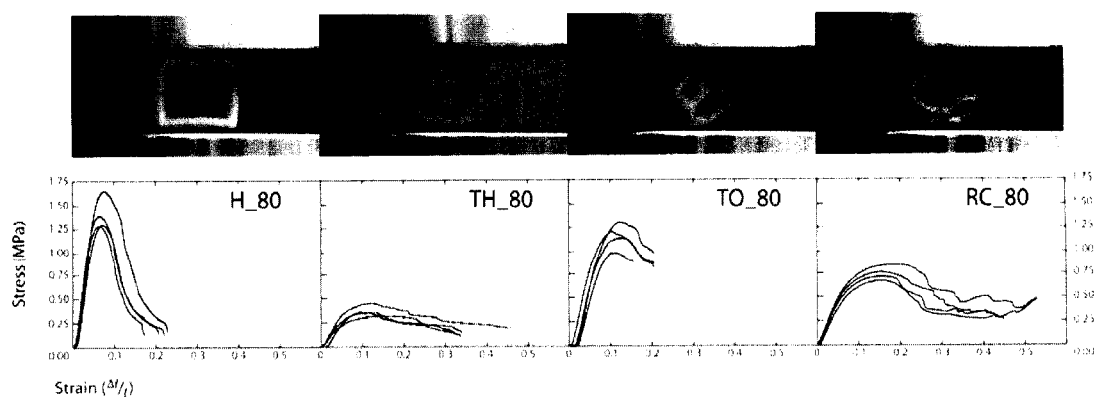
Figure 27. Stress / Strain Diagram of 80% porous architectures.

The TO fractured at a stress nearly equal to its yield point whereas the H fractured at a stress value near zero. The TH had the lowest modulus and yield point but the strain at fracture was twice that of the H and TO. Of all the architectures, the RC had the longest plastic region following the ultimate point which can be distinguished as a densification characteristic of cellular solids. Following this period of densification and strain hardening, the architecture experiences a secondary fracture at a value greater than any other architecture.
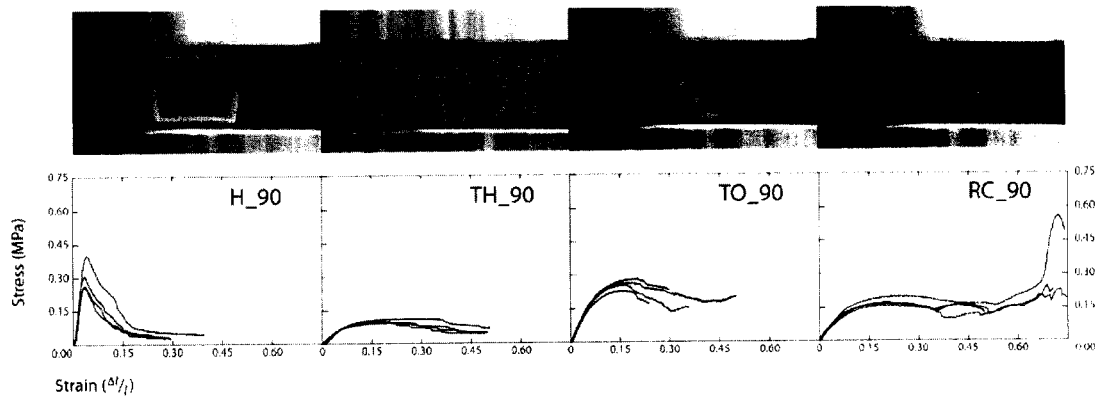
Figure 28. Stress / Strain Diagram of 90% porous architectures.

Differences in the mechanical loading profile were seen in the architecture simply by adjusting their volumes, as shown in Figure 28 where the polyhedra are now at 90% porosity. The H still has the highest modulus and yield point and the TH still has the lowest of both. At this porosity, all of the architectures demonstrated a much better strain response with fracture strain occurring at higher strains than the same architecture at a lower porosity. The H and the TO again had similar fracture strains which at both porosities were the lowest of the four architectures. The TO began to show the signs of a densification region, with a strain hardening response that increased the stress immediately following the ultimate strength point. The RC again had densification regions, this time resulting in an ultimate strength which occurred during a secondary

peak for several of the samples. This secondary peak gives the RC a secondary modulus and strength which was higher than any of the other architectures at the same porosity. Obviously, because of this the RC has the highest ultimate strain and fracture strain while the H has the lowest.

The modulus of the architectures was directly compared to the finite element results discussed in Section 3.1. Using the adjusted values for porosity in the FEA modeling equation we were able to predict the
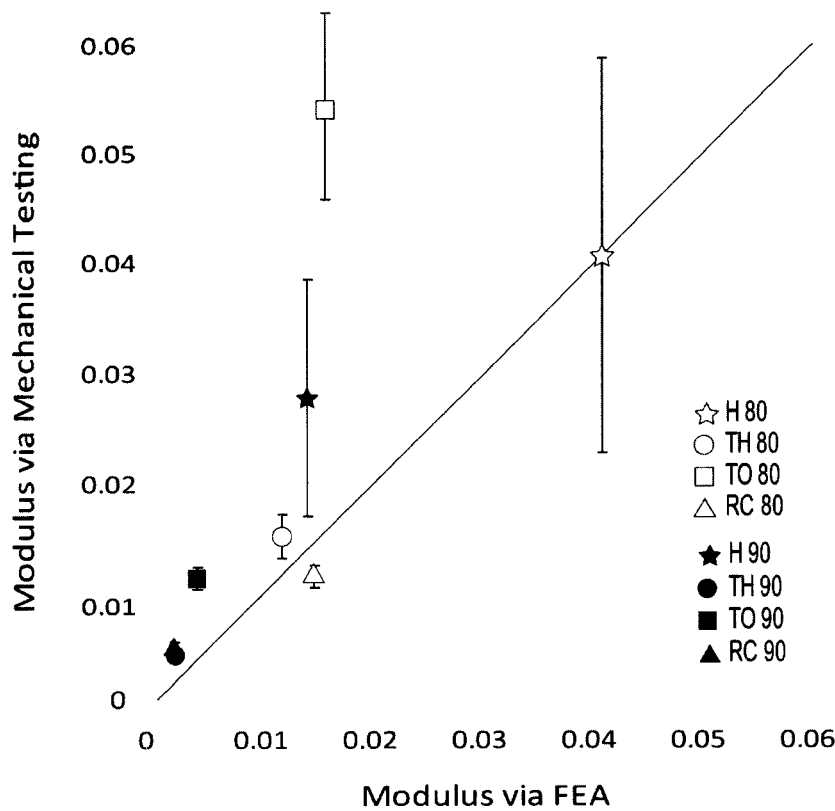
Figure 29. Normalized mechanical testing modulus vs. Normalized FEA modulus for all architectures.

modulus of the

actual polyhedra using the actual porosity values. The results (Figure 29) show that the finite element model under predicted the modulus values of the architectures for both porosities. The line on the graph is a line with a slope of 1 indicating where the values would lie if the prediction was correct. The mean (±stdev) error between normalized experimental modulus and normalized FEA modulus was 0.05.

Figure 30. Energy absorption efficiency (EAE) and strength vs. stiffness.

Further comparison of the architectures was completed by evaluating their energy absorption efficiency. The Energy Absorption Efficiency (EAE) is a measure of the energy storing ability of each of the polyhedra. The value is a ratio of the area under the curve and the area of the rectangle corresponding to an ideal plastic material. Viewing the top of Figure 30, and ignoring the H, the trend for the architectures was that an increase in porosity resulted in constant or slightly increased EAE (throwing out the single RC sample which fractured prematurely, changing the EAE to 0.68). The H did not follow this trend and the energy absorption of the architecture actually decreased with a porosity increase. Additionally, the range of the H's EAE was completely different than any of the other shapes; in between 0.4-0.6; the other shapes had an EAE ranged between 0.6 and 0.80. Viewing the EAE and the stiffness, we can see that the two are unrelated as

Table 4. Properties of the mechanically tested polyhedra.

	H		TH		RC		TO	
	80%	90%	80%	90%	80%	90%	80%	90%
E (MPa)	10.9	7.4	4.0	1.1	3.8	1.2	14.5	3.0
S (N/mm)	360	179	99	22	121	30	253	59
ε_f ($\Delta l/l$)	0.21	0.30	0.38	0.50	0.48	0.67	0.19	0.35
EAE	0.51	0.39	0.69	0.74	0.66	0.68	0.69	0.74

H=hexahedron, TH=truncated hexahedron, RC=rhombitruncatd cuboctahedron, TO=truncated octahedron

constant energy absorption efficiency can exist over a 300MPa stiffness range. Likewise, this same energy absorption efficiency can be seen with architectures with strengths ranging from 0.1 to almost 1.5 MPa. From the strength vs. stiffness results we can see that there is roughly a linear correlation between the two but that specific geometric arrangement of the architectures and not simply their volume fraction is the controlling factor in the properties of the architectures.

3.2.4 Discussion

Information concerning the fracture and failure mechanisms for the architectures can be obtained by viewing the stress-strain diagrams. The fracture of the TO near the yield point indicates that fracture is not as a result of bending because of the short beam lengths. The low fracture point of the H points to a fracture mechanism as a result of single beam fracture rather than cellular collapse. Therefore, the fracture strength is as a function of the beam thickness and bending stiffness.

Comparisons of mechanical behavior can be made directly between architectures of similar properties: the TH and the TO had the same number of beams but mechanically performed very differently in various categories. The upper and lower truncations of the TH did nothing to promote vertical compressive strength and the strength of the architecture was due in whole to the bending stiffness of the middle beams, which in comparison to the H were less than half the diameter and less than a third the length. The

architectural complexity of the TH provided no support and the connectivity provided no aid in strengthening due to the arrangement of the architectural beams. The connectivity of the TO provided greater rigidity until the strain was sufficient to disengage the 45 degree connection between the vertically oriented beams.

Changes in the architecture's porosity modified the witnessed failure mechanism. The greatest difference witnessed in the architectures was that the increase in porosity made all the architectures more ductile and less prone to fracture at low strain levels. The TO did act like a characteristic cellular solid with something that resembled the beginning of a densification region, however, the short beam length meant that the beams fractured before true densification may occur. This lead us to believe that the TO is strong for low deformation values but is extremely brittle. The failure of the RC was as a function of the diameter of the inner vertical beams fracturing through compression or bending, rather than the outer extents of the architecture. The added beams in the RC combined to strengthen the architecture rather than detracting from the overall strength, such as occurred in the TH. Additionally, the RC was overall the strongest shape at high strains because the compression of the truncated portion on the top and bottom of the architecture prevented bending of the vertical beams and added extra support to these beams so that they can exist in compression only.

The results of the mechanical compression allowed us to compare similar architectures with different porosity values to draw conclusions about the deformation profile and the effect of beam arrangement and beam diameter. By increasing porosity one decreased the strut diameter without a similar length adjustment. As a result, shapes had reduced strength, modulus and yield points. However, as mentioned, these

architectures became more ductile and the plastic region and strain at fracture increased. In the case of the TO, a decrease of 10% material meant that the shape did begin to densify before catastrophic mechanical failure. In the case of the RC, the densification region extended and the architecture regained strength and in one case tripled its strength. In short, architectures sustained simple fractures but are less likely to catastrophically fail at low stress/strain values.

The energy absorption efficiency results allowed us to discuss the effect of actual architectural contribution to the strength of architectures, aside from porosity. The general trend seen here was that an increase in porosity will result in higher energy storage and increased ductility. This was as a function of the increased complexity of the architectures and the dispersion of the material over a more diverse volume. The hexahedron however, had the material organized in a fashion that promotes axial stiffness at any porosity rather than becoming more ductile at higher porosities. The result of this was that the hexahedron is actually *less* efficient at storing energy at higher porosities and thus intolerant of defects or of fracture. The other polyhedra, due to the higher number of beam numbers can tolerate defects or loads in directions other than simply uniaxial due to the added complexity and beam matching.

Architectures were scanned with micro-computed tomography to measure whether rapid prototyping was indeed ready to create architectures which can be repeatably tested. The scans with the SLS models were over the porosity levels by a minimum of 5% and a maximum of 7%, indicating that compensative models will need to be created in the future to address under compensation of the design dimensions by the laser. Characteristics of idealized polyhedra were adjusted to account for these volumetric

discrepancies so that comparisons between the polyhedra and the actual models could be accomplished. Models built using another rapid prototyping process, 3DP, over compensated for the designed parameters, indicating not just that compensative models are process specific but that there is an inherent error that exists for each type of rapid prototyping build process. This additionally demonstrates that these processes are not yet at a point where models may be easily created for repeatable testing.

Architectures with higher surface area (see Figure 19) more closely approximated the intended porosity due to the larger perimeter length of the 2D slice and thus greater slice cross-sectional area. The results of the analysis of the rapid prototyped architectures showed that the printing process under compensated for the architecture, which was build process specific. Extra models built using another rapid prototyping process, 3DP, over compensated for the designed parameters, indicating that rapid prototyping for structural analysis was not yet at point where completely repeatable results are possible without adjustment for each build process (not shown).

Because the deformation of these polyhedra are strongly controlled by the morphological parameters and not the density, we took a detailed look at the deformation profile of the most complicated architecture, the Rhombitruncated Cuboctahedron. The compression occurred in several steps: 1) the top region and the bottom region compressed, 2) this region ultimately flattened and fractured, 3) subsequently, the middle region, double braced vertical struts, carried all of the load. At this point the RC mimics the H in that all of the load was vertical in orientation. Additionally at this point the platen was pushing against a much greater surface area as a result of the compressed region of the polyhedra. This can be seen in the actual diameter of the beams that are

being compressed. At 90% porosity, the cross-section of the H beams are 3.7 times the diameter of the RC beams. The RC is a desirable shape to study mechanically because it sacrifices a third of it's height in order to double its strength at high strain values. Additionally, at low strains, few beams break while the structure remains intact. This means that if the shape was to fracture, it would fracture at the weakest point, this weakest point just happens to be exactly where it would crumple and support load to increase the strength three-fold from the original value immediately. Other shapes suffer catastrophic immediate failure when they fracture and do not provide additional support until the architecture itself has been compressed to strain levels of 75% or more.

Deformation mechanism is as a result of the difference in mechanical properties of the edge vs. the wall. In one case the edge is stronger than the cell wall and in the other case, the cell wall is stronger than the edge. For $n=1$, the cell wall is stretching thus the cell wall is stronger than the edges (in plane), for n=2 the cell walls are thinner than the cell edges thus the deformation is governed by edge-bending. (out of plane) for $n=3$ the cell wall bends thus the cell wall is stronger than the edge (out of plane). For small deformations or high loads, a stronger shape would be desired. But for large strains at any load, an architecture which has added complexity to its skeleton would be most advantageous for structural support. This is because while these architectures do not match the strength of other shapes, following a failure they still are able to provide mechanical stability due to the arrangements of their struts. Whereas a simpler shape, which is stronger, experiences catastrophic failure at fracture point and load bearing ability drops to zero. In cases of extremely complicated architectures, such as the RC, the

densification region creates a secondary modulus, yield point and strength which is twice as high as the strongest architecture.

3.2.5 Conclusion

The results of this study have shown us that while density is the strongest determinant of elastic properties of an architecture, morphological parameters more heavily control the deformation, strength and plastic properties of an architecture when subjected to large deformations. These morphological parameters are especially important post yield point and post ultimate point for controlling the strength and deformation profile of an architecture. Speaking in terms of mechanical stability for design purposes: for small deformations and/or high loads, a stronger shape such as the Hexahedron would be desired. However, if we are speaking systems which will be subjected to large deformations ($\varepsilon > 0.05$), an architecture with architectural complexity (such as the Rhombitruncated Cuboctahedron) would be advantageous for structural support. While these architectures cannot match the strength of architectures which have the majority of their material oriented in the loading direction, following a small fracture they are able to provide mechanical stability due to the complex arrangements of their struts. While a simpler architecture may be stronger, catastrophic failure occurs at fracture point and load bearing ability drops to zero. In cases of extremely complicated architectures, such as the RC, the densification region creates a secondary modulus, yield point and strength which is twice as high as the strongest architecture.

Chapter 4: Determination of the effect of material organization on the architectural properties of random architectures.

The goal of this section was to study the effects of void volume arrangement on the structural and fluid flow characteristics of porous architectures. Here we attempted to quantify the effect of pore architecture organization of scaffolds encompassing similar material volume upon the structural and fluid flow properties of those scaffolds. While the previous course of study took the outside-in approach to exploring relationships based on material arrangment, this approach took the inside-out approach to explore relationships based on void volume. As before, scaffolds were compared by holding porosity constant, allowing comparisons to be drawn between dissimilar architectures. We hypothesized that as a result of material organization, diverse values can be obtained for such structural properties as stiffness and strength and material properties of modulus and ultimate stress, and fluid flow properties. Specifically, by varying surface area, pore architecture and pore volume for the void volume of random, porous architectures we proposed to describe relationships between void volume components and the structural and material properties as well as the dominant design characteristics governing the strength of such porous architectures. Equations derived from capillary tube models, phenomenological models, hydraulic radius and drag theories using these relationships can then be used to describe the structural properties of an architecture based solely on the aggregation of the known characteristics of the void volume.

Although the previous study included equal parts of modeling and physical experiments, random aggregation computational models will not be utilized here. Instead, physical models were built utilizing rapid prototyping processes to validate the experiments and for the derivation of relationships. In order to create a designed void

architecture, pore characteristics such as surface/volume ratio, and pore architecture were varied. The random aggregation of these embedded particles created a porous architecture and subsequent leaching of these particles is responsible for the void volume architecture. These experiments are relevant for both hydrologists and those generating architectures for tissue engineering.

4.1 Modulation of Permeability through Architectural Modulation of the Void Volume of Randomly Porous Solids

4.1.1 Introduction

The fluid properties of resorbable porous tissue engineered scaffolds are an important research focus because transport properties play a deciding role in the degree of de novo tissue invasion within the scaffold post implantation and biodegradation. Unlike more regulated parameters such as mechanical properties and biocompatibility, tissue engineered scaffolds are most often randomly oriented porous structures with fluid properties that vary wildly spatially and directionally. This complexity increases the modeling difficulty and disrupts the possibility of repeatability between studies. As a recent review article by Hutmacher argues, a new approach that minimizes modeling and measurement error while exploring the parameters affecting fluid properties should be introduced for the design of tissue engineered constructs [170].

The basic design demand of tissue engineered scaffolds are that they be porous enough to support interconnectivity [101, 171] which has been demonstrated to be around 80% porosity by volume [113]. There are inherent problems that arise due to using a random porous solid for applications which require temporary mechanical stability. Exact control over porosity is not possible because creation rests upon a wt% mixture rather than a volumetric one. This is not to say that specific correlations between volume and weight are absent but it is simpler to utilize weight over volume when mixing. A resulting complication is that the random aggregation of particles imbues a large variation in mechanical and fluid properties even between similar porosities and pore architectures

[170, 172]. This variability provides impermeable regions or regions of mechanical instability. Finally, there is a miss-stated design demand of "an interconnected network" when what is actually desired is a conduit that is fully permeable. Permeability is a measure of the ease with which fluid may flow through a porous solid developed by Darcy to calculate water seepage through sand beds [138].

Multiple studies exist in the field of tissue engineering that address the transport properties of porous solids as they are designed for tissue invasion and regeneration. Agrawal et al has shown that interconnectivity and porosity can modulate the degradation of the solid itself. In a study with varied porosities, the lower porosity created regions of high acidity which increased the speed of degradation but would prove unsustainable for cellular life [9]. The results of this study provided a measure for tailoring the degradation time of a porous scaffold for PLGA materials or those that degrade hydrolytically. Recent studies by Hollister have incorporated permeability as a design parameter for tissue engineered scaffolds [107]. In restricted topological optimization studies, a dual optimization between modulus and permeability has resulted in symmetric scaffolds with designed permeability and modulus. The permeability of these studies is regulated via centrally located channels which pass through the assembled scaffold openly. These types of scaffolds may only be built using direct fabrication using rapid prototyping however this manufacturing process affords additional repeatability across samples.

To study the effect of architecture on fluid properties of porous solids we can begin with previous research in hydrology and the study of porous solids. Stochastic methods have shown promise in the evaluation of random networks but minute differences in the architecture can result in large discrepancies in the flow results [139].

Still, there are multiple models which exist to study porous solids that take into account variables such as neck, throat, pore volume, porosity and temperature to export a value for the permeability. Models exist such as Hydraulic Radius, Capillary based, Phenomenological and Drag Models. Scheidegger's "capillaric model" is the simplest which accounts for an n number of channels of uniform length and diameter. The "straight capillaric model" is a variation of the Carman-Kozeny [173] equation:

$$k = \frac{\phi \overline{\delta}^2}{32}$$

Where:

$\phi = Porosity$

$\overline{\delta} = Average\ Pore$

$Diameter\ (m^2)$

(2)
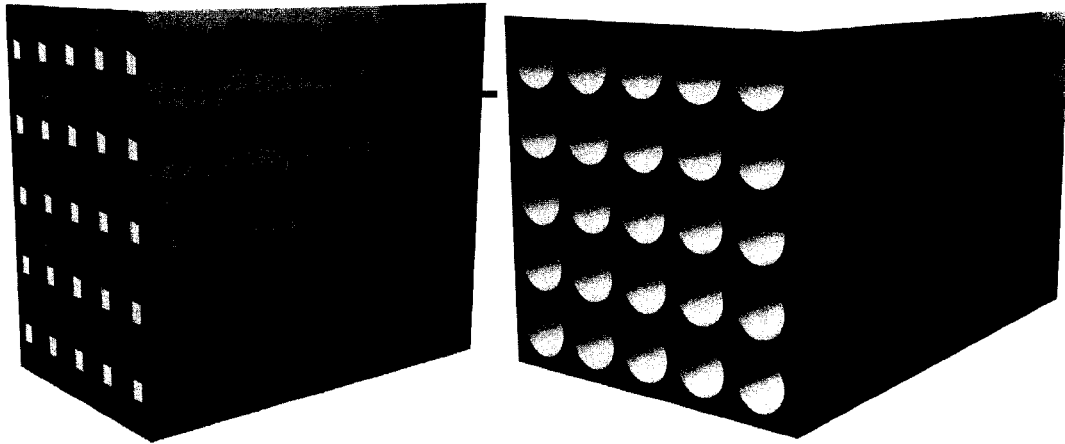
Figure 31. Pictoral representation of "straight capillaric" model of porous solid. At left, idealized [poor] assumption of the y-shapes arranged axially to form linear channels. At right, idealized assumption of straight cylindrical capillaries.

The "parallel capillaric" model makes a further assumption to account for orthogonal flow in the scaffold. The assumption (which builds upon the previous model of orthogonal flow only), is that 1/3 of the flow occurs orthogonally, thus the model takes the form:

$$k = \frac{\phi \bar{\delta}^2}{96} \qquad (3)$$

The final capillaric model is the "serial model."

$$k = \frac{\phi \bar{\delta}^2}{96T^2} \qquad \qquad Where: \qquad \qquad T = Tortuosity = \frac{ds}{dx} = \frac{s}{x} \qquad (4)$$
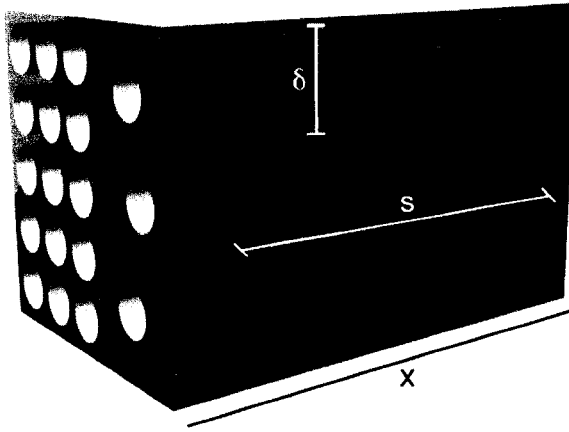
Figure 32. Pictoral representation of "serial capillaric" model. An average of different pore diameters are accounted for.

In the serial model capillaries of varying diameter are assembled in series; this model takes into account the different capillary diameters and adds a Tortuosity term. This term gives a ratio of the length of the flow channel to the length of the porous medium [174].

Hydraulic Radius models of fluid flow properties build upon the capillary models to assume that permeability has dimensions in m^2, therefore, a length characteristic (Termed the hydraulic radius) should exist which is linked to the channels that the porous medium is thought to be analogous to. One simple measure is of the ratio of the volume to the surface of the void space. This model has been shown to work well for packed solids which depending on the porosity of the studied solid can be an appropriate model to use [173]. In the Kozeny-Carman relation the Hydraulic Radius model takes the form of:

$$Where:$$

$$\phi = Porosity$$

$$S_0 = Specific\ Surface$$

$$k = \frac{\phi^3}{5S_0^2(1-\phi)^2}$$

$$Area\left(m^2/m^3\right)$$

(5)

In the Drag Model of permeability the walls of the pores are instead treated as obstacles to flow. The drag on the walls is estimated from Navier-Stokes and the summation of the drag is assumed to be the resistance to flow [174]. The advantage of the drag model is the ability to model the porous nature as fibers or spheres. Unlike other models, permeability is a function of flow rate. Utilizing the Darcy substitution for the fiber model, the equation takes the form:

$$Where:$$

$$\mu = Vis\cos ity\ (N \cdot s/m^2)$$

$$k = \frac{3}{16}\left(\frac{\phi\delta^2}{1-\phi}\right)\left(\frac{2-\ln(\delta Q_A \rho/\mu\phi)}{4-\ln(\delta Q_A \rho/\mu\phi)}\right)$$

$$Q_A = \frac{Flow\ Rate}{Unit\ Area}\ (m^3/s)$$

(6)

$$\rho = Apparent\ Density\ (1-\phi)$$

$$\delta = Average\ Fiber\ Diameter\ (m)$$

The final model explored is a Phenomenological models where a permeation factor, k, is related to the geometric parameters. This particular equation includes empirically derived parameters and assumes an inverse natural log relationship between the parameters and the permeation factor, k [173]. The form of the Phenomenological Model is:

$$K = e^{(3.84V_1+0.2V_2+(0.56x10^{-6})TD-8.09\phi-2.53)}$$

(7)

$$K = Water\ Permeation\ Factor\ (m/s)$$

$$V_1,V_2 = Volume\ of\ two\ classes\ of\ pores\ (m^3)$$

$$TD = Threshold\ Diameter\ (m)$$

$$\phi = Modified\ Total\ Porosity$$

While these models provide a basis of discussion for the properties of porous solids they really do not provide us any angle of attack to address the problem of modeling and repeatability for the controlled exploration of these solids using an engineering problem solving approach. Additionally, as has been previously shown [138, 139, 175], no relationship exists between porosity and permeability which, ultimately, is the end goal for design of tissue engineered scaffolds. The inability to predict permeability based on volumetric porosity is a problem because scaffold success will only be seen with full control over parameters which affect tissue ingrowth. A possible point of entry is based on work by Scheidegger that demonstrated that it *may* be possible to derive a relationship between void volume surface area and resulting permeability [174]. This is promising as surface area of porous solids may be calculated via multiple corroborative methods such as μCT, mercury porisimetry or even the labor intensive least attractive option of serial sectioning and imaging. Utilizing Scheidegger's research we can arrive at a model which takes us one step closer to that goal by modulating the architecture and surface area of the void phase of a solid and correlate that to the permeability.

Armed with a tool to approach permeability modeling based on surface area analysis, we must employ a repeatable system for investigation of these architectures. The use of rapid prototyping for the creation of scaffolds with designed permeability need not exist solely for regular, symmetric architectures such as Hollister created with his architecture optimization algorithms. Indeed, there are cases where rapid prototyping may not be able to create the fine detail desired for specific tissue systems [14]. To match current research techniques for the creation of randomly porous solids, rapid prototyping

could be utilized for the creation of microparticles with standard geometric properties to use as porogens. A fluid flow study utilizing leached solids with pore architectures from those designed porogens could tighten control over some of the previously explored parameters and allow exploration of additional parameters such as surface to volume ratio and pore geometric properties.

In this study we built upon the previous research of others in the field of porous solids to generate a series of porous solids with varied pore characteristics for the exploration of permeability. We employed rapid prototyping to create porogens that can be embedded in a solvent casting procedure to create a porous solid following leaching. Through the creation of porous solids with void architecture mimicking the novel architectures and evaluation of the permeability of the solid we aim to demonstrate the effect of surface area on the permeability of porous solids. The proposed methodology would allow experimental evidence to back up or check current flow theories with a quick, inexpensive, methodology to create porous media.

4.1.2 Methods

Generation of Porogen Architectures

Porogen architectures were generated using CAD processes using Rhino and IronCAD. Designed architectures were based on simple two dimensional shapes extruded into the z-direction. Several different architectures were generated; all containing the same volume, but with a varying surface area as a result of the material arrangement. The volume of the porogens was matched to sieved NaCl particles often used in particulate leaching to generate porous architectures and regarded as gold-standard in this

study. Grids of these porogens were generated using CAD with each grid containing

thousands of the porogens in one plane and exported as .stl files for rapid prototyping

processes.

Rapid Protoyping of Porogen Architectures

Scalability of the intended rapid prototyping system used to print the porogens

was first explored through an evaluation of the resolution of the PatternMaster.

Minimizing build time and material cost were the design demands to evaluate while

approximating the shape. A model to evaluate the resolution of the machine is displayed

in Figure 33; it can be seen that this block consisted of a series of holes and pillars of

defined size. Following the build of the object and the dissolving of the support structure,

the dimensions of the model were evaluated with SEM pictures. Pictures of the pillars
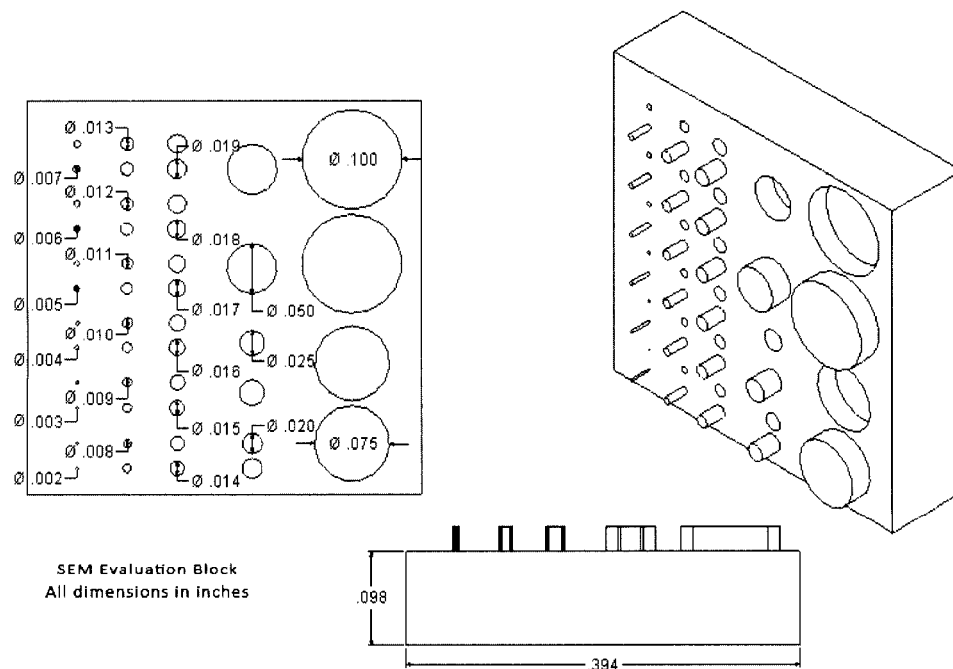
Figure 33. Benchmark part for evaluating error in the PatternMaster. A series of pillars and holes are designed on a block. The pillars and holes range from below to an order of magnitude above the resolution of the rapid prototyping machine.

and holes were taken and image analysis was completed in Adobe Photoshop (Adobe Systems, San Jose, CA). The pixel dimensions of each hole and pillar were measured and normalized to the actual dimensions scale bar displayed in the SEM photos. The point where the error is minimized as a function of the hole/pillar diameter was the resolution the polyhedra were built at.

Porogens were generated using RP processes as detailed. First, the CAD file was exported as a .stl file, which is an approximation of the defining surface of an object as a mesh of triangles. Next, the file was opened in Magics RP (Materialise, Minneapolis, MN) or DeskArtes (Helsinki, Finland) and visually inspected for errors. The .stl was then manually adjusted or automatically fixed by the program if the file contained errors. The modified .stl was re-exported. 3D Phase Change Printing (3DPC) with the PatternMaster (SolidScape, Merrimac, NH) was used to build the porogen bed. The PatternMaster prints models layer-by-layer using two materials, a build material (ProtoBuild) that generates the object and a support material (ProtoSupport) which provides for oblique angles and gives structural support to the object as it builds. After each layer is built, a cutter mills the layer to the proper height, then the build plate moves down one increment and the subsequent layer is printed on top of the previous layer. Following the completion of the build of the object, the support structure is dissolved using BioACT® VSO (Petroferm Inc., Fernandina Beach, FL), a kerosene based liquid.

Following the build process, retrieval of the porogens progressed with the dissolving of the ProtoSupport with BioACT® VSO. Following the dissolution of the support structure, the particles were washed twice with H_2O and then placed in a vacuum for 24 hours to remove the BioACT® VSO and H_2O. Following the drying process,

$$N_p = \frac{V_p (1.25E^{-03} \frac{g}{mm^3})}{Weight_{\#_p}}$$ (8)

particles were collected and weighed to roughly approximate the number of porogens retrieved from the process. Density (d) of the ProtoBuild is 1.25 g/ml. Based on the calculated error calculations from Specific Aim 1 we determined the range of sizes of the porogens. The number of porogens per batch was determined by:

Generation of Porous Architectures

Porous scaffolds were fabricated from a mixture of commercially available acrylic generated using the method of particulate leaching. A two part solution of initiator A (10% by volume) and crosslinker solution B (90% by volume) was mixed evenly. A measured amount of porogen or NaCl particles were then added and mixed until evenly distributed. Three different porosities were mixed, 50, 60, and 70 volume percent porosity. A minimum of 5 samples were prepared per porosity; mixtures were transferred into cylindrical GPC vials (2ml) and allowed to harden for 24 hours post mixing. Following hardening, scaffolds were cut with a diamond saw to length of 13mm.

Particulate leaching was accomplished with H_2O for the NaCl porogens and Acetone for the printed porogens. Samples were placed in 50mL of the respective solvent and placed on a shaker table at 50RPM and leached for 72 hours. Solvents were changed twice daily on the first day and once daily for the subsequent days.

Permeability Evaluation of the Porous Solids

A *permeameter* was set up similar to figures and descriptions in [9, 147, 148], with a water reservoir above the sample delivering fluid media and hydraulic pressure to

the sample via a tube. Gravity driven water from the reservoir travels axially through the scaffold and then is deposited in a reservoir below the scaffold. A manometer is placed both immediately before and after the scaffold in the flow apparatus. The reservoir to the left of the apparatus contains a known volume of water and the reservoir on the right is on a weighing scale to determine the exact amount of water permeated. The scaffold is placed in the apparatus with care that no gaps exist between the scaffold walls and the tube surrounding the scaffold. After the scaffold is secured and tight, the flow of water is begun. All leaks are sealed with silicone or Vaseline. All air bubbles that exist in the system are worked out by manipulation of the tubes. Calculation of the permeability begins after the flow rate of water is determined to be constant. The amount of water to pass through the scaffold for a given time interval as well as the pressure before and after the scaffold is measured. Values obtained during the permeability test were used to calculate intrinsic permeability of the scaffold architecture based on a modified version of Darcy's Law of fluid flow through porous media [138, 148], where:

$$Q_A = \frac{k(\Delta P)A}{\mu(\Delta L)}$$

$Where:$

$Q_A = Flow\ Rate\ (L^3/T)$

$k = Intrinsic\ Permeability\ (L^2)$

$\mu = Dynamic\ Viscosity\ (NT/M^2)$

$A = Cross\ Sectional\ Area\ (M^2)$

$\Delta P/\Delta L = Pressure\ Gradient\ (FL^{-3})$

(9)

The evaluated scaffold architectures were composed of a random packing of void structures and thus great variability existed throughout each scaffold. For this reason, a standard curve of fluid flow through the scaffold was constructed prior to taking data for each scaffold. The curve evaluated the fluid flow through the scaffold was fitted for a 1:1

line. Additionally, the permeability of an empty tube was measured to check against the values for the scaffolds. Each scaffold was run three times to construct a standard curve.

Permeability Prediction of Porous Solids Using Geometric Models

Capillary, hydraulic radius, phenomenological, and drag theory models were applied to the porous solids based on the given information in the studies for porosity, pore distribution, pore architecture, and pore volume [139, 173]. Additional required parameters were derived empirically.

4.1.3 Results

Resolution Evaluation of Rapid Prototyping Process

A block with pillars and holes with known diameters was generated using CAD and built with the PatternMaster for the purpose of evaluating the resolution of the rapid prototyping machine. Results are displayed in Figure 34. The resolution for the pillars closely matched a 1:1 linear fit with an increase in dimensional error when pillar diameter increased for both the x and y-directions. Resolution of holes did matched a 1:1 fit but under printed the hole diameter for all surveyed dimension range. It was determined that a scale up of at least 3x is adequate for the complete approximation of a polyhedral architecture. Restated, diameters of struts greater than 2 mm are adequate for reducing the error of the machine while minimizing both build time and material cost. There was a distortion error that was witnessed for both the pillars and the holes in the y-direction as a function of the cutter.

A Resolution of Pillars (200-1400 µm)

B Resolution of Holes (200-1400 µm)

C Average Resolution of PatternMaster

Figure 34. Resolution of the PatternMaster in relationship to a 1:1 designed vs. actual dimensions. (A) Resolution of printing pillars, (B) resolution of printing holes, (C) average resolution in both.

Construction of Porogen Architecture

Porogens based on simple two-dimensional shapes were designed using CAD processes. Three porogens were created with varying surface to volume ratios. Figure 35 illustrates the differences in the structural properties of each porogen as well as the two architectures that were generated. The volume of each porogen was resized to match the volume of a NaCl crystal of unit side length of 500-700µm.

Porogen	Surface Area (mm^2)	Volume (mm^3)
sphere	1.767	0.221
heptagon	2.102	0.221
hexagon	2.102	0.221
pentagon	2.152	0.221
cube	2.196	0.221
equilateral triangle	2.398	0.221
arrow	2.623	0.221
pill	2.655	0.221
isosceles triangle	2.821	0.221
Y-shape	2.894	0.221
L-shape	2.98	0.221
Cross	3.109	0.221
E-shape	3.405	0.221
Asterisk	3.535	0.221

Y Shape
0.45 mm
0.288 mm
0.984 mm
Asterisk
0.275 mm
1.185 mm

Porogen	Volume (mm^3)	Surface Area (mm^2)
NaCl	0.221	2.2
Y	0.221	2.9
Asterisk	0.221	3.5

NaCl (cube)
0.5-0.71 mm

Figure 35. Illustration of porogen architectures, volume and surface areas.

Using the SEM block evaluation to determine the allowable error of the RP process, the resolution for printing the porogens was determined. Figure 36 demonstrates the different build processes that could be used to generate the star shape. Process 407 was chosen for the star pattern and 408 was chosen for the Y shape (see Figure 43). Following the determination of the resolution, several parts were built using the PatternMaster. The resolution of the completed architecture were evaluated using SEM and were shown to be within the resolution of the machine for the error in the part dimensions. The porogens were built using the PatternMaster in batches of thousands. They were reclaimed by dissolving the part in BioACT VSO and then were washed in H$_2$O twice and dried in a vacuum. It was calculated that > 95% of the porogens can be reclainmed through the process.

Build Process 407   Build Porcess 408   Build Process 501

Figure 36. Build processes of the PatternMaster for the star porogen architecture. A plotter path is calculated for each object. Based on the build process setting, the plotter path differs in its approximation of the shape. The total length of the star shape is approximately ~0.750 mm.

Porogens were built in batches of thousands with ~175,000 being the total number of particles per architecture required. Using the benchmark part to evaluate the resolution of the PatternMaster, the resolution of building one porogen architecture was evaluated. The allowable range of the architectures that could be built required the modification of finer points of the architecture in order for the resolution of the RP machine to be able to generate the porogen architecture. The build process of the rapid prototyping was chosen for each specific architecture. Specific build processes (Figure 36) plot the outline of an object differently and the specific build setting that accurately generates the object will be used.

Micro-Computed Tomography

μCT scanning of the samples was completed for the porous architectures. It has previously been demonstrated that the determination of the porosity and surface area of the total scaffold can be determined as a result of thresholding out either the density of the NaCl or the rapid prototyped material [116]. Results of the μCT scan demonstrated that the actual porosities of the scaffolds were lower than the intended values for all of the scaffolds by 4-6%, giving total porosities of 55, 64, and 76 vol %.

Permeability Evaluation of the Porous Architectures

The permeability of porous architectures was measured using a constant head permeameter. Calculated permeability of the scaffolds is shown in Figure 37.

Hydraulic Permeability
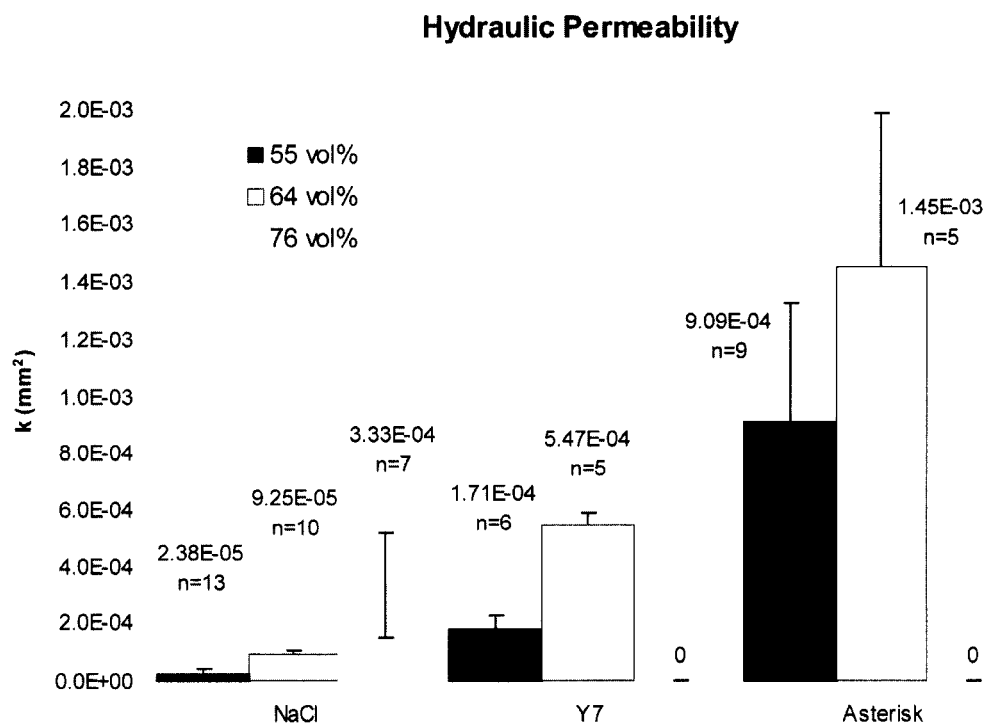
Figure 37. Permeability of the porous solids. All the permeability values for the three porogens were within the ranges of trabecular bone [148]. A. Y-shape pore architecture was 6x more permeable and asterisk pore architecture was 15.7x more permeable. B. Y-shape was 7x more permeable, asterisk was 38x more permeable. C. Scaffolds generated with Y-shape and asterisk pore architecture had no mechanical integrity after crosslinking and broke apart, thus no permeability evaluation was possible.

The permeability of the scaffolds using Y shape architecture was at least 6 times higher than the control (NaCl scaffold) and the scaffolds using the asterisk shape were at least 15.7 times more permeable than the control scaffold with NaCl. Although the standard deviation is high, this is not due to the measuring method because each sample exhibited high repeability but large variability existed across the samples. The reason for this was

due to the fact that we are evaluating and attempting to quantify a random system with few controllable parameters. No data could be obtained for the y-shaped or asterisk shaped samples at 76% porosity because they had no mechanical integrity following the porogen leaching step.

Permeability Modeling of the Porous Solids

Models derived by Scheidegger and others [173, 174] were applied to the geometric parameters of the y-shape and the NaCl porous architectures as obtained via design characteristics and empirically derived values. Table 5 shows the exact permeability predictions utilizing Capillary, Hydraulic Radius, Phenomenological and Drag Models and Figure 38 displays a log plot of the permeability.

Table 5. Permeability (in mm^2) of randomly porous solids as predicted by geometric fluid models.

COMPARISON OF MODELS TO EXPERIMENTAL RESULTS

	55% Y-Shape	64% Y-Shape	55% NaCl	64% NaCl	76% NaCl
Measured Permeability	1.71E-04	5.47E-04	2.38E-05	9.25E-05	3.33E-04
Straight Capillary	1.04E-08	1.21E-08	2.08E-05	2.42E-05	2.87E-05
Serial Capillary	9.47E-09	1.10E-08	5.57E-08	6.48E-08	7.70E-08
Hydraulic Radius	3.88E-08	7.05E-08	5.52E-09	1.00E-08	2.68E-08
Drag Theory	2.20E-07	3.22E-07	1.27E-15	1.86E-15	3.31E-15
Phenomenological	7.64E-03	1.58E-02	9.31E-04	4.49E-04	1.70E-04

The Straight Capillary Model most closely predicted the permeability of the NaCl scaffold for all three porosities but poorly predicted the permeability of the y-shape samples. The Serial Capillary model grossly under predicted permeability for both architectures and similar to the Straight Capillary model reports permeability values for the y-shape which are lower than the permeability of the NaCl at similar porosities. Hydraulic Radius predicted similar but low permeabilities for all architectures although the permeability trend of the y-shape vs. the NaCl was correctly predicted. Drag theory
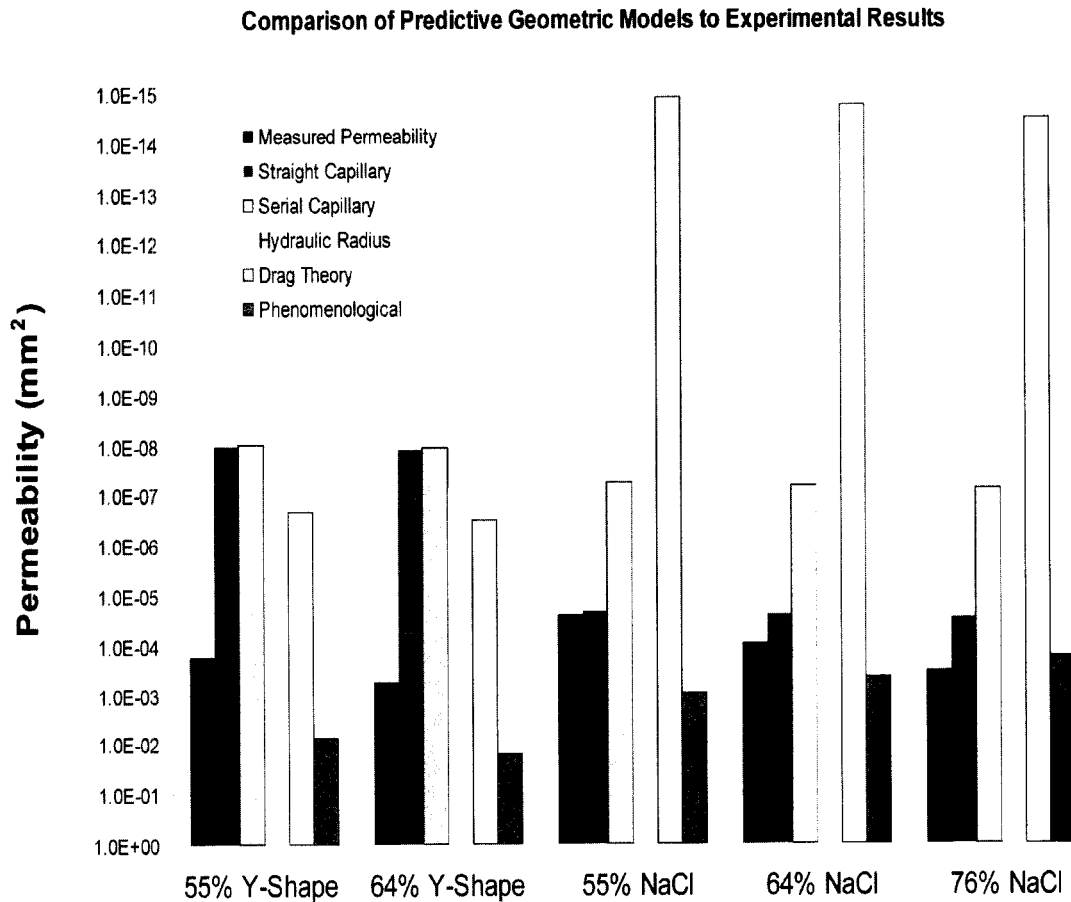
Figure 38. Permeability calculated from geometric models of fluid flow.

under predicted the NaCl greater than any other model but was the second closest

prediction of permeability for the y-shape porous solid. The Phenomenological Model

was the only model that over predicted permeability and did so for all samples save the

76% porous NaCl samples. Incidentally, the phenomenological model was the closest

approximation for both porosities for the y-shape porogen architecture and the 55% and

76/% NaCl porogen.

4.1.4 Discussion

The goal of this study was to modulate the pore volume parameters of a porous solid for an exploration of the effect upon permeability. A fluid flow study was carried out on porous solids with novel pore architectures and a standard porogen architecture both generated via standard porogen leaching processes. Through the use of rapid prototyping we were able to vary geometric properties while holding the volume constant, which allowed us to compare only the effects of architecture and surface area. Applied phenomenological models to the geometric parameters of each porous solid demonstrated that close approximations to the permeability may be achieved at but no model can yet correctly predict the resulting permeability.

We selected rapid prototyping as the focus for the exploration of the effects of architecture on the void phase based on its known repeatability and high throughput capabilities. We first needed to verify that the process was able to create architectures at the dimensions similar to standard porogen sizes, on the order of $<700 \mu m$ in side length usually. We selected a rapid prototyping process that provided the possibility of porogen removal following the build process with a solvent process: the PatternMaster. The phase change printer was the best choice for this study because the build material is an organic wax that can be easily be removed with an organic solvent leaving no remnants of the material after dissolving. The validation study that we conducted with the PatternMaster evaluated the machine's ability to create rounded positive and negative structures across a range of diameters. The results showed that there is a drift with respect to the y-axis due to the cutting blade that mills each layer to a horizontal plane to prepare for the next level to be laid on top of the previous one. This property is inherent to the machine and the

build process and should be accounted for in CAD models. An x-axis drift was negligible, ranged between -20% and +20% error but the average was near ~5% error. The holes demonstrated a large dimensional shift for the y-axis again and also for the x-axis indicating that the hole topology was not conserved. This was indeed corroborated by SEM pictures which show an oval-like opening and additionally by viewing the overall dimensional error of the PatternMaster to print holes at a low resolution (Figure 34B,C). The pillars, although experiencing a large dimensional shift over several z layers has low error in the shape conservation and approximation of intended diameter (Figure 34A). Overall, what this validation study has shown is that there must be compensation in the y-axis (along the blade cutting path) for the resolution evaluated, additionally that void spaces should be oriented orthogonal to the cutting blade rather than parallel to its path. This build orientation of the parts can improve the resolution of fine detailed models, and for a discussion of approaching the PatternMaster for specific dimensions, see Section 4.2.

The validation of the process allowed us to control the architecture that we printed to use as porogens. Standard porogens are usually cubic, as in NaCl or spherical, such as the case of gelatin microparticles. However, the type of architectures that we built had the added complexity of arms extending at angles greater than 30 degrees. While we theorize that this improves contact between adjacent microparticles, it additionally introduces tortuosity. The other difference in architecture between the standard porogens and those used in this study were the surface areas due to the design complexity of the microparticles. The asterisk shape is 1.5 times the surface area of the NaCl shape and the y-shape has 1.3 times the surface area of the cube. Working off of Scheidegger's research

into permeability as a function of surface area allows us to, in the resulting solids, clearly see the difference between the permeabilities as a function of surface area.

The measured permeability of the porous scaffolds provided several interesting results. First of all, the fact that the higher surface area scaffolds broke is a wetting issue. There is a point above which the surface area of porogens is too high for the polymer to coat the particles and still contain enough mechanical integrity to hold together. For the y-shape and the asterisk this was achieved at the 76% porosity value, indicating that this process may not be useful for the generation of scaffolds that are highly permeable, rather these designed architecture may be best suited for fluid flow research purposes. Secondly, the results do indicate that there may be a relationship between surface area of the void volume and the resulting permeability of the solid. This comes with the caveat that there are several other factors which come into play with these specific porogens as it is not known whether there is a wetting difference with the wax or whether the surface properties of the resulting void space were altered. However, the percolation threshold of the scaffolds as controlled by the neck and throat is much higher in the scaffolds with the novel architecture and thus we believe that the surface area must play a role to overcome this fact and result in a higher permeability over the NaCl porous scaffolds.

Although permeability is a useful measure to determine the ability of fluid to perfuse a scaffold, it is only a static measure and it is also a coefficient that depends on both the matrix and fluid properties which change across systems and architectures. There are limitations to both the evaluation of porosity and permeability as well as the argued importance of either of the terms. Porosity can be restated as void volume which is the absence of material in a solid. Often when particles are embedded in a solid and the

solid is then hardened, particles get trapped inside the solid (Figure 39). Following

leaching of the porogens (assuming that pore will be leached), the resulting void structure

contributes to porosity, but not permeability. This is but one example of why there are no
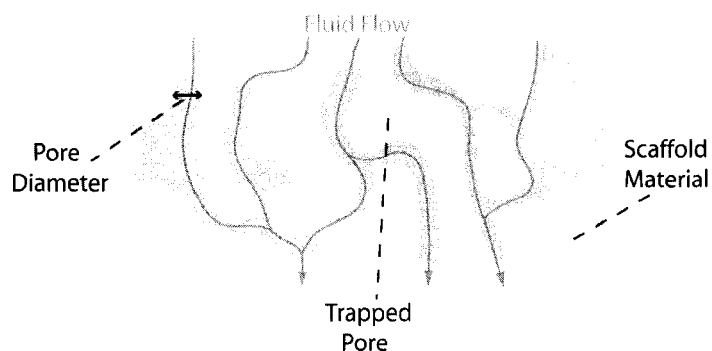
Figure 39. Contribution of trapped pores to permeability.

direct relationships between permeability and porosity. Other reasons that the two quantities cannot be compared are the surface charge of the solid, effects due to random nature and

difficulty to quantify the random aggregation of random sized, and numbered pore

architectures into a relationship with high correlation. Additionally, if a scaffold

characterized in this study were to be used in a tissue engineering application, the

permeability would change greatly as a result of fluid viscosity, temperature and pressure

especially upon implantation. While this may be, the characterization of architecture and

also permeability may be a useful measure by which we can create models for both the

importance of architecture to contribute to structural properties but also for the creation

of models that can predict tissue deposition upon specific architectures.

The most basic models that we have to work with currently are geometric based

fluid flow models which we applied to predict permeability. These models predicted

permeability poorly; two of the models actually predicted the opposite trend of the

observed experimental results. This merely highlights the fact that current theoretical

models (especially those shown) do not take into account complex geometry and that

small differences in the input parameters result in wildly varied predictions differing by magnitudes. The straight capillary model assumes a bundle of open channels and other than porosity, the only parameter controlling the permeability is the average pore diameter which, when assuming axial organization of the y-shapes as shown in Figure 31 is lower than that for the NaCl cubes of ranged side length 0.5 – 0.7mm explains the large permeability difference. The serial capillary model takes a step towards geometric variability by adding a simple tortuosity constant based on the length and diameter of differing diameter channels. This accounted for the low predicted permeability for this model, below that of the NaCl, because based on geometry alone, the dimensions of the y-shape were smaller in the axially oriented direction which counts against the permeability. Hydraulic Radius was the most interesting of all the models because it's the one case where the complexity of the porogen architecture plays a large predictive role in the permeability of the scaffold. And yet, it is only able to correctly predict the trend, not the actual values, of which are near the predictive results for the other models. The drag model actually ended up predicting the NaCl scaffolds worse than any other model but adequately predicts the y-shape scaffold. This is a function of the y-shape parameters lending themselves to modeling as a fibre which sheds light on a possible combined model being the best for overall prediction. Additionally, the drag model highlighted the effect of minute differences in topology on the resulting permeability, as shown from the major controlling factor being the effective fiber radius. The final model explored were phenomenological models which most closely predicted the actual permeability for the architectures indicating that one possible future direction is to derive a novel phenomenological model that is architecture specific. Overall, current theoretical models

(especially those shown) do not take into account complex geometry and we may need to use reverse engineering to develop predictive model through curve fitting rather than a mathematically derived set of equations.

Modeling an arrangement of a complex geometry as a simplified architecture or as a simple arrangement of that architecture ensures large amount of error introduction. Such is the case with the simplest fluid flow models employed for predictive purposes here. These models are unable to account for the branching nature of the y-shape nor the length as everything was assumed to be a collection of straight channels. The models themselves under predicted the permeability by several magnitudes as a result of the inability to properly account for geometry. The y-shape was additionally penalized in calculations which hinge upon cross-sectional area because the shape itself has a lower cross-sectional area than a simpler shape, such as the NaCl porogens.

4.1.5 Conclusion

In this study we utilized a rapid prototyping system to produce objects with complicated geometry that can be used as porogens in a leaching process similar to what is currently de facto standard for the creation of porous conduits for tissue engineered scaffolds. We evaluated the resolution and validated the PatternMaster as a viable rapid prototyping system for the (generally) speedy creation of thousands of small porogens with repeatable architecture as measured via microscopy for visual inspection. We demonstrated the versatility of these particles and their chemical properties by incorporating them into a solid matrix and dissolving them using Acetone to return a porous network. The measurement of the permeability of these architectures showed that there is an increase in the permeability of the porous solids for porogens with higher

surface area and more complex geometry, the first which is supported by research by Scheidegger [174] and the latter which is counter intuitive. Finally, utilizing multiple geometric models to calculate fluid properties, we predicted permeability for these samples. Results showed that for randomly porous scaffolds such as were evaluated in this manuscript, Phenomenological models most closely predicted the resulting permeability. These results are important for the optimization of the permeability of the scaffold because we can determine how the material is deposited and to what effect, if any, permeability of the scaffold plays in the resulting tissue engineered scaffold. A closely regulated study combined with imaging analysis would be able to pinpoint the effect of surface area between two porous solids and how the modulation may affect resulting permeability.

*4.2 Fabrication of Micro-Particle as use for Porogen Using Rapid Prototyping and Soft Lithography Principles**

4.2.1 Introduction

Soft Lithography techniques have found wide use in tissue engineering for micro-fluidics [176, 177], stamping [178-180], patterning techniques [11, 181] and various methodologies that require high precision and spatial control. Silicon molds generated from masters are inert and sterilizable which enables them to be reused multiple times. The optical clarity of these molds facilitates the use of photocrosslinkable polymers, increasing the speed of part production and reclamation [182]. One disadvantage, however, is the cost and time required to prepare these molds [183]. Conventional techniques utilize a micro-fabricated photolithographic master for which the equipment and cost is prohibitive. The silicon plates (which are used to create the positive masters) are fragile and expensive, and the harsh processing steps only increase their fragility. Complex patterns are not easily manufactured and must typically be created as two-dimensional patterns extruded into the third dimension [177]. These factors reduce the overall use and flexibilities of the molds. A less expensive and more versatile methodology for creating the masters would be advantageous. Several processes have already been explored in regards to cost reduction. An accepted method involves the selective photocrosslinking of a two-dimensional pattern onto a plate with the use of a mask generated with dark and light spots. This has been successful in the crosslinking of hydrogels and other photocrosslinkable biomaterials [184-187]. Several rapid

prototyping processes are also currently available to reduce costs, increase the detail, and decrease the production time.

One attractive candidate we have investigated for the creation of positive masters for lithographic purposes is three-dimensional phase change printing. This process is capable of creating a stiff wax object including oblique angles using a layer-by-layer build process. The resolution of this machine allows the creation of objects with feature sizes at or below $100\mu m$. We have previously demonstrated the ability to generate numerous parts with varying complexity at or below the discussed feature size and with a volume less than 0.25 mm^3, see section 4.1, also Wettergreen et al. [188]. However, the lengthy and tedious preparation steps required to build large numbers of these parts all but prevents the use of this technique. Studies have shown that parts created in this manner maintain some mechanical integrity, and while not biocompatible, are able to be dissolved or melted with simple processing steps. The created part could therefore be translated into a master for mold transfer. Furthermore, RTV silicone has been used in the past to mold other crosslinkable biomaterials, such as PPF/ PPF-DA, and lactic or glycolide derivatives into orthopaedic implants and porous conduits for tissue regeneration studies. While a one-use mold for interconnected structures has been manufactured via rapid prototyping, the use of a repeatable master has not yet been shown.

In this study we describe a new technique for master mold fabrication for the pre-existing technology of soft lithography. In particular, we illustrate a process for the creation of porogens with increasing geometric complexity and varying surface to

volume ratios. Volumetric shrinkage of the molded networks was evaluated to understand the dimensional inaccuracies that may occur with this mold processing.

4.2.2 Methods

Rapid Prototyping. Particles with identical volumes but ranged surface to volume ratios were created using CAD (Figure 40). Employing IronCAD (Innovation, Atlanta, GA) and Rhinoceros3D (Robert McNeel Associates, Seattle, WA), micro-particles were designed as two dimensional architectures extruded in the third dimension as previously described [188]. A cube, y-shape, and asterisk were generated: designed dimensions are presented in XFigure 40X. The architectures were generated at twice the volume of a standard sodium chloride (NaCl) crystal (side length 750μm, volume 0.422mm³) for comparison purposes. While the volume of each architecture was held
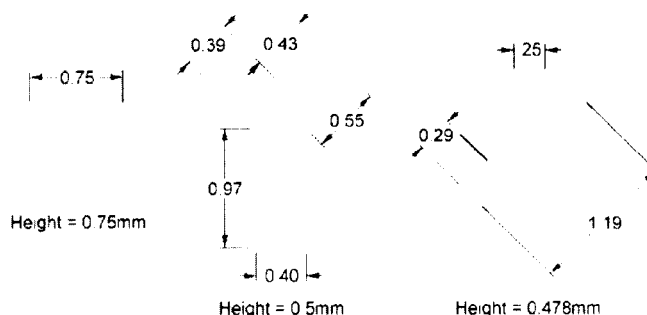
Figure 40. CAD drawing of designed micro-particles. The volume of all micro-particles is the same (0.422 mm3). Surface area of the micro-particles varied as a function of geometric complexity.

constant, surface area varied based on the geometry. All architectures were generated with a bounding box of no greater than 1.5mm x 1.5mm x 1.5mm.

Architectures were built using the PatternMaster (SolidScape, Merrimac, NH), a fused deposition printer (see Figure 12, bottom). The PatternMaster uses two thermoplastic waxes to generate objects in a layer by layer fashion. One wax is used to build the object and the second is used as a support material, and for overhang compensation. The accuracy of the PatternMaster is quoted at 12.7μm in the z-direction

and 25.4μm in the x and y directions (in plane). The road width of each strip of printed

material is 76μm [189]. Architectures were designed above the quoted accuracy and

modified to reduce build error associated with dimensions not divisible by the quoted

resolution. Architectures were exported as stereolithography files (.stl) from

Rhinoceros3D and imported to ModelWorks 6.1 (SolidScape, Merrimac, NH) for

preprocessing. Fabrication was completed with the PatternMaster (SolidScape, Merrimac,

NH). Part preparation was accomplished by dissolving the support wax in BioAct

(Petroferm, FL). A subsequent H_2O wash was performed and the parts were dried.

Soft Lithography Mold Preparation. A mold of the micro-particles was created from

PDMS (see Figure 41). A thin layer (1-2mm) of a 10:1 mass ratio of Silicones Inc. (High

Point, NC) P-44 was degassed in a high vacuum until minimal air bubbles were observed.
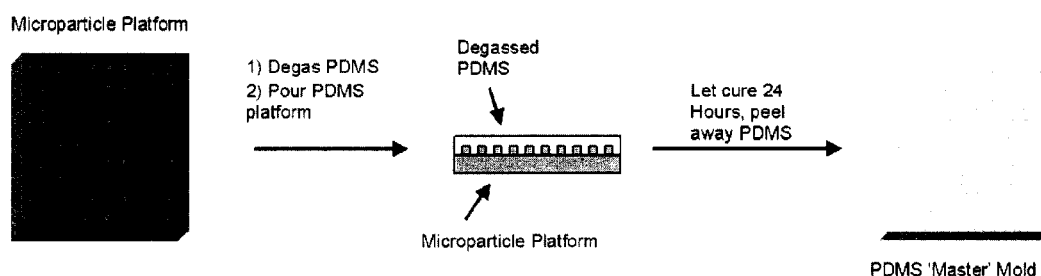
Figure 41. Schematic Procedure for creating PDMS mold using RPM (not to scale).

The liquid silicone was then poured over the micro-particles, allowed to cure for 24

hours, and gently separated from the wax prototype. The PDMS mold was washed in

100% ethanol to remove residual solid material. The washes were repeated until no

discernable material remained on the molds.

Micro-particle Fabrication. Upon curing of the PDMS mold, micro-particles were

fabricated as illustrated schematically in Figure 42. The mold was placed on a glass plate

of dimensions 12cm x 15cm. Five hundred micro-liters of PPF was dissolved in DEF,

with 0.5 wt% of the photoinitiator BAPO. The solution was pipetted onto the PDMS

mold. The PPF-DEF was spread into a thin, evenly dispersed layer over the interior of the

mold. The mold was then covered by another glass plate of equal dimensions,

sandwiching the mold between plates, and forcing excess material from the mold. Metal

clamps were applied to all edges of the glass, holding it in position.
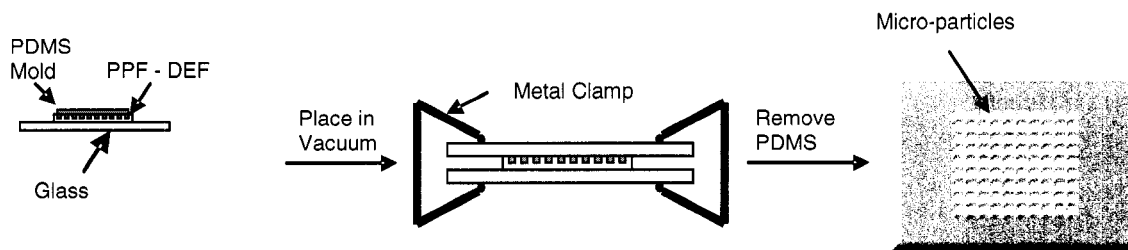
Figure 42. Schematic procedure for creating micro-particles from PDMS mold (not to scale).

The mold with clamps was placed in a UV exposure chamber for 1 hour. After curing,

the clamps were removed and the PDMS was peeled away from the glass leaving the

micro-particles on the glass plate. Particles were reclaimed using a razor blade swept

across the plate to separate the bottom edge of the particles from the plate. A film existed

around the edges of the PDMS mold which was peeled away.

4.2.3 Results and Discussion

Rapid Prototyping. Micro-particles were designed using CAD processes, resulting in

three architectures containing the same volume but with varying geometric complexity.

Modulation of surface to volume ratio as a result of the geometric complexity is

displayed in Table 6.

The y-shape and the asterisk
had 1.25 and 1.5 times greater
surface area than the cube,

Table 6. Comparison of idealized surface area and volume between various micro-particles.

	Cube	Y	Asterisk
Surface Area (mm^2)	3.375	4.23	4.945
Volume (mm^3)	0.422	0.422	0.422
SA-Volume Ratio	8.00	10.02	11.72

respectively. The dimensions of these architectures approached the build resolution of the rapid prototyping machine. To determine the best method to build these architectures, single versions of each shape were built to test for inconsistencies. Slice files were prepared using ModelWorks 6.1 with a corresponding build layer height of 12.7μm in the z-direction. Architectures were processed with the three settings available at that resolution, 407, 408, and 501; each process corresponds to a specific plotter path and filling method with the inkjet heads. Option 407 builds parts using two rows of build material and four rows of support material and is recommended for parts with delicate features and rounded edges. Option 408 builds with one row of build material and two rows of support and is recommended for intricate parts with small, thin cross-sectional areas. Setting 501 uses three rows of support and two rows of build and includes a double close-off row which aids in the replication of intricate geometry. Process specific patterns are illustrated in Figure 43.

Build process 408 resulted in holes at the outer extremities of each arm of the y-shape. Build process 501 generated an adequate approximation save for an inconsistency in the center of the part. The build process 407 generated the exact shape without errors and the y-shape was built using this process. Each architecture was built using all three processes and the configuration for each which adequately represented the true shape without gaps or distortion was accepted.
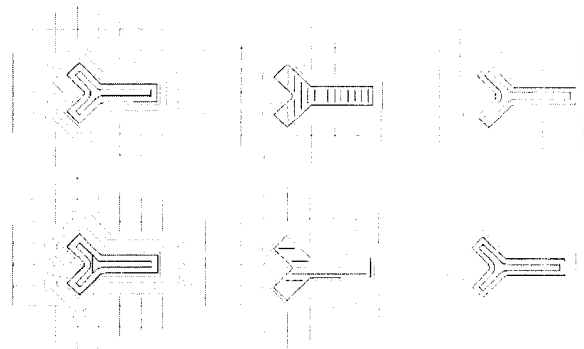
Figure 43. Build process preparation with ModelWorks (SolidScape, Merrimac, NH). The lines correspond to the intended build path of the inkjet heads. Red represents the support material and green represents the build material. Left, alternating slices using build.

Dimensional modifications were made to each architecture to prevent build inconsistencies. The final dimensions are shown in Figure 40.

For scale-up purposes, each architecture was arranged in a 15x15 array on a flat platform of global x and y dimensions of 5cm x 5cm with spacing between particles no less than 1.0mm in each direction. The model was prepared for fabrication in layers, determined according to the build process selected for each architecture. All architectures were built using the PatternMaster. Due to material problems (curling and delamination effects between layers), there are difficulties in building flat horizontal plates so the build platform was modified. An extruded rim was added to the bottom of the platform. Bending could still be observed on the bottom of the part but the transferred silicon was able to lay flat and the particles were created with no additional error (

Figure **44**).
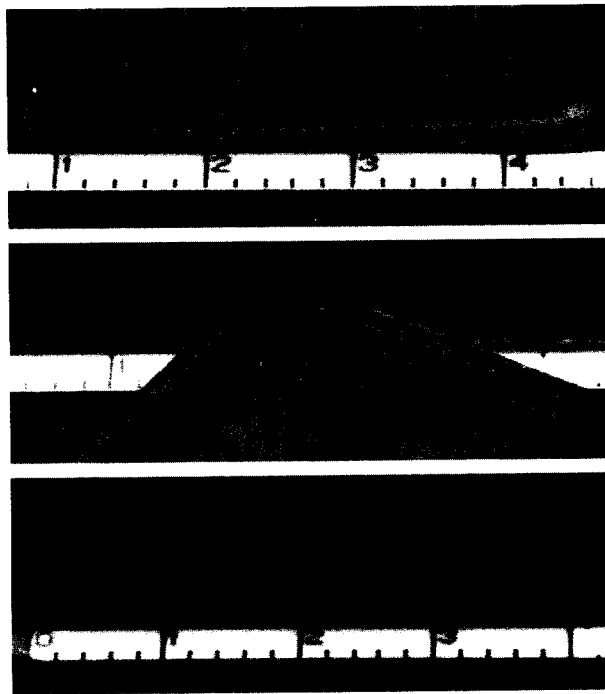
Figure 44. Damage to build plates through improper design. When building horizontal platforms, adhesion between adjacent layers is less than the force of separation due to curling. The damage to the plate as seen in A can be fixed by adding a rim surrounding the plate as shown in B. The final part with no damage and minimal bending as a result of the force of curling is shown in C. In this part, only 5 of the 225 cubes were damaged. The global curvature of the plate observed in C does not affect the creation of the silicon plates used as molds.
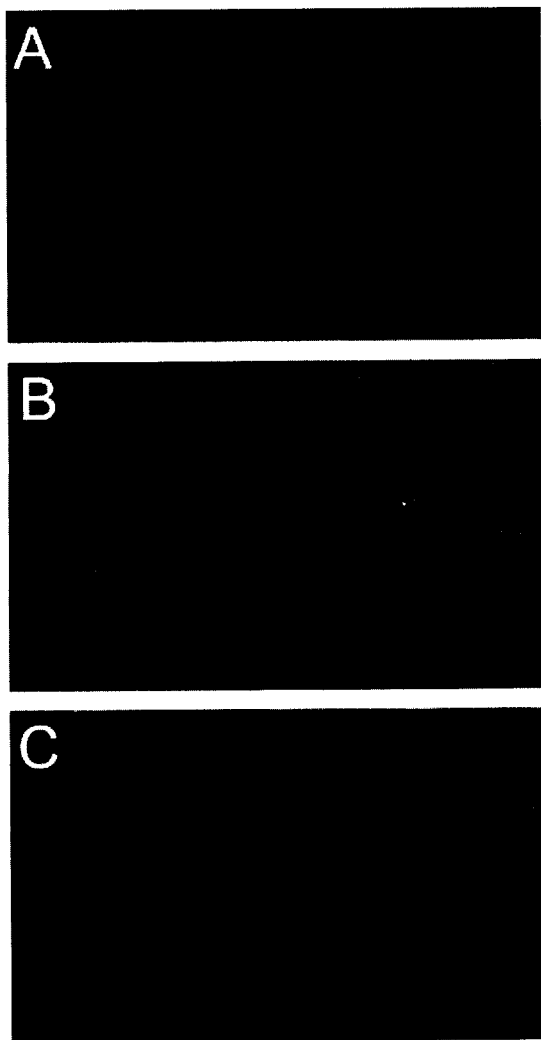
Figure 45. Stereoscopic image of all architectures illustrating the detail of the shapes. Errors can be observed in the architectures as a result of the geometric complexity. The asterisk demonstrated the least "clean" reproduction with some blurring of the arm extensions. The cube shows the best transfer from design to shape and the y-shape has several errors due to a lack of adhesion between layers.

The architectures build with the rapid prototyping machine matched the overall shapes as designed. Close-ups of the architectures are displayed in Figure 45. Visual inspection of the architectures showed that the successive geometric complexity increased error into the part and decreased the sharpness of each pattern. Still, all samples retained the global shape of the designed architecture. From a top-view (Figure 46), the dimensions of the architectures were measured and are displayed in Table 7. The greatest deviation between the designed dimension and the reproduced dimension was in the branch of the y shape architecture, which was 14.1 % larger in the rapid prototyped reproduction. The architecture that most closely represented the designed shape was the cube architecture. The global shape of the asterisk was generated but the fine features (arms) were poorly

represented.

Soft Lithography. Silicon negatives were created from the rapid prototyping positives. Figure 46 illustrates the transfer between the rapid prototyping part and the resulting mold. Silicon molds exactly matched the global shape of the rapid prototyping parts. Shrinkage measured in all dimensions is displayed in Table 7. The greatest deviation between the designed dimension and the reproduced dimension was in the
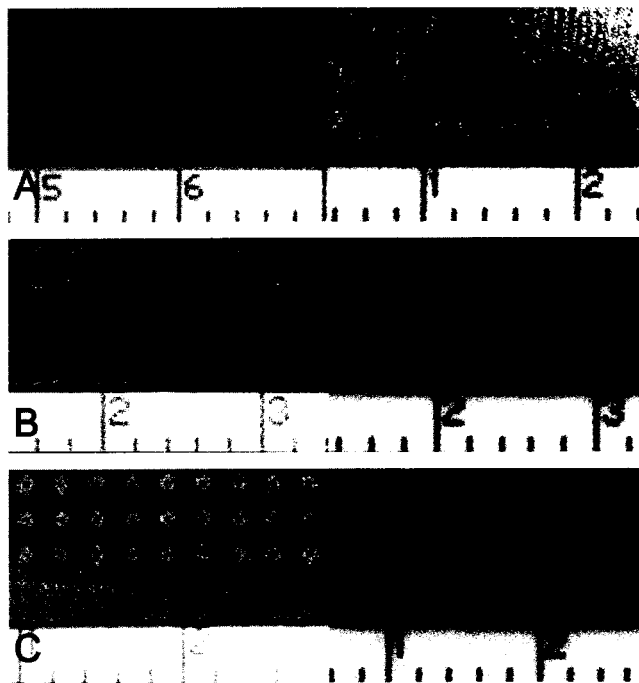
Figure 46. Build plates with the resulting molds generated from the positive shapes. A: cube, B: y-shape, C: asterisk. Complete transfer of the architecture is observed in all architectures but with a degree of shrinkage in all shapes.

y-shape. While the error in the trunk was less then one percent, the branches of that architecture were 29.6 % less than the designed dimension. Upon visual inspection, there is a blurring of the vertex between the trunk and the branches making it difficult to clearly determine the transition. The cube shape had the least distortion, while the asterisk had the largest variation in global shape. The asterisk produced via rapid prototyping poorly replicated the exact geometry of the designed particle at the scale investigated, but exact transfer to PPF-DEF was found.

Table 7. Dimensional measurements of micro-particles. Shrinkage was measured in all micro-particles.

	Cube	Y-Shape	Asterisk
CAD			
Width (μm)	75	97 (Trunk) 55 (Branch)	119
Rapid Prototyping			
Width (μm)	75.75	91.95 (Trunk) 62.76 (Branch)	114.3
% Deviation	1.0 %	5.2 % (Trunk) 14.1% (Branch)	-3.9 %
PDMS Mold			
Width (μm)	73.92	97.45 (Trunk) 38.71 (Branch)	114.49
% Deviation	-1.4 %	0.5 % (Trunk) -29.6 % (Branch)	-3.8 %
Final Particles			
Width (μm)	33.13	40.33 (Trunk) 23.5 (Branch)	54.32
% Overall Deviation	-55.2%	-58.4 % (Trunk) -57.3 % (Branch)	-54.4 %

Micro-particles were successfully generated from the molding process with the photocrosslinkable polymer PPF-DEF (Figure 47). The build plates containing the porogens included a surface roughness visible on the vertical surface of the porogens which exactly matched that of the surface roughness from the rapid prototyping platforms. An average of three of the 225 architectures per plate were lost during the post-build preparation process, representing a 98.6% reclamation rate.

When reclaiming the particles there was an observable thin film surrounding the particles of residual crosslinked PPF. The height of the film was found to be a function of the pressure between the glass plates and the silicon mold. When excess material was forced out, the film was negligible allowing reclamation of the particles by a scrape of a razor blade to separate them from the glass plate.

Micro-particles exhibited geometry from the silicon mold with an average deviation of 56.3 % in any one dimension. The discrepancy, however, was volumetric due to shrinkage (Table 7). The greatest deviation between the designed dimension and the reproduced dimension was in the length of the trunk of the y-shape, registering shrinkage of 58.4 % (Figure 47). The shrinkage is a result of the material properties of the polymer used for crosslinking. Therefore, to obtain particles of a specific size, dimensional modification would be needed from the outset of the CAD design. Air bubbles were found in some of the particles as a result of incomplete filling. These observed bubbles were on the interior of the shapes and did not affect their global dimensions. Molds produced from rapid prototyping were able to be used a minimum of ten times before plastic damage occurred in the mold interior. This is consistent with previous research by Xia and Whitesides demonstrated during the pioneering of soft lithography techniques [187]. In the portions of the build plate where porogens did fracture, the silicon completely covered the build plate with no appreciable difference.

Figure 47. Architectures molded in PPF-DEF. Left, cube micro-particles. The effect of the layered build process can clearly be observed. Middle, the y-shape micro-particles. The remnants of the thin film from the material may be observed on the bottom of the architectures. Right, asterisk micro-particles. While the rapid prototyped part represented a reduction in the definition of the original shape, the extremities of the arms were an exact transfer of the build plate in the generated micro-particles.

The major innovation of this study was to use rapid prototyping to generate the master molds. This technique provides a considerable cost reduction in the rapid prototyped master, and is versatile enough to be used with any of the current methodologies employing silicone templates. Coincidentally,

it has all the same associated benefits and difficulties, i.e. mold filling, sterilization of materials, and distortion of molds after repeated use. Unfortunately, there is a size constraint imposed by this technique on the resolution which is not present in photolithography, as has been demonstrated by the asterisk parts. Achievable rapid prototyping resolution (~50μm, though shape dependent) is inferior to photolithography, which is quoted far below 50μm. Naturally, the resolution discrepancy translates into a difference in the surface roughness as well.

Build time is also a major consideration in the use of this technique. The rapid prototyped master required 6 hours of build time and two hours of post-build preparation. While this technique was introduced with small particles, it is assumed to be applicable for a larger, connected pattern as well.

Additionally, it is conceivable that many other materials may be used in this technique as with other soft lithography practices. This technique is also not limited to the current rapid prototyping system. Stereolithography and fused deposition modeling could generate a mechanically durable, master molds. Powder binding and liquid deposition, however, are not suitable with this technique due to their insufficient resolution and lack of mechanical stability, respectively.

4.2.4 Conclusion

In conclusion, we have demonstrated a new procedure that allows the fabrication of biocompatible micro-particles with high surface to volume ratios using rapid prototyping in combination with soft lithography. The technique is fast and convenient for the fabrication of parts that are much larger than would be normally built using photolithography. The smallest features we have fabricated to date have dimensions on

the order of ~300μm. We believe this procedure may be used to reduce the time and cost often associated with the creation of positive structures with photolithography. This technique may be used with a wide variety of materials, but is best suited for polymers which may be photocrosslinkable. Future work involves investigating the ability of this process to create particles used in a porogen leaching process, and encapsulating porogens for drug delivery purposes.

Chapter 5: Modulation of Material Organization for use in Computer Aided Tissue Engineering Applications

This final chapter illustrates the application of Computer Aided Tissue Engineering principles to current clinical problems across several studies. Here we applied the three concepts of CATE: tissue informatics, scaffold design and manufacturing. Using tissue informatics we characterized the mechanical environment of a human vertebral body, determined patterns in the microarchitecture of trabecular bone and imaged a soft tissue defect. The tissue informatics portion of these studies was combined with scaffold design either through unit CAD libraries, application of porosity results or by the construction of novel tissue repair approaches. The final step in each of the studies was fabrication of device, implant, or scaffold in which the engineering principles applied to the process is highlighted in the creation of a tangible object.

As a summation to the research detailed in Chapters 3 and 4, a combinatory approach to problem solving was applied which matched equal parts of modeling with experimentation. The results of these studies highlighted the use of Computer Aided Tissue Engineering and the importance of tailoring of scaffold apparent properties for the success of the designed system. These studies are relevant both for the future studies that they open the doors to but also as bookends themselves as demonstration of the validity of this technique of approach as well as the aid given to patients who have had tissue defects repaired with the use of this technology.

5.1 Creation of a Unit Block Library of Architectures for Use in Assembled Scaffold Engineering [*]

5.1.1 Introduction

Guided tissue regeneration focuses on the implantation of a scaffold architecture which acts as a conduit for stimulated tissue growth. Successful scaffolds must fulfill three basic requirements: provide architecture conducive to cell attachment, support adequate fluid perfusion, and provide mechanical stability during healing and degradation. The first two of these concerns have been addressed successfully with standard scaffold fabrication techniques. The use of solvent casting or gas leaching [116] and melt molding [6] has produced scaffolds that are globally porous with void architectures large enough to support cellular adhesion, migration, and differentiation. At high enough porosities (>60%), these scaffolds provide adequate fluid flow to deliver nutrients and remove degradation products [9, 14, 113, 190]. In instances where load bearing implants are required, such as in treatment of the spine and longbones, application of these normal design criteria is not always feasible. The scaffold may support tissue invasion and fluid perfusion but with insufficient mechanical stability, likely collapsing upon implantation and subsequent loading as a result of the contradictory nature of the design factors involved. It is believed that the random architecture due to the fabrication process contributes to low mechanical integrity. Also, a compensatory increase of porosity for fluid perfusion considerations innately results in reduced mechanical properties. Using solvent leaching with NaCl particulates, porosity must be at least 60% by volume to provide an open-cell architecture for adequate fluid

---

perfusion, a level which seriously compromises the mechanical stability of all but the strongest materials [113], none of which are resorbable [191].

Addressing mechanical stability of a resorbable implant requires specific control over the scaffold design. With design and manufacturing advancements, such as rapid prototyping [110, 124, 192] and other fabrication methods, research has shifted towards the optimization of scaffolds with both global mechanical properties matching native tissue [193], and micro-structural dimensions tailored to a site-specific defect [7]. Recent work by Kelsey et al. [194], proposed a selection process for composite implants based on patient specific parameters coupled with a finite element code. The authors purport that a criterion based selection system will improve the matching of patient defect to implant size and reduce the failure rate of the implant. While this study demonstrated the need to design patient-specific implants, it only highlighted the ability to select the most adequate implant for entire prostheses. Hollister et al. [18] generated a scheme for regular, repeating architectures, which have the advantage of being described by constitutive equations relating microstructure to global structure based on homogenization theory. For example, a cube was generated with intersecting, hollow, orthogonal, embedded cylinders. Indices describing the architecture were related to modulus and stiffness and optimized in a way to maximize porosity whilst maintaining stiffness [18]. The advantage of these systems is that the architecture is designed to promote strength independently of material, thus maximizing material arrangement.

While these preliminary studies have demonstrated improved research into the role of material organization of bioengineered scaffolds, certain deficiencies still exist which make direct application of these improvements difficult [195]. The previous

research has demonstrated the ability to create architectures of repetitious microstructures and characterize them. However, the ideal implant is one that would readily be assembled in series or parallel, each location corresponding to specific mechanical and perfusion properties. This implant would aid in load transfer as well as match the already existent geometry of the defect. Furthermore, current databases or libraries of architectural building blocks are incomplete in describing the load transfer environment, as determined strengths and stiffness are not necessarily representative of actual physiological load transfer from one unit block to the next. The lack of a common interface can result in stress lines and border fractures, but can be overcome with well planned Computer Aided Tissue Engineering (CATE) [100].

The goal of this study was to design a library of implantable micro-structures (unit blocks) which may be combined piecewise, and seamlessly integrated, according to their mechanical function. Once a library of micro-structures is created, a material may be selected through interpolation to obtain the desired mechanical properties and porosity. This procedure will allow a tissue engineering approach to focus solely on the role of architectural selection by combining symmetric scaffold micro-structures in an anti-symmetric or anisotropic manner as needed. Our study incorporated a linear, isotropic, finite element analysis on a series of various micro-structures to determine their material properties over a wide range of porosities [196]. Furthermore, an analysis of the stress profile throughout the unit blocks was conducted to investigate the effect of the spatial distribution of the building material.

5.1.2 Biomimetic Design Theory and Implementation

Bone and other architectures contain complex geometry with mechanical properties that vary spatially and with anatomic site. In a region of interest (ROI) at least two continuous phases (bone matrix and interstitial fluid) are responsible for the global mechanical properties. Subdivisions of this ROI will contain smaller regions of discrete architecture and thus mechanical properties which when summed together result in the global properties. If for example, the defect site contained both cortical and trabecular bone, then homogenization theory would correctly assume the global properties but would fail in the determination of the properties of the subregions of the ROI. To complete and replicate load transfer upon implantation of an implant, especially in a region containing varied architecture and properties, an engineered scaffold must mimic the variants with respect to direction. In this regard, the interior properties of the bone under study can be obtained by a quantitative computed tomography based approach (QCT). The CT slices of the ROI can be queried to obtain the CT# for a discrete number of voxels within the ROI of volume V_m, given by:

$$\varphi_k(x, y, CT\#) * N_k * t = V_m, \quad k = 1, 2, \cdots n \qquad (10)$$

where x, y, z represent the position of the voxel within the coordinate space; N_k represents the number of voxels within the slice; t, the thickness of each slice; n represents the total number of slice planes. Phi is a function that relates the outer contour of the slice to the contained voxels. This functions serves as a database of information containing the density of the voxel as well as a description of the contour of the region of

interest of each slice. Mechanical property characterization can be achieved by correlating the CT# to density by a linear interpolation using relations available in published literature. This density can in turn be then related to E, the Young's modulus of the tissue structure, allowing the heterogeneous elasticity of the bone to be defined [197, 198]. The ROI is then subdivided into discrete units, with each unit associated with its own characteristic Young's Modulus, E.

The intended 3D scaffold that replaces V_m, will be composed of discrete sub unit architectures V_i:

$$V_m = V_1(P_1, S_1) \bigcup V_2(P_2, S_2) \bigcup V_3(P_3, S_3) \bigcup \cdots \bigcup V_i(P_i, S_j)$$

(11)

where sub-volume V_i denotes the unit block, P_i denotes the spatial position of the unit block and S_j denotes the characteristic unit block assembled in V_m. Each unit block has specific mechanical properties and will be matched based on the initial mechanical property characterization using data set available in (1). Varying mechanical properties can be achieved by either altering the porosity of the unit block or changing the internal architecture of the unit block while keeping the porosity the same. Thus, subdivisions of the engineered scaffold must mimic the select architectural properties of these regions. We propose that the micro-architecture be designed to replicate the site specific mechanical properties at a resolution that match the achievable feature size of current solid freeform fabrication methods.

Design of unit blocks with varying architectural properties may result in non-congruous borders when matched with adjacent neighboring blocks. These discontinuities

will critically reduce the mechanical properties of the solid along the borders of the architectures and invalidate the model design. To prevent this, a common interface is required along the borders of each unit block. This common interface will need to be a shape that does not detract from the overall strength of the unit block itself but also enacts a complete load transfer between adjacent blocks as a result of the border. In addition, the design of unit blocks demands that the scaffold should contain architecture which promotes both cell viability functions and fluid transfer throughout the scaffold. These demands would be satisfied by the generation of an architecture, which is at a porosity near those of the non-specific scaffold preparation methods. These properties may be improved by adding regularity to the design of the architectures.

5.1.3 Example – Generation of Unit Block Library

CAD Generation of Architectures

Unit block polyhedral models were generated using Rhinoceros 3D (McNeel Associates, Seattle, WA). All polyhedra were generated within the same bounding box of 3mm x 3mm x 3mm which placed constraints upon the possible size of each structural element[195] . All generated architectures exhibit symmetry along the three axes and were thus considered orthotropic with respect to geometry, with isotropic behavior with respect to the built material. Two types of models were generated, the first based on solid geometry with the inclusion of void spaces to create porosity and the second based on geometric regular polyhedra.

The first type of architecture was a space filling solid structure, such as a sphere or cube. A void structure was superimposed onto a solid structure using standard Boolean processes [165], resulting in hollow or shelled structure exhibiting the desired geometry.

Void structures were applied in such a manner as to result in an architecture which was symmetric in three directions. Porosity of these solid architectures was determined from the ratio of solid volume to the global bounding box volume. The porosity of the solid architectures was adjusted to predetermined values by modifying the volume of the void elements until the porosities matched.

The second type of architecture generated were wireframe approximations of the basic set of geometric polyhedra, the Archimedean and Platonic solids [164]. The advantage of using these polyhedra as models is that they are regular, that is both equiangular and equilateral, and thus exhibit the desired symmetry. These models were initially employed as volumetric representations, as illustrated in Figure 48A for the case of the rhombicubeoctahedron. Each edge was converted to a beam of the corresponding length. As shown in Figure 48B, the resulting shape contains the same number of beams as the original shape had edges. Each beam was equilateral and had the same diameter. The porosity of the architectures was determined from the
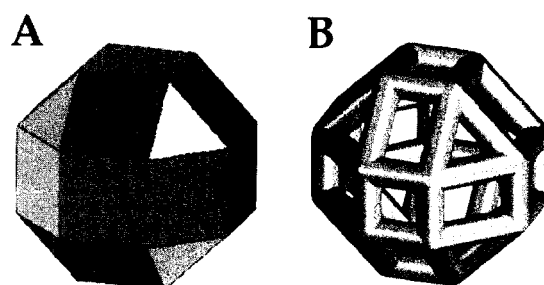
Figure 48. A. Rhombicubeoctahedron, space filling solid model. B. Wireframe approximation of rhombicubeoctahedron. Each beam has the same length and diameter as the edges of the space filling equivalent.
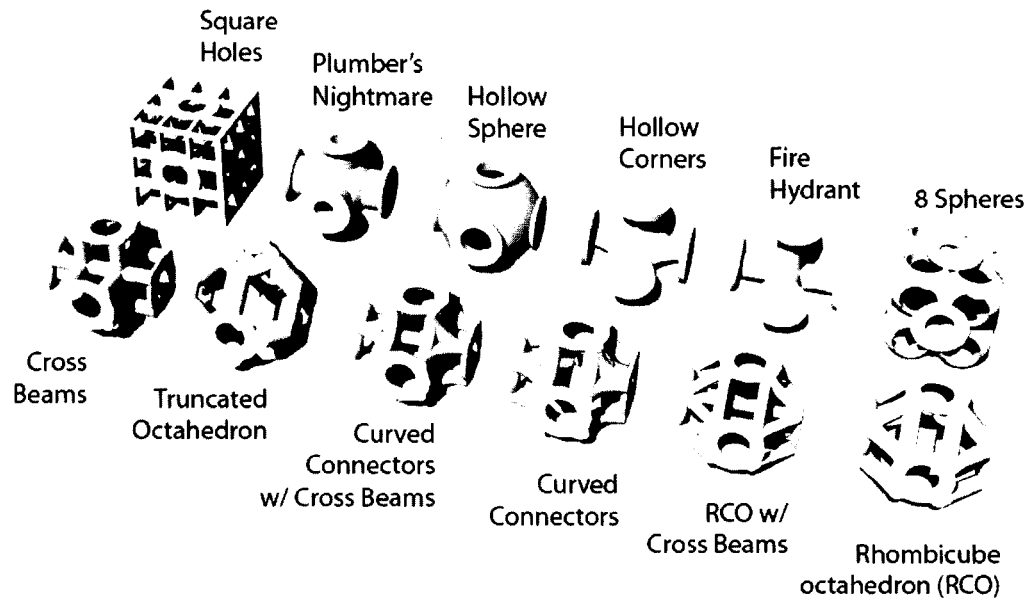
Figure 49. Polyhedra generated as unit blocks. All polyhedra contain the same material volume (20%) and are bounded by the same dimensions. Only the architectural arrangement and spatial distribution of material differs between architectures. The interconnecting tori are the same dimensions across all shapes.

ratio of the summation of the beam volumes to the volume of the bounding box. Porosity adjustment was accomplished by globally modifying the beam diameters until the desired value was obtained, while compensating for shrinkage of the bounding box.

The final porosity of each architecture was resized to 80% volumetric porosity, a value corresponding to the porosity of trabecular bone. The twelve architectures generated including their common interface are displayed in Figure 49. Briefly, the square holes architecture is a solid cube with square void placed in orthogonal directions. The plumber's nightmare was taken from a common structural organization of lipid bilayers and is composed of hollow orthogonal pillars with a shelled sphere central to the architecture. The hollow sphere is the superposition of a solid sphere with a void sphere applied to the center of the shape, while the hollow corners architecture has four void spheres applied to the corners. The fire hydrant is composed of three orthogonally

arranged beams. The eight spheres architecture is composed of eight shelled spheres arranged adjacent to each other. The cross beams scaffold consists of four beams equi-spaced around the center of the volume copied orthogonally to each other. The truncated octahedron and the rhombitcubeoctahedron are exact approximations of platonic solids. The curved connectors is composed of three, quarter tori at each corner connecting the common interface. The previously listed three shapes were also modified to include cross beams in the center of the architecture. The cross beam architecture was generated at additional porosities of 50, 60 and 70 % porosity to illustrate the effect of volume on material properties.

Inclusion of common interface

Previous studies that have discussed the use of a unit library for the creation of scaffold architectures utilizing continuum modeling such as homogenization theory[194]. These theories account for the determination of the mechanical properties of a single architecture with the constraint that the micro-architecture be used throughout the global architecture or within the modeled continuum[18]. When matching two continuums of differing micro-architectures, stress discontinuities will occur. No studies have yet addressed the manner in which objects such as these may be joined together to create a global scaffold with mechanical properties dependent upon location. In this study, we have applied a common interface in the form of a torus. This shape was added to each side of the polyhedra to add regularity to each architecture and aid with load transfer when connected in series and in parallel. The torus was sliced axially so that each side had one half torus, thus when two shapes were combined, a whole torus was produced. An illustration of the torus concept
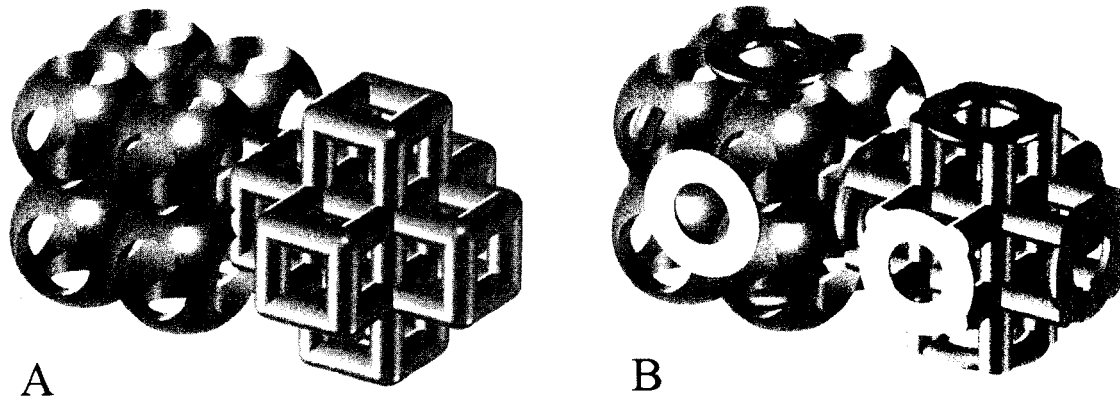
Figure 50. Illustration of improved matching between dissimilar architectures (cross beams and eight spheres) with the addition of an axially sliced torus to each of the 6 sides of an architecture.

of matching sides is depicted in Figure 50. The dimensions of each torus were kept constant for complete load transfer during joining. Following the addition of the torus, all architectures were checked and resized to the appropriate porosity if required and subsequently exported as .igs files in preparation for finite element analysis (FEA).

Finite Element Analysis

Finite element analysis was completed on the architectures of the building blocks to determine their apparent material properties due to specific material arrangement. Each polyhedra was imported into ABAQUS CAE (ABAQUS Inc., Pawtucket, RI) from the prepared .igs file and subjected to a linear, prescribed displacement test. An illustration of the finite element procedure is provided in Figure 51. Isotropic material properties for each polyhedra were assigned with an elastic modulus of E = 2 GPa and a Poisson's ratio of 0.3, approximating currently available biomaterials [32]. Each polyhedra was displaced the equivalent of 1% and the reaction force (RF) was calculated from the top nodes of that polyhedra. Young's Modulus (E) was calculated by the ratio of RF over the bounding box area divided by the strain. First, a convergence study was
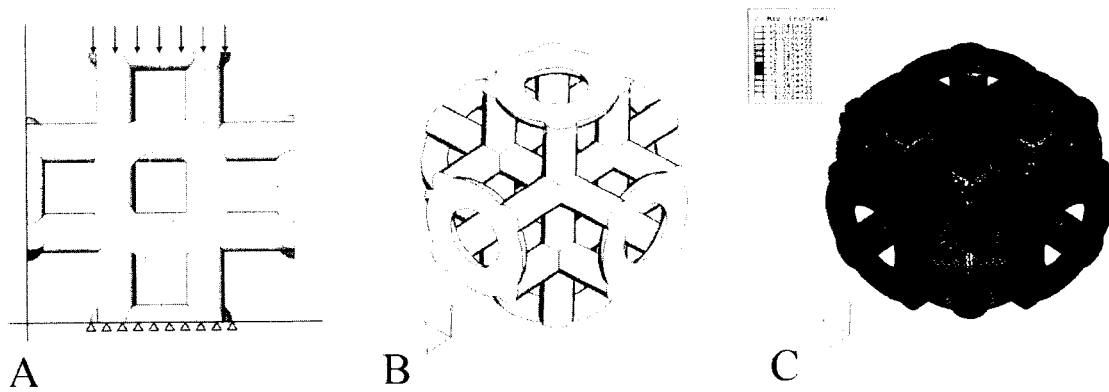
Figure 51. Illustration of finite element procedure. A, unit block, seen in plane with bottom face fixed in translation in the y direction and the top face displaced in the y-direction. All polyhedra were subjected to 1% strain at the top face. B, boundary conditions applied to the unit block in the y-direction. C, contour plot of maximum principal stress within the architecture. The inner central regions of the architecture (light regions) are the regions of high stress while elsewhere (dark color) stress values are minimal.
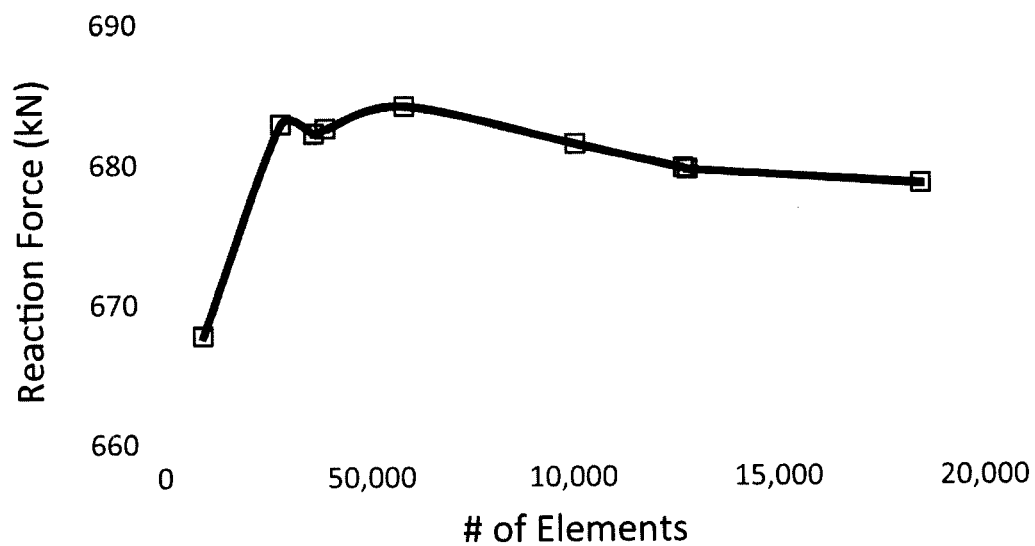
Figure 52. Linear convergence study of Cross Beams 80% volume porosity polyhedra with the unit block reaction force as evaluation criteria.

completed with the cross beam architecture to determine the required mesh density for the analysis. The architecture was meshed at varying seed densities with tetrahedral

elements and subjected to a linear pertubation test. Results of this study are illustrated in

Figure 52. Convergence was achieved when the model contained more than 50,000

elements (RF error less than 1% compared to highest mesh density). Consequently, we

chose a seeding density of 0.075 (ABAQUS CAE option) for all polyhedra at 80%

porosity which resulted in meshes with roughly 75,000 elements.

Linear displacement load analysis of the polyhedra was completed for two cases,

confined and unconfined compression. Confined compression included roller boundary

conditions on the vertical faces, which restricted a bulging effect during displacement.

The confined case illustrates the properties of the polyhedra as it may act when placed

within a continuum in a global scaffold. The unconfined case represents the deformation

characteristics of the polyhedra without the influence of adjacent cells. The loading
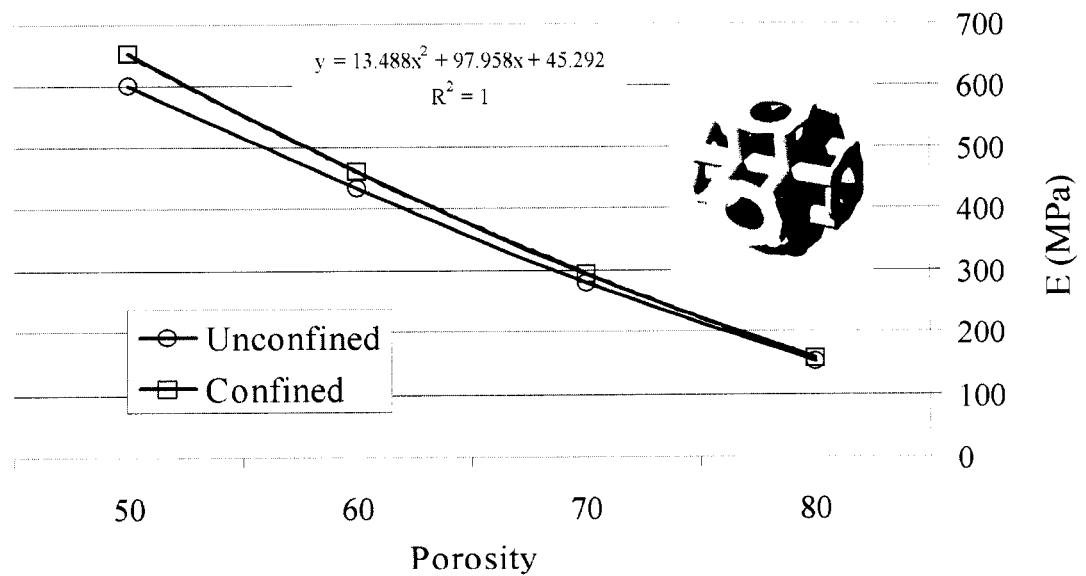
Figure 53. Effect of unit block porosity on apparent mechanical properties.

scenario subjected to a unit block in a large scaffold will most likely be in between the

investigated cases. Figure 53 displays the results of the displacement test for the Cross

Beam polyhedra at the varying porosities. At the highest material volume fraction, the elastic modulus of the architecture was 652 MPa and 600 MPa for confined and unconfined, respectively. As material volume decreased, so did the modulus in both cases according to a squared polynomial equation. At 80 % volumetric porosity, the elastic modulus between confined and unconfined compression differed by less than 3%.
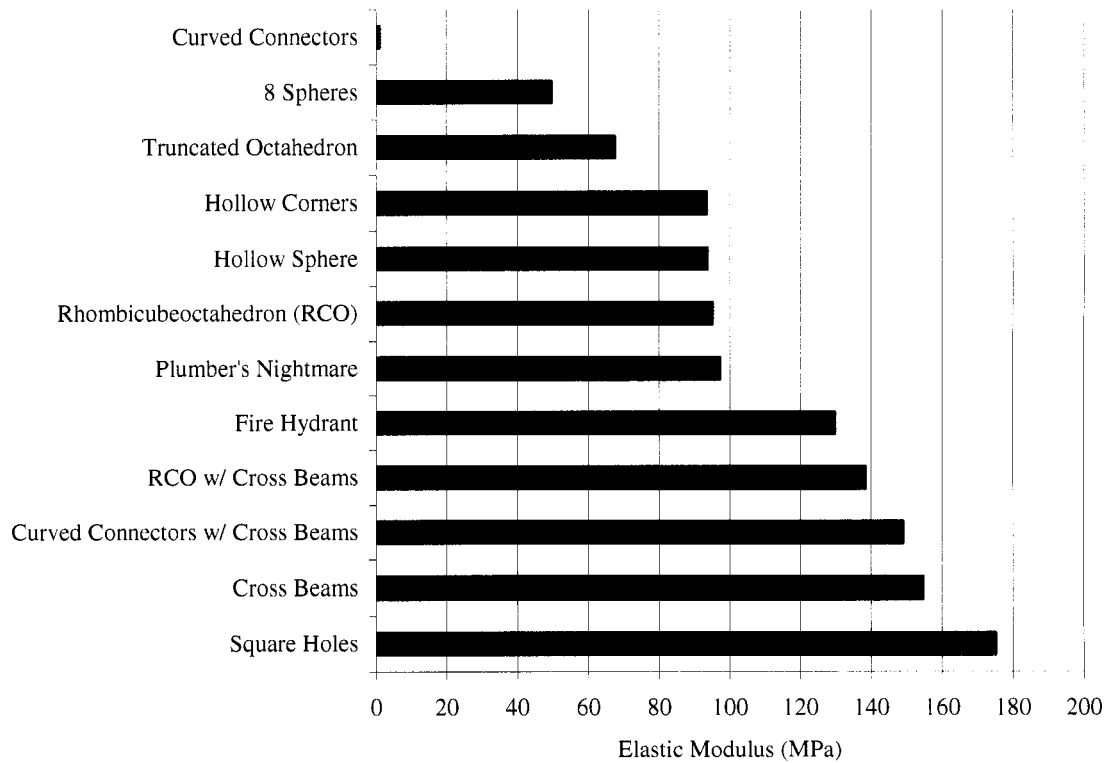
Figure 54. Results of prescribed displacement tests for unit block architectures at 80% porosity. All polyhedra were displaced to 1% strain to obtain reaction force and modulus. Results from combined and unconfined compression were averaged to obtain displayed values.

Figure 54 illustrates the calculated elastic moduli for all architectures evaluated. These values represent the average of the confined and unconfined case for each unit block. Despite the fact all shapes, for a given porosity, contain the same amount of material and material properties, there was a large range of modulus values obtained.

The weakest architecture (curved connectors) had a modulus of 0.96 MPa, while the strongest architecture (square holes) had an elastic modulus of 174 MPa.

Elemental principle stress distribution was evaluated for each polyhedra as a method to characterize the loading on each architecture as a result of the spatial arrangement of the building material. For each prescribed displacement, the maximum principle stress was calculated and outputted as a histogram normalized to the number of elements per architecture. Selected results of this analysis are displayed in Figure 55. As can be seen from Figure 55 (top), the material volume plays a direct role in the resulting stress profile for each architecture. The majority of the elements in the 80 percent porous cross beams architecture experienced little to no stress. This is the first trend that was illustrated from the analysis of the stress profiles. As the material volume increases, the stiffness of each architecture also increasespeak stress that is experienced on the cross beams architecture increases and also the stress profile spreads out to encompass more values as a result of increased elements contained in the architecture. All of the shapes exhibit a distinct final peak that occurs at approximately -25.0 MPa. This outer peak is a trend that was observed in other architectures as seen in Figure 55 (at right) such as the fire hydrant architecture. Also to be observed from this figure is the similarities in stress profile at and around zero stress for the two dissimilar architectures of the fire hydrant and the hollow corners. In Figure 55 (top right), it can be observed that the cross beams 80 architecture has twice as many elements that are near zero stress as the other four architectures. The cross beams architecture also exhibits two distinct peaks while the remaining shapes may be more widely dispersed or have more peaks.

145
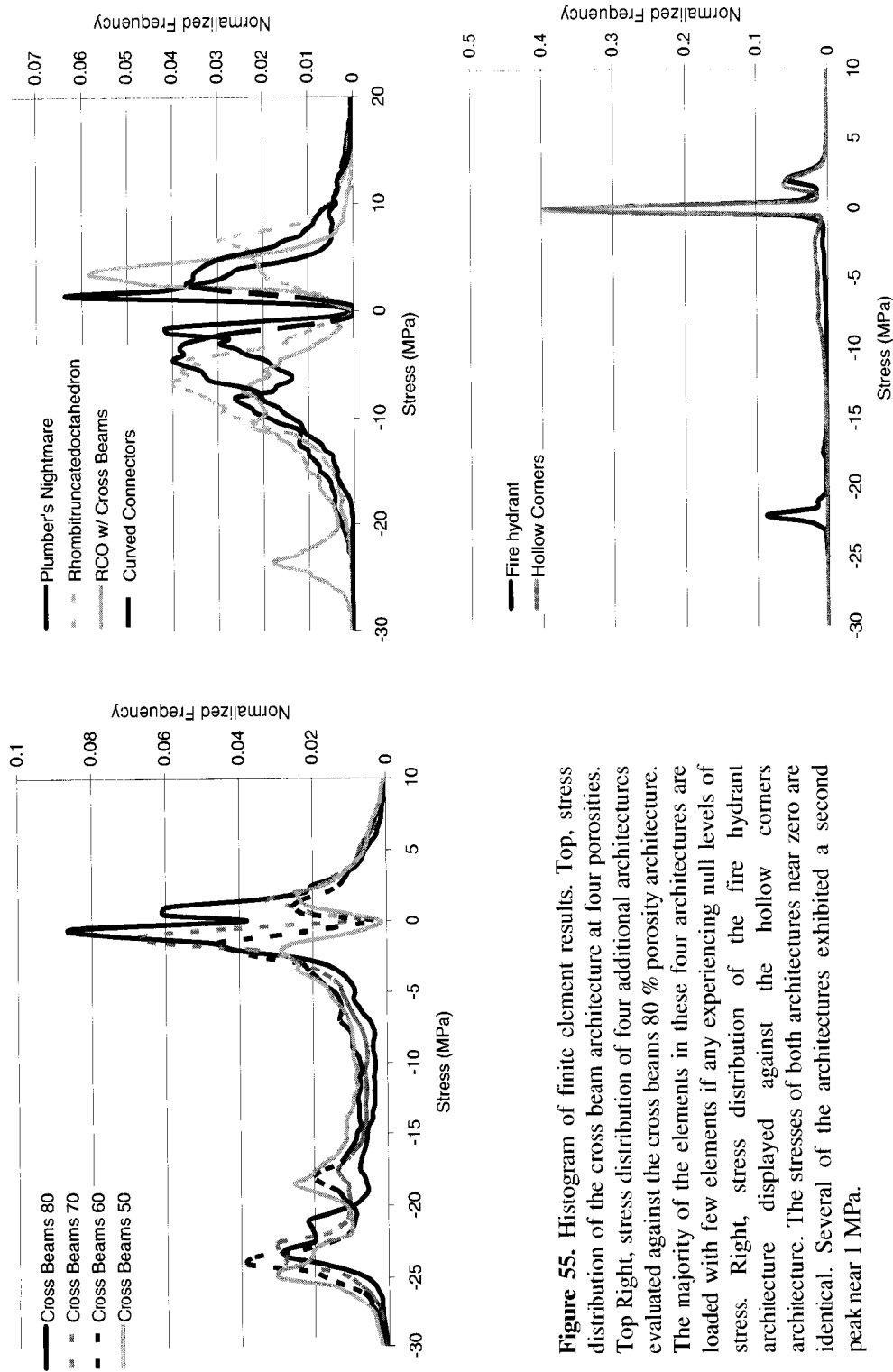
Figure 55. Histogram of finite element results. Top, stress distribution of the cross beam architecture at four porosities. Top Right, stress distribution of four additional architectures evaluated against the cross beams 80 % porosity architecture. The majority of the elements in these four architectures are loaded with few elements if any experiencing null levels of stress. Right, stress distribution of the fire hydrant architecture displayed against the hollow corners architecture. The stresses of both architectures near zero are identical. Several of the architectures exhibited a second peak near 1 MPa.

5.1.4 Conclusions

In this study we have demonstrated the creation of a unit library of architectures that can be used to assemble a complex scaffold of individual, well characterized microstructures. This strategy allows the scientist to tailor the mechanical properties of localized regions while maintaining the integration between adjacent microstructures. The mechanical properties of microstructures of a different porosity or even shape from those outlines may be intelligently interpolated through Figure 53 and Figure 54. Additionally, design characteristics such as strength instead of modulus can be also be deduced, as linear finite element analyses were conducted. As was illustrated with the cross beam polyhedra, the mechanical properties vary with material volume. Due to demands imposed by the need for tissue ingrowth, solid materials will not allow adequate tissue ingrowth or fluid perfusion. For these reasons, a porous material is required which may support such demands.

There are gross differences in the global properties of several of the unit blocks which are directly related to the architecture. The curved connectors shape contains material only in the corners of the shape thus offering no structural support to any mechanical deformation. Even with a 90% increase in modulus from the unconfined to the confined case, the shape is still the weakest by two orders of magnitude. As seen in Figure 53, there is little difference in the elastic moduli between a confined and unconfined case for the cross beams. This may be due to the uniform material arrangement which positions the majority of the load to be transferred directly through the architecture. As a result, as seen from the histogram in Figure 55, the majority of the

elements for the 80% porosity were completely unloaded. This supports the previous claim that the arrangement of the material supports the stress in all three directions.

The stress profile serves to demonstrate the contribution of architecture to the global loading. Counter-intuitively, the cross beams architecture at 80% porosity has more elements that are not loaded than the other three similar architectures with lower porosity values (Figure 55). This means that the higher the porosity of an architecture, the greater dependence is placed upon elements that truly add to the strength of the architecture whereas in the lower porosity architectures, less dependence is placed upon the material organization and thus more elements are able to carry higher stress values overall. The contribution to specific stress profiles can be seen in Figure 55 (top right) in comparison of the RCO, RCO w/ cross beams and the cross beams architecture. The RCO exhibits a two peak stress profile but the RCO w/ xbeams includes a third peak which is reminiscent of the cross beams architecture. We posit that this peak is due to the cross beams which are present in the center region of these architectures but which are missing from the original RCO architecture. Additionally in Figure 55 (bottom right), we see that hollow corners exhibits a related, yet optimized stress profile to the fire hydrant, despite their very distinguishable material organization.

Studies have shown that mineral deposition and cell dependent growth is correlated to the mechanical environment of cells [199]. We hypothesize that stress profiles with uniform distributions may do better at promoting cell adhesion. A comparison of a cutaway profile for the fire hydrant and plumber's nightmare can be seen in Figure 56. Stress distributions in the dominant loading direction for the plumber's nightmare reveal an axial transfer of stress to the non loading direction as
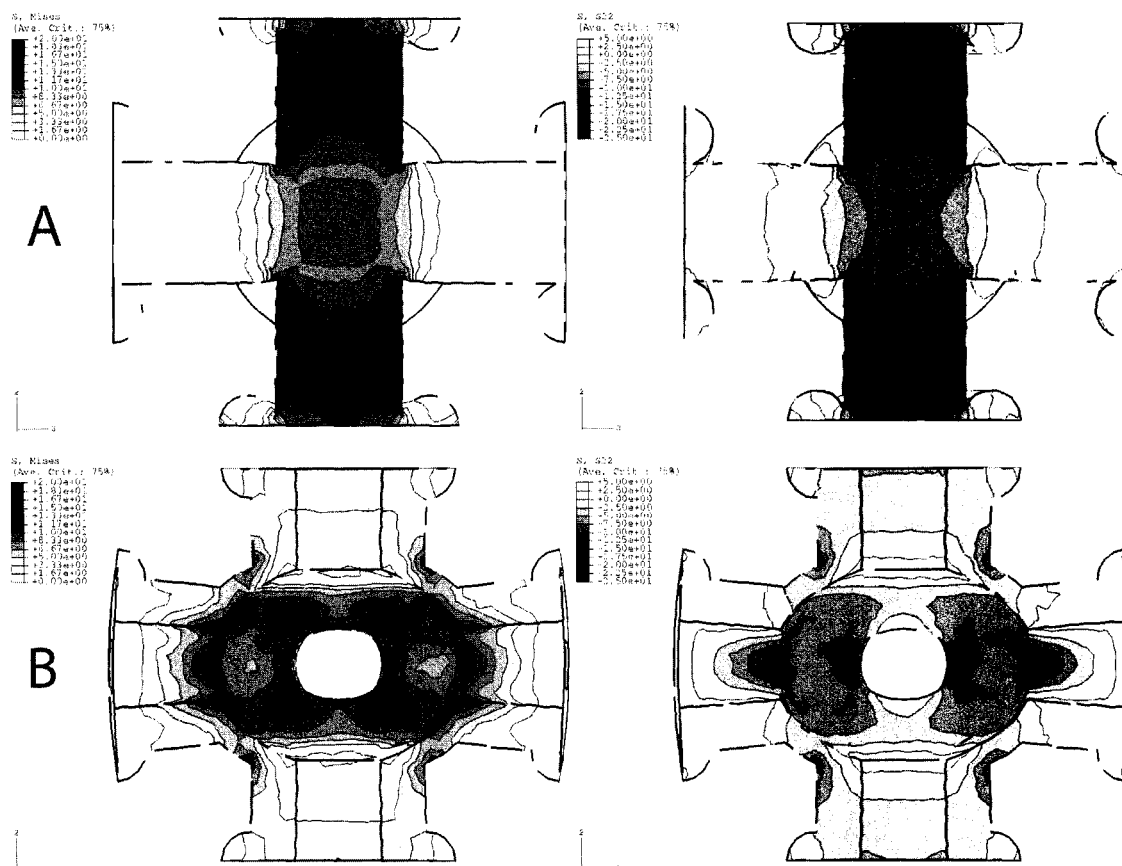
Figure 56. Display of the stress profiles in two architectures for both the Von Mises stress and the principal stress in the loading direction. A, the fire hydrant architecture experiences most of its loading along the dominant axis and elsewhere stress is zero. B, the plumber's nightmare distributes more stress in non-loading directions as a result of the spherical, hollow, center chamber.

evidenced through elements in tension on the periphery due to buckling. Additionally, there are no stress-free elements in the plumber's nightmare which possibly provides a biologically favored architecture, as evidenced through the Von Mises stress distribution. The solid framed fire hydrant exhibits a more predictable stress profile with minimal off axis stress distribution.

Previous studies have demonstrated the need to document a library of scaffolds which may be assembled, but did not provide an adequate means in which to join parts of varied architecture [18, 200]. With the addition of a common border in the form of a torus between the shapes, even grossly dissimilar architectures can be joined together to

obtain a stress free border, which is important in the design and fabrication of a complex implantable vertebral body replacement. In the case of cortical bone which exhibits porosities much lower than trabecular bone, there would be a mismatch between the borders of the shapes due to material volume. Furthermore, steps to actually develop a library of different shapes and summarize the mechanical property trends, had not previously been undertaken for a number of shapes. Here we have documented 12 shapes as the beginning of sizeable library. Future steps include improvement of this library by increasing the availability of shapes, surface optimization schemes to reduce stress concentrations, and introduction of anisotropic architectures and material properties. Experimental studies need to be designed to create the compromise between the engineering aspect of the scaffold micro-architecture as presented here and the biological component responsible for tissue ingrowth.

5.2 Computer-Aided Tissue Engineering of a Human Vertebral Body [*]

5.2.1 Introduction

Tissue engineering aims to restore tissue function through the incorporation of biological materials such as cells, growth factors, and biopolymers. This approach is atypical of current reparative treatments, which focus mainly on drugs that encourage the body to battle disease on its own or to replace a damaged area using grafting. With more than 700,000 vertebral fractures occurring each year and limited longevity of spinal fixation devices, alternatives to metal implants capable of restoring joint function are desperately needed.[201] A given vertebral body (VB) segment experiences various forms of mechanical loading including compression, lateral bending, torsion, and flexion–extension, and thus structural design demands of a replacement will need to be mechanically robust. In this study, we propose a general methodology incorporating noninvasive imaging with computer-aided tissue engineering (CATE) to create patient-specific tissue constructs and to enumerate potential methods for the reconstruction of an entire human VB. We include a brief detailing of the concepts governing this process, current state of the art research, as well as current limitations.

The advent of noninvasive imaging allows information to be gathered about a specific location in the body without causing damage usually incurred by biopsies. The combination of computer-aided design (CAD) with imaging techniques has recently been applied to surgical guides and the design of defect-specific constructs.[19, 200, 202] Generation of computer models based on defect sites helps to plan complex surgeries

---

where geometric boundaries or features may be obscured [203]. The unity of imaging modalities and computer-based design affords the potential to create a functionally viable tissue and is the basis for CATE. CATE is useful for inexpensively exploring design strategies and for providing personalized engineered solutions (from design to manufacture). Its current disadvantage is, likewise, the amount of patient and health care provider resources expended to bring these solutions to fruition. The three important concepts encompassing the use of CATE are 1) tissue modeling, 2) tissue informatics, and 3) scaffold design and manufacturing. The first step of the process involves obtaining a three-dimensional (3D) model of the tissue, either by extraction from imaging modalities or with CAD generation of a tissue template [204]. Tissue informatics concerns characterizing native tissue properties using the tissue model or through the use of finite element models or assays that characterize the biochemical environment, such as gene analysis or microarrays [205]. However, tissue informatics in its broadest definition defines compiling information about each tissue from organ to subcellular level but is most specifically referred to when analyzing the type and interaction of genes and proteins within tissues. The final step in the process is the design of a scaffold based on both the required location and the treatment type [206]. Interplay between the three disciplines may yield a functional scaffold without ever breaking the skin before surgery.

A description of the method for design of a VB will be followed by the preliminary work of creating its pieces, or building blocks, which is limited by current technology. Although the method that we detail here is not presently translatable into a clinical application, several aspects of this treatment are already heavily in use, such as material property extraction from imaging and the rudimentary printing of structures

using rapid prototyping [19, 42]. With the improvement of computing power, direct fabrication resolution, and a comprehensive knowledge of 3D constructs, we may hope to generate an engineered tissue in the near future. The advantage of this proposed methodology is the specific development of individual steps that may be used to generate any organ, regardless of anatomical site.

5.2.2 Methods and Conceptual Design

Generation of Bone Geometry.

Creation of a defect-specific implant begins with obtaining a 3D model of the organ, defect site, and microstructure. One option would be to invasively remove the organ of choice, evaluate its tissue and mechanical properties, and design an implant based on these demands. Because this strategy creates a serious tissue trauma while the implant is designed and fabricated, it is an improbable option. An additional problem with invasive technologies is that they require the patient to be rendered unconscious unnecessarily, which can facilitate complications due to anesthesia allergic reactions. An alternative method is to use nondestructive imaging modalities to evaluate bone properties via assessment of bone density with dual energy x-ray absorptiometry (DEXA) [207, 208], quantitative computed tomography (QCT) [209, 210], magnetic resonance imaging [42, 211] or quantitative ultrasound [109]. These noninvasive imaging methods for obtaining tissue information may be completed in real time or pre-op and are beneficial for use in surgical planning, implant design, and defect healing. The type of information readily obtained from one or more of these techniques is density and global structural parameters like intertrabecular distance. Few limitations apply to the use of these technologies aside from minimal radiation damage and resolution concerns [212].

Low resolution of 2D imaging techniques such as DEXA is unfit for a fabrication process that yields control over the 3D properties of the replacement material. For these processes, the use of QCT would be the most advantageous manner to noninvasively determine the appropriate properties sought for a human VB.

Estimation of Material Properties from QCT or X-Rays

Quantitative computed tomography is one of the more powerful imaging modalities, specifically for obtaining information about dense structures, such as a VB. The technique has an attainable resolution of 1.0 mm, however, with the caveat of possible DNA damage due to excessive radiation exposure [213-215]. New scanning technology limits exposure to a minimum. Density prediction using QCT is relatively straightforward and has been proven with the use of phantoms for calibration. Additionally, QCT is useful not only for the generation of tissue model properties but also for measuring the reduction in bone mineral density of cortical and trabecular bone separately due to osteoporosis or other diseases. The results are digital, which ease the generation of tissue models[216]. Numerous programs exist to extract raw CT data and translate it into 3D models such as Analyze or Mimics. The methodology of the programs can be simplified to three steps: 1) reconstruction, 2) segmentation, and 3) volume creation. In the first part, the raw projection data are reconstructed into 3D density data. Next, segmentation of the image is completed to generate surface geometry. During this process, information such as density, porosity, and bone mineral volume can be obtained. In the third and final step, a volume of the material is created that can be manipulated using CAD programs.

Determination of bone mechanical properties is one of the main advantages of CT imaging. The regional bone stiffness is calculated by first converting the CT absorbance into Hounsfield units. By incorporating a phantom of several compositions of a material with known mineral density in the QCT scan, a linear regression curve is established between the given CT Hounsfield units and bone density. By knowing the calculated bone density in conjunction with previously obtained *in vitro* relationships, it is then possible to calculate the modulus of elasticity and subsequently the remaining material properties[158, 217].

When recreating a whole bone where submillimeter resolution of the overall geometry is not of great import, it may be possible to forego the use of CT scans. Multiple X-rays taken at different angles, in conjunction with an algebraic reconstruction technique (ART), can be used instead in the interest of lowered costs and accessibility. ARTs were originally used in crystallography [218], but attempts have been made to adapt its use to medical applications where a 3D image is desirable but CT is not available [219, 220]. Similar to CT reconstruction, the number of projections limits the resolution of the final picture. However, in cases such as the proposed treatment where the geometry can be estimated or evaluated through different means, ART is an effective means of reconstructing the regional density of the bone with only three to five projections [221].

Design of Building Blocks.

Computer-generated 3D models of tissue can be altered and modified through CAD processes. Several groups have previously proposed the use of simplified shapes to approximate a complex architecture based on these model groups. Imaging techniques

and CAD processes have been used to generate geometry that is the same as the tissue replacement [222, 223]. The effect of the architecture of simple polyhedra on modulus and stiffness has been explored in 3D [18[Wettergreen MA, 2002 #621]. An entire discipline within materials research, cellular solids, focuses solely on the determination of the mechanical performance of simplified shapes such as honeycombs for their use in composite solids [16]. On the basis of the success of previous studies, we propose the creation of a library of shapes that can be used as building blocks to generate inhomogeneous replacement materials from the tissue level up to the apparent level. Determination of the material properties of each building block creates a library with comprehensive knowledge about each building block's porosity material characteristics and deformation patterns. The shapes in the library can then be assembled (similar to legos) to create a composite structure that is a 3D representation of the global tissue, including its anisotropic and inhomogeneous material properties distribution.

Generation of this library of unit shapes requires the use of numerous CAD file databases and the use of finite element analysis (FEA) for cellular solid property characterization. We propose the smallest microstructures generated confined within a 27.0 mm^3 volume (bounding box edge length 3mm), a product of the superposition of three 1.0 mm resolution QCT layers in three orthogonal directions. These microstructures also represent the smallest tissue volume that can currently be built using rapid prototyping systems. Elementary shapes such as beams, cylinders, and spheres may be arranged within these confines producing well-defined isotropy or anisotropy as needed. Quantification of the material properties of these cubes can be completed with the aid of

FEA. Subjecting the building blocks to a prescribed displacement (Figure 57) allows the calculation of force, stiffness, and finally
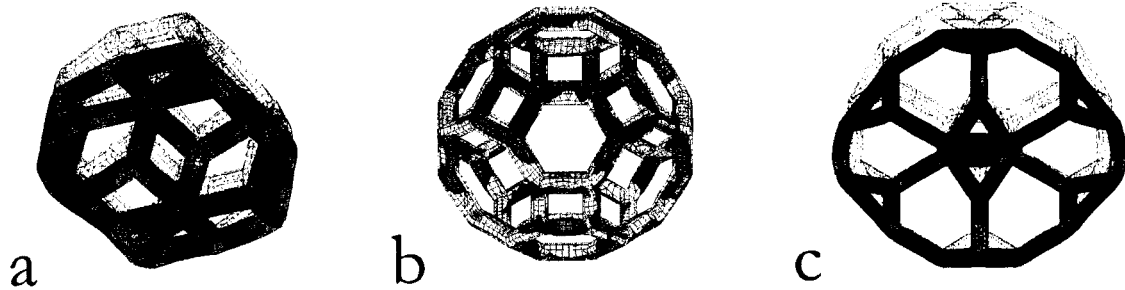
Figure 57. Illustrations of results of prescribed displacement on three polyhedra for the determination of structural properties. Connecting link (torus) not shown for clarity.

a stress-strain diagram for each shape. This quantification is due to the structural organization of the material solely and is material independent, assuming the same material is used for every unit cell.
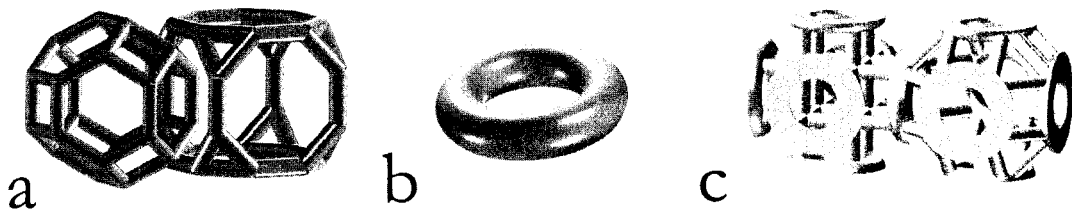
Figure 58. Illustration of the need for a common interface between building blocks. (a) Example of two polyhedra lacking a common interface. Notice that at the interface between the two polyhedra, no material interaction occurs. (b) A torus used for common interface between building blocks. (c) Example of the matching between two dissimilar polyhedra containing a common interface of a split torus.

Combining the shapes into a composite structure requires merging them with some preventative measure to reduce edge effects. The efficacy of generating building locks based on mechanical demands has been shown. However, lack of a common interface will distort finite element results (Figure 58A) [224]. We propose a common interface between the building blocks in the form of a torus. Each side of the cube would

157

contain a torus sliced through its long axis (Figure 58B). By matching two adjacent

cubes, the torus halves are joined together (Figure 58C). We believe the torus is a good

structural choice because of its rounded and subsequent reduced stress concentrations.

The inherent mechanical properties of the building blocks can be used to mimic

the material properties of the VB. With the creation of a number of building blocks with

separate stiffnesses determined from the tissue level model, a library can be compiled

ranging from 100 MPa to 2 GPa, a range of values encompassing both bone and implant

stiffnesses. Choosing a building block size of 27.0 mm^3 each, with total VB dimensions

of 48.0 mm × 24.0 mm × 27.0 mm, implies that there will be around 1008 total building

blocks which should be sufficient to approximate a VB [225]. At the border of the VB is

the cortical bone that has a much greater stiffness and lower porosity than the trabecular

bone contained in the center of the VB. Building blocks contained in these outer

extremities would have a higher material volume and a much lower porosity to

approximate the cortical shell. Wrapping a nonporous shell around the border of the VB

would improve the mechanical stability and also prevent any fluid leakage, as well as

reduce mechanical discontinuities due to edge effects.

Optimizing the Microarchitecture Based on Mechanotransduction Principles

Generation of building blocks from CAD and subsequent evaluation of apparent

stiffness with FEA will not properly account for the biological integration of the global

construct. Other exogenous parameters, such as local chemical moieties and pH, will

certainly affect its postsurgical success. Of the parameters readily accessible to the

designer, intra unit-cell material orientation (or internal microarchitecture) is paramount.

Thus, there is a need to optimize materials that do not already exemplify both ideal

biological and mechanical properties. For example, scalability of the construct's size will have implications on its cell–substrate interactions due to the fixed size of a given cell, but not on its mechanical properties that depend only on relative dimensions. Recent advancement in the design and manufacture of scaffolds using continuum-based voxel models, homogenization theory, rapid prototyping, or casting techniques have provided the means for very specifically designed scaffolds. Much research has been conducted into the use of repeated microstructures or building blocks to delineate between apparent and tissue level properties in trabecular bone. To our knowledge, little work has been conducted in the area of scaffold design based on mechanotransduction principles— principles that investigate how cellular and biological responses are induced from mechanical stimuli [226, 227].

Previous studies exploring the effect of geometry on material properties have been able to demonstrate in 2D and 3D an improvement in mechanical quantities such as bending and porosity. Using simultaneous nonlinear optimization, it has been shown that various material properties may be altered according to predefined constraints like minimum pore size [18]. The rearrangement of material in a structure may result in a stronger architecture or higher effective stiffness. Indeed, this is similar to the rearrangement of bone *in vivo*. To this end, Ruimerman *et al.* have created an iteratively based program that simulates bone remodeling based on the mechanotransduction stimuli derived from osteocytes [228]. Still others have approached remodeling from a cellular automata standpoint using simple rules acting on a large problem set [227].

Since the initial steps in bone tissue formation include adherence of bone cells onto a synthetic (biodegradable) template, differentiation in the case of mesenchymal

stem cells, and the production of osteoid, it becomes obvious that the surface environment will largely affect the success or failure of a scaffold. Surface characteristics are complex, however, and describe energies involved in protein–integrin binding as well as mechanical deformation applied from the surrounding locality. As a first step toward understanding the effect of surface activity, we propose a hypothesis based on mechanical characteristics alone: tissue growth will be accentuated through a uniform surface energy distribution. Justifiably, extremely large energies will encourage crack propagation and discourage cellular attachment either from migrating or from seeded cells. A non-uniform driving force (ultimately resulting in a uniform end state) as a mechanical objective has been examined on the whole bone level as well [201, 226]. As follows, voxel models are created of previous scaffold microstructures, and the geometry altered based on finite element results to distribute the material in such a way to eliminate peak stresses, strains, or strain energy densities (Figure 59). We believe that these types of optimized shapes will play a major role in the improvement of topology and internal architecture and will definitely contribute to the determination of mechanical stimuli involved in bone growth and cell–scaffold interactions.

The use of microstructural units is advantageous because it supplies biological scalability while maintaining constant mechanical properties. Though it is true that apparent mechanical properties will differ from those on the microstructural scale, any shift in the overall size of the construct, while keeping relative dimensions consistent,
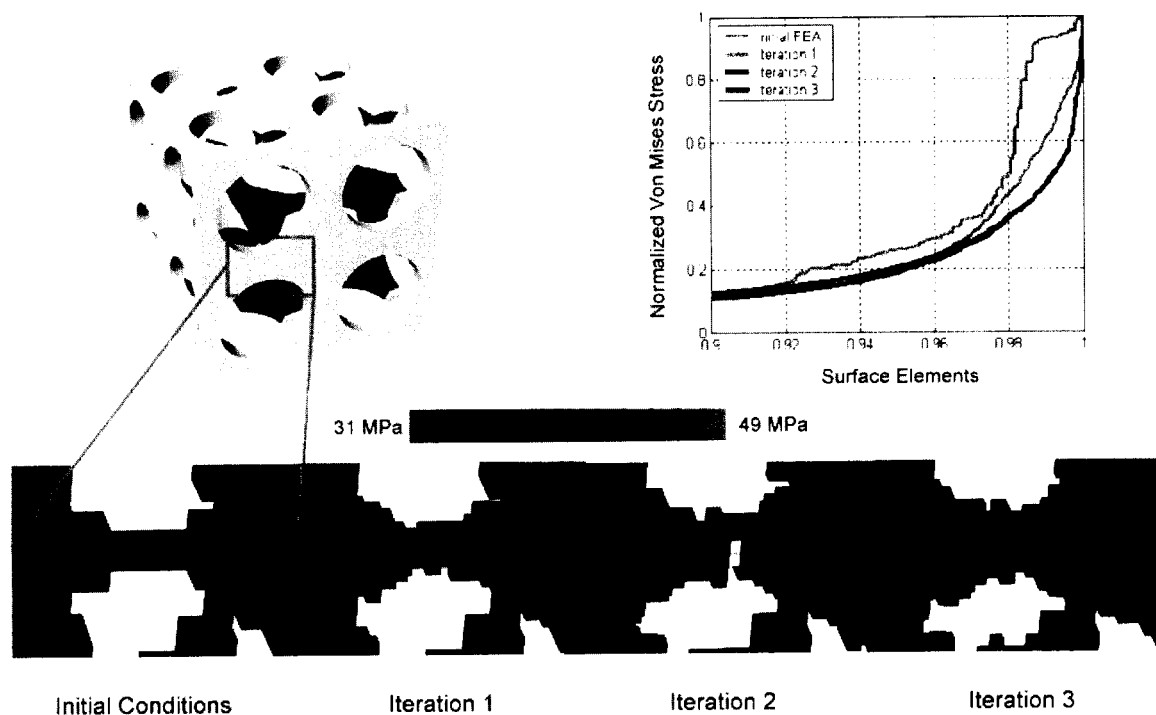
Figure 59. Voxel-based microstructural unit initially and after one iteration. Finite element results were tabulated under unite ompressive displacement (into page) and a fully constrained opposite face. Note that material reinforces areas of high strain energy (the objective function in this case) and are taken from areas of low energy to narrow the energy profile.

should not affect its overall mechanical response. However, size increases or decreases will affect the cellular response to the scaffold (since the ECM and cells do not have the ability to be proportionately scaled). In this way, fine tuning of the scaffold's biological response may be conducted simply by altering its size. Certainly, there exits a bandwidth in which scaling will not prove biologically favorable, most likely, when an interconnected pore structure is not possible. Yet, by mixing and matching different microstructural units, increasing some and decreasing or skewing others, a net biological advantage may be achieved.

Arrangement of Building Blocks into Composite Structure

Following their construction and the optimization of building blocks to match specific stiffness values, the building blocks need to be arranged appropriately in the VB

based on the determined material demands. Using a modulus map generated from the imaging modalities, a building block can be placed in the location of each corresponding stiffness value. Previous studies evaluating the strength and density of lumbar vertebral trabecular bone have demonstrated a difference based on anatomical site for both quantities. Mechanical testing was completed on sectioned lumbar vertebral trabecular bone, which showed an increased strength in the central posterior portion of the VB that corresponded to stress maximums for *in vivo* loading [225]. QCT has been used to show that density differences of the VB were also localized to this area [229]. From the 3D map of stiffness values for the VB obtained from literature values or imaging modalities, a building block would be selected from the library which approximates the estimated property. Using CAD, the cubes can be arranged in series or parallel resulting in a layered reconstruction of the bone (Figure 60) [224, 230].

Following the construction of the array of building blocks in the proper location, a general approximation of a VB exists. However, the global shape requires a continuous boundary. To accomplish this, Boolean or cutting functions that are innate to all CAD programs can be used. A simple analogy of this process is making cookies using a cookie cutter. As illustrated in Figure 60, a surface with a complex border is placed over the complex shape, represented here by a cube. The excess material that overlaps outside of the border is then removed, leaving the former object with the complex shape that defined the border of the surface.

Arrangement of the posterior elements proves to be a much more daunting problem based on location and function. While the posterior elements are responsible for
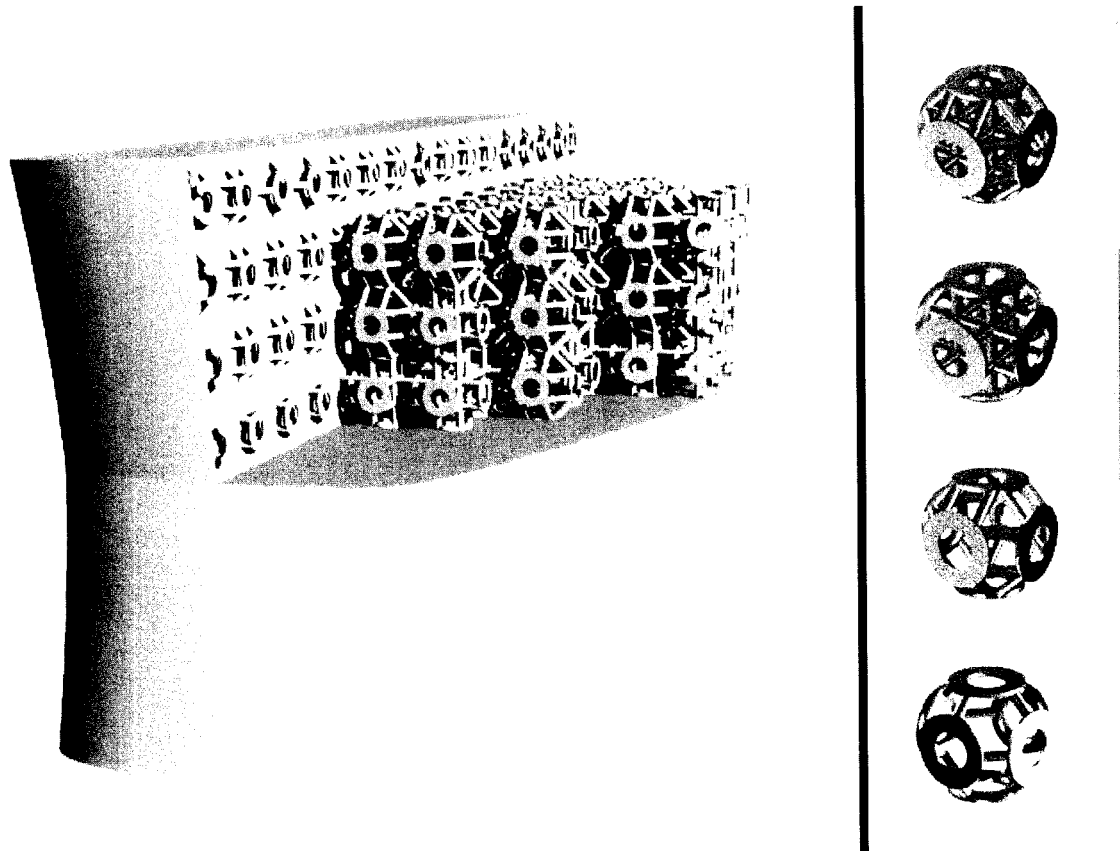
Figure 60. Using a library of building blocks to generate a global shape. The library at the right can be used in any location that is required to approximate the material demands of the vertebral body. The global shape approximates a vertebral body following the assignment of the building blocks to their respective locations.

30% of the total load transfer of the VB [231, 232], it is important to include them both for the protection of the spinal cord but also consistency of meshing with adjacent vertebrae. Since the posterior elements are to a significant degree simply cortical bone, these elements can be approximated as a thick shell with a hollow channel running through the center [41]. The complex global shape of the posterior elements can be obtained using the previous imaging techniques, and its manufacturability may be dependent on a piecewise Boolean of largely fluctuating surfaces (Figure 61).
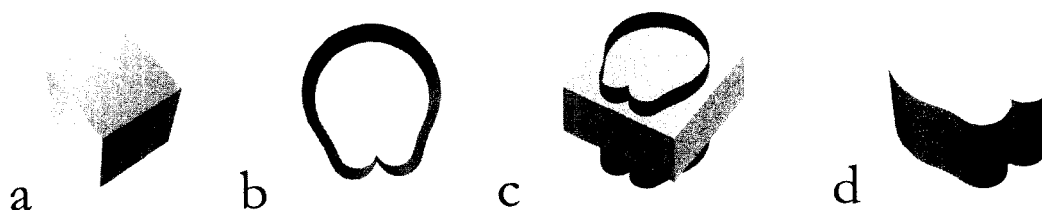
Figure 61. Explanation of one type of a Boolean difference function. Simple shape (a) is overlaid with a complex border (b) shown in panel C. Adapted from a process described previously. After the Boolean difference, the simple shape now has the complex border with the excess material deleted (d).

Fabrication Techniques

Creation of a tissue level model of a VB using building block structures is followed by fabrication of the construct. Because the complex structure is near to the resolution of the microarchitecture of bone, precise manufacturing methods must be used to generate the models. Several rapid prototyping processes, such as stereolithography and fused deposition modeling (FDM), are nowable to generate an entire bone model including complex microarchitecture at or near the size of individual trabeculae [110, 223].

Stereolithography utilizes a precision laser driven on a plotter which crosslinks a polymer in predetermined arrangements. At the time this study is in press, Stereolithography cannot attain the resolution of FDM, but laser technology will eventually surpass all other processes in achievable resolution. One distinct advantage of stereolithography over other methods is the ability to fabricate structures using photocrosslinkable polymers. Poly(propylene fumarate) was previously used with Stereolithography to produce simple structures [128], which is the first step toward generating entire scaffolds out of an implantable biomaterial. Complex structures are

currently a problem for stereolithography because the process uses only one material to build objects and lacks adequate support structure to generate complex architectures or structures with oblique angles.

The ability to print a scaffold using the implantable material is indeed an attractive promise, one which other rapid prototyping systems, besides stereolithography, are attempting to deliver. Research groups have built stand alone machines that utilize materials such as thermoplastic hydrogels and agarose [216]. Therics Inc. uses a particle binding system with six printheads offering increased production, while maintaining high resolution required for internal morphology (Therics Inc., Princeton, NJ). Sciperio Inc. has created a system that is able to print on a complex surface with a variety of materials including fibrin glue, cells and polymers, and eventually live cells. The machine uses two lasers to guide the printheads to deposit material on an object, even one moving at 10 Hz. Mironov *et al.* discuss the development of a rapid prototyping system capable of delivering cells, gels, and cell aggregates into defined locations and whole cells into predetermined locations [233]. However, if the resolution cannot generate the structures needed for a functional implant, then even a versatile rapid prototyping machine is limited, as is currently the case with these systems.

3D Phase Change Printing is currently the most versatile rapid prototyping process and works like an inkjet printer with a movable z-stage. The printhead deposits a thermoplastic material onto the stage in a two-dimensional pattern resulting in a slice of the final geometry. A second material is printed surrounding the build material, enabling oblique angles. The PatternMaster (SolidScape, Manchester, NH) wields two thermoplastic waxes for build and support, and several different solvents to remove the

reinforcement material [124]. The ability to remove support materials makes 3DPCP a good candidate for investment casting. By printing the inverse of an object and removing the support material, a mold of the object is created. This mold will be a template for injection of the casting material, following removal of the build material. This process can be used with any material (even metal) as long as the melting temperature and the chemical solvents are conducive with the casting material. Interpore Cross currently uses this technology to generate titanium VB replacements (Biomet, Irvine, CA). More complex molds can be generated that allow the implementation of multiple biomaterials [192, 234]. Incorporating separate rapid prototyped parts into a single mold allows the use of a wide range of materials, while maintaining the resolution required for a bone-like architecture.

Functional Integration

Functional integration of the implant into the anatomic site is essential to address load transfer demands. After crafting the implant based on perceived specifications for loading and mechanical stability, functional integration is necessary to prevent implant failure and loosening. Loosening persists for anymetal implant resulting in its dislodge from the bone in 10–15 years, and generally causes severe pain [235]. To prevent stress shielding and subsequent implant failure, it is the current belief that the biomechanical properties of the implant must approximate the original bone properties and that the implant must be functionally integrated into the surrounding tissue.

The successful implantation of the vertebral replacement requires that the muscles, tendons, ligaments, and other tissue be rejoined to the VB in the same location as they were before they were removed. While this is currently not possible, the intended future attachment must be in amanner that promotes their functional integration during tissue healing. For example, specific fillets could be designed into the VB shell that would allow for connective tissue to be sutured or tied to the outside of the implant.

Resorbable fixation devices could be useful for the fixation of the constituents of the spine as well as the external parts; previous studies have already demonstrated the efficacy of joining tendons and ligaments with screws and pins [236]. Other options include the use of
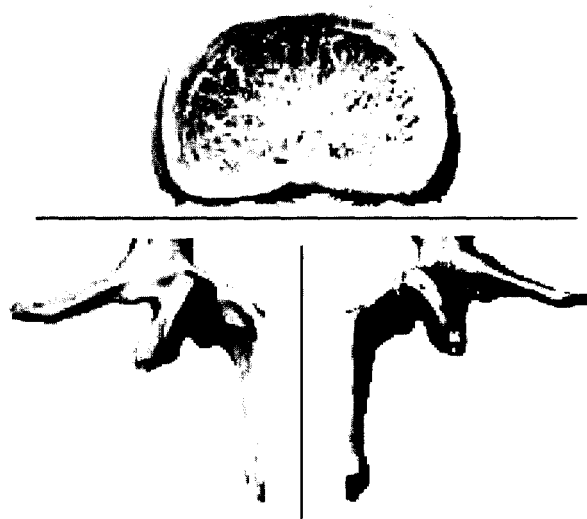
Figure 62. Diagram of lumbar vertebral body. Functional integration of the vertebral body into the location in the body would required the splitting of the body into three segments. These three segments will facilitate the assembly of the vertebrae around the spinal cord without damaging it. Tissue glue can be used to rejoin the three parts together.

bone cements that contain stiffness and strength much closer to bone than other polymeric materials [237]. Additionally, optimal performance of the VB *in vivo* requires that posterior elements are matched with the spinal cord to protect and enact load transfer. Tissue glues such as fibrin glue, a popular natural adhesive, do provide connections between two tissue counterparts and are fully resorbable, yet questions

remain regarding its adhesive threshold for this application. The hollow channel present in the posterior elements is a convenient anatomical attachment point for connecting the two lateral elements [238, 239]. Figure 62 depicts the splitting of the vertebrae that would be required for implantation to work surrounding the spinal cord. The invertebral disc above and below the VB could also be joined to the surface of the implant with fibrin glue, combined with therapeutic drugs, sutured, or fixed closed with bioresorbable materials.

Material Selection

The scaffold material determines both the mechanical robustness and the biological coupling of the scaffold with its environment. The material should be selected with prior knowledge of the anatomical implant site as well as the production method used in its manufacture. For example, various pretreated titanium products have shown detrimental effects caused by unexpected surface oxide reactions *in vivo* that differ depending on base material [108]. Likewise, if a specific microstructure is desired, or resolution is an issue, the use of stereolithography or FDM would be advisable [6]. There is a limit on the types of materials that can be produced with rapid prototyping technologies and also the types of materials suitable to be cast into molds [234]. Materials such as hydroxyapatite and calcium phosphates, which are formed from sintered powder particulates, are certainly less conducive to fabrication though technologies utilizing subtractive molds do exist [240]. Furthermore, the preparation of biodegradable polymers commonly used as templates for tissue engineering involves toxic solvents or cross-linking agents, some of which will not be completely denatured

from the construct [113]. The personal selection of any material will have to gain the final approval of the FDA.

As discussed in the previous sections, through spatial redistribution and organization of a material, the structural properties can be significantly increased [18]. Materials are often chosen based on their mechanical and biological compatibility which is a factor of anatomic location. A large problem noted early on in the development of hip replacements was stress shielding: a phenomenon whereby the brunt of the load carried by the stiffer material, usually titanium, which resulted in reduced deformation of the surrounding bone to below equilibrium states, stimulating osteoclastic bone resorption and eventual implant loosening [109]. Other shortcomings in mechanical properties can be attributed to ultimate strength, fatigue life, and elasticity. Unfortunately, biocompatible materials—materials that minimize an immune response—do not in most cases have the mechanical strength or stiffness to mimic bone. These materials should not be discarded, however, as they may be favored biologically through hydrolytic breakdown or their ability to cause minimal pH changes in the environment.

Composites have been explored as a natural compromise, since no one material possesses all of the ideal properties for a given problem. Composites can be as simple as the application of peptide sequences onto a carbon–carbon backbone, or as complex as developing negative stiffness or "smart" materials. Many biocomposites seek to offer surface modifications or specify binding for a particular application. Other types of composites make use of a biocompatible base material enforced with stronger nodules

such as carbon nanotubes [241]. These materials offer a good compromise in gross properties, but increase the complexity of chemical interactions occurring within the architecture, making them more difficult to study and safely apply.

5.2.3 Results

As a demonstration of both the possibility and limitations of this technique, a simple model of a VB was generated. Using the governing concepts for CATE, a lumbar lumbar vertebrae was scanned using a QCT and was reconstructed using Analyze (Analyze Direct 5.0, Lenexa, KS). The elastic moduli were calculated from mapping pixel values onto FEA grids and then were matched with predefined correlations between Hounsfield units and bone mineral density. The mean trabecular density was calculated as 0.13 g/cm^3 (range 0.01–0.25 g/cm^3 with an average cortical density of 0.6 g/cm^3. Modulus values for trabecular bone averaged 390 MPa (range 0.01–770 MPa) using accepted correlations [217]. Modulus values per region were grouped into four regions corresponding to four different building blocks evaluated in a previous study [122] shown at the right of Figure 60. Building blocks were modified to global dimensions of 3.0 mm × 3.0 mm × 3.0 mm, which would result in 1008 total blocks for the complete approximation of the VB. The porosities ranged from 80 vol% porosity up to 92% porosity, values encompassing bone porosities. On the basis of the generated modulus map, the building blocks were arranged into their respective locations. CAD processes reached the upper limits of memory usage long before the assembly of the entire 1008 building blocks. The memory limit of Windows XP was also a limiting factor. As a result, only half of the approximated VB was built using the PatternMaster as a proof of concept (Figure 63). While the overall dimensions were replicated, fine features

Figure 63. Approximation of a human lumbar vertebral body generated using computer aided tissue engineering principles and the PatternMaster.

were often error prone. In summary, we have demonstrated that this process can be completed on a rudimentary scale but that fine tuning is required for each step of the process. For this process to be successful in the future, both computing processes and the resolution of rapid prototyping will have to increase.

5.2.4 Conclusions

The presentation for a patient-specific approach for constructing a complete VB via building blocks has been conducted. A summary of the procedure starting with image capture through surgical implantation is depicted in Figure 64. Though some of the methods described cannot be realized with current technology, the necessary advances are not far off. Computing resources do not currently allow the generation and manipulation of models larger than we have proposed. Computing power and CAD programs need to improve slightly to allow the rapid generation of complex models that would ease the fabrication of an appropriate number of building blocks. In materials
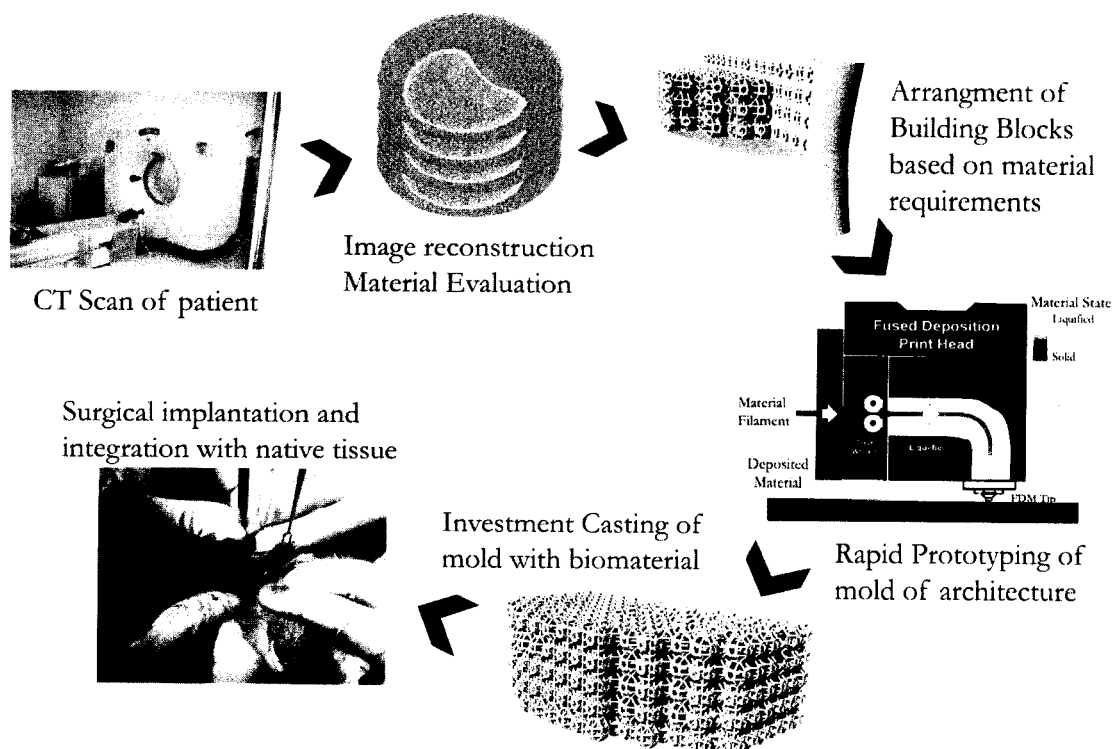
Figure 64. Conceptual diagram of the process of computer-aided tissue engineering. Three-dimensionalmodel of tissue is obtained using an imaging modality. Reconstruction of the image occurs with a sectioning program. Following this, the CAD model of the part is generated using building blocks. This architecture is then built using rapid prototyping and cast with the biomaterial of choice to yield an implant, which is then surgically inserted into the body.

research, there is much effort directed at varying the modulus and surface chemistry of materials, especially important for load bearing implants. Already, previous studies have evidenced rapid prototyping models which use a repeated structure in large size models [222, 224]. With the improvement of rapid prototyping speed and resolution, machines will be able to print with a wider range of materials. A current goal of several companies is the ability to incorporate live cells into their printed scaffolds [242].

The main bottleneck of the process described in this study is the general lack of knowledge of human mechanobiology and the role of cellular interactions on artificial substrates. Assuming these biological parameters can be identified, a scaffold may be designed with a proper pore size and interconnectivity,microstructure, degradation rate,

and surface chemistry. The advantage of the outlined process lies in adjustment of the vertebral compliance first to ensure adequate load transfer, an important property for vertebral replacement. Subsequently, net biological properties can be fine tuned by simply scaling the final construct. Further alterations can be accomplished by choosing a new microstructure from the available library of shapes with a different biological property but similar unit stiffness. Mixing and matching of geometries may be utilized to design asymmetric scaffolds or scaffolds that exhibit a discontinuous microstructural stiffness with the goal of accentuating fluid flow. Finally, while these techniques lend themselves to the formulation of bone constructs, they can be used for other parts of the body as well that do not require load-bearing support.

5.3 Bone-derived CAD Library for Assembly of Scaffolds in Computer-Aided Tissue Engineering[*]

5.3.1 Introduction

The idea of designing synthetic scaffolds for guided tissue regeneration [22, 101] is attractive for several reasons. First, by supplying a base material, the locations upon which tissue will integrate with the surrounding environment are known a priori. As a consequence, several schemes may be developed based on the degradation of the scaffold or changes in morphology over time [243-246] which can influence how subsequent tissue may form. Secondly, by controlling the shape, or at least the surface contour, one can manipulate the mechanical environment in which tissue exists [105-107]. This was shown to be influential on cellular metabolism [49, 247]. Additionally, the morphology indicates, based on a superposition of isostress/isostrain measurements, which areas of the scaffold would be overloaded once implanted at an osteoporotic site and could thus lead to tissue necrosis [75, 248, 249]. Finally, with control over the scaffold domain comes control over the scaffold interfaces, or transitions from one type of architecture to another, which if joined incongruously can lead to disjoint stress profiles as well as cellular sparsity.

The goal of this study is to present a library of tissue primitives (unit building blocks and interfaces) to be implemented in computer aided tissue engineering (CATE) [32, 100]. These unit blocks may be merged according to various qualities, some of which are illustrated in this manuscript. The characteristics are open to the designer, but

---

[*] This section appears in the book Virtual Prototyping (Springer Verlag), Ed. Bidanda, P. as Wettergreen MA, Bucklen BS, Liebschner MAK, Sun W "CAD Assembly Process for Bone Replacement Scaffolds in Computer-Aided Tissue Engineering." This work represents the shared collaboration between Bucklen and Wettergreen. For continuity purposes, the entire manuscript has been included. the sections directly related to Bucklen's work are topology solutions, ESO and Intelligent Cavity Creation.

we demonstrate the ability to match tissue primitives according to a density map of the subregions within a human vertebral body. Density or volume fraction is a suitable metric determined from image intensity, though we expect that more significant metrics related to tissue regeneration will need to be identified. Nevertheless, the correlation between bone mechanical properties (stiffness and strength) to apparent density is well established [250, 251]. Using principles of an assembled library, scaffolds may be created in a site-specific manner with conformations that resemble bone. This process may be preferred over current scaffold generation techniques that make use of random processes of solvent casting or gas leaching to create the necessary void spaces [6, 252].

To date, many of the biomaterials used as scaffolding have mechanical behavior inferior to the constituency of bone [250, 253, 254]. Therefore their design cannot always be biomimetic (or at least derived biomimetically) as proposed here. Given a case where the architecture of the scaffold needs to deviate from natural tissue, as in fulfilling the demand of exceptional stiffness, we recommend an assembly of derived analytical shapes [249]. In the absence of this necessity, a biomimetic approach using bone-derived architectures is beneficial for the many of the non-mechanical tangibles (e.g. volume fraction) and qualitative intangibles (e.g. fluid perfusion, metabolic waste removal, and those listed previously).

5.3.2 Unit Cube and Interfaces

There are two types of design approaches to consider when creating scaffold building blocks. The first is to create a variety of scaffold shapes which are characterized throughout the spectrum of the independent design variable. This is particularly useful if
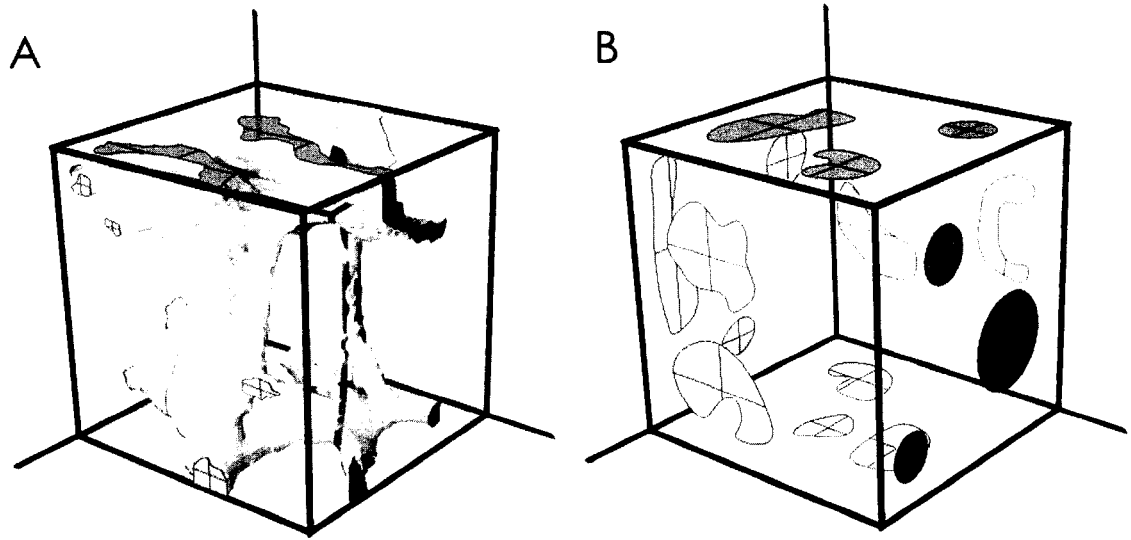
Figure 65. Unit cube and interface methods of primitive design. The unit cube architecture is known (A), or the interface (B) and loading conditions are known.

a specific shape or repeated pattern is recognized from the outset. For example if one preferred a design favoring the volume fraction of a given shape, experience indicates that scaffolds need at least 60 % porosity to account for nutrient delivery and below approximately 90 %, the mechanical integrity will be suspect [9, 14, 249]. On the other hand, if the shape is the unknown, but the interfaces and contact angles of adjacent unit blocks are known, then the inverse problem, usually a shape/topology problem, may be solved as long as a design rule or objective is provided. Figure 65 illustrates the two conceptual differences.

Though the focus of this study will be on shape recognition of tissue primitives, i.e. a known shape, we provide an example to illustrate the interface method. The solution of the inverse problem is a topology optimization problem. These types of problems are difficult to solve. One has to find a representation of the shape that can capture the fine scales of tissue and that allows the application of mathematical optimization. Among the available approaches are density functions [103, 255], level-set

methods [256], evolutionary structural optimizations (ESO) [257-259], and other implicit function based methods [102].

For demonstrative purposes and ease of implementation, a heuristic method was chosen known as the modified method of intelligent cavity creation (ICC) which is a subclass of ESO. This method has the advantage of dictating the number of cavities (voids) created during the process, and is relatively easy to implement. The major disadvantages are that the optimization goal is not well formulated and the computational order is of the scaffold dimension cubed. Briefly, a completely solid material is used as the starting geometry and reduced to a final shape through a combination of surface erosion (nibbling ESO) and cavity creation. The reduction serves to minimize the addition of peak stresses caused by material reduction, by removing only "unneeded" material. A metric is used to determine "unneeded" material and when the internal stress state may tolerate the addition of a cavity (for a complete description see [257]). The fixed number of cavities regularizes the problem and the numerical instabilities often associated with the inverse description.

The interfaces and contact angles of the bone cube in Figure 65 were estimated to create boundary conditions (Figure 66A). Assumed displacement boundary conditions of equal magnitude were applied along the trabecular axes. The elastic modulus of the solid material was 1×10^6 times stronger than void material and had a Poisson's ratio of 0.3. The created routine used an interactive routine to retrieve the von Mises stress (ABAQUS, Inc., Pawtucket, RI) (Figure 66B) with optimization rejection ratios of 0.01 and a maximum of two internal cavity initiations. The final internal architecture had a porosity of 36 % (Figure 66C). The advantage of this technique is that the interfaces to
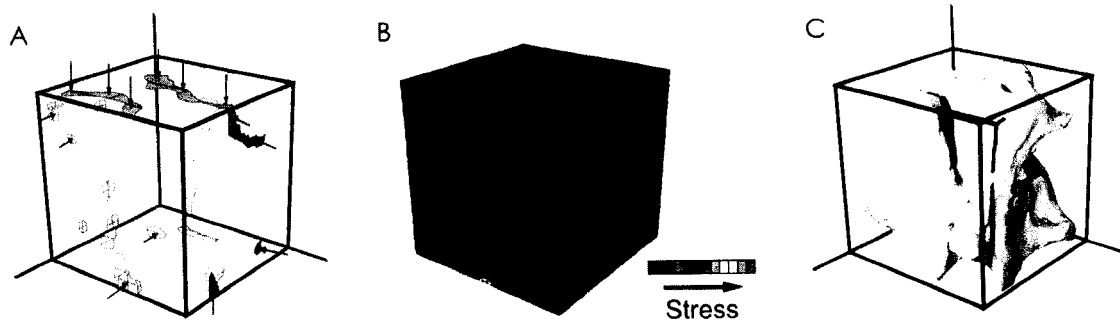
Figure 66. Interface method. The boundary conditions (A) determine the stress state (B) which dictates the final shape (C) of any optimization method (in this case ESO).

the adjacent cube structure are already known and each cube can be separately analyzed/optimized.

5.3.3 Presentation of Tissue Primitives

Identification of primitives

The goal of this study was to identify and implement patterns of trabecular bone into a descriptive stiffness library composed of unit cubes and interfaces. Each library unit is referred to as a primitive, and is the combination of one unit cube and six interfaces. The feasibility of joining two primitives is handled by a library subset of seven dissimilar interfaces, which share a common surface area (Figure 67B). The stiffness of unit cubes was calculated (Section 4.2), and was used, along with its morphology (Figure 67A) to present an example of the application of the library to a partial scaffold assembly (Section 5).

In an effort to isolate repeating patterns within trabecular architectures, 20 sections from 10 T-9 human vertebral bodies were scanned (μCT Scanco80, Basserdorf,

A

| Truncated Icosahedron | Truncated Dodecahedron | Deltoidal Icositetrahedron | Triakistetrahedron | Truncated Octahedron |

| Cuboctahedron | Bi-Augmented Triangular Prism | Augmented Hexagonal Prism | Truncated Tetrahedron |

| Armchairs | Archway | Folding Chair | Ball and Stick | Sunglasses |

B

z
x   y
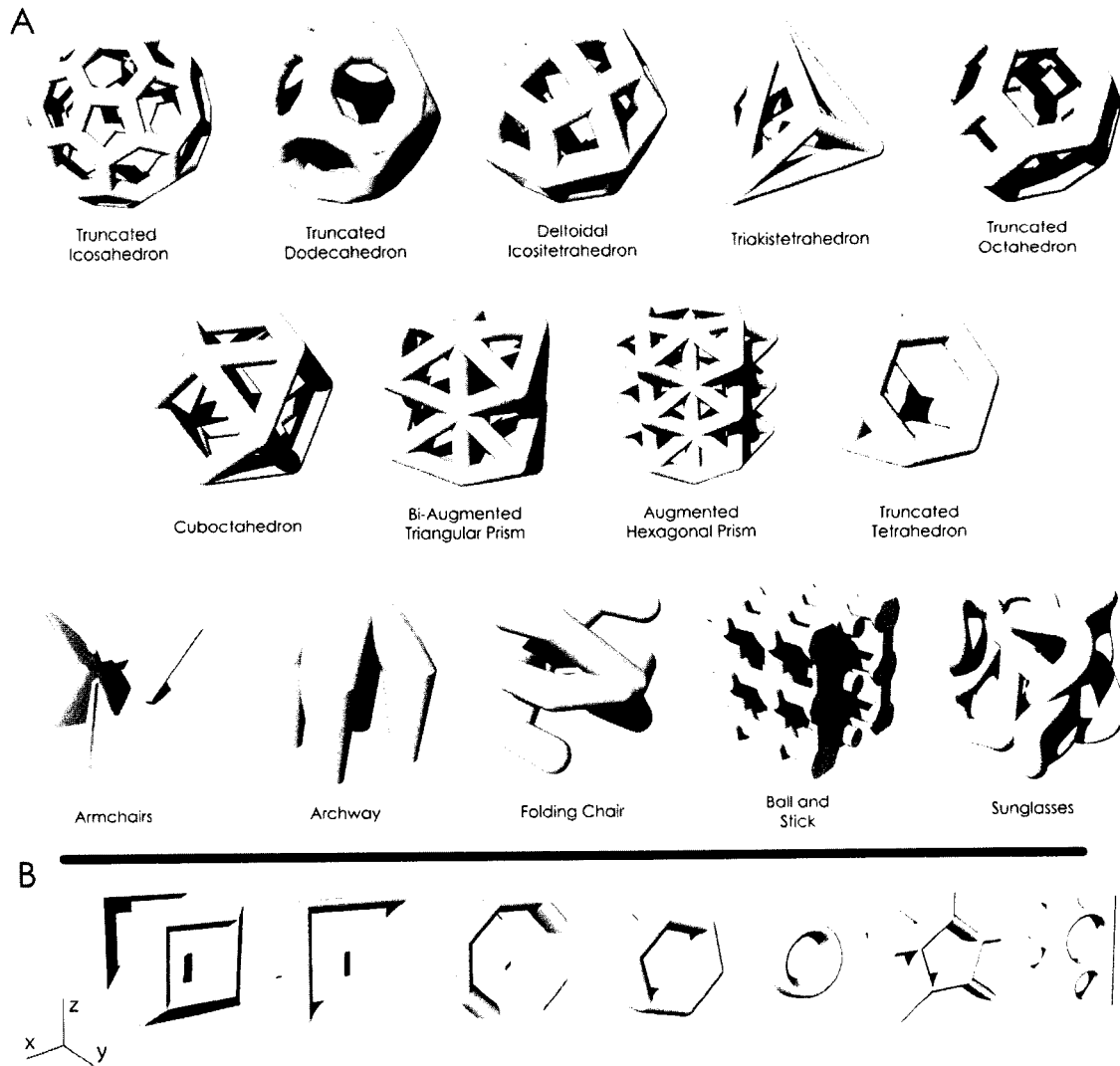
Figure 67. Tissue primitive library. The unit blocks (A) are attached with interfaces on all six sides (B) resulting in a tissue primitive. Unit blocks are limned at their "native" volume fraction (see Figure 70).

Switzerland) at 30 μm isotropic resolution. We reconstructed the image sets into segmented, binary, trabecular bone datasets of voxel slice dimensions 2048 x 2048. Architectures were loaded into an image processing suite (Analyze Direct, Inc., Lenexa, KS) and viewed in the three physiological planes in > 2 mm thick sections. In most cases, trabecular subsections were translated into stereolithography files for 3-D viewing (Figure 68A). Because each individual bone contains many complex repeating patterns, often joined with other repeating patterns, the number of each unit shape could not be

Figure 68. Identification of tissue primitives. Tissue primitives were identified on several length scales in several physiological directions from µCT scans. They were identified (A), derived into CAD representations (B), from emergent, repetitious patterns (C) within the samples.

documented. Nevertheless, there was enough evidence to construct computer models of derived tissue interfaces (Figure 67 B) and unit cubes (Figure 67A).

The architecture of bone was examined on three length scales. The first and simplest length scale representing a junction of two single rods or a junction of rod with a plate was not considered significant. The second length scale was unit blocks witnessed on at least two trabecular lengths. The final scale, lengths of more than four trabecular lengths were scarcely found with any consistency, possibly due to difficulties in manual identification, but most likely because trabecular bone is seemingly a random conglomeration of simpler repeating units. Therefore, this length was not included at

any point in the library. Repeated patterns, such as the highlighted regions in Figure 68A, were translated into tissue primitives (Figure 68B) for the library. Emergent patterns could be found in numerous locations illustrated by the abridged version of the Sunglasses shape portrayed in Figure 68C.

The primitive library consists of five Archimedean, five tissue-derived, two Johnson, and two Catalan solids. The solids are respectively: (Truncated Icosahedron, Truncated Dodecahedron, Truncated Octahedron, Truncated Tetrahedron, Cuboctahedron), (Armchairs, Archway, Folding Chairs, Ball and Stick, Sunglasses), (Bi-Augmented Triangular Prism, Augmented Hexagonal Prism), and (Deltoidal Icositetrahedron, Triakistetrahedron). Incidentally, the Catalan solids are duals of the Small Rhombicuboctahedron, and Truncated Tetrahedron, respectively. Morphological features of the non-wireframe versions of these polyhedra have been well documented [260]. In all cases, architectural features were noted repeatedly within bone samples. In most cases, closed 3-D versions did not exist, but were included in closed form for space-filling and regularity purposes. For example, in Figure 68A a partial, wireframed version of a combined face of the Deltoidal Icositetrahedron (highlighted, bottom-left) can be clearly seen, with the appropriate angles (~98° face edge, ~21° protrusion), but does not exist in closed form as pictured in Figure 67.

Tissue-derived shapes which bore no resemblance to previously recorded polyhedra were also documented. The Armchairs unit cube consists of 4 curvilinear plates joined at a central junction. The Archway represents a distorted "X" interface extruded in a curvilinear fashion along the height. The Folding Chairs is a spring-like shape which when projected in two of three directions forms a commonly occurring

hexagonal pattern. The Ball and Stick model is a basic orthogonal rod model, where the created rhombi exist at 60° angles, also corresponding to a regularly observed trend. The final Sunglasses shape was a 3-D version of a curvilinear figure-eight pattern (Figure 68C). The locations of the primitives within the bone was location dependent, but not exclusive. For example, the hexagonal projections tended to exist in axially cut sections while in coronal views, the orientation of the struts was in-line with loading, resulting in more rectangular interfaces and rectangular unit cubes. Often the transition from pentagonal shape to a rectangular shape could be observed by a diminutive or unused strut, within the coronal view.

Interfaces

For effective load transfer, tissue primitives connect to other tissue primitives through designed interfaces (Figure 67B). Figure 69 portrays interface matching and the common surface area between adjoining interfaces. The diagonal entries represent a perfect joining with a normalized surface area of one. The off-diagonal elements reflect the common area and symmetrically the relative percent of cross-section filling, calculated as the fraction of the common portion over the superposition of both areas (intersection/union). Each interface has a basis of values which describe how well a given interface relates to another. For example, the circular interface matches only with itself or the hexagonal interface with any mechanical integrity, reflecting the limitations of the library, and the necessity of multiple interfaces.

Ideally, each primitive's interface would provide a perfect matching. However, because unit cube architectures were derived, and not designed, a universal interface is
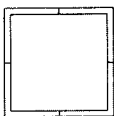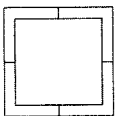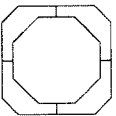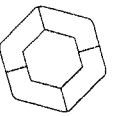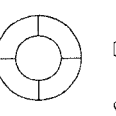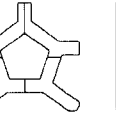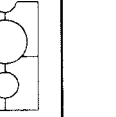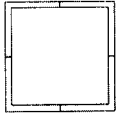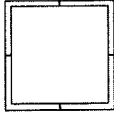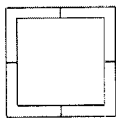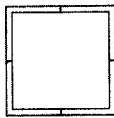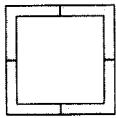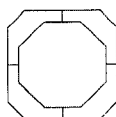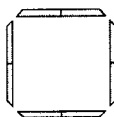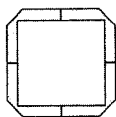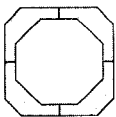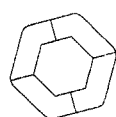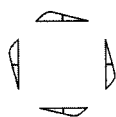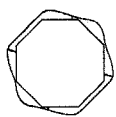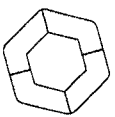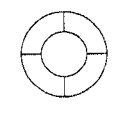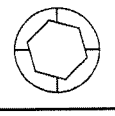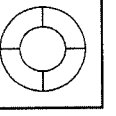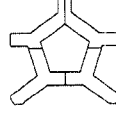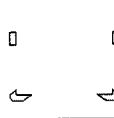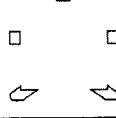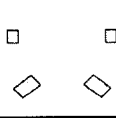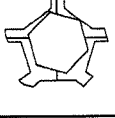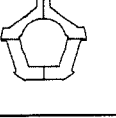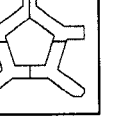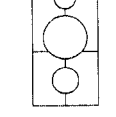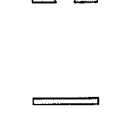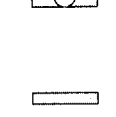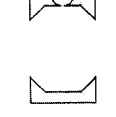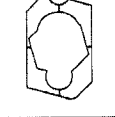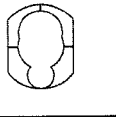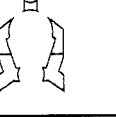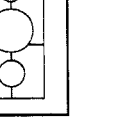
Figure 69. Interface matching. Seven interfaces can be matched with each other according the relative fraction of intersecting areas. Each interface forms a mathematical basis which has a spectrum of values.

not possible. Moreover, simple solid plate attachments or similar constructs would hinder the permeability and porosity of the scaffold. For that reason, native bone interfaces were derived as well. Architectures with drastically dissimilar or similar stiffness values are readily attachable in order to avoid further stress concentrations.
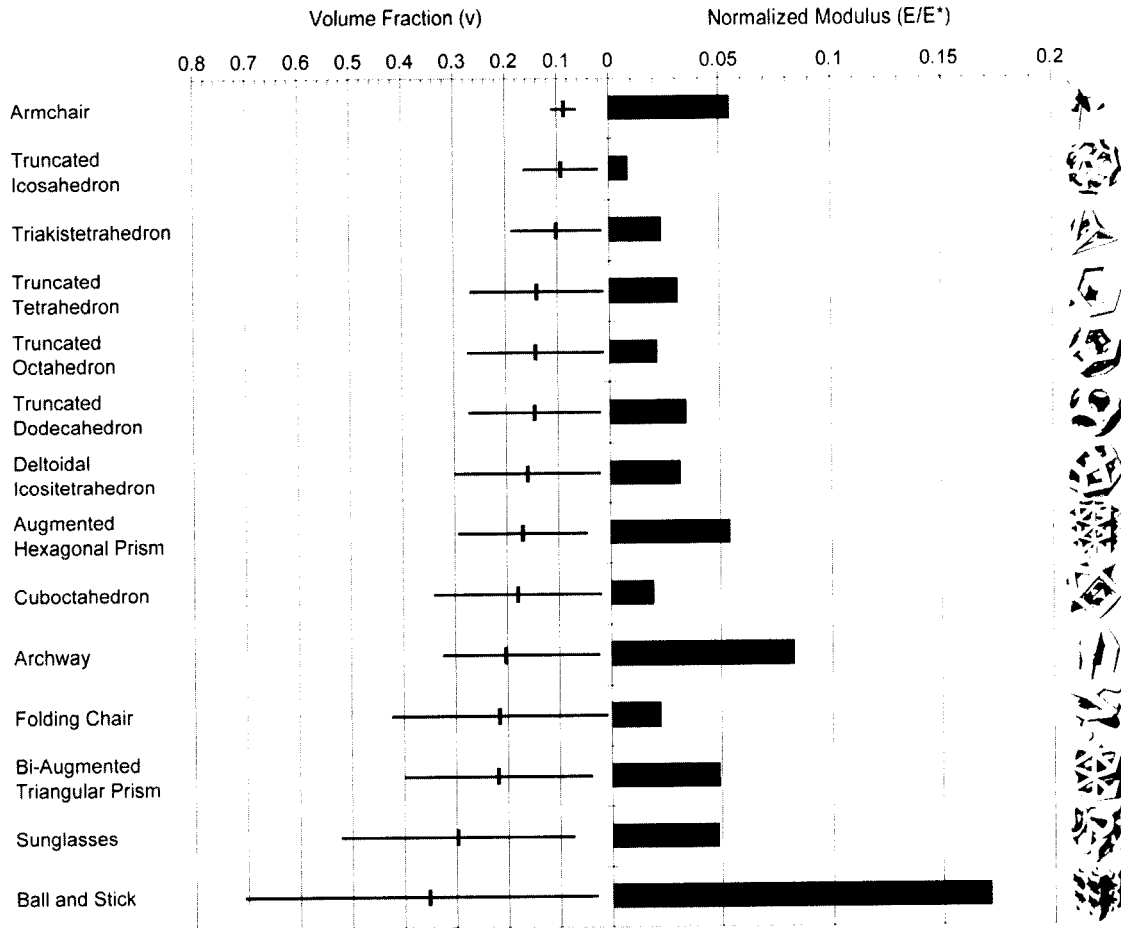
Figure 70. Volume fraction and scaled modulus. The range in volume fraction of each unit cube (left) and normalized elastic modulus, with respect to the average volume fraction (right).

5.3.4 Characterization of Primitives

Morphological Analysis

Morphological analysis was conducted on each unit cube in order to assist in characterizing the properties of the library. A "native" volume fraction for each unit cube was determined by calculating the mean of the range of possible volumes (Figure 70). The lower bound was calculated in each unit cube with similar strut diameters, signifying that it is a function of the number of struts and spatial arrangement. We determined the upper bound by expanding each diameter until a unique feature of the shape was

obscured (such as a hole closing in on itself). The only exception was the Arm Chair which was given an average plate thickness commensurate to the strut diameter. The Armchair and Truncated Icosahedron were the most porous while the Ball and Stick was the least. Similarly the range in material volumes tended to increase with respect to the mean value. In other words the least porous material also existed over the widest range (Ball and Stick). Table 8 portrays a more robust analysis of each architecture. Volume fractions range from 0.09 - 0.35, though most of the shapes are within 80 – 90 % porosity, which is suitable for scaffold engineering. In general, a high surface to volume ratio (S/V) is advantageous as the available area for fluid flow over attached cells will be higher. Of the identified shapes, the Armchair has the largest surface to volume ratio, and Archway the smallest. The average Connectivity Index, or number of struts connecting to a vertex, and length to diameter ratio is also reported (Table 8).

Table 8. Morphology of tissue primitive unit blocks.

	Volume Fraction (v)	Surface / Volume	Connectivity Index (avg.)	ℓ / d
Armchair	0.09	1.87	3	11.50
Truncated Icosahedron	0.09	1.65	3	1.96
Triakistetrahedron	0.10	1.22	4.5	4.25
Truncated Tetrahedron	0.14	0.90	3	2.21, 7.08
Truncated Octahedron	0.14	1.05	3	1.92
Truncated Dodecahedron	0.14	0.99	3	0.93
Deltoidal Icositetrahedron	0.16	1.08	3.5	1.89, 2.45
Augmented Hexagonal Prism	0.17	1.55	5	3.14
Cuboctahedron	0.18	1.04	4	3.79
Archway	0.20	0.61	4	2.00
Folding Chair	0.22	0.75	2	1.83
Bi-Augmented Triangular Prism	0.22	1.27	5	3.75
Sunglasses	0.30	1.10	4.5	2.66
Ball and Stick	0.35	0.95	4	2.86

Finite Element Analysis

A finite element analysis was conducted on each unit cube in order to characterize the spectrum of modulus values. The unit block modulus could be later used as a parameter to select shapes for the assembly of a site-specific scaffold. The analysis was completed in ABAQUS. A seeding density of 0.75 was used in most cases providing on average 37,000, linear tetrahedral elements. Each architecture was assigned isotropic material properties of $E = 2GPa$ and $v = 0.3$. The stiffness and elastic modulus in the loading direction were calculated in the standard manner through the summation of the reaction forces. The normalized values (with respect to the isotropic modulus) and the orientation in which they were tested are reported in Figure 70.

5.3.5 Assembly of the Scaffold

Generation of a Density Map

A density map was constructed which represents the local volume fraction of material within 3 mm sub-volumes, chosen to be the bounding dimension of the each primitive unit. Each section of this three-dimensional matrix maps an averaged volume fraction to that region. Through this procedure, apparent properties may be used to identify the placement of primitives which were designed at a length scale of several trabeculae based on manufacturability and available materials.

The modulus (stiffness) of each primitive was assumed to correlate well with apparent density. Only the relative distribution of values were important for this proof of principle, though any number of correlation relationships, linear or power law, have been used in the literature. The density map was created by averaging a series of binary slices of one vertebral body, progressively, in order to reduce memory requirements needed for

processing an entire vertebral body. The map provided a means in which patient/site specific properties of the bone may be assigned to the scaffolding.

Scaffold Assembly

The modulus values were ranked according to their magnitude, and the density map subdivided into 14 ranges, representing each of the 14 shapes. The available matching of an interface onto a unit cube is depicted through Table 9. The fraction reported is the contact volume of the internal side of the interface and unit cube, divided by the volume of the interface. In practice, Boolean operations in Rhinoceros 3D (McNeel Associates, Seattle, WA) provided this functionality. Each row of the table corresponds to one of six faces. Values below a certain threshold provide decidedly poor contact volume for load transfer through the interface and into the unit cube, and therefore, should be avoided. We chose a threshold of 0.1; however the exact number may be modified by the user depending upon the input criteria. The scaffold assembly, then, was produced in the following fashion:

1. Unit cubes were placed according to their ranking (modulus) in Cartesian space.

2. Interfaces were selected between each face by applying the threshold value for Table 9, below which an interface is not considered suitable to transfer the load from its designated unit cube. A perfect match is always chosen between adjacent unit cells when available, under the assumption no perfect match has preference over another (i.e. each has an adequate area for load transfer).

3. When no perfect match is available, select between the available interfaces (Table 9), those which provide the largest relative match (Figure 69).

Table 9. Interface matching to tissue primitives. The seven interfaces can be matched to the primitive unit blocks based on the percentage of common contact volume.

Interfaces

Shape	1	2	3	4	5	6	7
Augmented Hexagonal Prism	0.15	0.02	0.03	0.32	0.43	0.31	0.29
	0.15	0.02	0.03	0.32	0.43	0.31	0.29
	0.05	0.00	0.00	0.08	0.11	0.10	0.07
	0.05	0.00	0.00	0.21	0.11	0.10	0.07
	0.11	0.01	0.02	0.21	0.24	0.20	0.32
Cuboctahedron	0.23	0.20	0.14	0.53	0.63	0.43	0.33
	0.23	0.20	0.14	0.53	0.63	0.43	0.33
	0.23	0.20	0.14	0.53	0.63	0.43	0.33
	0.23	0.20	0.14	0.53	0.63	0.43	0.33
	0.23	0.20	0.14	0.53	0.63	0.43	0.33
Archway	0.09	0.00	0.00	0.09	0.28	0.25	0.27
	0.23	0.01	0.16	0.37	0.43	0.13	0.15
	0.30	0.09	0.17	0.36	0.42	0.42	0.28
	0.30	0.09	0.18	0.36	0.42	0.41	0.27
	0.30	0.09	0.16	0.37	0.43	0.41	0.28
Folding Chair	0.29	0.14	0.17	0.32	0.19	0.14	0.37
	0.29	0.14	0.17	0.32	0.19	0.14	0.37
	0.04	0.00	0.00	0.02	0.06	0.06	0.12
	0.04	0.00	0.00	0.02	0.06	0.06	0.12
	0.30	0.14	0.17	0.32	0.24	0.20	0.48
Bi-Augmented Triangular Prism	0.24	0.13	0.16	0.34	0.46	0.39	0.39
	0.24	0.13	0.16	0.34	0.46	0.39	0.39
	0.24	0.06	0.14	0.29	0.17	0.13	0.24
	0.28	0.14	0.25	0.42	0.30	0.23	0.37
	0.28	0.14	0.25	0.42	0.30	0.23	0.37
Sunglasses	0.12	0.04	0.10	0.23	0.39	0.32	0.30
	0.12	0.04	0.10	0.23	0.39	0.32	0.30
	0.14	0.04	0.09	0.18	0.22	0.20	0.24
	0.14	0.04	0.09	0.17	0.22	0.20	0.24
	0.14	0.04	0.09	0.17	0.22	0.20	0.23
Ball and Stick	0.45	0.45	0.53	0.56	0.50	0.51	0.51
	0.45	0.45	0.54	0.56	0.51	0.51	0.51
	0.47	0.38	0.38	0.39	0.26	0.32	0.29
	0.47	0.32	0.46	0.39	0.26	0.32	0.42
	0.47	0.47	0.46	0.38	0.27	0.32	0.42

Interfaces

Shape	1	2	3	4	5	6	7
Armchair	0.06	0.02	0.08	0.15	0.18	0.15	0.09 +z
	0.06	0.02	0.08	0.15	0.18	0.15	0.10 - z
	0.03	0.05	0.04	0.02	0.01	0.02	0.04 +y
	0.03	0.05	0.05	0.02	0.01	0.02	0.04 - y
	0.03	0.05	0.05	0.02	0.01	0.04	0.03 +x
	0.03	0.05	0.05	0.02	0.01	0.04	0.02 - x
Truncated Icosahedron	0.06	0.00	0.00	0.05	0.10	0.09	0.11
	0.05	0.00	0.00	0.05	0.08	0.07	0.10
	0.06	0.00	0.00	0.08	0.19	0.15	0.11
	0.07	0.00	0.00	0.08	0.20	0.16	0.12
	0.06	0.00	0.00	0.06	0.13	0.11	0.06
Triakis -tetrahedron	0.12	0.05	0.04	0.17	0.27	0.24	0.18
	0.12	0.05	0.04	0.17	0.27	0.27	0.15
	0.06	0.03	0.02	0.07	0.09	0.06	0.09
	0.06	0.03	0.02	0.07	0.09	0.06	0.09
	0.06	0.03	0.02	0.07	0.09	0.12	0.05
Truncated Tetrahedron	0.02	0.00	0.00	0.05	0.16	0.15	0.22
	0.42	0.13	0.18	0.64	0.55	0.38	0.40
	0.08	0.01	0.02	0.08	0.10	0.09	0.18
	0.25	0.08	0.11	0.30	0.21	0.17	0.23
	0.18	0.04	0.05	0.23	0.27	0.20	0.23
	0.15	0.03	0.05	0.20	0.28	0.24	0.24
Truncated Octahedron	0.00	0.00	0.00	0.03	0.12	0.12	0.17
	0.00	0.00	0.00	0.03	0.12	0.12	0.17
	0.03	0.00	0.00	0.05	0.11	0.10	0.14
	0.04	0.00	0.00	0.05	0.11	0.10	0.14
	0.03	0.00	0.00	0.05	0.11	0.10	0.14
Truncated Dodecahedron	0.06	0.00	0.00	0.07	0.27	0.24	0.18
	0.06	0.00	0.00	0.07	0.27	0.24	0.18
	0.05	0.00	0.00	0.04	0.12	0.12	0.12
	0.05	0.00	0.00	0.04	0.13	0.12	0.12
	0.06	0.00	0.00	0.05	0.13	0.11	0.12
Deltoidal Icosa - tetrahedron	0.04	0.00	0.00	0.07	0.19	0.18	0.20
	0.06	0.00	0.00	0.07	0.19	0.18	0.19
	0.06	0.00	0.00	0.06	0.21	0.19	0.17
	0.06	0.00	0.00	0.08	0.15	0.19	0.17
	0.06	0.00	0.00	0.07	0.21	0.20	0.17

An example of a portion of an assembled scaffold for human vertebral body is presented

in Figure 71.
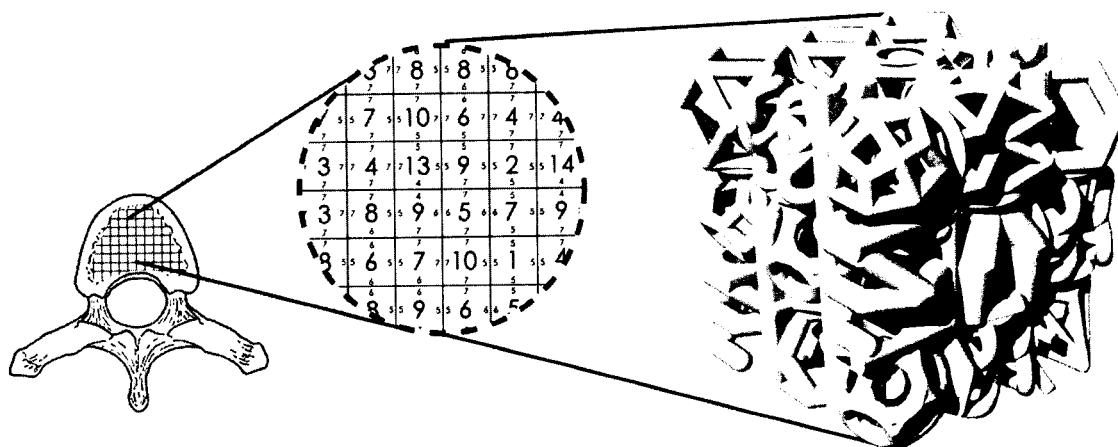
Figure 71. Assembly of scaffold using density map. Primitive unit blocks are assigned based on the density map and Figure 6. Interfaces are assigned based on Table 2 and Figure 5.

5.3.6 Conclusions

We have presented a building block library based on the assembly of regularly oriented tissue primitives in an attempt to improve the techniques of scaffold design. Though many of the factors and appropriate cues of what makes a good scaffold have yet to be elucidated, we believe that this technique can be effective even in the absence of this knowledge because its derivation utilizes the architecture of bone. An exact bone scaffold would be ideal, but the means to manufacture a biopolymer on the scale of bone for a substantial scaffold, is not currently attainable. Therefore, we have introduced a library in which the apparent properties, not tissue properties, may be matched in a patient/site specific manner, yet the architecture maintains much of the same tissue level shape (porosity, permeability) that are essential for its biological functionality. The shortcomings of this technique are that a single scalar relationship (density, modulus) is used as the scaffold assembly mapping, yet it is known that architecture as well as the

density is necessary for a strength description. Moreover, the modulus value was obtained only in one loading direction, and a more thorough analysis would involve finding all the elasticity constants, and, therefore, defining a very specific map. Nevertheless, even in this case, there would be the possibility of multiple architectural configurations that have similar elastic properties [107].

Of the designed unit cubes, the majority had porosities native to bone and were well within the window suitable for scaffold design. The S/V of each shape existed over a relatively small range (0.61 – 1.87). The Archway had the second largest normalized modulus value, but with a poor S/V, denoting that it is most useful as a support element, while the Arm Chair had the largest S/V, suitable for fluid perfusion, yet its l/d value of 11.50 could signify buckling, except for the strongest materials. Most l/d values were low, and safely under the buckling threshold. The Truncated Tetrahedron exhibited two distinct ratios within the same unit cube, signaling that bending or partial buckling is a possible failure mode. We did find that many of the observed moduli values were in the same neighborhood, which introduced some error in the method of ranking the shapes in absolute terms. The modulus values corresponded with the volume fraction only weakly. The Arm Chair is a notable example which has the smallest material volume range (and material volume mean value), yet the third largest mean modulus value. At the other extreme, the Folding Chair and Cuboctahedron have large volume fractions, but behave poorly mechanically. Intuitively, the Ball and Stick fares well mechanically and has 65 % material volume.

The need for regularizing the domain into cubic volumes is necessary from an assembly and property matching perspective. A classical analog is splitting up a complex

mechanics problem into finite elements that can be solved individually. Obviously, this engineered regularization does not occur naturally in bone. For example, a common question when identifying primitives was: "Where does one border end and the next begin?" Additionally, many of the unit cubes did not exist in the three orthogonal planes, yet we plan to assemble them as such. These types of problems are not easily avoided with an architecture as complex as bone. Nevertheless, since scaffolds are intended as temporary structures, nature may take care of this on its own.

Selecting the best interface for each face of a given unit cube is a problem that has multiple solutions. Load transfer from one primitive to the next requires that enough volume is present between the contact area of the unit cube and interior portion of the interface and that there is enough common surface area between interfaces, so that localized stress concentrations do not occur. Our currently methodology of selecting a tolerance to apply to Table 9, in order to decide which interfaces may be placed on a unit cube, is the factor responsible for allowing multiple solutions. Auxiliary methodologies, such as a mathematical optimization which maximizes the weighted average of the "unit cube – interface" and "interface – interface" contact values (Table 9, Figure 69) is plausible, and could induce a unique solution for any modulus map; Though negative consequences to any optimization objective function do exist, i.e. a maximum average connection area does not imply anything about individual unit cubes; Moreover, one stress concentration may be sufficient to trigger the scaffold's failure.

Lastly, other alternatives such as interface methods were discussed and an example provided (Figure 66). The main shortcoming is the computational order of such optimization strategies. Because an entire continuum is used, the order is of the

dimension cubed, which is not yet conducive to large bone samples. Moreover, it is generally not clear what internal loading vectors are present on the face of a unit cube at this time.

5.4 Design Of An Injectable Composite Bone Cement With Engineered Micro-Structure And Varied Permeability[*]

5.4.1 Introduction

Many cancers (for example renal cell carcinomas, about 30% of breast cancers, lung tumors, etc.) are prone to metastasize to the spine leading to progressive neurological dysfunction and, almost invariably, a reduced life-span. Primary spinal tumors (namely chondrosarcoma, chordoma), although far fewer in number, pose additional treatment dilemmas due to the relative paucity of effective adjuvant therapies and the extremely high propensity for local recurrence [261]. Complications such as untreated neoplastic spinal cord compression results in progressive paralysis, sensory loss, sphincter dysfunction [262] and lytic vertebral body collapse which can cause severe axial back pain [263, 264]. Effective therapy for spinal tumors must improve the patient's quality of life and provide durable local control of the disease.

Over the last several decades, a number of developments have improved the treatment of patients with spinal tumors [264]. First, the widespread use of magnetic resonance imaging (MRI) has provided earlier and more accurate diagnoses [265]. Second, spinal instrumentation has allowed surgeons to perform safe, effective

---

[*] Adopted from Wettergreen MA, Abbe RA, Sun K, Hess KR, Rhines LR, Liebschner MAK, "Modulation of Drug Release Kinetics of Doxorubicin from Composite Polymethyl Methacrylate Bone Cement" In Preparation.

reconstructions and stabilization of the spine after tumor resection [266, 267]. Third, improved surgical approaches have permitted more aggressive tumor removal [268]. Finally, advances in radiation and chemotherapy have allowed for better control of the growth of some tumors [269, 270]. Despite these improvements, the local control of threatening spinal lesions has remained a vexing problem. The complex structure of the spine (including the spinal cord, nerves, and, in the cervical spine, vertebral arteries coursing through it) and critical paraspinal anatomy (aorta, vena cava, esophagus) make complete surgical resection of any spinal tumor extremely difficult [271, 272]. Even when the visible disease is removed, the likelihood of microscopic tumors remaining is high, creating an immediate source for local recurrence. Chemotherapy, the current standard post-operative treatment following tumor resection may play a role in delaying recurrence; however, the local concentrations of drug agents in the spine following systemic administration may not be sufficiently high to control the tumor, particularly after the local blood supply has been compromised by prior surgery or radiation [273, 274]. Dose limiting effects such as immune suppression and destruction of the oral mucosa prevent the usage of high local concentrations needed to effectively treat the area [275, 276].

Consequently, drug treatment effectiveness for chemotherapy lies in targeted delivery. While the ideal drug profile for secondary tumor prevention in cancer treatment is unknown, a burst release to quickly treat any remaining cancerous cells followed by a sustained release to properly remove any long-term arising tumors is believed to be most effective [277]. This local delivery approach allows for much greater tissue drug concentrations than can be achieved with systemic administration due to proximity of the

drug-laced implant to the tumor site, decreased systemic toxicity and the ability to bypass limitations of the local vascular supply or the blood tissue barrier. Local delivery of chemotherapy directly at the site of disease has proven to be a successful strategy in organ systems other than the spine [278, 279]; in the brain, a biodegradable polyanhydride polymer impregnated with Carmustine (BCNU) chemotherapy has been shown in a randomized, double-blind, placebo-controlled trial to improve the survival of patients with malignant gliomas [280]. Application of composites to load bearing regions, like the spine, has been attempted with the use of bioactive bone ceramics such as tri-calcium phosphates and hydroxyl apatite loaded with peptides and other molecules driven to stimulate new bone formation [281]. Thomson et al. addressed the need for an implant which sustained mechanical integrity while balancing cell adhesion and invasion while the primary study illustrated a dependency of cell adhesion preference of apatite over Calcium Phosphate laden implants [282]. Additional studies in bone research have yielded scaffolds which contained a hydroxyapatite carrier loaded with peptides which demonstrated bone formation [283, 284].

The goal of this study was to investigate the release kinetics of a drug from an injectable bone cement used clinically. We employed (poly)methyl methacrylate (PMMA), an acrylic bone cement that is biostable with good mechanical properties [285]. Preliminary drug release studies utilizing PMMA have proven that although the material possessed superior mechanical properties, it showed poor release due to its low diffusion capabilities. We utilized an *in vitro* model to assess if release was enhanced by increasing the surface area of the composite through the incorporation of a porogen phase. We integrated doxorubicin (i.e. the trade name was Adriamycin) an anthracycline antibiotic

that binds to nucleic acid synthesis and damages DNA by intercalation of the anthracycline portion, metal ion chelation, or by generation of free radicals [286]. Doxorubicin is an effective and approved chemotherapeutic agent but could cause tissue necrosis if high enough drug concentrations are found outside of the vascular injection site. PMMA loaded with doxorubicin has been shown to be effective at the site in bones but little is known about its benefit when metastasized tumors migrated to the spinal cord [134]. Rosa et al. [287] studied cylinders of acrylic cement containing Methotrexate, Cisplatin or doxorubicin in-vitro on MCF7-7 human breast cancer cells. Each drug had a different effect on cell viability demonstrating that this method may provide local treatment to bone metastases. The aim of this study was to demonstrate the release of doxorubicin over the time course of a 28 day release cycle and illustrate that the release is modulated by the surface area of the composite.

5.4.2 Methods

Preparation of drug-laden composite bone cements

Sodium Chloride (NaCl) particles were sieved to separate particles of side length 500-700 micrometers. The NaCl particles were when mixed with PMMA utilized in proportions which would result in three volumetric porosities of 20, 33 and 47 percent. The final density of non-porous PMMA was calculated to determine the amount of NaCl required to achieve these porosities. Powdered Surgical Simplex® (Stryker Howmedica, NJ) was mixed with salt porogens on a shaker table until a fully heterogeneous mixture was obtained. Powdered 2.5 (wt%) doxorubicin was mixed with the PMMA and NaCl porogens on the shaker until equally distributed. Liquid monomer was added to this mixture in a ratio of 1:2 monomer to powder. PMMA was mixed to uniformity with a

doughing time of four minutes or less as measured by when the cement was fully mixed and did not stick to the bottom of the mixing plate. Wet cement was packed into HPLC (High Performance Liquid Chromatography) tubes and allowed to harden for a minimum of 30 minutes before removing them from the glass tubes. Small hemispheres (3mm diameter and 3mm height) were also created for preliminary studies to investigate the effects (if any) of the drug release methodology upon the embedding into PMMA prior to drug release.

Cylindrical samples were weighed using an analytical balance and diameter and length measured with a digital caliper. Subsequently, the samples were placed in 1.0 ml of PBS at 37° C. For the duration of the experiment samples were stored on a rocking plate in a humidified dark room at physiological temperature. An experimental model of 5 testing groups was established with each testing group containing a minimum of 4 cements. The sample groups consisted of two controls, each at 0% porosity: a positive control (PMMA + doxorubicin), a negative control (PMMA − doxorubicin), as well as 20, 33 and 47 percent porosity by volume experimental samples containing doxorubicin.

Measurement of release kinetics

Release kinetics of the composite cements were measured temporally via absorbance for up to 28 days using a spectrophotometer at 530 nm. The standard curve for this drug had an r = 0.9985. Following each reading, one ml of fresh PBS at 37° C was added and the tubes were transported back to the humidified 37° C incubator, where they were gently rocked. Concentrations of doxorubicin were summed over time and all tabulations took into account the individual weights of each PMMA scaffold. In a

separate preliminary study, HPLC was used to verify the measurement of the release using spectrophotometer (Figure 72). Two different stock solutions in PBS were prepared on three separate days.

Doxorubicin standard from HPLC and Spectrophotemeter (ugs/mL)

Figure 72. Standard curve relating High Pressure Liquid Chromatography (HPLC) to spectrophotometer readings of doxorubicin concentrations. The two readings correlate well demonstrating visible spectrophotometry as a simple yet effective manner to calculate the release of doxorubicin.

These stocks were measured via spectrophotometry and one piece at each concentration was analyzed with HPLC (one stock using three measurements as is completed in HPLC analysis).

Bioactivity of released doxorubicin

To determine the bioactivity and cytopathic effect of the doxorubicin released from the PMMA, tissue culture assays with drug laden hemispheres were used. We conferred that this drug had an effect on U87 MG human multiforme glioma cells via three modes. First, we used just the drug alone, second we used PMMA alone and the third we used PMMA + 0.5% doxorubicin. Prior, we performed dose-dependent curves to assess cytopathic effects to the U87 MG cells. Three independent experiments using the trypan blue exclusion method were carried out and the cells were counted on day 5 in 24 well plates.

The established U87 MG (multiforme glioblastoma) cell-line was obtained from the American Type Tissue Culture collection (ATCC). Cells were grown in enriched DMEM medium that contained 10% fetal calf serum and antibiotics at 37°C in a humidified 5% CO_2 incubator. The cells were passaged for continuous growth when they reached approximately 80% confluence, harvested via trypsin treatment, and replated for further experiments. No passages greater than 25 were used from the original vial.

Microcomputed Tomography

Following the drug release portion of the experiment, samples were removed from the tubes, weighed and dried. Samples were scanned using micro-computed tomography with a methodology described previously [116]. Samples were evaluated for porosity, surface to volume ratio, degree of anisotropy and remaining salt (if any).

Permeability Testing

Composites were non-destructively tested for their axial hydraulic permeability using a custom built hydraulic pressure driven permeameter similar to that described in [9, 147, 148], with water forced through the scaffold collected in a reservoir. Calculation of the permeability is calculated via Darcy's Law of fluid flow through porous media [138, 148], (see 101). Each scaffold was run a minimum of n=3 times to account for flow deviations dur to architectural variability.

Mechanical Testing

Drug laden composites were compressively tested to failure using an MTS with a crosshead speed of 1.0 mm/min. Samples which with non-uniform topology were not included in this analysis due to expected measurement errors. Load-displacement curves were recorded and converted to stress-strain curves using the known initial cross-

sectional area and height/length of the specimens. Compressive modulus was calculated as the slope of the linear portion of the stress-strain curve and ultimate stress was derived from the peak of the stress-strain curve.

Statistical Analysis

Analysis was accomplished by merging the data from all experiments into a single dataset. With four volume fractions of NaCl and 13 time points (1 h to 28 d), there are 52 design points. The mean number of replicate observations at each design point was 23 with range from 20 to 27 for fractions 0, 20 and 33, while 9 replicates were used at each time point for fraction 47. There were a total of 965 observation points. Initial data plots showed that means increased rapidly with time in the first few days but after about day 3, the means increased much more slowly (but still roughly linear). Thus we constructed a linear model allowing the time effect to change slope at 3 days (i.e., we used a bent-line or hockey-stick linear regression model). The NaCl volume fraction effect was not linear and thus this variable was treated as a factor variable (comparing each non-zero level to zero). In plotting the data, we chose to use a robust running lines smoother called LOWESS (locally weighted scatterplot smoother).
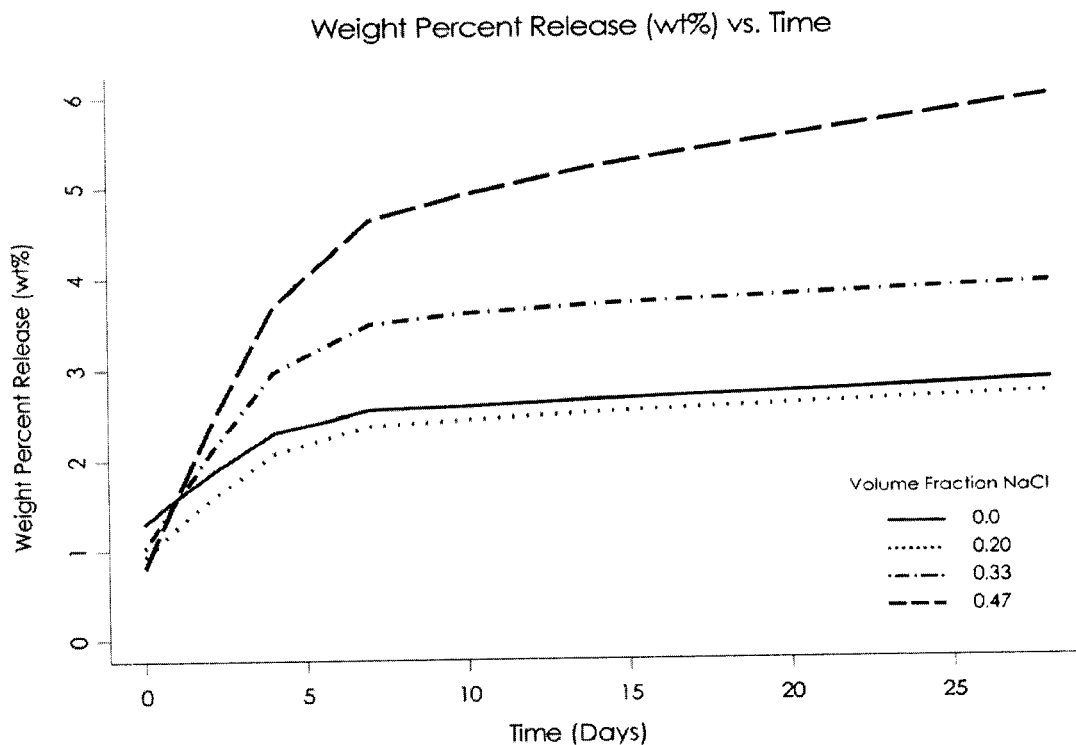
Figure 73. Cumulative weight percent release of doxorubicin from composite bone cements over a 28 day release period. A burst release is viewed up to 4 days, following which the release continues with a constant slope.

5. 4.3 Results

Release of doxorubicin from composite bone cements was increased with increasing porosity and surface area (Figure 73). Greater than 50% of the total drug release was discharged within the first 4 days of the study, with the remainder of the drug being liberated cumulatively throughout the 28 day study. We fit a two phase model with a corresponding burst release followed by a linear release which was sustained through

Figure 74. Scatter plot of the cumulative weight percent release of doxorubicin from composite bone cements over a 28 day release period. The large range in the data illustrates the variability as a result of the mixing of randomly packed particles to create surface area.

(wt%) vs. Time, 20% Porosity

(wt%) vs. Time, 47% Porosity

(wt%) vs. Time, 0% Porosity

(wt%) vs. Time, 33% Porosity
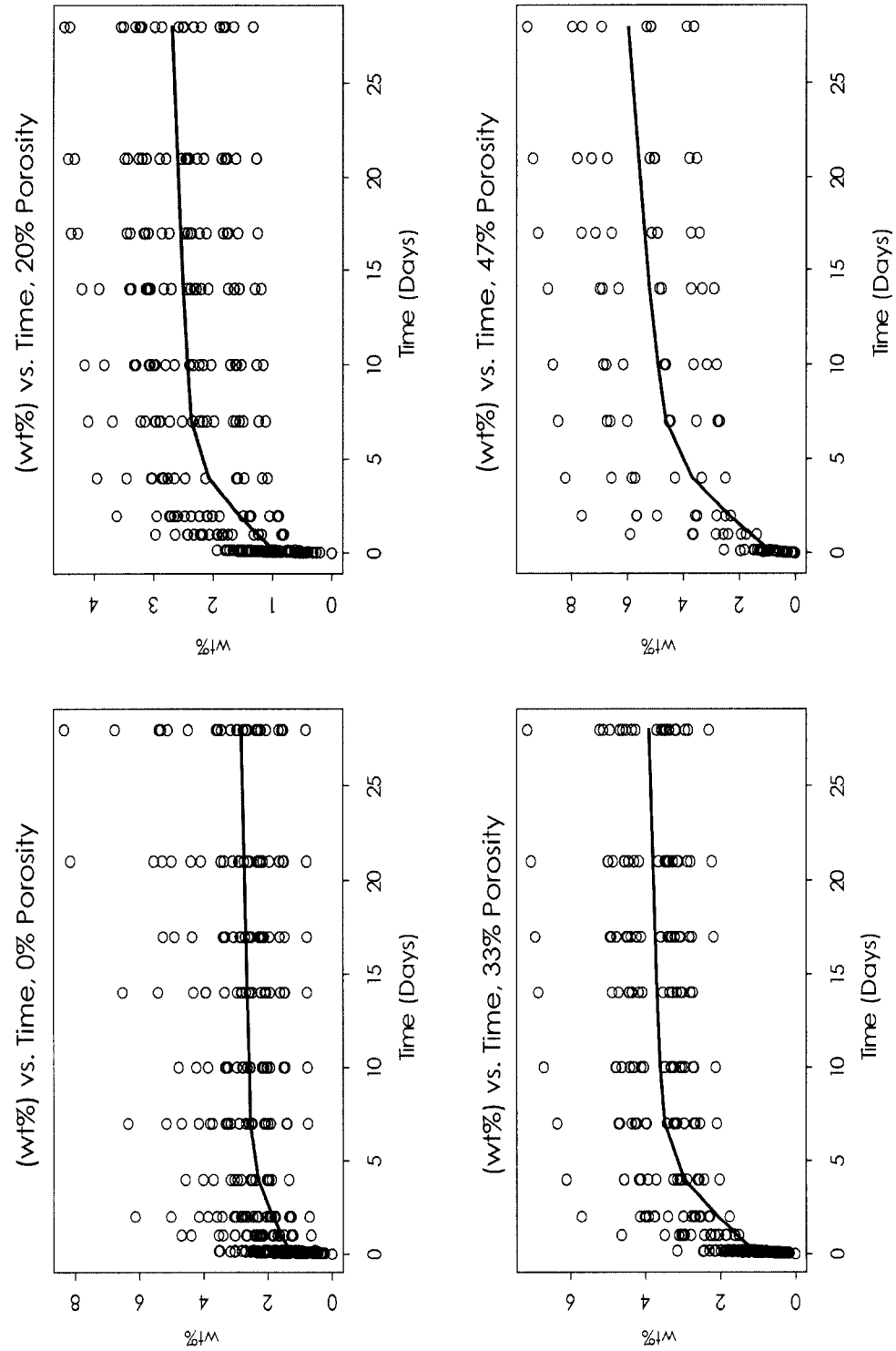
the end of the study. Drug release was significantly high ($p<0.001$) when compared to the positive control in the 33% and 47% porous samples but not with the 20% samples. Prior to day 3, the time slope was 0.78 for weight percent and 0.11 after day 3. The mean weight release difference between 20% and 0% salt was −0.38 (se = 0.102), the mean difference between 33% and 0% was 0.42 (se=0.112) and the mean difference between 47% and 0% was 1.22 (se=0.135). For the concentration, the time slope was 54.7 µgs per day before day 3 and 7.7 units per day after day 3; the mean difference between 20% and 0% salt was 0 (se = 6.7), the mean difference between 33% and 0% was 51 (se=7.4) and the mean difference between 47% and 0% was 112 (se=8.9) (Figure 74).

Table 10. Morphological measurement of one sample of each group of composite bone cements taken from micro-computed tomography scans.

	Control (+Dox)	Control (-Dox)	20% (+Dox)	33% (+Dox)	47% (+Dox)
BV/TV	0.99	0.98	0.91	0.72	0.47
S/V ratio	1.00	1.40	2.08	4.99	11.18
Degree of Anisotropy	2.14	1.69	1.34	1.06	1.13
Intended Porosity	0	0	20	33	47
µCT Measured Porosity	0.61	1.48	7.89	27.15	51.35

Mathematical morphological measurements of the samples yielded information pertaining to the final porosity and surface area of the samples (Table 10). Visual inspection of the micro-computed tomography scans (Figure 75) revealed that salt remained even in the 20% porous sample at the end of the 28 day period. Morphological calculations demonstrated that the intended porosities of 0.0 (+Dox), 0.0 (-Dox), 20%, 33% and 47% corresponded to actual porosities of 0.6%, 1.5%, 7.89%, 27.15% and 51.35% respectively. Non-porous PMMA samples with no salt added exhibited air

0 %

20 %   33 %   47 %

1mm
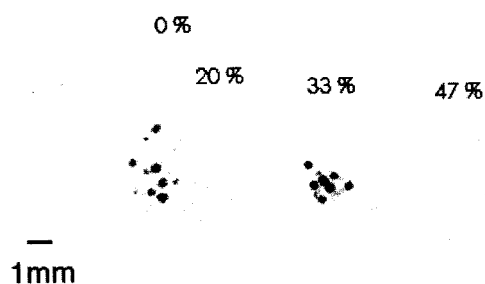
Figure 75. Microcomputed tomography picture of the cross-section of the bone cements. The fully solid sample on the left (0% porosity) can be seen to contain some porosity as a function of surface topology. The central portions of the 33% and 47% porous samples can be seen to contain entrapped NaCl particles (black) which lower the intended porosity.

bubbles which raised the porosity from the intended value of 0.0. The 20% porosity samples included a large amount of unleached salt in the interior of the scaffold, further demonstrating that PMMA is impermeable to water in gently rocked conditions. Surface to volume ratio of the 20 percent samples was 2.0 compared to the non-porous samples which had a value of 1.4. Surface to volume ratios of the 33% and 47% samples were 10.0 and 14.0, respectively.

Doxorubicin maintained bioactivity and was cytopathic following encapsulation in PMMA. Doxorubicin alone at 4.31 μM left only 14.2 (SD = 2.96%) cells remaining in the wells, while at 21.6 μM, only 9.31 (SD = 0.377%) were resident. PMMA hemispheres without drug had no effect on the cell numbers compared to controls. The weight of the

Bioactivity of Doxorubicin

Figure 76. Doxorubicin maintained bioactivity and was cytopathic following encapsulation in PMMA hemispheres. The study was completed in triplicate in twenty-four well plates.

PMMA hemispheres ranged from 24.0 to 28.4 mgs in the 3 experiments. PMMA

hemispheres laden with doxorubicin demonstrated a mean of 17.6 (SD = 4.22%) remained.

Permeability of the drug laden composites was measured via a pressure driven hydraulic permeameter. The permeability of the samples ranged from 1.7 E-12 ±2.2E-12 to 9.2 E-12 ±1.1 E-11. The 47% samples were three times more porous than the other three porosity samples and statistics indicate that the 47% porous sample was statistically distinct from the other three porosities. No statistical difference could be found between the permeabilities of the remaining three samples. The architectural variability in the 47% sample resulted in extremely high standard deviation and also affected the structural integrity of the samples. During the removal of several samples from the permeameter they were rendered unable to be used for mechanical testing purposes.

Mechanical properties of the drug laden composites were evaluated in uni-axial compression. Sample numbers for the four porosities (0, 20, 33, 47) were 18, 20, 11, and 8, respectively. The compressive modulus of the doxorubicin laden PMMA composites ranged from 177 ± 276 MPA to 695 ± 231 MPa. Modulus values varied the most in the highest porosity sample and were near similar for the remaining three porosity samples.

5.4.4 Discussion

In this study we developed a drug release vehicle combining a clinically available acrylic cement and a widely used chemotherapeutic drug for the application of secondary spinal tumor control and prevention. PMMA is a standard injectable bone cement with excellent compressive properties that has been used for the treatment of the spine

Permeability of Drug Laden Composites
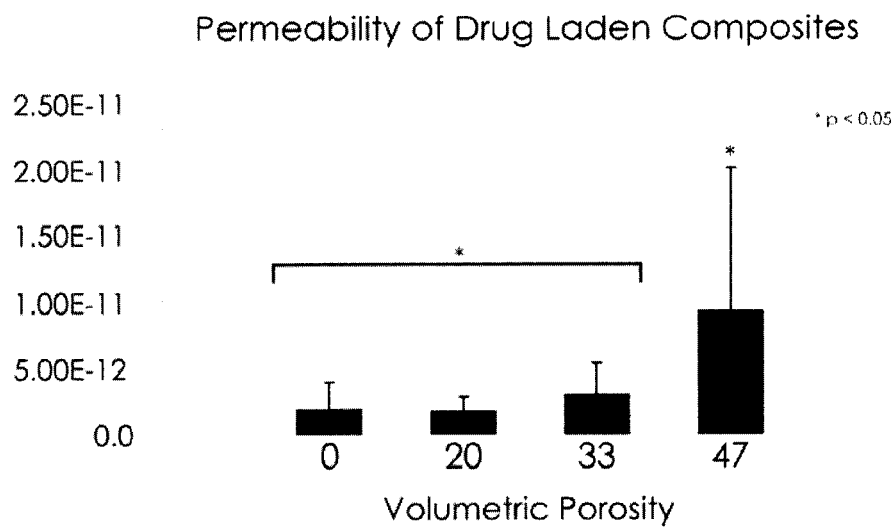
Figure 77. Axial hydraulic permeability of porous doxorubicin laden PMMA composites.

Compressive Modulus of Drug Laden Composites
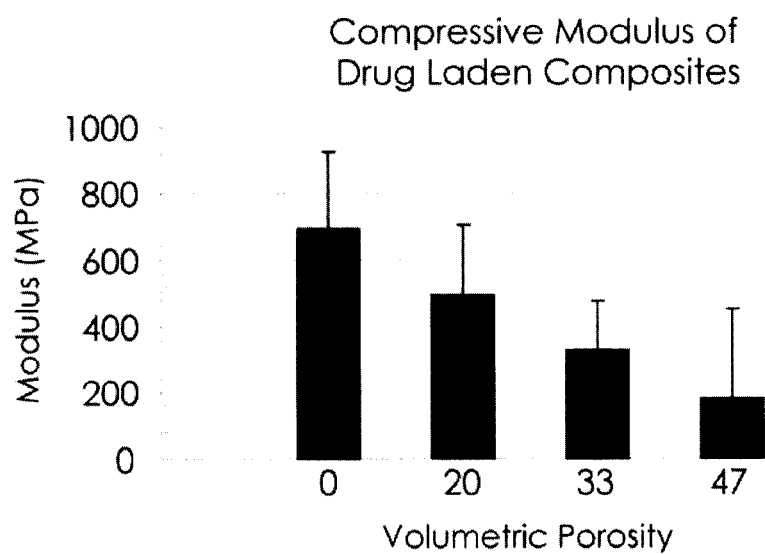
Figure 78. Compressive Modulus of composite drug laden composites.

following tumor-related spinal procedures [285]. Doxorubicin is an effective and approved chemotherapeutic agent shown to be successful in the treatment of spinal tumors [134]. To obtain a higher release from the notoriously poor drug vehicle (PMMA), we incorporated a solid phase NaCl porogen. The subsequent leaching of the porogen created a porosity in the solid based upon a calculated volume fraction. Three experimental groups were created: 20, 33 and 47 percent porosities along with a control group.

Drug-laden composite bone cements were created with and without the incorporation of NaCl. Scaffolds were produced in the dimensions as designed with variability in the surface topology visible along the length of each scaffold. The hardening time of the cements was negatively affected by the amount of NaCl incorporated into the solids, reducing the doughing time; with 47%, the mixing was more difficult. The experiments completed with the hemispheres concerned with the swelling of PMMA without salts in the presence of PBS yielded no dimensional or weight change of the PMMA hemispheres on day 2 (n=3 experiments) as a result of the incubation in PBS.

Morphological measurements from the micro-computed tomography scans demonstrated a high degree of error in the intended porosities versus the final obtained volume fractions with the closest intended porosities observed in the controls and the 47% sample groups. This effect is consistent with the results presented by Fisher et al. in a study elucidating the optimal porosity result in the mixing of a porogen and biomaterial phase [113]. We account for the reduction in actual porosity of the cement as a result of the mixing proportions of the cement as well as the visible incorporated NaCl remaining

in the PMMA following a leaching step seen in Figure 75. In a study by Fisher it was been shown that porosities above 80% are required for full interconnectivity, corroborating the permeability results of the NaCl in only the 47% porosity samples [113]. The lower porosity samples were chosen to address the reduction of mechanical properties due to the introduction of void space. Given the difficulty in mixing the 47% porous samples, we set this as the upper limit of the volume fraction of NaCl which could be incorporated and still maintain mechanical integrity of the resulting solid with elastic modulus values within the hundreds of Mega Pascals in value.

The release kinetics of the drug loaded composite followed previous drug release studies demonstrating a burst release followed by a steady linear release. Statistical results showed a two-tailed approach was valid in modeling of drug release, corresponding to a two-phase release profile. Aberrant results in the 20% porous sample can be explained by viewing Figure 74. Looking at the range of wt% for the 20% and 0% we can see that they are mostly similar throughout the 28 day release except for specific outliers present in the non-porous sample. We hypothesize that this is due to the surface to volume ratio of the solids; the surface to volume ratio of the 20% sample was very close to that of the non-porous solid, 2.0 to 1.4 respectively. Since the statistical results demonstrated that the important component of the entire release vehicle is due to the burst release and the 20% sample has a lower surface area than the solid composite on the exterior due to NaCl occupying space, there is a reduced drug release over the time course, even though the final surface to volume ratio of the 20% sample is higher. An additional proposition is that the surface roughness of the non-porous sample is higher

because of the lack of NaCl. Unfortunately, micro-computed tomography images do not have the resolution to capture this roughness.

Previous studies have demonstrated that doxorubicin release from PMMA is primarily via surface elution [274]. This is evident from our results as the weight percent variations are modest which proves that the increase in surface area modulates the drug release. While we cannot say whether diffusion is also a dominant mechanism, it is implied because we still see release, albeit low, in the 0 and 20 percent porous samples up to day 28. The surface area to volume ratio of the 33% and 47% porosities were significantly higher than the 20% and non-porous samples for the entire time course of the experiment and demonstrated significant release over the other two groups. The release profile of the 33 percent sample continues at a slope similar to the 0 and 20 percent sample, a trend that we attribute to the increased surface area but not permeability as the statistics for the permeability results indicate that the sample itself is impermeable. The slope of the release profile for the 47 percent sample increases sharply even following burst release, indicating that it is the increased surface area as well as the permeability of the sample that is driving the diffusion of the drug from the porous solid.

Numerous factors are responsible for the amount of doxorubicin release from the composite cements. Porosity, available surface area and permeability may play the largest role in modulating the release kinetics but factors such as pH, surrounding liquid, temperature and initial doxorubicin concentration are all variables that may be modified to enact a higher release. The release of the doxorubicin from the composite cements was consistent with other studies that used doxorubicin in similar conditions. The study by Rosa et al. mixed around 7 weight percent doxorubicin powder with acrylic cement and

demonstrated that cell survival with this concentration was 14.2 ± 1.9% 15 days following the composite creation, indicating that our composites would possibly also have a cell toxic effect [287]. Modulation of the release of the doxorubicin was attempted with a lower pH and glucose instead of PBS (data not shown) which resulted in a higher release. However, since the pH was not physiological, only preliminary studies were done. It is possible that PMMA even hinders drug release. For example with SDDS, sometimes as much as 90% of drug was retained in PMMA [288, 289]. Yu et al. [290] reported that PMMA shrank during setting that left a defect in the polymeric cement with marginal mechanical support. However, PMMA (from Stryker) is used in regular clinical practice today. Therefore, we believe that it is an adequate drug delivery vehicle when used in a system with higher surface area.

For the statistical analyses of release p-values smaller than 0.001 were taken as being significant. It was important that the inferences were made between the groups / conditions. Inferences were made about experimental conditions using data from merged datasets from all the tubes. The term control group meant that it was a collection of repeated experiments. It is important that adding salt alone had only a minuscule effect by day 28. Specifically, 6 controls (i.e. 2.5% doxorubicin minus salt), 4 with 33% salt, and 3 with 47% salt experiments were done. One of the 47% pieces chipped while it was made and was not used. Other than swelling or loss in weight, standard errors were used in his statistical program. For the rest, standard deviations were used.

An important design demand of this drug release composite is the maintenance of mechanical integrity during and following the sustained drug release. The modulus reduction is a function of the increased incorporation of the porogen phase as can be seen

from the mechanical testing results. This modulus decrease followed the power law reduction profile of that of a porous solid, with the lowest modulus of 177 MPa. In a previous study, the effect on the modulus due to the incorporation of the doxorubicin has been previously shown to be minimal [291]. However, the modulus values for the 0 percent composite cement was lower than the stated modulus value of 1150 MPa [292]. Although the value of 177 MPa for the highest porosity is lower than the amount of support that is required for a vertebral body to support the body's weight [43], this sample showed the most attractive release to be considered for therapeutic purposes: the surface to volume ratio was twice that of the next lowest porosity and the release profile was ultimately twice that of the next lowest porosity.

5.4.5 Conclusion

In this study, we detailed the preliminary steps towards the creation of a tailorable drug release composite for load bearing applications. We demonstrated the ability to modulate the release of a chemotherapeutic drug via the incorporation of porogens into a clinically approved acrylic cement. The results of these experiments suggest that systemic toxicity may be partially ameliorated if this mode of drug release is used. Although the release was low as a function of the poor release vehicle, when we view it in terms of the magnitude of the tumor size versus the overall weight of a body, it may be important. The advantages of developing a tailorable drug composite would allow for the treatment of spinal tumors following resection and would hopefully reduce the occurrence of secondary tumors.

Since the underlying design demands are both (1) high strength and (2) high sustained drug release rate, it may be useful to utilize a particle in the bone cement which

contains a higher surface area than is created by a currently available, cube-shaped, NaCl porogen. Additionally, the use of porogens as a method to create porosity in the implant has the advantage of increased mechanical stability at the beginning of the life of the implant, when the surrounding tissue requires the implant to take the load. As the porogens degrade, the surrounding tissue is forced to take the load while also being provided with a region for cell ingrowth. Future directions will focus on the sustained delivery of the specific peptide or drug to the localized area with varied approved materials.

Chapter 6: Conclusions and Future Work

The field of bioengineering was borne from practical clinical solutions, thus biocompatibility and host/scaffold integration has always been a larger research issue than addressing the proper architecture for a porous conduit. Success of a tissue engineered scaffold *is* primarily dependent upon the biocompatibility; the secondary concern is architecture and geometric fine tuning. Additionally, this wealth of research has resulted in scaffolds which, independent of focus shed on architecture, have shown great success in the repair of tissue. In fact, the field has all but glossed over mechanical aspects as a valid contributor to its paradigm and to focus on biological tissue integration. Unfortunately, this is because few of these studies have been conducted in load bearing models. In the case of mechanically active sites, such as the spine, biological tissue integration is *dependent* upon the mechanical parameters of the system. Furthermore, as we showed with the mechanical usage window (Figure 5), portions of bone adaptation can only be reached via mechanical stimulation; neither drugs nor growth factors can stimulate the growth of that much bone. The role of mechano-biology and architecture must be addressed in the design of tissue engineered scaffolds to facilitate positive integration between native bone and the replacement material.

In Chapter 3, the contribution of material arrangement on the mechanical properties of regular, symmetric porous architectures was evaluated. Relationships drawn using geometric characterization demonstrated that for architectures with high beam numbers, surface area exhibited a parabolic relationship with a maxima near 70% porosity (Figure 19). Shape change between porosities was shown to be controlled more by surface area contraction/expansion than volumetric arrangement of the architectures

(Figure 20). The ratio of the volume exterior to the polyhedra vs. the interior of the polyhedra (OV/IV) changed with a power law relationship with respect to porosity. Using finite element analysis to compare the structural modulus of the architectures (similar to [16, 160]) illustrated that density is the strongest factor in controlling modulus, though we showed that optimal material arrangement can result in similar modulus values even with volumetric discrepancies of up to 10%. Rapid prototyping of the architectures and subsequent mechanical testing validated the finite element modeling and showed that the finite element method under predicted the modulus for all architectures and porosities. Although density again proved to be the strongest determinant of strength (expected), morphological parameters played a larger role in the plastic deformation and post yield behavior of an architecture when subjected to large deformations (unexpected). Speaking in terms of mechanical stability for design purposes: for small deformations and/or high loads, simple, rigid shapes (such as the Hexahedron) are desired, though catastrophic failure occurs at fracture point and load bearing ability drops immediately to zero. Architectures with additional architectural complexity (such as the Rhombitruncated Cuboctahedron) are desired for situations experiencing large deformations ($\varepsilon > 0.05$) providing mechanical stability post fracture due to the complex beam arrangements. Architectures with geometric complexity become more ductile with increased porosity, in contrast, simple architectures like the Hexahedron store less energy at higher porosities (Figure 30).

In Chapter 4 the contribution of architecture on the fluid flow properties of a porous solid were evaluated. This was the inverse of the aim of Chapter 3 but with a shift in focus to promoting fluid transfer to facilitate tissue ingrowth rather than aiming for

mechanical reinforcement. We demonstrated that large numbers of porogens with novel architecture and surface area can be repeatably built using a phase change rapid prototyping process. These architectures can be used in a porogen process to explore the fluid flow properties of a random solid. We extend the creation of the novel architectures to soft lithography creating a process which transfers the architectures into a biomaterial. The applications for this technique are not limited to porogens as the architectures could be used for drug delivery purposes as microparticles in a solid matrix. Porous scaffolds made from the rapid prototyped porogens were evaluated for their permeability and it was shown that the novel architectures had a higher permeability than the standard NaCl porogen at identical volume fractions. Although the measurable parameters indicate that the permeability difference is as a result of the surface area difference between the particles of same volume, a conclusion that is supported by work completed by Scheidegger [174]. Utilizing geometric models to calculate fluid properties, we showed that for randomly porous scaffolds such as evaluated in this study, Phenomenological models most closely predict the resulting permeability. Current theoretical models of permeability do not take into account complex geometry therefore reverse engineering may be required to develop a predictive model through curve fitting. The impact of these studies on the design of tissue engineered scaffolds is that through characterization of the exact surface area of a scaffold (something that we can do by utilizing regular polyehdra from Section 4.1 and 4.2) we can determine how material is deposited and to what effect, if any, permeability of the scaffold plays in the resulting tissue engineered scaffold.

In Chapter 5 the framework of Computer Aided Tissue Engineering is used as a demonstration of the effects of the modulation of the solid phase or the void phase in the

design of implants. The advantage of this technique is that it can create patient specific implants or an implant with locally tailored properties. We highlighted the iterative scaffold design procedure through its successive steps of imaging, modeling and scaffold fabrication. In section 5.1 we created a library of architectures of the same porosity with a modulus ranged by an order of magnitude (Figure 53). In Section 5.2, we executed the entire CATE process utilizing architectures from that library, assembled and prototyped a scaffold based on a density map obtained from CT scans of a cadaveric vertebrae (Figure 62). The focus of Section 5.3 was to address mechanical discontinuities between adjacent cubes through an interface library that matches faces to unit cubes based on metrics of percent area and volume overlap. In Section 5.4 we switched focus from mechanical augmentation to the effects of fluid flow design on implants and demonstrated the ability to modulate the release of a chemotherapeutic drug via the incorporation of porogens into a clinically approved acrylic cement. Although the release was low as a function of the poor release vehicle, the bioactivity of the released drug suggests that systemic toxicity may be partially ameliorated if this mode of drug release is used.

This dissertation was an exegesis on the modulation of architecture to tailor structural properties of tissue engineered scaffolds. By geometrically characterizing both the positive and the negative space we have set the vocabulary for an informed future discussion about architecture as it relates to mechanically active physiological regions. Future directions for the positive space should come in the form of an automated model to assemble porous scaffolds based on imaging modalities. Further work in the tailoring of the negative space can follow with the development of correlative models based on

hierarchical models using topological concepts combined with empirically derived

parameters.

REFERENCES

1. Sherwood, J.K., et al., *A three-dimensional osteochondral composite scaffold for articular cartilage repair.* Biomaterials, 2002. 23(24): p. 4739-51.
2. White, R.A., J.N. Weber, and E.W. White, *Replamineform: a new process for preparing porous ceramic, metal, and polymer prosthetic materials.* Science, 1972. 176(37): p. 922-4.
3. Chu, T.M., et al., *Manufacturing and characterization of 3-d hydroxyapatite bone tissue engineering scaffolds.* Ann N Y Acad Sci, 2002. 961: p. 114-7.
4. Chu, T.M., et al., *Mechanical and in vivo performance of hydroxyapatite implants with controlled architectures.* Biomaterials, 2002. 23(5): p. 1283-93.
5. Abell, A.B., K.L. Willis, and D.A. Lange, *Mercury Intrusion Porosimetry and Image Analysi of Cement-Based Materials.* Journal of Colloid and Interface Science, 1999. 211: p. 39-44.
6. Hutmacher, D.W., *Scaffold design and fabrication technologies for engineering tissues - state of the art and future perspectives.* J Biomater Sci Polym Ed, 2001. 12(1): p. 107-124.
7. Simon, J.L., et al., *Engineered cellular response to scaffold architecture in a rabbit trephine defect.* J Biomed Mater Res, 2003. 66A(2): p. 275-82.
8. Pearce, P., *Structure in nature is a strategy for design.* 1990, Cambridge, Massachusetts: MIT Press. 245.
9. Agrawal, C.M., et al., *Effects of fluid flow on the in vitro degradation kinetics of biodegradable scaffolds for tissue engineering.* Biomaterials, 2000. 21(23): p. 2443-52.
10. Agrawal, C.M. and R.B. Ray, *Biodegradable polymeric scaffolds for musculoskeletal tissue engineering.* J Biomed Mater Res, 2001. 55(2): p. 141-50.
11. Bhatia, S., M. Yarmush, and M. Toner, *Micropatterning Cells in Tissue Engineering*, in *Methods in Molecular Medicine*, J. Morgan and M. Yarmush, Editors. 1998, Humana Press: Totowa, NJ. p. 349-363.
12. Cukierman, E., et al., *Taking cell-matrix adhesions to the third dimension.* Science, 2001. 294(5547): p. 1708-12.
13. Galban, C.J. and B.R. Locke, *Effects of spatial variation of cells and nutrient and product concentrations coupled with product inhibition on cell growth in a polymer scaffold.* Biotechnol Bioeng, 1999. 64(6): p. 633-43.
14. Zeltinger, J., et al., *Effect of pore size and void fraction on cellular adhesion, proliferation, and matrix deposition.* Tissue Eng, 2001. 7(5): p. 557-72.
15. Wake, M.C., C.W. Patrick, Jr., and A.G. Mikos, *Pore morphology effects on the fibrovascular tissue growth in porous polymer substrates.* Cell Transplant, 1994. 3(4): p. 339-43.
16. Gibson, L.J. and M.F. Ashby, *Cellular Solids: Structure and Properties.* 1988, New York: Pergamon Press. 357.
17. Erben, R.G., *Embedding of bone samples in methylmethacrylate: an improved method suitable for bone histomorphometry, histochemistry, and immunohistochemistry.* J Histochem Cytochem, 1997. 45(2): p. 307-13.

18. Hollister, S.J., R.D. Maddox, and J.M. Taboas, *Optimal design and fabrication of scaffolds to mimic tissue properties and satisfy biological constraints.* Biomaterials, 2002. 23(20): p. 4095-103.

19. Kai, C., *Three-dimensional rapid prototyping technologies and key development areas.* Computing and Control Engineering Journal, 1994: p. 200-206.

20. Sun, W. and P. Lal, *Recent development on computer aided tissue engineering - A review.* Computer Methods and Programs in Biomedicine, 2002. 67(2): p. 85-103.

21. Leong, K.F., C.M. Cheah, and C.K. Chua, *Solid freeform fabrication of three-dimensional scaffolds for engineering replacement tissues and organs.* Biomaterials, 2003. 24(13): p. 2363-78.

22. Widmer, M.S. and A.G. Mikos, *Fabrication of Biodegradable Polymer Scaffolds for Tissue Engineering*, in *Frontiers in Tissue Engineering*, C.W. Patrick, A.G. Mikos, and L.V. McIntire, Editors. 1998, Elsevier Science: New York. p. 107-120.

23. Botchwey, E.A., et al., *Bone tissue engineering in a rotating bioreactor using a microcarrier matrix system.* J Biomed Mater Res, 2001. 55(2): p. 242-53.

24. Elgendy, H.M., et al., *Osteoblast-like cell (MC3T3-E1) proliferation on bioerodible polymers: an approach towards the development of a bone-bioerodible polymer composite material.* Biomaterials, 1993. 14(4): p. 263-9.

25. Freed, L.E., et al., *Biodegradable polymer scaffolds for tissue engineering.* Biotechnology (N Y), 1994. 12(7): p. 689-93.

26. Lin, A.S., et al., *Microarchitectural and mechanical characterization of oriented porous polymer scaffolds.* Biomaterials, 2003. 24(3): p. 481-9.

27. Temenoff, J.S., E. Steinbis, and A.G. Mikos, *Biodegradable Scaffolds.* 2002.

28. van Tienen, T.G., et al., *Tissue ingrowth and degradation of two biodegradable porous polymers with different porosities and pore sizes.* Biomaterials, 2002. 23(8): p. 1731-8.

29. Liebschner, M.A., *Biomechanical considerations of animal models used in tissue engineering of bone.* Biomaterials, 2004. 25(9): p. 1697-714.

30. Li, S.H., et al., *Accurate geometric characterization of macroporous scaffold of tissue engineering.* Key Engineering Materials, 2003. 240-242: p. 541-546.

31. Hollister, S.J., et al., *Engineering craniofacial scaffolds.* Orthod Craniofac Res, 2005. 8(3): p. 162-73.

32. Sun W, D.A., Starly B, Nam J, *Computer-Aided Tissue Engineering:Overview, Scope, and Challenges.* Biotechnology and Applied Biochemistry, 2004. 39: p. 29-47.

33. Majeska, R., *Cell Biology of Bone*, in *Bone Biomechanics Handbook*, S.C. Cowin, Editor. 2001, CRC Press LLC: Boca Raton. p. (2)1-(2)-24.

34. van der Linden, J.C., et al., *Trabecular bone's mechanical properties are affected by its non-uniform mineral distribution.* J Biomech, 2001. 34(12): p. 1573-80.

35. Lucchinetti, E., *Composite Models of Bone Properties*, in *Bone Biomechanics Handbook*, S.C. Cowin, Editor. 2001, CRC Press LLC: Boca Raton. p. (12)1-(12)19.

36. Liebschner, M.A.K. and M.A. Wettergreen, *Optimization of Bone Scaffold Engineering for Load Bearing*

Applications, in *Topics In Tissue Engineering*, N. Ashammakhi and P. Ferretti, Editors. 2003.

37. Wikipedia. *Femur*. 2008 [cited; Available from: http://en.wikipedia.org/wiki/Femur.

38. Yaszemski, M.J., et al., *Evolution of bone transplantation: molecular, cellular and tissue strategies to engineer human bone*. Biomaterials, 1996. 17(2): p. 175-85.

39. *Blue Histology*. 2003 [cited 2003 12.2]; Available from: http://www.lab.anhb.uwa.edu.au/mb140/MoreAbout/bonedynamics.html.

40. Hollister, S.J. *Bone Structure*. 2003 [cited 2003 12.2]; Available from: http://www.engin.umich.edu/class/bme456/bonestructure/bonestructure.htm.

41. Jee, W., *Integrated Bone Tissue Physiology: Anatomy and Physiology*, in *Bone Biomechanics Handbook*, S.C. Cowin, Editor. 2001, CRC Press LLC: Boca Raton. p. (1)1-(1)68.

42. Borah, B., et al., *Three-dimensional microimaging (MRmicroI and microCT), finite element modeling, and rapid prototyping provide unique insights into bone architecture in osteoporosis*. Anat Rec, 2001. 265(2): p. 101-10.

43. Kopperdahl, D.L. and T.M. Keaveny, *Yield strain behavior of trabecular bone*. J Biomech, 1998. 31(7): p. 601-8.

44. Smith, T.S., et al., *Surface remodeling of trabecular bone using a tissue level model*. J Orthop Res, 1997. 15(4): p. 593-600.

45. Katz, J.L., et al., *Multiscale mechanics of hierarchical structure/property relationships in calcified tissues and tissue/material interfaces*. Mater Sci Eng A Struct Mater, 2007. 27(3): p. 450-468.

46. Sikavitsas, V.I., J.S. Temenoff, and A.G. Mikos, *Biomaterials and bone mechanotransduction*. Biomaterials, 2001. 22(19): p. 2581-93.

47. Smith, D.H., J.A. Wolf, and D.F. Meaney, *A new strategy to produce sustained growth of central nervous system axons: continuous mechanical tension*. Tissue Eng, 2001. 7(2): p. 131-9.

48. Huiskes, R., et al., *Effects of mechanical forces on maintenance and adaptation of form in trabecular bone*. Nature, 2000. 405(6787): p. 704-6.

49. Mullender, M.G. and R. Huiskes, *Proposal for the regulatory mechanism of Wolff's law*. J Orthop Res, 1995. 13(4): p. 503-12.

50. Prendergast, P.J. and R. Huiskes, *The biomechanics of Wolff's law: recent advances*. Ir J Med Sci, 1995. 164(2): p. 152-4.

51. Frost, H.M., *From Wolff's law to the Utah paradigm: insights about bone physiology and its clinical applications*. Anat Rec, 2001. 262(4): p. 398-419.

52. Hung, C.T., et al., *Real-time calcium response of cultured bone cells to fluid flow*. Clin Orthop Relat Res, 1995(313): p. 256-69.

53. Hudlicka, O., *Mechanical factors involved in the growth of the heart and its blood vessels*. Cell Mol Biol Res, 1994. 40(2): p. 143-52.

54. Liu, S.Q., *Biomechanical basis of vascular tissue engineering*. Crit Rev Biomed Eng, 1999. 27(1-2): p. 75-148.

55. Kim, J., et al., *Muscle tissue engineering for partial glossectomy defects*. Arch Facial Plast Surg, 2003. 5(5): p. 403-7.

56. Hickey, D.G., S.R. Frenkel, and P.E. Di Cesare, *Clinical applications of growth factors for articular cartilage repair.* Am J Orthop, 2003. 32(2): p. 70-6.

57. Woo, S.L., et al., *Tissue engineering of ligament and tendon healing.* Clin Orthop Relat Res, 1999(367 Suppl): p. S312-23.

58. Butler, D.L., S.A. Goldstein, and F. Guilak, *Functional tissue engineering: the role of biomechanics.* J Biomech Eng, 2000. 122(6): p. 570-5.

59. Sikavitsas, V.I., et al., *Flow perfusion enhances the calcified matrix deposition of marrow stromal cells in biodegradable nonwoven fiber mesh scaffolds.* Ann Biomed Eng, 2005. 33(1): p. 63-70.

60. Angele, P., et al., *Cyclic, mechanical compression enhances chondrogenesis of mesenchymal progenitor cells in tissue engineering scaffolds.* Biorheology, 2004. 41(3-4): p. 335-46.

61. Mauck, R.L., et al., *Functional tissue engineering of articular cartilage through dynamic loading of chondrocyte-seeded agarose gels.* J Biomech Eng, 2000. 122(3): p. 252-60.

62. Hung, C.T., et al., *A paradigm for functional tissue engineering of articular cartilage via applied physiologic deformational loading.* Ann Biomed Eng, 2004. 32(1): p. 35-49.

63. Darling, E.M. and K.A. Athanasiou, *Biomechanical strategies for articular cartilage regeneration.* Ann Biomed Eng, 2003. 31(9): p. 1114-24.

64. Fan, J. and K.B. Walsh, *Mechanical stimulation regulates voltage-gated potassium currents in cardiac microvascular endothelial cells.* Circ Res, 1999. 84(4): p. 451-7.

65. Curi, M.A., et al., *Differential mechanical activation of mitogen-activated protein kinases in intact human blood vessels.* J Surg Res, 2002. 108(2): p. 198-202.

66. Akhyari, P., et al., *Mechanical stretch regimen enhances the formation of bioengineered autologous cardiac muscle grafts.* Circulation, 2002. 106(12 Suppl 1): p. I137-42.

67. Sarkar, S., et al., *Vascular tissue engineering: microtextured scaffold templates to control organization of vascular smooth muscle cells and extracellular matrix.* Acta Biomater, 2005. 1(1): p. 93-100.

68. Papadaki, M., *Cardiac muscle tissue engineering.* IEEE Eng Med Biol Mag, 2003. 22(3): p. 153-4.

69. Neumann, T., S.D. Hauschka, and J.E. Sanders, *Tissue engineering of skeletal muscle using polymer fiber arrays.* Tissue Eng, 2003. 9(5): p. 995-1003.

70. Cowin, S.C., ed. *Bone Mechanics Handbook.* 2001, CRC Press LLC: Boca Raton, FL.

71. Marcus, R., *Clinical review 76: The nature of osteoporosis.* J Clin Endocrinol Metab, 1996. 81(1): p. 1-5.

72. Johnston, C.C., Jr. and C.W. Slemenda, *Pathogenesis of osteoporosis.* Bone, 1995. 17(2 Suppl): p. 19S-22S.

73. Groger, A., et al., *Tissue engineering of bone for mandibular augmentation in immunocompetent minipigs: preliminary study.* Scand J Plast Reconstr Surg Hand Surg, 2003. 37(3): p. 129-33.

74. Sanders, K.M., et al., *The exclusion of high trauma fractures may underestimate the prevalence of bone fragility fractures in the community: the Geelong Osteoporosis Study.* J Bone Miner Res, 1998. 13(8): p. 1337-42.

75. Frost, H.M., *Changing views about 'Osteoporoses' (a 1998 overview).* Osteoporos Int, 1999. 10(5): p. 345-52.

76. Wolff, J., *Das Gesetz der Transformation der Knochen.* 1892, Berlin: Hirschwald Verlag.

77. Turner, C.H., *Functional determinants of bone structure: beyond Wolff's law of bone transformation.* Bone, 1992. 13(6): p. 403-9.

78. Cowin, S.C., *A resolution restriction for Wolff's law of trabecular architecture.* Bull Hosp Jt Dis Orthop Inst, 1989. 49(2): p. 205-12.

79. Frost, H.M., *Bone's mechanostat: a 2003 update.* Anat Rec A Discov Mol Cell Evol Biol, 2003. 275(2): p. 1081-101.

80. Frost, H.M., *The Skeleton's Mechanical Usage Window*, in *The Utah Paradigm of Skeletal Physiology.* 2004, International Society of Musculoskeletal Neuronal Interactions: Greece. p. 224-41.

81. Lanyon, L.E., et al., *Bone deformation recorded in vivo from strain gauges attached to the human tibial shaft.* Acta Orthop Scand, 1975. 46(2): p. 256-68.

82. Frost, H.M., *Bone "mass" and the "mechanostat": a proposal.* Anat Rec, 1987. 219(1): p. 1-9.

83. Frost, H.M., *On Wolff's Law and Some Related Matters*, in *The Utah Paradigm of Skeletal Physiology.* 2004, International Society of Musculoskeletal and Neuronal Interactions: Greece. p. 41-73.

84. Duyck, J., et al., *The influence of static and dynamic loading on marginal bone reactions around osseointegrated implants: an animal experimental study.* Clin Oral Implants Res, 2001. 12(3): p. 207-18.

85. Mahmoudifar, N. and P.M. Doran, *Tissue engineering of human cartilage in bioreactors using single and composite cell-seeded scaffolds.* Biotechnol Bioeng, 2005. 91(3): p. 338-55.

86. Forwood, M.R., et al., *Increased bone formation in rat tibiae after a single short period of dynamic loading in vivo.* Am J Physiol, 1996. 270(3 Pt 1): p. E419-23.

87. Liebschner M. A., W., M.A., *Optimization of Bone Scaffold Engineering for Load Bearing Application*, in *Topics in Tissue Engineering*, P. Ferretti and N. Ashammakhi, Editors. 2003, http://www.oulu.fi/spareparts/ebook_topics_in_t_e/list_of_contr.html.

88. van Rietbergen, B. and R. Huiskes, *Elastic Constants of Cancellous Bone*, in *Bone Biomechanics Handbook*, S.C. Cowin, Editor. 2001, CRC Press LLC: Boca Raton, FL. p. 15.1-15.24.

89. Guo, X.E., *Mechanical Properties of Cortical Bone and Cancellous Bone Tissue*, in *Bone Mechanics Handbook*, S.C. Cowin, Editor. 2001, CRC Press LLC: Boca Raton, FL. p. 10.1-10.23.

90. Grande, D.A., et al., *Evaluation of matrix scaffolds for tissue engineering of articular cartilage grafts.* J Biomed Mater Res, 1997. 34(2): p. 211-20.

91. Weinbaum, S., S.C. Cowin, and Y. Zeng, *A model for the excitation of osteocytes by mechanical loading-induced bone fluid shear stresses.* J Biomech, 1994. 27(3): p. 339-60.

92. Perren, S.M., *Physical and biological aspects of fracture healing with special reference to internal fixation.* Clin Orthop Relat Res, 1979(138): p. 175-96.

93. You, J., et al., *Substrate deformation levels associated with routine physical activity are less stimulatory to bone cells relative to loading-induced oscillatory fluid flow.* J Biomech Eng, 2000. 122(4): p. 387-93.

94. Cowin, S.C. and S. Weinbaum, *Strain amplification in the bone mechanosensory system.* Am J Med Sci, 1998. 316(3): p. 184-8.

95. You, L., et al., *A model for strain amplification in the actin cytoskeleton of osteocytes due to fluid drag on pericellular matrix.* J Biomech, 2001. 34(11): p. 1375-86.

96. Kunnel, J.G., J.L. Gilbert, and P.H. Stern, *In vitro mechanical and cellular responses of neonatal mouse bones to loading using a novel micromechanical-testing device.* Calcif Tissue Int, 2002. 71(6): p. 499-507.

97. Ruimerman, R., et al., *The effects of trabecular-bone loading variables on the surface signaling potential for bone remodeling and adaptation.* Ann Biomed Eng, 2005. 33(1): p. 71-8.

98. Hollister, S.J., et al., *An image-based approach for designing and manufacturing craniofacial scaffolds.* Int J Oral Maxillofac Surg, 2000. 29(1): p. 67-71.

99. Biggemann, M., D. Hilweg, and P. Brinckmann, *Prediction of the compressive strength of vertebral bodies of the lumbar spine by quantitative computed tomography.* Skeletal Radiol, 1988. 17(4): p. 264-9.

100. Sun W, S., B., Darling A., Gomez C., *Computer-Aided Tissue Engineering: Application to Biomimetic Modelling and Design of Tissue Scaffolds.* Biotechnology and Applied Biochemistry, 2004. 39: p. 49-58.

101. Hutmacher, D.W., *Scaffolds in tissue engineering bone and cartilage.* Biomaterials, 2000. 21(24): p. 2529-43.

102. Belytschko, T., S.P. Xiao, and C. Parimi, *Topology Optimization with Implicit Functions and Regularization.* International Journal for Numerical Methods in Engineering, 2003. 57(8): p. 1177-1196.

103. Bendsoe, M.P. and N. Kikuchi, *Generating Optimal Topologies in Structural Design.* Comp Methods Appl Mech and Eng, 1988. 71(2): p. 197-224.

104. Van Rietbergen, B., et al., *Tissue stresses and strain in trabeculae of a canine proximal femur can be quantified from computer reconstructions.* J Biomech, 1999. 32(4): p. 443-51.

105. Mattheck, C., *Design in Nature.* Interdisciplinary Science Reviews, 1994. 19(4): p. 298-314.

106. Mattheck, C., *Is There a Universal Optimum Notch Shape?* Materialwissenschaft Und Werkstofftechnik, 2004. 35(9): p. 582-586.

107. Lin, C.Y., N. Kikuchi, and S.J. Hollister, *A novel method for biomaterial scaffold internal architecture design to match bone elastic properties with desired porosity.* J Biomech, 2004. 37(5): p. 623-36.

108. Larsson, C., et al., *Bone response to surface-modified titanium implants: studies on the early tissue response to machined and electropolished implants with different oxide thicknesses.* Biomaterials, 1996. 17(6): p. 605-16.

109. Prins, S.H., et al., *The role of quantitative ultrasound in the assessment of bone: a review.* Clin Physiol, 1998. 18(1): p. 3-17.

110. Yang, S., et al., *The design of scaffolds for use in tissue engineering. Part II. Rapid prototyping techniques.* Tissue Eng, 2002. 8(1): p. 1-11.

111. Fisher, J.P., et al., *Soft and hard tissue response to photocrosslinked poly(propylene fumarate) scaffolds in a rabbit model.* J Biomed Mater Res, 2002. 59(3): p. 547-56.

112. Gibson, L.J., *The mechanical behaviour of cancellous bone.* J Biomech, 1985. 18(5): p. 317-28.

113. Fisher, J.P., et al., *Synthesis and properties of photocross-linked poly(propylene fumarate) scaffolds.* J Biomater Sci Polym Ed, 2001. 12(6): p. 673-87.

114. Ishaug, S.L., et al., *Bone formation by three-dimensional stromal osteoblast culture in biodegradable polymer scaffolds.* J Biomed Mater Res, 1997. 36(1): p. 17-28.

115. Malda, J., et al., *The effect of PEGT/PBT scaffold architecture on the composition of tissue engineered cartilage.* Biomaterials, 2005. 26(1): p. 63-72.

116. Behravesh, E., et al., *Evaluation of the in vitro degradation of macroporous hydrogels using gravimetry, confined compression testing, and microcomputed tomography.* Biomacromolecules, 2002. 3(6): p. 1263-70.

117. Qiu, Q.Q., P. Ducheyne, and P.S. Ayyaswamy, *Fabrication, characterization and evaluation of bioceramic hollow microspheres used as microcarriers for 3-D bone tissue formation in rotating bioreactors.* Biomaterials, 1999. 20(11): p. 989-1001.

118. Hollister, S.J., J.M. Brennan, and N. Kikuchi, *A homogenization sampling procedure for calculating trabecular bone effective stiffness and tissue level stress.* J Biomech, 1994. 27(4): p. 433-44.

119. Landers, R., et al., *Rapid prototyping of scaffolds derived from thermoreversible hydrogels and tailored for applications in tissue engineering.* Biomaterials, 2002. 23(23): p. 4437-47.

120. Nuttelman, C.R., S.M. Henry, and K.S. Anseth, *Synthesis and characterization of photocrosslinkable, degradable poly(vinyl alcohol)-based tissue engineering scaffolds.* Biomaterials, 2002. 23(17): p. 3617-26.

121. Gomes, M.E., et al., *A new approach based on injection moulding to produce biodegradable starch-based polymeric scaffolds: morphology, mechanical and degradation behaviour.* Biomaterials, 2001. 22(9): p. 883-9.

122. Liebschner, M.A. and M.A. Wettergreen. *Scaffold Optimization for Load Bearing Applications.* in *Southern Biomedical Engineering Conference.* 2002. Bethesda, MD: Medical and Engineering Publishers.

123. Stampfl, J., et al. *Biodegradable Stereolithography Resins with Defined Mechanical Properties.* in *Virtual and Rapid Manufacturing.* 2007.

124. Taboas, J.M., et al., *Indirect solid free form fabrication of local and global porous, biomimetic and composite 3D polymer-ceramic scaffolds.* Biomaterials, 2003. 24(1): p. 181-94.

125. Ren, L., et al., *Novel approach to fabricate porous gelatin-siloxane hybrids for bone tissue engineering.* Biomaterials, 2002. 23(24): p. 4765-73.

126. Chang, R., J. Nam, and W. Sun, *Effects of dispensing pressure and nozzle diameter on cell survival from solid freeform fabrication-based direct cell writing.* Tissue Eng Part A, 2008. 14(1): p. 41-8.

127. Cao, T., K.H. Ho, and S.H. Teoh, *Scaffold design and in vitro study of osteochondral coculture in a three-dimensional porous polycaprolactone scaffold fabricated by fused deposition modeling.* Tissue Eng, 2003. 9 Suppl 1: p. S103-12.

128. Cooke MN, F.J., Dean D, Rimnac C, Mikos AG., *Use of stereolithography to manufacture critical-sized 3D biodegradable scaffolds for bone ingrowth.* J Biomed Mater Res, 2003. 64B(2): p. 65-69.

129. Wicker, R.B., F. Medina, and C.J. Elkins. *Multiple Material Micro-Fabrication: Extending Stereolithography to Tissue Engineering and Other Novel Applications.* in *Proceedings of the 15th Annual Solid Freeform Fabrication Symposium.* 2004. Austin, TX.

130. Cooke, M.N., et al., *Use of stereolithography to manufacture critical-sized 3D biodegradable scaffolds for bone ingrowth.* J Biomed Mater Res, 2003. 64B(2): p. 65-9.

131. Therics, I., *Therics, Inc. - Tissue Engineering Specialists.* 2003.

132. Wettergreen, M.A., et al. *Scaffold Optimization for Load Bearing Applications in Orthopaedics.* in *Conference for the Houston Society for Engineering in Medicine and Biology.* 2003. Houston, TX.

133. Marra, K.G., et al., *In vitro analysis of biodegradable polymer blend/hydroxyapatite composites for bone tissue engineering.* J Biomed Mater Res, 1999. 47(3): p. 324-35.

134. Rogers-Foy, J.M., et al., *Hydroxyapatite composites designed for antibiotic drug delivery and bone reconstruction: a caprine model.* J Invest Surg, 1999. 12(5): p. 263-75.

135. Wolfe, M.S., et al., *In vitro degradation and fracture toughness of multilayered porous poly(propylene fumarate)/beta-tricalcium phosphate scaffolds.* J Biomed Mater Res, 2002. 61(1): p. 159-164.

136. Mickiewicz, R.A., A.M. Mayes, and D. Knaack, *Polymer--calcium phosphate cement composites for bone substitutes.* J Biomed Mater Res, 2002. 61(4): p. 581-92.

137. Zhang, Y. and M. Zhang, *Three-dimensional macroporous calcium phosphate bioceramics with nested chitosan sponges for load-bearing bone implants.* J Biomed Mater Res, 2002. 61(1): p. 1-8.

138. Bear, J., *Dynamics of Fluids in Porous Media.* 1972, Toronto, Ontario: American Elsevier Publishing Co., Inc. 764.

139. Bagel, L. and V. Zivica, *Relationship between pore structure and permeability of hardened cement mortars: on the choice of effective pore structure parameter.* Cement and Concrete Research, 1997. 27(8): p. 1225-1235.

140. De Wiest, R.J.M., ed. *Flow Through Porous Media.* 1965, Princeton University Press. 530.

141. Mikos, A.G., et al., *Preparation and Characterization of Poly(L-Lactic Acid) Foams.* Polymer, 1994. 35: p. 1068-1077.

142. Tsakiroglou, C.D. and A.C. Payatakes, *Characterization of the pore structure of reservoir rocks with the aid of serial sectioning analysis, mercury porosimetry and network simulation.* Advances in Water Resources, 2000. 23(7): p. 773-789.

143. Liang, Z., M.A. Ioannidis, and I. Chatzis, *Permeability and electrical conductivity of porous media from 3D stochastic replicas of the microstructure.* Chemical Engineering Science, 2000. 55(22): p. 5247-5262.

144. Garboczi, E.J. and D.P. Bentz, *The effect of statistical fluctuation, finite size error, and digital resolution on the phase percolation and transport properties of the NIST cement hydration model.* Cement and Concrete Research, 2001. 31(10): p. 1501-1514.

145. van Breugel, K., *Numerical simulation of hydration and microstructural development in hardening cement-based materials (II) applications.* Cement and Concrete Research, 1995. 25(3): p. 522-530.

146. Ye, G., K. Van Breugel, and A.L.A. Fraaij, *Three-dimensional microstructure analysis of numerically simulated cementitious materials.* Cement and Concrete Research, 2003. 33(2): p. 215-222.

147. Alshamsi, A.M. and H.D.A. Imran, *Development of a permeability apparatus for concrete and mortar.* Cement and Concrete Research, 2002. 32(6): p. 923-929.

148. Arramon, Y.P. and E.A. Nauman, *The Intrinsic Permeability of Cancellous Bone*, in *Bone Biomechanics Handbook*, S.C. Cowin, Editor. 2001, CRC Press: Boca Raton, FL. p. 25-1 - 25-17.

149. Spain, T.L., C.M. Agrawal, and K.A. Athanasiou, *New technique to extend the useful life of a biodegradable cartilage implant.* Tissue Eng, 1998. 4(4): p. 343-52.

150. van Breugel, K., *Numerical simulation of hydration and microstructural development in hardening cement-based materials. (I) Theory.* Cement and Concrete Research, 1995. 25(2): p. 319-331.

151. Van Breugel, K., A.L.A. Fraaij, and G. Ye, *Experimental study on ultrasonic pulse velocity evaluation of the microstructure of cementitious material at early age.* Heron, 2001. 46(3): p. 161-167.

152. Ball, P., *The Self-Made Tapestry: Pattern Formation in Nature.* 1999, Oxford: Oxford University Press. 287.

153. Gibson, L.J., *Biomechanics of cellular solids.* J Biomech, 2005. 38(3): p. 377-99.

154. Mosekilde, L., *Vertebral structure and strength in vivo and in vitro.* Calcif Tissue Int, 1993. 53(Suppl 1): p. S121-5; discussion S125-6.

155. Sander, E.A., et al., *A cellular solid model of the lamina cribrosa: mechanical dependence on morphology.* J Biomech Eng, 2006. 128(6): p. 879-89.

156. Beaupre, G.S. and W.C. Hayes, *Finite element analysis of a three-dimensional open-celled model for trabecular bone.* J Biomech Eng, 1985. 107(3): p. 249-56.

157. Elson, E.L., *Cellular mechanics as an indicator of cytoskeletal structure and function.* Annu Rev Biophys Biophys Chem, 1988. 17: p. 397-430.

158. Ulrich, D., et al., *The ability of three-dimensional structural indices to reflect mechanical aspects of trabecular bone.* Bone, 1999. 25(1): p. 55-60.

159. Gibson, L.J., Ashby, M.F., Schajer, G.S., and Robertson, C.I., *The Mechanics of Two Dimensional Cellular Materials.* Proceedings Royal Society London, 1982. A382: p. 25-42.

160. Roberts AP, G.E., *Elastic Moduli of Model Random Three-Dimensional Closed-Cell Cellular Solids.* Acta Materilia, 2001. 49: p. 189-197.

161.   Vajjhala, S., A.M. Kraynik, and L.J. Gibson, *A cellular solid model for modulus reduction due to resorption of trabeculae in bone.* J Biomech Eng, 2000. 122(5): p. 511-5.

162.   Silva, M.J. and L.J. Gibson, *Modeling the mechanical behavior of vertebral trabecular bone: effects of age-related changes in microstructure.* Bone, 1997. 21(2): p. 191-9.

163.   Thompson, D.W., *On Growth and Form.* 1942: Cambridge University Press. 1142.

164.   Cromwell, P.R., *Polyhedra.* 1997, Cambridge: Cambridge University Press. 451.

165.   Sun, W. and X. Hu, *Reasoning Boolean Operation Based CAD Modeling for Heterogeneous Objects.* Computer Aided Design, 2002. 34: p. 481-488.

166.   Roberts, A.P. and E.J. Garboczi, *Elastic moduli of model random three-dimensional closed-cell cellular solids.* Acta Materialia, 2001. 49(2): p. 189-197.

167.   Woesz, A., J. Stampfl, and P. Fratzl, *Cellular Solids Beyond the Apparent Density - An Experiemental Assessment of Mechanical Properties.* Adv Engr Matls, 2004. 6(3): p. 134-138.

168.   Gottesman, T. and Z. Hashin, *Analysis of viscoelastic behaviour of bones on the basis of microstructure.* J Biomech, 1980. 13(2): p. 89-96.

169.   Lohfeld, S., et al., *Manufacturing of small featured PCL scaffolds for bone tissue engineering using selective laser sintering.* J Biomech, 2006. 39(Supplement 1): p. S216.

170.   Hutmacher, D.W. and H. Singh, *Computational fluid dynamics for improved bioreactor design and 3D culture.* Trends Biotechnol, 2008. 26(4): p. 166-72.

171.   Bonfield, W., *Designing porous scaffolds for tissue engineering.* Philos Transact A Math Phys Eng Sci, 2006. 364(1838): p. 227-32.

172.   Agrawal, C.M., et al., *The Use of the Vibrating Particle Technique to Fabricate Highly Porous and Permeable Biodegradable Scaffolds*, in *Synthetic Bioabsorbable Polymers for Implants.* 2000, American Society for Testing and Materials.

173.   Dullien, F.A.L., *Porous Media: Fluid Transport and Pore Structure.* 1979, New York, NY: Academic Press.

174.   Scheidegger, A., *The Physics of Flow Through Porous Media.* 1974, Toronto: University of Toronto Press. 353.

175.   Breysse, D. and B. Gerard, *Modelling of Permeability in Cement-Based Materias: Part 1-Uncraked Medium.* Cement and Concrete Research, 1997. 27(5): p. 761-775.

176.   Beebe, D.J., et al., *Functional hydrogel structures for autonomous flow control inside microfluidic channels.* Nature, 2000. 404(6778): p. 588-90.

177.   Tan, W. and T.A. Desai, *Microfluidic patterning of cells in extracellular matrix biopolymers: effects of channel size, cell type, and matrix composition on pattern integrity.* Tissue Eng, 2003. 9(2): p. 255-67.

178.   Xia, Y., D. Qin, and G.M. Whitesides, *Microcontact Printing with a Cylindrical Rolling Stamp: A Practical Step Toward Automatic Manufacturing of Patterns with Submicrometer-Sized Features.* Advanced Materials, 1996. 8(12): p. 1015-1017.

179. Tien, J., C.M. Nelson, and C.S. Chen, *Fabrication of aligned microstructures with a single elastomeric stamp.* Proc Natl Acad Sci U S A, 2002. 99(4): p. 1758-62.

180. Folch, A. and M. Toner, *Cellular micropatterns on biocompatible materials.* Biotechnol Prog, 1998. 14(3): p. 388-92.

181. Folch, A., et al., *Microfabricated elastomeric stencils for micropatterning cell cultures.* J Biomed Mater Res, 2000. 52(2): p. 346-53.

182. Timmer, M.D., et al., *Fabrication of poly(propylene fumarate)-based orthopaedic implants by photo-crosslinking through transparent silicone molds.* Biomaterials, 2003. 24(25): p. 4707-14.

183. Zhao, X., Y. Xia, and G.M. Whitesides, *Fabrication of Three-Dimensional Micro-Structures: Microtransfer Molding.* Advanced Materials, 1996. 8(10): p. 837-840.

184. Vozzi, G., et al., *Fabrication of PLGA scaffolds using soft lithography and microsyringe deposition.* Biomaterials, 2003. 24(14): p. 2533-40.

185. Chiu, D.T., et al., *Patterned deposition of cells and proteins onto surfaces by using three-dimensional microfluidic systems.* Proc Natl Acad Sci U S A, 2000. 97(6): p. 2408-13.

186. Kane, R.S., et al., *Patterning proteins and cells using soft lithography.* Biomaterials, 1999. 20(23-24): p. 2363-76.

187. Xia, Y. and G. Whitesides, *Soft Lithography.* Angew. Chem. Int. Ed., 1998. 37: p. 550-575.

188. Wettergreen MA, M.A., Liebschner MAK. *Evaluation of an Injectable Composite Bone Cement with Engineered Micro-Architecture.* in *Groupe de Recherche Interdisciplinaire sur les Biomateriaux Osteoarticulaires Injectables.* 2003. Baltimore, MD.

189. SolidScape. *SolidScape.* 2004 [cited; Available from: www.solid-scape.com.

190. Nauman, E.A., K.E. Fong, and T.M. Keaveny, *Dependence of intertrabecular permeability on flow direction and anatomic site.* Ann Biomed Eng, 1999. 27(4): p. 517-24.

191. Buckwalter, J.A. and E.B. Hunziker, *Orthopaedics. Healing of bones, cartilages, tendons, and ligaments: a new era.* Lancet, 1996. 348 Suppl 2: p. sII18.

192. Sachlos, E., et al., *Novel collagen scaffolds with predefined internal morphology made by solid freeform fabrication.* Biomaterials, 2003. 24(8): p. 1487-97.

193. Griffith, L.G., *Emerging design principles in biomaterials and scaffolds for tissue engineering.* Ann N Y Acad Sci, 2002. 961: p. 83-95.

194. Kelsey, D. and S.B. Goodman, *Design of the femoral component for cementless hip replacement: the surgeon's perspective.* Am J Orthop, 1997. 26(6): p. 407-12.

195. Wettergreen, M.A., et al., *Computer-Aided Tissue Engineering of a Human Vertebral Body.* Ann Biomed Eng, 2004. 33(10): p. 1394-1404.

196. Keaveny, T.M., et al., *Trabecular bone exhibits fully linear elastic behavior and yields at low strains.* J Biomech, 1994. 27(9): p. 1127-36.

197. Rho, J.Y., M.C. Hobatho, and R.B. Ashman, *Relations of mechanical properties to density and CT numbers in human bone.* Med Eng Phys, 1995. 17(5): p. 347-55.

198. Rice, J.C., S.C. Cowin, and J.A. Bowman, *On the dependence of the elasticity and strength of cancellous bone on apparent density.* J Biomech, 1988. 21(2): p. 155-68.

199. Cowin, S.C., *The mechanical and stress adaptive properties of bone.* Ann Biomed Eng, 1983. 11(3-4): p. 263-95.

200. Dean, D., K.J. Min, and A. Bond, *Computer Aided Design of Large-Format Prefabricated Cranial Plates.* J Craniofac Surg, 2003. 14(6): p. 819-832.

201. Riggs, B.L. and L.J. Melton, 3rd, *The worldwide problem of osteoporosis: insights afforded by epidemiology.* Bone, 1995. 17(5 Suppl): p. 505S-511S.

202. Winder, J., et al., *Medical rapid prototyping and 3D CT in the manufacture of custom made cranial titanium plates.* J Med Eng Technol, 1999. 23(1): p. 26-8.

203. Davis, J., *Till Death Do Us Part*, in *Wired*. 2003. p. 110-120.

204. Jacobs, C.R., et al., *NACOB presentation to ASB Young Scientist Award: Postdoctoral. The impact of boundary conditions and mesh size on the accuracy of cancellous bone tissue modulus determination using large-scale finite-element modeling. North American Congress on Biomechanics.* J Biomech, 1999. 32(11): p. 1159-64.

205. Winslow, R.L. and M.S. Boguski, *Genome informatics: current status and future prospects.* Circ Res, 2003. 92(9): p. 953-61.

206. Sun W, S., B., Darling A., Gomez C., *Computer Aided Tissue Engineering Part I: Overview, Scope and Challenges.* Journal of Biotechnology and Applied Biochemistry, 2003.

207. Davidson, E.T., J.G. Evans, and Y.D. Coble, Jr., *Bone mineral density testing by DEXA.* J Fla Med Assoc, 1996. 83(8): p. 567-8.

208. Jones, L.M., A. Goulding, and D.F. Gerrard, *DEXA: a practical and accurate tool to demonstrate total and regional bone loss, lean tissue loss and fat mass gain in paraplegia.* Spinal Cord, 1998. 36(9): p. 637-40.

209. Markel, M.D., et al., *Quantification of bone healing. Comparison of QCT, SPA, MRI, and DEXA in dog osteotomies.* Acta Orthop Scand, 1990. 61(6): p. 487-98.

210. Ito, M., et al., *Bone mineral and other bone components in vertebrae evaluated by QCT and MRI.* Skeletal Radiol, 1993. 22(2): p. 109-13.

211. Webb, P.A., *A review of rapid prototyping (RP) techniques in the medical and biomedical sector.* J Med Eng Technol, 2000. 24(4): p. 149-53.

212. Mayo, J.R., J. Aldrich, and N.L. Muller, *Radiation exposure at chest CT: a statement of the Fleischner Society.* Radiology, 2003. 228(1): p. 15-21.

213. Brody, A.S., *CT scanner design and patient radiation exposure.* Pediatr Radiol, 2002. 32(4): p. 268-71.

214. Nishitani, H., et al., *[Radiation exposure in CT].* Nippon Igaku Hoshasen Gakkai Zasshi, 2002. 62(7): p. 347-51.

215. Wiest, P.W., et al., *CT scanning: a major source of radiation exposure.* Semin Ultrasound CT MR, 2002. 23(5): p. 402-10.

216. Kusnoto, B. and C.A. Evans, *Reliability of a 3D surface laser scanner for orthodontic applications.* Am J Orthod Dentofacial Orthop, 2002. 122(4): p. 342-8.

217. Kopperdahl, D.L., E.F. Morgan, and T.M. Keaveny, *Quantitative computed tomography estimates of the mechanical properties of human vertebral trabecular bone.* J Orthop Res, 2002. 20(4): p. 801-5.

218. Gordon, C.L., et al., *Image-based assessment of spinal trabecular bone structure from high-resolution CT images.* Osteoporos Int, 1998. 8(4): p. 317-25.

219. Guan, H., et al., *CT reconstruction by using the MLS-ART technique and the KCD imaging system--I: low-energy X-ray studies.* IEEE Trans Med Imaging, 1999. 18(4): p. 355-8.

220. Rangayyan, R.M. and R. Gordon, *Computed tomography from ordinary radiographs for teleradiology.* Med Phys, 1983. 10(5): p. 687-90.

221. Templeton, A., D. Cody, and M. Liebschner, *Updating a 3-D vertebral body finite element model using 2-D images.* Med Eng Phys, 2004. 26(4): p. 329-33.

222. Feinberg, S.E., et al., *Image-based biomimetic approach to reconstruction of the temporomandibular joint.* Cells Tissues Organs, 2001. 169(3): p. 309-21.

223. Sun W and L. P, *Recent development on computer aided tissue engineering--a review.* Comput Methods Programs Biomed, 2002. 67(2): p. 85-103.

224. Starly B, L.W., Fang Z, Sun W. *"Biomimetic" Model For Heterogeneous Bone Scaffold.* in *Southern Biomedical Engineering Conference.* 2002. Washington, DC: Medical and Engineering Publishers.

225. Keller, T.S., et al., *Regional variations in the compressive properties of lumbar vertebral trabeculae. Effects of disc degeneration.* Spine, 1989. 14(9): p. 1012-9.

226. Adachi, T., et al., *Trabecular surface remodeling simulation for cancellous bone using microstructural voxel finite element models.* J Biomech Eng, 2001. 123(5): p. 403-9.

227. Toffoli, T., *Cellular Automata,* in *The Handbook of Brain Theory and Neural Networks,* M.A. Arbib, Editor. 1995, The MIT Press: Cambridge, MS.

228. Ruimerman, R., et al., *A 3-dimensional computer model to simulate trabecular bone metabolism.* Biorheology, 2003. 40(1-3): p. 315-20.

229. McCubbrey, D.A., et al., *Static and fatigue failure properties of thoracic and lumbar vertebral bodies and their relation to regional density.* J Biomech, 1995. 28(8): p. 891-9.

230. Sun W, S., B., Darling A., Gomez C., *Computer Aided Tissue Engineering Part II: Application to biomimetic modeling and design of tissues.* Journal of Biotechnology and Applied Biochemistry, 2003.

231. Asano, S., et al., *The mechanical properties of the human L4-5 functional spinal unit during cyclic loading. The structural effects of the posterior elements.* Spine, 1992. 17(11): p. 1343-52.

232. Yang, K.H. and A.I. King, *Mechanism of facet load transmission as a hypothesis for low-back pain.* Spine, 1984. 9(6): p. 557-65.

233. Mironov, V., et al., *Organ printing: computer-aided jet-based 3D tissue engineering.* Trends Biotechnol, 2003. 21(4): p. 157-61.

234. Wettergreen MA, M.A., Liebschner MAK. *Design of a Three-Dimensional Composite Scaffold with Varied Engineered Micro-Architecture.* in *Groupe de Recherche Interdisciplinaire sur les Biomateriaux Osteoarticulaires Injectables.* 2003. Baltimore, MD.

235. Prendergast, P.J., *Bone Prostheses and Implants*, in *Bone Biomechanics Handbook*, S.C. Cowin, Editor. 2001, CRC Press: New York. p. 35-1 - 35-29.

236. Kotani, Y., et al., *The effects of spinal fixation and destabilization on the biomechanical and histologic properties of spinal ligaments. An in vivo study.* Spine, 1998. 23(6): p. 672-82; discussion 682-3.

237. Chu, K.T., et al., *Hydroxyapatite/PMMA composites as bone cements.* Biomed Mater Eng, 2004. 14(1): p. 87-105.

238. Ono, K., et al., *Bone-fibrin mixture in spinal surgery.* Clin Orthop, 1992(275): p. 133-9.

239. Soffer, E., J.P. Ouhayoun, and F. Anagnostou, *Fibrin sealants and platelet preparations in bone and periodontal healing.* Oral Surg Oral Med Oral Pathol Oral Radiol Endod, 2003. 95(5): p. 521-8.

240. Tan, K.H., et al., *Scaffold development using selective laser sintering of polyetheretherketone-hydroxyapatite biocomposite blends.* Biomaterials, 2003. 24(18): p. 3115-23.

241. Horch, R.A., et al., *Nanoreinforcement of poly(propylene fumarate)-based networks with surface modified alumoxane nanoparticles for bone tissue engineering.* Biomacromolecules, 2004. 5(5): p. 1990-8.

242. Sciperio. *Sciperio, Inc. - A Science Revelation.* 2004 [cited; Available from: www.sciperio.com.

243. Yaylaoglu, M.B., et al., *Development of a calcium phosphate-gelatin composite as a bone substitute and its use in drug release.* Biomaterials, 1999. 20(8): p. 711-9.

244. Holland, T.A., et al., *Transforming growth factor-beta 1 release from oligo(poly(ethylene glycol) fumarate) hydrogels in conditions that model the cartilage wound healing environment.* J Control Release, 2004. 94(1): p. 101-14.

245. Alsberg, E., et al., *Regulating bone formation via controlled scaffold degradation.* J Dent Res, 2003. 82(11): p. 903-8.

246. Cheah, C.M., et al., *Automatic algorithm for generating complex polyhedral scaffold structures for tissue engineering.* Tissue Eng, 2004. 10(3-4): p. 595-610.

247. Mullender, M., et al., *Mechanotransduction of bone cells in vitro: mechanobiology of bone tissue.* Med Biol Eng Comput, 2004. 42(1): p. 14-21.

248. Marks, S.C., Jr., M.J. Cielinski, and K.T. Sundquist, *Bone surface morphology reflects local skeletal metabolism.* Microsc Res Tech, 1996. 33(2): p. 121-7.

249. Wettergreen, M.A., et al., *Computer-aided tissue engineering of a human vertebral body.* Ann Biomed Eng, 2005. 33(10): p. 1333-43.

250. Nicholson, P.H., et al., *Structural and material mechanical properties of human vertebral cancellous bone.* Med Eng Phys, 1997. 19(8): p. 729-37.

251. van Rietbergen, B., et al., *A new method to determine trabecular bone elastic properties and loading using micromechanical finite-element models.* J Biomech, 1995. 28(1): p. 69-81.

252. Hutmacher, D.W., M. Sittinger, and M.V. Risbud, *Scaffold-based tissue engineering: rationale for computer-aided design and solid free-form fabrication systems.* Trends Biotechnol, 2004. 22(7): p. 354-62.

253. Niebur, G.L., et al., *Sensitivity of damage predictions to tissue level yield properties and apparent loading conditions.* J Biomech, 2001. 34(5): p. 699-706.

254. Keaveny, T., *Strength of Trabecular Bone*, in *Bone Biomechanics Handbook*, C. SC, Editor. 2001, CRC Press LLC: Boca Raton. p. 1-42.

255. Bendsoe, N., *Characterization of a new amino acid transport system in human epidermal Langerhans cells: the L-dopa influx/efflux cycle.* Ups J Med Sci, 2003. 108(3): p. 161-92.

256. Sethian, J.A. and A. Vladimirsky, *Fast methods for the eikonal and related hamilton-jacobi equations on unstructured meshes.* Proc Natl Acad Sci U S A, 2000. 97(11): p. 5699-703.

257. Kim, H., et al., *Determination of an optimal topology with a predefined number of cavities.* AIAA Journal, 2002. 40(4): p. 739-744.

258. Kim, H., et al., *A method for varying the number of cavities in an optimized topology using Evolutionary Structural Optimization.* Structural and Multidisciplinary Optimization, 2000. 19(2): p. 140-147.

259. Xie, Y.M. and G.P. Steven, *Evolutionary Structural Optimization.* 1997, London: Springer.

260. Mathworld. *Archimedean Solids.* 2008 [cited; Available from: http://mathworld.wolfram.com/ArchimedeanSolid.html.

261. Tatsui, H., et al., *Survival rates of patients with metastatic spinal cancer after scintigraphic detection of abnormal radioactive accumulation.* Spine, 1996. 21(18): p. 2143-8.

262. Byrne, T.N., *Spinal cord compression from epidural metastases.* N Engl J Med, 1992. 327(9): p. 614-9.

263. Ho, C.S., et al., *Metastasis in vertebra mimicking acute compression fractures in a patient with osteoporosis: MRI findings.* Clin Imaging, 2005. 29(1): p. 64-7.

264. Fourney, D.R. and Z.L. Gokaslan, *Spinal instability and deformity due to neoplastic conditions.* Neurosurg Focus, 2003. 14(1): p. e8.

265. Baraliakos, X., et al., *Radiographic progression in patients with ankylosing spondylitis after 2 years of treatment with the tumour necrosis factor alpha antibody infliximab.* Ann Rheum Dis, 2005. 64(10): p. 1462-6.

266. Wei, F., et al., *[Surgical factors underlying the recurrence of primary spine tumor].* Zhonghua Wai Ke Za Zhi, 2005. 43(4): p. 221-4.

267. Fourney, D.R., et al., *Use of pedicle screw fixation in the management of malignant spinal disease: experience in 100 consecutive procedures.* J Neurosurg, 2001. 94(1 Suppl): p. 25-37.

268. Tomita, K., et al., *Total en bloc spondylectomy and circumspinal decompression for solitary spinal metastasis.* Paraplegia, 1994. 32(1): p. 36-46.

269. Hasegawa, K., et al., *Effects of surgical treatment for cervical spondylotic myelopathy in patients > or = 70 years of age: a retrospective comparative study.* J Spinal Disord Tech, 2002. 15(6): p. 458-60.

270. Milas, L., et al., *Chemoradiotherapy: emerging treatment improvement strategies.* Head Neck, 2003. 25(2): p. 152-67.

271. Abe, E., et al., *Total spondylectomy for primary malignant, aggressive benign, and solitary metastatic bone tumors of the thoracolumbar spine.* J Spinal Disord, 2001. 14(3): p. 237-46.

272. Sundaresan, N., et al., *Vertebral body resection in the treatment of cancer involving the spine.* Cancer, 1984. 53(6): p. 1393-6.

273. Aulisa, L., et al., *Biomechanics of the spine*. Rays, 2000. 25(1): p. 11-8.

274. McLaren, A.C., *Alternative materials to acrylic bone cement for delivery of depot antibiotics in orthopaedic infections*. Clin Orthop Relat Res, 2004(427): p. 101-6.

275. Macey, D.J., et al., *Estimation of radiation absorbed doses to the red marrow in radioimmunotherapy*. Clin Nucl Med, 1995. 20(2): p. 117-25.

276. Sonis, S.T., et al., *Prevention of chemotherapy-induced ulcerative mucositis by transforming growth factor beta 3*. Cancer Res, 1994. 54(5): p. 1135-8.

277. Clavo, B., et al., *Effect of cervical spinal cord stimulation on regional blood flow and oxygenation in advanced head and neck tumours*. Ann Oncol, 2004. 15(5): p. 802-7.

278. Tamargo, R.J., et al., *Interstitial chemotherapy of the 9L gliosarcoma: controlled release polymers for drug delivery in the brain*. Cancer Res, 1993. 53(2): p. 329-33.

279. Rhines, L.D., et al., *O6-benzylguanine potentiates the antitumor effect of locally delivered carmustine against an intracranial rat glioma*. Cancer Res, 2000. 60(22): p. 6307-10.

280. Brem, H., et al., *Placebo-controlled trial of safety and efficacy of intraoperative controlled delivery by biodegradable polymers of chemotherapy for recurrent gliomas. The Polymer-brain Tumor Treatment Group*. Lancet, 1995. 345(8956): p. 1008-12.

281. El-Ghannam, A., C.Q. Ning, and J. Mehta, *Cyclosilicate nanocomposite: a novel resorbable bioactive tissue engineering scaffold for BMP and bone-marrow cell delivery*. J Biomed Mater Res A, 2004. 71(3): p. 377-90.

282. Thomson, R.C., et al., *Hydroxyapatite fiber reinforced poly(alpha-hydroxy ester) foams for bone regeneration*. Biomaterials, 1998. 19(21): p. 1935-43.

283. Lee, J.Y., et al., *Transforming growth factor (TGF)-beta1 releasing tricalcium phosphate/chitosan microgranules as bone substitutes*. Pharm Res, 2004. 21(10): p. 1790-6.

284. Tampieri, A., et al., *Porous phosphate-gelatine composite as bone graft with drug delivery function*. J Mater Sci Mater Med, 2003. 14(7): p. 623-7.

285. Cameron, H.U., et al., *The structure of polymethylmethacrylate cement*. Clin Orthop Relat Res, 1974(100): p. 287-91.

286. Tsuchiya, M., et al., *Superoxide generated by cigarette smoke damages the respiratory burst and induces physical changes in the membrane order and water organization of inflammatory cells*. Ann N Y Acad Sci, 1993. 686: p. 39-52.

287. Rosa, M.A., et al., *Acrylic cement added with antiblastics in the treatment of bone metastases. Ultrastructural and in vitro analysis*. J Bone Joint Surg Br, 2003. 85(5): p. 712-6.

288. Levin, P.D., *The effectiveness of various antibiotics in methyl methacrylate*. J Bone Joint Surg Br, 1975. 57(2): p. 234-7.

289. Goodell, J.A., et al., *Preparation and release characteristics of tobramycin-impregnated polymethylmethacrylate beads*. Am J Hosp Pharm, 1986. 43(6): p. 1454-61.

290. Yu, D., et al., *Self-setting hydroxyapatite cement: a novel skeletal drug-delivery system for antibiotics*. J Pharm Sci, 1992. 81(6): p. 529-31.

291. Fan, H. and A.K. Dash, *Effect of cross-linking on the in vitro release kinetics of doxorubicin from gelatin implants.* Int J Pharm, 2001. 213(1-2): p. 103-16.

292. Peter, S.J., et al., *Crosslinking characteristics of an injectable poly(propylene fumarate)/beta-tricalcium phosphate paste and mechanical properties of the crosslinked composite for use as a biodegradable bone cement.* J Biomed Mater Res, 1999. 44(3): p. 314-21.